

A DYNAMIC MONTE CARLO AND
EXPERIMENTAL STUDY OF ORGANIC
SOLAR CELLS

By

Krishna Feron
BSc (Cum Laude)

A THESIS SUBMITTED TO THE UNIVERSITY OF NEWCASTLE
FOR THE DEGREE OF
DOCTORATE OF PHILOSOPHY IN PHYSICS
SEPTEMBER 2013



THE UNIVERSITY OF
NEWCASTLE
AUSTRALIA

Declaration

Statement of Originality This thesis contains no material which has been accepted for the award of any other degree or diploma in any university or other tertiary institution and, to the best of my knowledge and belief, contains no material previously published or written by another person, except where due reference has been made in the text. I give consent to this copy of my thesis, when deposited in the University Library, being made available for loan and photocopying subject to the provisions of the Copyright Act 1968.

Acknowledgement of Collaboration I hereby certify that the work embodied in this thesis has been done in collaboration with other researchers, or carried out in other institutions. I have included as part of each chapter in this thesis a statement clearly outlining the extent of collaboration, with whom and under what auspices.

Acknowledgement of Authorship I hereby certify that the work embodied in this thesis contains substantive components of published papers of which I am a joint author. I have included as part of each relevant chapter in this thesis a written statement attesting to my contribution to the joint publications.

Krishna Feron

Acknowledgements

A research project is never a one-man show and my PhD project is no exception. For this reason, I dedicate this section to thanking everyone who had a significant contribution to my development as a researcher or directly to my PhD project.

I had the pleasure to work with two research groups, the Solar PV team at CSIRO Energy Technology and the Priority Research Centre of Organic Electronics at University of Newcastle. These two groups have a fruitful collaboration and established the Joint Research Centre for Organic Photovoltaics (JRCOE). The expertise and facilities of each group were invaluable in the realisation of this PhD project. I would like to thank CSIRO Energy Technology for giving me the opportunity to work with the JR-COE through their PhD internship programme. Through this programme I not only received financial support, but the programme also enhanced my PhD experience by allowing me to be an employee of CSIRO in addition to being a student at University of Newcastle.

I am grateful for the guidance that I received from my supervisors Dr Chris Fell, Prof Paul Dastoor, Dr Warwick Belcher and Dr Xiaojing Zhou. Chris and Paul not only guided me through the PhD research process, but also looked beyond the PhD period and helped me to grow as a scientist. Paul's enthusiasm and inherent desire to help people in their professional and personal development have made my PhD journey an enjoyable one. In addition to my four official supervisors, I would also like to acknowledge Tim Nagle for his help and guidance in developing the photocurrent mapping system. I am also grateful for the helpful discussions that I had with members

of either research groups.

Several factors contribute to a person's success. In addition to all the professional help I received, I was also fortunate to be surrounded by a supporting family. I thank my sister for her moral support throughout my PhD. Finally, I would like to express my endless gratitude to my mother and father who have helped me in every aspect of my life including this PhD project. Their guidance and support were key to my success and allowed me to be the best that I can be.

List of Publications

- K. Feron, X. Zhou, W. J. Belcher and P. C. Dastoor, *Exciton transport in organic semiconductors: Förster resonance energy transfer compared with a simple random walk*. Journal of Applied Physics **111**, 044510 (2012)
- K. Feron, C. J. Fell, L. J. Rozanski, B. B. Gong, N. Nicolaidis, W. J. Belcher, X. Zhou, E. Sesa, B. V. King and P. C. Dastoor *Towards the development of a virtual organic solar cell: An experimental and dynamic Monte Carlo study of the role of charge blocking layers and active layer thickness*. Applied Physics Letters **111**, 193306 (2012)
- K. Feron, T. J. Nagle, L. J. Rozanski, B. B. Gong and C. J. Fell *Spatially-resolved photocurrent measurements of organic solar cells: Tracking water ingress at edges and pinholes*. Solar Energy Materials and Solar Cells **109**, 169-177 (2013)
- K. Feron, W. J. Belcher, C. J. Fell and P. C. Dastoor *Organic solar cells: Understanding the role of Förster Resonance Energy Transfer*. International Journal of Molecular Sciences **13**, 17019-17047 (2012)

Contents

| | |
|--|------------|
| Declaration | iii |
| Acknowledgements | v |
| List of Publications | vii |
| Abstract | xv |
| 1 Context | 1 |
| 2 Organic Photovoltaics | 5 |
| 2.1 Introduction | 5 |
| 2.2 Photoconversion mechanism | 6 |
| 2.2.1 Organic semiconductors | 6 |
| 2.2.2 Optical properties | 7 |
| 2.2.3 Exciton creation and transport | 9 |
| 2.2.4 Exciton dissociation mechanisms | 12 |
| 2.2.5 Charge-transfer state | 15 |
| 2.2.6 Charge transport | 15 |
| 2.2.7 Charge extraction | 17 |
| 2.2.8 Overview of the photoconversion mechanism in organic solar cells | 18 |
| 2.3 Device architectures | 19 |
| 2.3.1 Bilayer structure | 19 |

| | | |
|----------|--|-----------|
| 2.3.2 | Bulk heterojunction structure | 20 |
| 2.3.3 | Interdigitated structure | 22 |
| 2.3.4 | Nanoparticle structures | 24 |
| 2.4 | Modelling organic photovoltaic devices | 25 |
| 2.4.1 | Electrical equivalent circuit model | 25 |
| 2.4.2 | Drift-diffusion based modelling | 26 |
| 2.4.3 | Dynamic Monte Carlo model | 27 |
| 2.5 | Stability | 28 |
| 3 | Experimental | 29 |
| 3.1 | Device fabrication | 29 |
| 3.1.1 | Substrate preparation | 30 |
| 3.1.2 | Spin-coating thin films | 31 |
| 3.1.3 | Evaporative deposition | 32 |
| 3.1.4 | Encapsulation | 33 |
| 3.2 | Device and materials characterisation | 33 |
| 3.2.1 | UV-VIS absorption spectroscopy | 33 |
| 3.2.2 | Photoluminescence measurements | 33 |
| 3.2.3 | Profilometry | 33 |
| 3.2.4 | Atomic Force Microscopy | 34 |
| 3.2.5 | X-ray photoelectron spectroscopy depth profiling | 34 |
| 3.2.6 | Current-voltage characteristics | 34 |
| 3.2.7 | External Quantum efficiency measurements | 37 |
| 4 | Monte Carlo modelling | 39 |
| 4.1 | Introduction | 39 |
| 4.2 | Monte Carlo method | 41 |
| 4.3 | Setting up the morphology | 47 |
| 4.4 | Light absorption | 50 |
| 4.5 | Energy considerations | 51 |
| 4.5.1 | The Gaussian energetic disorder model | 52 |

| | | |
|----------|--|------------|
| 4.5.2 | Built-in electric field | 54 |
| 4.5.3 | Coulomb interaction | 55 |
| 4.5.4 | Surface charge induced at the electrodes | 56 |
| 4.6 | Exciton transport and recombination | 56 |
| 4.6.1 | Förster Resonance Energy Transfer | 59 |
| 4.6.2 | Random Walk | 61 |
| 4.7 | Charge Transport | 62 |
| 4.7.1 | Miller-Abrahams expression | 63 |
| 4.7.2 | Marcus theory | 63 |
| 4.8 | Charge extraction and injection at electrodes | 68 |
| 4.9 | Charge recombination | 74 |
| 4.10 | Determining performance parameters from simulations | 76 |
| 5 | Förster resonance energy transfer theory compared to a simple random walk | 81 |
| 5.1 | Introduction | 81 |
| 5.2 | Simulation Methodology | 84 |
| 5.3 | Results and Discussion | 86 |
| 5.3.1 | Validation of the implementation of FRET | 86 |
| 5.3.2 | Impact of fabrication process on energetic disorder | 86 |
| 5.3.3 | FRET compared with a random walk: exciton diffusion | 88 |
| 5.3.4 | FRET compared with a random walk: photoluminescence | 89 |
| 5.3.5 | FRET compared with a random walk: energy relaxation and long-range hopping | 92 |
| 5.3.6 | Exciton diffusion and sensitivity to domain size variations | 97 |
| 5.4 | Conclusion | 99 |
| 6 | Experimental validation of the dynamic Monte Carlo model: thickness dependence of organic photovoltaic performance and the impact of charge blocking layers | 101 |
| 6.1 | Introduction | 101 |

| | | |
|----------|--|------------|
| 6.2 | Experimental and modelling aspects | 102 |
| 6.3 | Results and Discussion | 109 |
| 6.3.1 | Thickness dependence of IQE and J_{SC} | 109 |
| 6.3.2 | Charge blocking layers | 109 |
| 6.3.3 | Recombination mechanisms | 111 |
| 6.3.4 | XPS analysis of interfaces | 112 |
| 6.4 | Conclusion | 117 |
| 7 | Anomalous current-voltage behaviour | 119 |
| 7.1 | Introduction | 119 |
| 7.2 | Simulation methodology | 123 |
| 7.3 | Results and discussion | 128 |
| 7.3.1 | Effect of energy traps on exciton transport | 128 |
| 7.3.2 | Traps in the bulk compared with traps at the electrode interfaces | 132 |
| 7.3.3 | Injected charge carriers vs photo-generated charge carriers | 135 |
| 7.3.4 | Charge recombination and s-shape severity | 137 |
| 7.3.5 | Isolating the effect of the compositional donor-acceptor distribu- tion at electrodes on I-V curves | 141 |
| 7.4 | Conclusion | 144 |
| 8 | Assessing nanoparticle morphologies | 147 |
| 8.1 | Introduction | 147 |
| 8.2 | Experimental and modelling aspects | 148 |
| 8.2.1 | Device fabrication and characterisation | 148 |
| 8.2.2 | Simulation parameters | 149 |
| 8.3 | Results and discussion | 149 |
| 8.3.1 | STXM imaging | 149 |
| 8.3.2 | Constructing the 3D morphology | 153 |
| 8.3.3 | Photovoltaic performance and nanoparticle size | 157 |
| 8.4 | Conclusion | 162 |

| | |
|--|------------|
| 9 Mapping photocurrent | 165 |
| 9.1 Introduction | 165 |
| 9.2 Experimental aspects | 167 |
| 9.2.1 Light beam induced current setup | 167 |
| 9.2.2 Beam profiling | 168 |
| 9.2.3 Intensity considerations | 170 |
| 9.3 Results and discussion | 171 |
| 9.3.1 Evaporative deposition: shadowing effect | 171 |
| 9.3.2 True photoactive area | 174 |
| 9.3.3 Identifying the impact of visual defects | 182 |
| 9.4 Conclusion | 189 |
| | |
| 10 Diffusion limited degradation | 191 |
| 10.1 Introduction | 191 |
| 10.2 Experimental and modelling aspects | 193 |
| 10.2.1 Device fabrication | 193 |
| 10.2.2 Environment control | 194 |
| 10.2.3 One-diode model | 195 |
| 10.3 Results and discussion | 195 |
| 10.3.1 General observations of encapsulated devices | 195 |
| 10.3.2 General observations in non-encapsulated devices | 196 |
| 10.3.3 Identifying the diffusant | 198 |
| 10.3.4 Searching for an oxide layer | 200 |
| 10.3.5 Degradation length | 200 |
| 10.3.6 Quantifying the increase in water uptake due to PEDOT:PSS | 203 |
| 10.3.7 Extracting the diffusion coefficient | 204 |
| 10.3.8 Quantifying ingress at pinholes | 206 |
| 10.3.9 Ingress in devices with a silver cathode | 209 |
| 10.3.10 Optimising lateral design for device durability | 210 |
| 10.4 Conclusion | 214 |

| | |
|---|------------|
| 11 Conclusion and Further Work | 217 |
| 11.1 Conclusion | 217 |
| 11.2 Further Work | 222 |
| A Random walk diffusion length relations | 225 |
| References | 227 |

Abstract

The main focus of this thesis was to develop a dynamic Monte Carlo (DMC) model that could act as a virtual organic solar cell, which would then be used to analyse and predict OPV performance.

The photoconversion process in organic solar cells consists of several molecular processes: light absorption, exciton transport, exciton dissociation, charge transport and extraction. The optical field and thus exciton generation profile is determined using transfer matrix techniques. Exciton transport is modelled using Förster resonance energy transfer (FRET) theory. Charge transport is described using Marcus theory and charge injection is known to follow Miller-Abrahams expressions. The DMC approach provides a platform where these various theories can be combined to model the entire photoconversion process.

Exciton transport can be modelled using a simple random walk or using a more rigorous and computationally more intensive theory such as FRET theory. The DMC model was used to investigate the consequence of either theories on exciton dissociation and charge transfer state separation. A random walk is computationally more efficient than FRET and is the preferred approach when modelling single component systems as found in photoluminescence experiments. However, neglecting energy relaxation and non-nearest neighbour hops leads to an underestimation of geminate recombination and an overestimation of photocurrent up to 2 % in organic solar cells.

Experimental validation of the DMC model was provided by modelling and experimentally measuring external quantum efficiency and short-circuit current as a function

of active layer thickness. Excellent agreement was found and the model was further used to analyse charge selectivity at the electrodes, interface recombination and bulk recombination. It was found that interface recombination is dominant for thin active layers and that a substantial gain in performance is expected by improving charge selectivity at the electrodes, in particular the anode.

Full I-V curves can be calculated using the DMC model. This capability was used to investigate s-shaped I-V curves. Electron traps were only found to induce s-shaped I-V behaviour when the traps are located at the electrode interfaces. Injected charge carriers do not induce s-shaped I-V curves; photogenerated charge carriers are necessary to observe this behaviour. Simulations suggest that OPV material systems that exhibit less charge recombination are more likely to exhibit s-shaped I-V curves. The open-circuit voltage does not always coincide with the centre of the 's' and could be changed by tuning charge recombination. DMC modelling was further used to investigate why thermal annealing removes s-shaped behaviour. Results suggest that vertical phase composition at the electrodes is not the cause of inflected I-V curves, rather charge traps is the cause of this anomalous behaviour. Energy traps were also found to affect exciton transport as they reduce the exciton diffusion length.

DMC models take into consideration the three dimensional nanostructure of the photoactive layer. This capability was used to investigate core-shell nanoparticle morphologies. Annealing was found to improve the efficiency of nanoparticle devices and modelling suggests that different annealing conditions to what is commonly used for BHJ devices are needed to increase the efficiency further. In addition, simulations indicate that annealing conditions should be re-optimised when changing the nanoparticle size. The performance of core-shell nanoparticles approaches that of the BHJ morphology, when optimised for both feature size and nanoparticle size. Hence, the core-shell morphology does not necessarily severely limit charge extraction and, in theory, optimised nanoparticle devices should yield similar efficiencies as optimised BHJ devices.

A high resolution light beam induced current (LBIC) setup was developed and used to investigate lateral non-uniformities that are the result of imperfect fabrication

techniques or degradation.

The primary degradation mechanism in standard organic solar cells is water diffusion limited oxidation of the aluminium cathode. A diffusion model was applied, which allowed for the determination of the diffusion rate and also the diffusivity of water in PEDOT:PSS. Diffusion through pinholes is quantified to be significantly slower than diffusion at the cathode edge. Lateral device design was shown to substantially influence the degradation rate and pattern.

1

Context

Mankind has witnessed an enormous increase in power consumption during the last 100 years. While in 1890 the yearly energy use per inhabitant was about 5800 kWh it reached 20200 kWh in 1970 [1]. Since 1970 the energy use has dropped to the present level of 19000 kWh, however the human population is still increasing rapidly. It is estimated that the world population will reach approximately 9 billion by 2050 [2, 3]. At the moment most of our energy is derived from fossil fuels. Fossil fuels produce greenhouse gas emissions, which is an environmental concern. Hence, other energy paradigms consisting of economical renewable energy sources have been investigated. Besides environmental concerns there are also political issues that favour the transition to renewable energy sources. Furthermore, the Earth's reserves of fossil fuels are finite and are likely to become resource depleted in this century [4]. All future scenarios of

the worldwide energy portfolio describing the transition to renewables include photovoltaics [2, 3]. In fact, most of them describe solar energy as one of the main sources of energy in the future [2, 3]. The earth receives 1.7×10^{14} kW from the sun, which is about 10,000 times more than the present energy consumption [5]. Photovoltaic (PV) conversion is the direct conversion of (sun)light into electricity by means of solar cells. Although the photovoltaic effect was discovered in 1839 by Edmund Becquerel, attempts at commercialization did not begin until more than a century later [6]. Crystalline silicon PV is the most mature type of solar cell in terms of commercialization and dominate the PV market [4]. Organic photovoltaics (OPV), on the other hand, have attracted a lot of attention in the last three decades only [5]. OPV offer the long-term potential of economically viable large-scale power generation as organic solar cells can be fabricated using high throughput, low-temperature approaches that employ established coating and printing techniques in a roll-to-roll process [7]. Compared to silicon based device fabrication techniques, these have the potential to be low-energy consuming techniques that require less capital investment [8]. Organic semiconductor materials are compatible with plastic substrates and have high absorption coefficients allowing fabrication of thin film flexible solar cells. All these advantages are compelling arguments favouring OPV if their efficiencies are good enough to be compared to inorganic PV. However, at the moment, the efficiency of organic solar cells at a module scale are still low. OPV devices on a small scale have been shown to exhibit efficiencies in excess of 10 % [9], but efficiency drops rapidly with increasing cell size. Module efficiency are generally around 2 % [10, 11]. The second drawback is the instability of OPV devices as they are susceptible to degradation, which may be induced by oxygen and/or water (i.e. ambient air).

The scope of this thesis includes modelling organic solar cells with the aim of creating a virtual organic solar cell. A virtual organic solar cell allows for easy exploration of individual material and device properties that are difficult to achieve in real-life experiments. Furthermore, such a model provides access to parameters that are not measurable or are difficult to measure. Device fabrication is difficult and costly (both in terms of materials and time), but a virtual solar cell would allow us to explore

many device scenarios without having to build them. In this manner device optimisation may be much faster and the lessons learned from the virtual solar cell could be immediately implemented in real solar cells. Chapter 2 describes the general device physics of organic solar cells. Chapter 3 serves to capture all experimental details of the work conducted for this thesis. In chapter 4, the dynamic Monte Carlo model, that is developed and acts as a virtual organic solar cell, is described. Chapter 5 focuses on exciton transport dynamics and compares two different modelling approaches. Chapter 6 compares experimentally measured performance with simulated performance. Excellent agreement is found thus validating the effectiveness of the dynamic Monte Carlo model. In this chapter, the impact of the photoactive layer thickness that of charge blocking layers are evaluated. Chapter 7 demonstrates that the model is capable of producing full current-voltage characteristics, which is the standard way of assessing photovoltaic performance. A model becomes more useful if it is capable of describing both efficient and inefficient devices. As such, the model is used to also assess inefficient anomalous effects experimentally seen in current-voltage measurements. Dynamic Monte Carlo models allow for assessing different kinds of morphologies. The advantage of this type of modelling is utilised to assess core-shell nanoparticle morphologies in chapter 8. When comparing modelled results to simulated results, it is important to take into consideration the variability in the fabrication process of organic solar cells. A photocurrent mapping technique was developed and used to assess spatial variations in current produced by an organic photovoltaic device. Several spatial effects are identified and discussed in chapter 9. Degradation effects can also affect the measured device performance and thus cloud the comparison of modelled and experimental measurements. Hence, the primary degradation mechanism is analysed in chapter 10. In this chapter, the use of a photocurrent mapping technique in assessing diffusion limited degradation processes is demonstrated.

2

Organic Photovoltaics

2.1 Introduction

This chapter describes the photoconversion mechanism whereby photons are converted to electrons in two distinct stages. Firstly, light is absorbed by the photoactive material, resulting in bound electron-hole pairs (excitons). After dissociation of these excitons, the free charge carriers can be transported to the appropriate electrodes giving rise to a photocurrent and photovoltage. Various device architectures are discussed as well as three common modelling approaches. One of these approaches is chosen to form the basis of the model that is developed in this thesis.

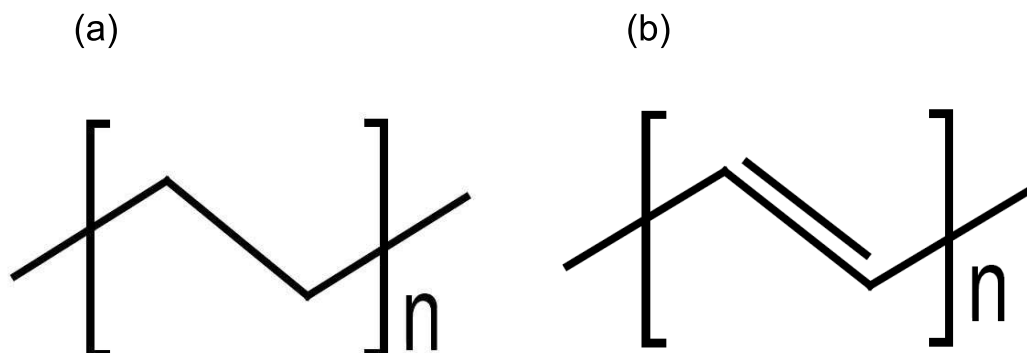


FIGURE 2.1: (a) polyethylene (non-conjugated) and (b) polyacetylene (conjugated).

2.2 Photoconversion mechanism

2.2.1 Organic semiconductors

Conjugated polymers are organic semiconductors and form the photoactive component in organic solar cells. The ability of conjugated polymers to behave like semiconductors find its origin in the molecular structure of these materials. Non-conjugated polymers have single bonds between each carbon atom (C-C-C-C-C) and are good insulators, i.e. the electronic (and optical) band gap is large. An example of a non-conjugated polymer is polyethylene and is shown in Figure 2.1(a). C-atoms in such a non-conjugated carbon backbone consist of sigma bonds only. Sigma bonded polymers generally have a large band gap and are consequently good insulators that do not absorb light in the visible spectrum [12]. Polyethylene has a band gap of 8 eV [12]. Conjugated polymers, on the other hand, are different, because they have alternating single and double or triple bonds (e.g. C-C=C-C=C). As a result, sigma and pi bonds are formed [13] as depicted in Figure 2.2. Pi electrons are generally more mobile than sigma electrons and can move by hopping from site to site [14]. Electrons in the p_z orbital are delocalised, meaning that they are in an orbital that extends over several atoms. The simplest example of a pi-conjugated system (not a polymer) is the benzene ring in Figure 2.2. The p_z orbital splits into two states, the bonding pi state and the antibonding pi* state, which correspond to the highest occupied molecular orbital,

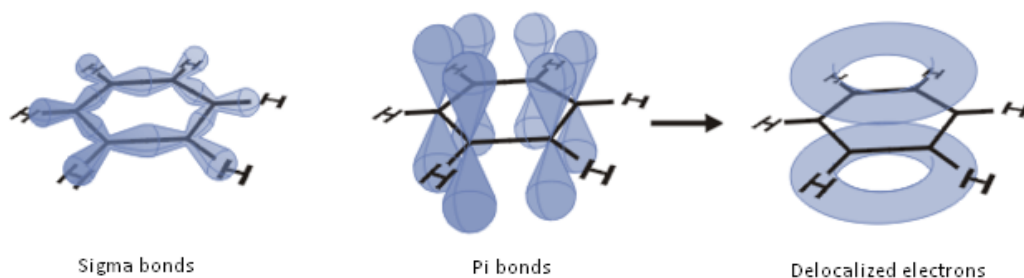


FIGURE 2.2: Alternating double bonds lead to pi bonds and give rise to delocalized electrons. Modified from [15].

HOMO, and the lowest unoccupied molecular orbital, LUMO, respectively [16]. There are no allowed states between the HOMO and LUMO and their energy difference is called the band gap energy. Roughly speaking, the HOMO corresponds to the valence band in the band structure model and the LUMO relates to the conduction band. However, it is incorrect to speak of conduction and valence bands when dealing with organic semiconductors, because there are not enough neighbouring molecules that sufficiently interact with each other to form a continuum of energy levels; the discrete nature of the energy levels can still be perceived and thus charge carriers hop between localised states instead of undergoing band transport [17]. Polyacetylene is a conjugated polymer, which looks similar to polyethylene, see Figure 2.1. However polyacetylene is conjugated and has a band gap of approximately 1.5 eV [18] as opposed to 8 eV for polyethylene. Conjugated polymers may therefore be referred to as organic semiconductors (as opposed to insulators).

2.2.2 Optical properties

An electron can be promoted from the HOMO to the LUMO by absorption of a photon and is also known as a $\pi - \pi^*$ transition, see Figure 2.3. The energy band gap determines which portion of the solar spectrum is efficiently absorbed. Commonly used OPV materials have a large (relative to silicon) optical band gap (typically 2.2 eV). Therefore only the short wavelength part of the spectrum is utilized. Also, the absorption bands are narrow compared to inorganic semiconductors, which means that

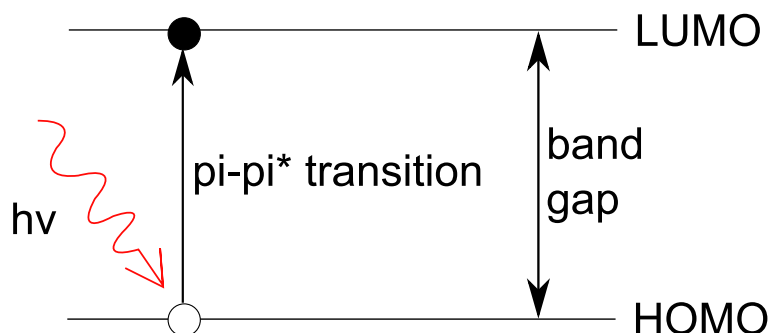


FIGURE 2.3: An electron (black dot) is promoted from the HOMO to the LUMO by absorption of a photon (red wiggly line) with energy ($h\nu$) equal to or larger than the band gap. After excitation of the electron, a hole (white dot) is created as well.

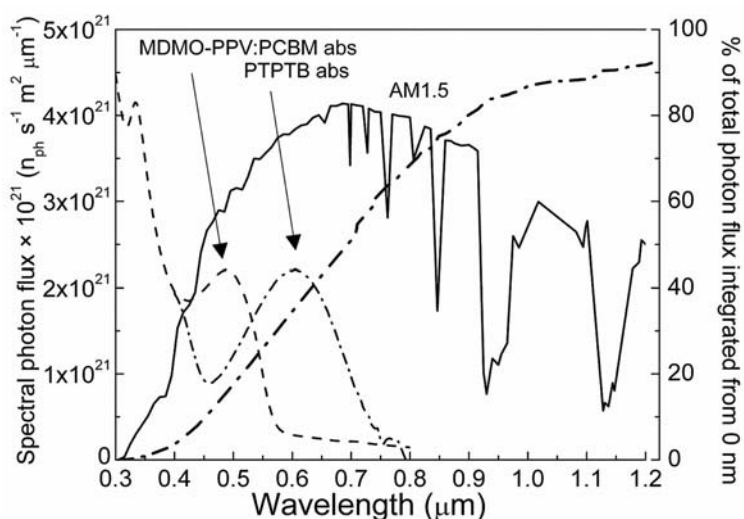


FIGURE 2.4: Absorption spectra of a MDMO-PPV:PCBM blend and a low band gap organic material. AM1.5 solar spectrum (solid line) and its integrated photon flux are also shown. After [23].

most of the solar spectrum remains unused [19]. Assuming that all photons with energy equal or higher than the band gap are absorbed, a band gap of 1.1 eV (silicon) is required to absorb 77 % of the solar spectrum. Unfortunately the majority of the semiconducting polymers have band gaps higher than 1.9 eV, which means that they cannot absorb more than 30 % of the solar spectrum [20]. Consequently, substantial efforts have been focussed on developing low band gap polymers [19, 21, 22]. An example of a low band gap polymer is shown in Figure 2.4 along with the absorption spectrum of a typical OPV device. To put these absorption spectra in a relevant

context, the AM1.5 solar spectrum and its integrated total flux are also shown. A significant amount of research is directed to harvesting the high wavelength part of the visible spectrum and it has proven to be a challenge to lower the band gap while still maintaining good device performance. While lowering the band gap will lead to more light absorption, the maximum attainable open circuit voltage (open circuit voltage is discussed in section 3.2.6) decreases linearly with the band gap [24, 25]. Hence, an optimum band gap exists. Organic thin films show optical absorption coefficients exceeding 10^5 cm^{-1} at the maximum of their absorption spectrum [19] and thus offer the possibility of very thin solar cells [20, 26]. Organic photoactive film thicknesses of a few hundred nm are sufficient to absorb most of the light at the peak absorption wavelength. The high absorption may be the result of direct band gap transitions [27–29].

Photovoltaics devices are normally constructed in a stacked layered fashion. Each layer has its purpose, but also its own distinct optical properties (index of refraction and layer thickness). Reflections at interfaces and interference effects occur. These effects affect the distribution of the optical field inside the device and are especially important in thin film devices where layers are thinner than the penetration depth and the wavelength of the incident light [30]. Highly reflective back electrodes such as the commonly used aluminium electrode enhance these effects even more. Figure 2.5 illustrates the change in the optical field when the thickness of a single layer is altered. An optically transparent spacer, with the goal of spatially redistributing the light in the device, has been introduced and resulted in improved power conversion efficiency due to increased light absorption in the photoactive layer [31]. It is important to consider the distribution of the optical field in the device when designing optimal device configurations [30, 31].

2.2.3 Exciton creation and transport

The conjugated aspect of organic semiconductors together with a low dielectric constant ($\epsilon_r \sim 2 - 4$ as opposed to ~ 10 for inorganic semiconductors) gives rise to a

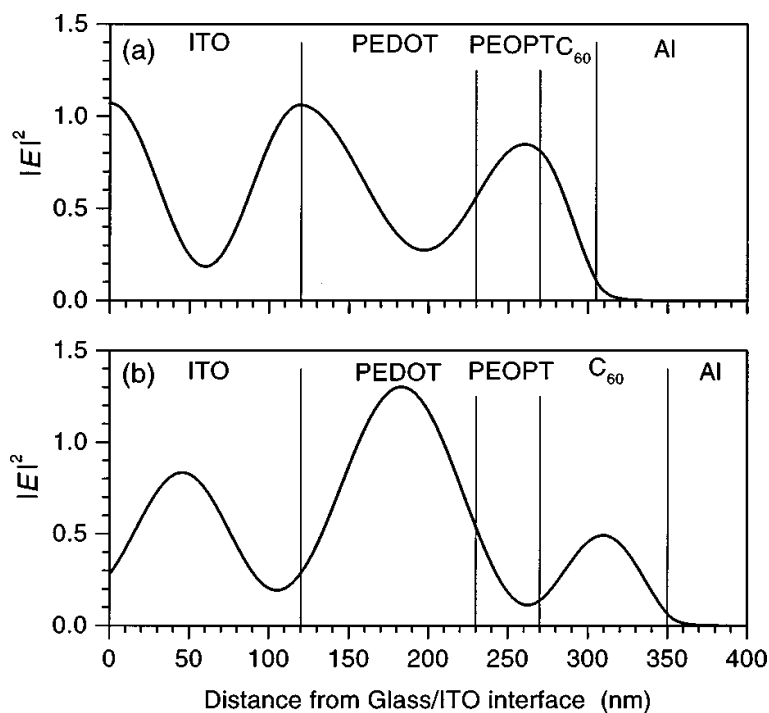


FIGURE 2.5: Calculated electric field, $|E^2|$, in a device with a C_{60} layer thickness of 35 nm (top) and 80 nm (bottom) for a wavelength of 460 nm. The thickness of the other layers were kept constant. Obtained from [30].

different photo conversion mechanism than that commonly found in inorganic solar cells [32]. Whereas free charge carriers are created directly in inorganic solar cells, bound electron-hole pairs (or excitons) are created upon light absorption in organic devices [33]. As such, the exciton population is directly related to the number of absorbed photons [34] and it is thus important to accurately determine the optical field in the device when modelling organic solar cells [30, 31]. The exciton is a mobile excited state and is electrically neutral. This electron-hole pair experiences strong Coulomb attraction owing to the low dielectric constant. Furthermore, the weak intermolecular forces localize the exciton on the molecules causing electron-hole pairs to also be structurally bound [20, 35]. The magnitude of the exciton binding energy has been of particular interest in the scientific community, because it plays an important role in the understanding of primary photoexcitations in polymers. In general, photon absorption may induce excitons with binding energies ranging from 0.05 to 1 eV [32]. The lower end of this range is associated with so called Wannier type excitons [19]. These are

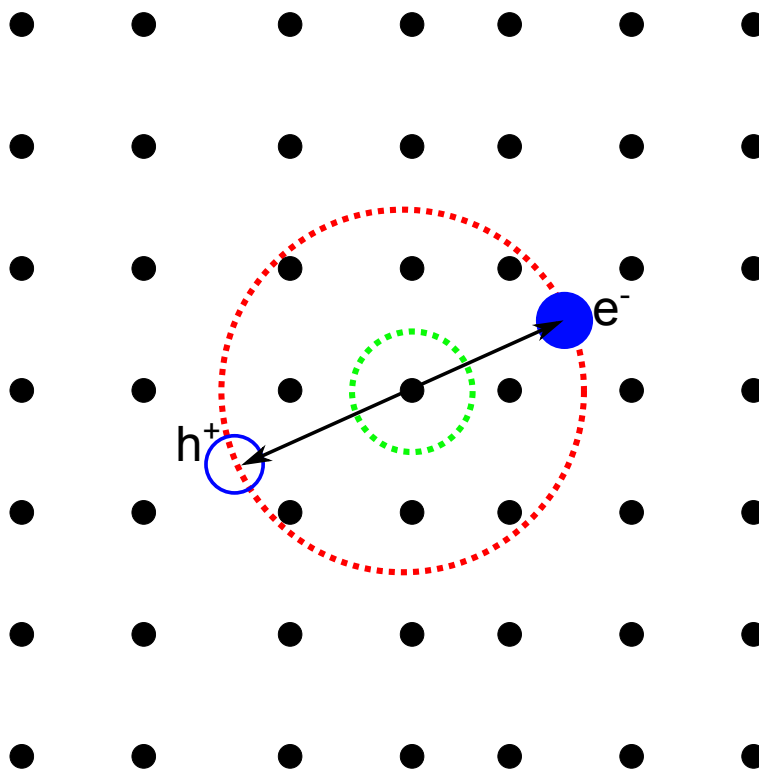


FIGURE 2.6: Depiction of the difference between a Wannier and a Frenkel exciton. The black dots represent a molecular lattice. A Wannier exciton consisting of an electron (blue filled dot) and hole (blue open dot) is shown together with a red dotted circle and arrows to indicate the electron-hole distance. The green circle represents the electron-hole distance of a Frenkel exciton. The Frenkel exciton essentially resides on a single molecule whereas the Wannier exciton is delocalised across multiple molecules.

relatively weakly bound and the electron-hole distance is relatively large. The ground bound state has a radius of tens of lattice constants (lattice constant is $\sim 10^{-9}$ m.) [36]. The second type of exciton is the strongly bound Frenkel exciton [19]. Here the electron and the hole are in a ground bound state with an effective Bohr radius approximately a lattice constant or less. The difference between Wannier and Frenkel type excitons is depicted in Figure 2.6. Knupfer and Fink compared the delocalization size of the lowest singlet excitation to the size of the molecule for various molecules including C_{60} and sexithiophene (6T), which are common OPV materials [37]. They confirmed that the exciton is delocalized over the entire molecule and thus confirmed that the electron and hole are both situated on the same molecule or atom. The interaction between Frenkel excitons can be neglected, because of their small radius

[36]. Most studies on organic photovoltaic materials indicate that only Frenkel excitons are generated in state-of-the-art organic photovoltaic devices [20, 35, 37–45]. As such, excitons in the average organic semiconductor are strongly bound and are practically unaffected by internal electric fields [32]. Another significant exciton property is the diffusion length. In many common OPV materials, excitons have a small diffusion length. Limited diffusivity of excitons limit the exciton dissociation efficiency and consequently the generation of free charge carriers [20] as is discussed in more detail in the next section. Although different diffusion lengths have been reported depending on the material, model used and measurement technique [46], they often have the same order of magnitude, 5-30 nm [16]. Evaporated small molecules often exhibit much larger exciton diffusion lengths. Examples are 6T with a diffusion length of 100 nm [47] and C₆₀ with 40 nm [46].

2.2.4 Exciton dissociation mechanisms

In order to generate photocurrent, excitons have to be dissociated into free charge carriers which can then be transported to the appropriate electrodes. Otherwise, excitons will decay and instead either yield photoluminescence or nonradiative back-transfer recombination [20]. In this thesis exciton decay is termed exciton recombination. A typical exciton binding energy (in OPV materials) is of the order of 0.25-1 eV [32] and is the minimum energy required to dissociate the exciton. In this section different dissociation mechanisms are discussed and the most prominent one is identified.

High temperatures

Inorganic semiconductors produce free electrons, because the exciton binding energy is small enough for thermal energy at room temperature (25 meV) to dissociate excitons [20, 48]. Organic semiconductors produce excitons with a binding energy, that is approximately an order of magnitude larger. To dissociate an exciton with a binding energy of 0.26 eV, temperatures of at least 3000 K are required. This option is obviously not viable in a normal environment. Excitons with energies higher than the

pi-pi* transition are called hot excitons. These excitons can fall back in a lower energy state and lose its excess energy. The excess energy is distributed among phonons on the polymer and as a result generating a vibrational hot bath with a temperature above the ambient temperature. This local increase in temperature could lead to exciton dissociation. However, dissipation of the vibronic energy is a fast process (femtosecond range [49]) and only few excitations can dissociate before the polymer cools down [50]. Hence, this way of dissociating excitons is an inefficient one.

High electric fields

High electric fields are able to break the coulomb attraction between the bound electron and hole. Given the typical values for the exciton radius (~ 1 nm), and binding energy (~ 0.25 eV), electric gradient assisted dissociation becomes competitive for fields higher than 10^6 V/cm [32, 48]. However, the electric field provided by the asymmetrical work functions of the electrodes is not sufficient to break up the excitons [20]. Since such high electrical fields are not commonly achieved in normal operating conditions, this option is not viable either.

Electron trap sites

Dissociation can also occur at electronic trap sites leading to one free charge carrier and one trapped carrier [32]. The kinetic factors controlling the probability of exciton dissociation at trap sites are still not well understood [20, 32]. Gregg and Hanna [32] state that electron trapping results in photoconductivity rather than a photovoltaic effect. Nearly all pi-conjugated polymers exhibit photoconductivity in their absorption range. Since impurities may act as charge trapping sites photoconductivity is thought to be the result of these unintended and practically unavoidable impurities [51, 52]. The free carrier yield of this process is low (quantum efficiency of $10^{-5} - 10^{-3}$ [52, 53]), because the dissociation product readily recombines [52]. Furthermore once a trap site is occupied, it cannot immediately be used to dissociate another exciton. Dissociation at trapping sites is thus considered to be a very inefficient process.

Heterointerface

Out of all dissociation mechanisms, by far the most efficient one is a mechanism that utilizes the interface between two different organic materials. This interface is commonly termed a heterointerface or heterojunction. The idea behind a heterojunction is to use two materials with different electron affinities and ionization potentials. The electron is likely to be accepted by the material with the larger electron affinity and the hole by the material with the lower ionization potential thus favouring exciton dissociation [17, 20]. In general the thermodynamic requirement for dissociation is that the band offset (HOMO-HOMO offset and LUMO-LUMO offset) is equal to or greater than the binding energy of the exciton [38]. Dissociation at a polymer-fullerene interface takes place within 50 fs [54]. Competing processes like photoluminescence (\sim ns) and non-radiative recombination of the exciton (\sim μ s) takes place on a much larger timescale [55, 56]. As a result charge separation is efficient and metastable, which means that the otherwise highly luminescent conjugated polymer exhibits strong photoluminescence quenching [57, 58]. The efficiency of the dissociation process is mainly limited by the ability of the exciton to reach the interface before it decays through photoluminescence. It is clear that the exciton diffusion length plays a critical role in the exciton dissociation efficiency. Organic-organic interfaces offer much more efficient exciton dissociation than inorganic-organic interfaces (i.e. at the electrodes) [59]. The reason for this is not fully understood yet [20, 32]. It is the concept of heterointerfaces that led to a breakthrough in performance of polymer based solar cells. In 1979 Tang made the first polymer based bilayer device with power conversion efficiency (PCE) of 1 % [60], which was far greater than efficiencies commonly achieved with single semiconductor devices before 1979 ($\sim 10^{-3}$ %) [61].

In conclusion, the heterointerface is the main dissociation mechanism in organic solar cells and is often treated as the only source of exciton dissociation [62].

2.2.5 Charge-transfer state

Excitons may lead to free charge carriers under the right conditions. However, this is not a one step process. An intermediate state can be distinguished between free charge carriers and excitons. Immediately after exciton dissociation at a heterointerface the electron resides on the electron acceptor LUMO orbital and the hole is localized on the electron donor HOMO orbital, but Coulomb attraction between the electron and hole still remains significantly greater than $k_B T$ (thermal energy) [50, 63]. Consequently, even though the exciton is dissociated, i.e. the electron and hole are situated on different molecules, one cannot refer to the electron and hole as free charge carriers. There exists a widely ranging nomenclature for these bound states including: geminate pair, bound radical ion pair, polaron-polaron pair, charge-transfer exciton, exciplex state and charge-transfer (CT) state [63–69]. Strictly speaking these are not all synonyms as they reflect particular characteristics of these states. For example, the term polaron also includes the accompanying lattice deformations induced by the electron and hole. In other cases different terminology is used to differentiate between thermally hot and thermally relaxed charge transfer states [66]. For simplicity the most common terminology is used in this thesis and all states that are intermediate between excitons and fully dissociated charges are referred to as charge-transfer (CT) states. CT states can recombine just like excitons and yield a measurable characteristic emission that relates to the $\text{HOMO}_{\text{donor}}\text{-LUMO}_{\text{acceptor}}$ gap [69]. Recombination of CT states is called geminate recombination [70]. The local electric field has a major impact on the charge separation efficiency [16]. Only when charge carriers escape their mutual attraction can they be referred to as free charge carriers.

2.2.6 Charge transport

In order to generate a photocurrent and voltage, free charge carriers have to be transported to the appropriate electrodes. However, these free electrons and holes may still recombine. This recombination type is referred to as bimolecular recombination. The difference between geminate recombination and bimolecular recombination is the origin

of the participating electron and hole. If both charge carriers originate from the same exciton the term geminate recombination is used, otherwise the term bimolecular recombination is used. In this thesis the term charge recombination is used to encompass both bimolecular and geminate recombination. It is crucial that dissociated charges get transferred away from the heterointerface, because if they remain near the heterointerface the chance of recombination is substantial given that this is the only location where significant numbers of holes and electrons coexist [32]. Bulk recombination (as opposed to surface recombination) of free charge carriers is the major recombination process in conventional inorganic solar cells, because the same material is used for both electron and hole transport. This recombination mechanism plays a smaller role in organic solar cells, because the bulk density of minority charge carriers is minimal due to the fact that the two carrier types are already separated across the interface upon dissociation and mixing of the two species in one of the moieties is thus prevented [38]. The previously mentioned localised energy level character, as opposed to a band structure, also becomes apparent in charge transport. As a result of the disordered arrangement of the molecules in typical organic semiconductors, the conventional band transport description is not applicable to these polymers. Charges move via thermally assisted intermolecular hopping between localized states, which typically results in lower charge transport mobilities compared to inorganic semiconductors [17, 71]. Some small molecules such as anthracene or pentacene do exhibit high carrier mobilities when evaporatively deposited [72–74]. These materials have been shown to exhibit true band transport, which is attributed to their highly crystalline structure. The mobility of charge carriers in organic materials seems to be highly dependent on morphology (i.e. detailed structure on the micro- to nano-scale) [33]. Morphology is influenced by many factors such as solvent used to spin the thin layer from, drying time, molecular mass, regioregularity, use of functionalized side chains, annealing time and temperature [75–78]. Consequently, mobility is as much material dependent as it is fabrication process dependent.

Charge transport is dominated by the electric field and coulomb interaction with other charge carriers. The latter is especially important within the Coulomb capture

radius (also known as the Onsager radius), which is defined as the radius at which the Coulomb attraction equals thermal energy, $k_B T$ [63, 79, 80]. The Coulomb capture radius is relatively large due to the small dielectric constant exhibited in organic semiconductors. A more in depth treatment of charge transport is given in Section 4.7.

2.2.7 Charge extraction

Once charges have found their way to the electrodes of the right polarity (i.e. electrons are to be extracted at the cathode and holes at the anode) they can be extracted leading to a photocurrent. Charge extraction efficiency at the organic-electrode interface is determined by the energy barrier between the LUMO/HOMO of the organic semiconductor and the work function of the metal electrode. Often a Schottky-Mott approach is taken to estimate these energy barriers, i.e. the work function of the metal is subtracted from the ionization potential of the organic material [71]. This relation holds for some materials. For example, the hole injection efficiency of TPD (a trap free polymer) is found to exponentially increase as the energy barrier decreases [81]. However, organic-electrode interfaces often give rise to a dipole layer, which alters the effective energy barrier [82, 83]. Ohmic contacts are considered best and are realised when the energy barrier is small [81, 84]. Charge extraction properties are commonly altered by inserting thin interface layers [85]. These interface layers often act as charge selective contacts (charge blocking layers), which prevents extraction of one type of charge carrier, but still allows the other type to be extracted. Other functions of interface layers are [85]:

- to decrease the energy barrier between the active layer and the electrode
- to prevent a chemical or physical reaction between the polymer and electrode
- to act as an optical spacer
- to act as an exciton blocking layer (preventing exciton recombination at electrode interface)

- to prevent physical damage to the organic layer when the top electrode is deposited

2.2.8 Overview of the photoconversion mechanism in organic solar cells

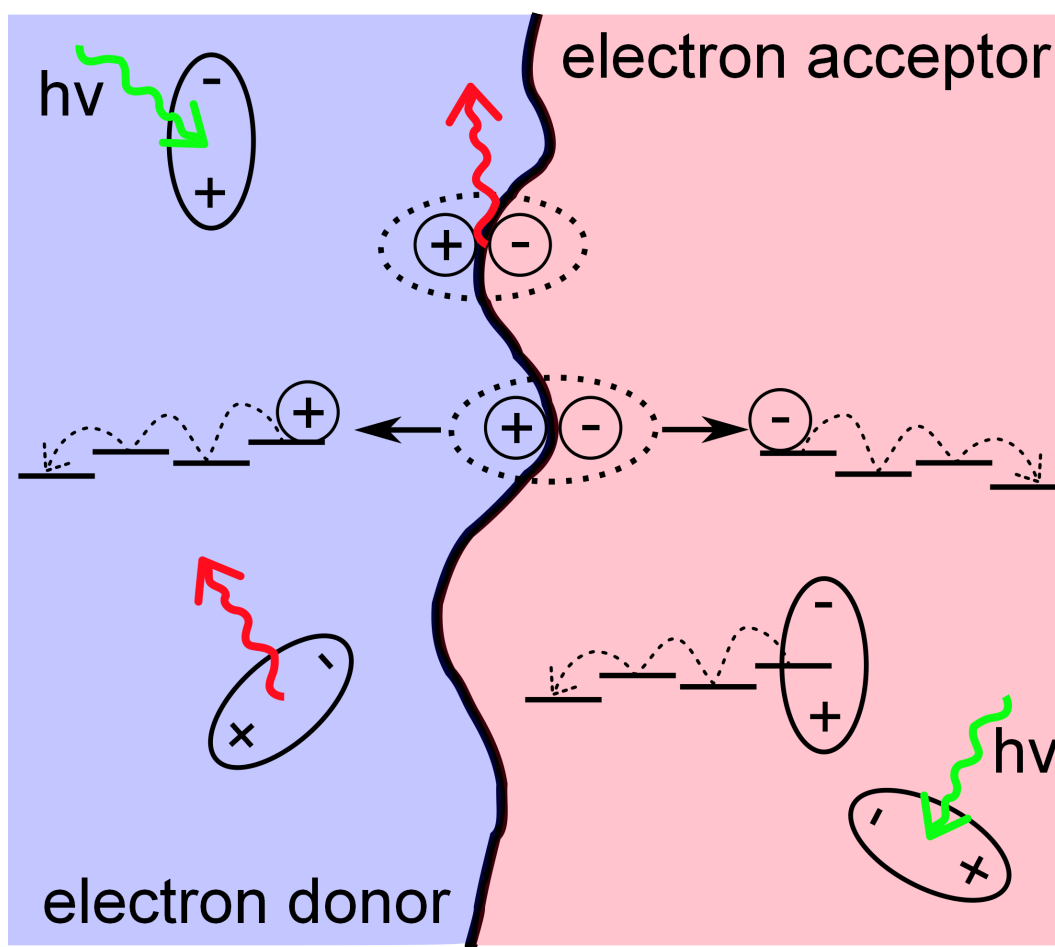


FIGURE 2.7: Summary of relevant processes in an organic photovoltaic device. The black line in the middle is the heterointerface between the electron donor material (purple, left) and acceptor material (pink, right). Excitons are created upon light (green wiggly lines) absorption. Excitons may hop through localised states and recombine (red wiggly line) or reach the heterointerface and form a CT state. The CT state may dissociate into free charge carriers or recombine (red wiggly line). Free charge carriers may hop toward the electrodes, but could still recombine if they meet a charge carrier of the opposite polarity at the heterointerface.

All relevant processes in an OPV device have been separately discussed. Figure

2.7 brings all these processes together and provides a visual summary. Photons are absorbed leading to excitons. In Figure 2.7 absorption occurs in the electron donor material only and although not shown in Figure 2.7 absorption readily occurs in the electron acceptor material as well. Excitons hop through localised energy levels and when they reach a heterointerface, they dissociate by donating an electron to the electron accepting material, while the hole stays in the hole transporting material. For excitons that are created in the acceptor material, dissociation occurs by donating a hole to the electron donor material, while the electron remains in the acceptor material. These separated charges still experience significant Coulomb attraction and although structurally separated they remain in a bound state with a finite lifetime [86]. If they do not recombine, they may find their way to an electrode where they are extracted and enter the external circuit. Once excitons are created, several recombination processes can occur: exciton recombination, geminate recombination, bimolecular recombination and charge extraction at the opposite polarity electrode.

2.3 Device architectures

In this section organic photovoltaic axial device architectures will be discussed. The axial (as opposed to lateral) axis is shown in Figure 2.8. The axial architecture refers to content of the stacked layers. In the previous sections it has become clear that morphology plays a key role in the performance of the device. Well designed axial architectures have already ushered in a new generation of organic solar cells; bulk heterojunction devices with efficiencies up to 10 % [9]. More advances in cell architecture may lead to improved charge extraction and exciton dissociation.

2.3.1 Bilayer structure

Excitons do not dissociate readily in most organic semiconductors and a heterojunction is needed. The simplest heterojunction architecture is the bilayer, see Figure 2.8. Indium tin oxide (ITO) is usually used as the front contact, because it is both transparent and conductive. On top of the ITO a thin layer of poly(3,4-ethylenedioxythiophene)poly(styrenesul

(PEDOT:PSS) is deposited to act as an electron blocking layer and to improve hole injection [87]. The hole conducting and light absorbing polymer is layered on top of the PEDOT:PSS. On top of that an electron conducting and light absorbing layer (usually a fullerene like PCBM) is placed to facilitate the planar heterojunction. Aluminium is commonly used as the back contact. A thin interface layer (such as LiF or bathocuproine) in between the aluminium and electron accepting layer can be included to improve device performance. Tang [60] made the first bilayer device with an efficiency of 1 %, which was a breakthrough at the time. In 1992 Sariciftci et al. [88] discovered photoinduced charge transfer from a polymer (MEH-PPV) to a buckminsterfullerene (C60) in a bilayer structure and observed high charge-transfer rates which further improved the efficiency of the device. The bilayer structure exhibits minimal bimolecular recombination. However, since only the excitons within approximately a diffusion length of the acceptor-donor interface have the possibility of contributing to photocurrent, most excitons recombine. In the case of PPV/C60, the photoactive layer contributing to photocurrent is only 10-30 nm thick [57, 89–91]. The poor exciton dissociation efficiency is the biggest downside of a bilayer architecture. Therefore other structures have been sought to increase the interfacial heterojunction area.

2.3.2 Bulk heterojunction structure

To overcome the deficiency of the bilayer structure, the interface area between the two active components need to be increased. Bulk heterojunction (BHJ) devices are designed to address this issue [92, 93], while still maintaining ease of fabrication, i.e. compatibility with large area printing and coating techniques that have the potential to be easily up-scaled. Figure 2.9 illustrates the BHJ structure. The two components are mixed in a common solvent. Commonly used solvents are chloroform, dichlorobenzene and toluene. Materials suitable for BHJ devices must be soluble in common solvents, which is realised by adding functional groups to the molecules. The obtained solution blend is then deposited, whereafter the solvent evaporates and a thin film comprising a mixture of the two active components remains. The morphology of this two component

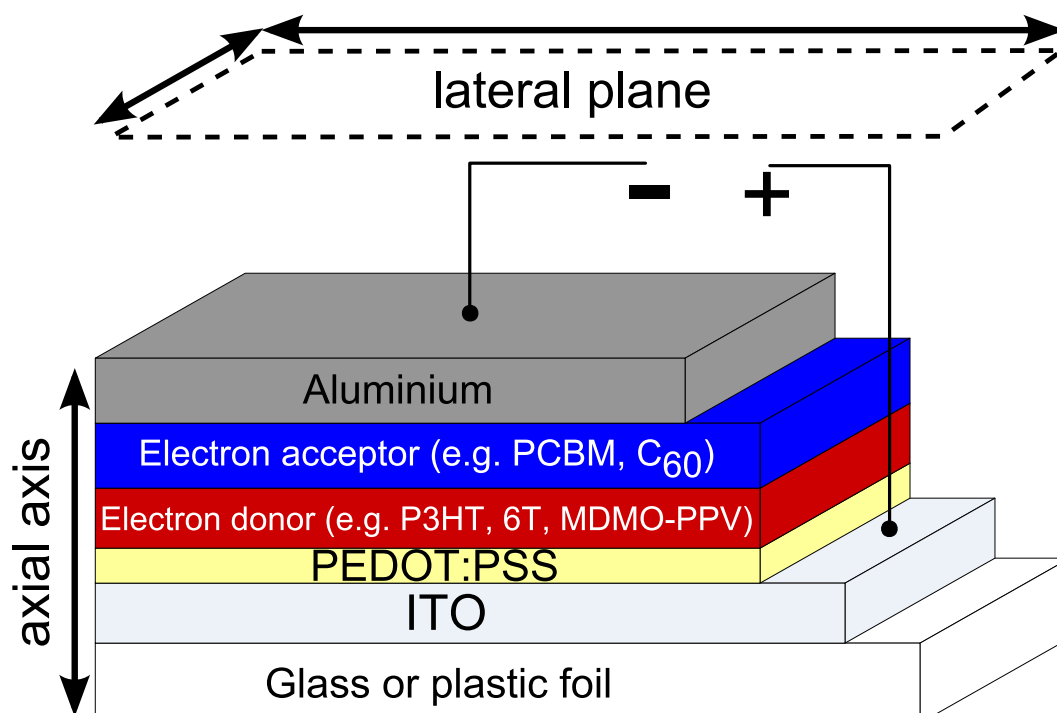


FIGURE 2.8: Bilayer device architecture. Axial and lateral directions are also shown.

system is often optimised through thermal annealing. A temperature larger than the glass transition temperature is used to induce a rearrangement of the two moieties [94]. Molecular rearrangement can also be realised using a solvent annealing technique [95, 96], where the active layer is exposed to a solvent vapour. Photoluminescence is almost completely quenched in BHJ devices [94, 97, 98], which shows that the exciton dissociation probability is high due to the large heterointerface area. The downside of a large heterointerface is that the probability of charge carriers of the opposite polarity meeting each other is large. Hence, bimolecular recombination is larger in these devices compared to a bilayer structure. In addition, islands that are not connected to the electrode may be present in BHJ structures. Charge carriers generated in these islands will not be able to get out of the device and are thus lost [70]. The alignment of the heterointerface in BHJ devices is not (always) perpendicular to the electric field (it is randomly oriented) as it is in a bilayer device. Hence, also relatively more geminate recombination is predicted [70]. These charge transport and charge carrier recombination issues are influenced through annealing techniques. An interpenetrating,

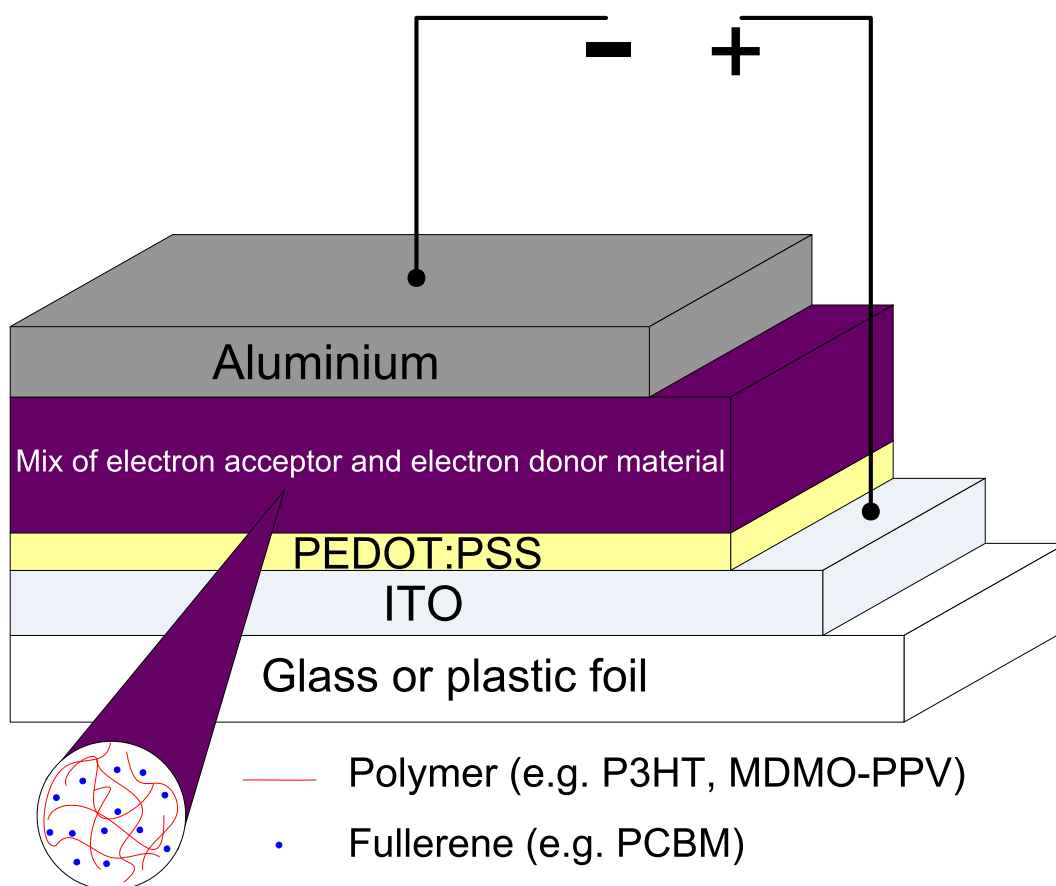


FIGURE 2.9: Bulk heterojunction device architecture

continuous network with a domain size of tens of nanometers is necessary for optimum morphologies. To date, the highest efficiencies have been realised using the BHJ device structure [99].

2.3.3 Interdigitated structure

Throughout this thesis multiple references are made to morphology and its consequences. A structure with a domain size on the order of the diffusion length and clear pathways to electrodes are key to high performing devices. Contemplation on optimal structure has lead to the ideal architecture [33, 100] see Figure 2.10. Besides performance related facets this ordered structure is easier to understand and model which adds to its scientific appeal. There are three important features to this structure:

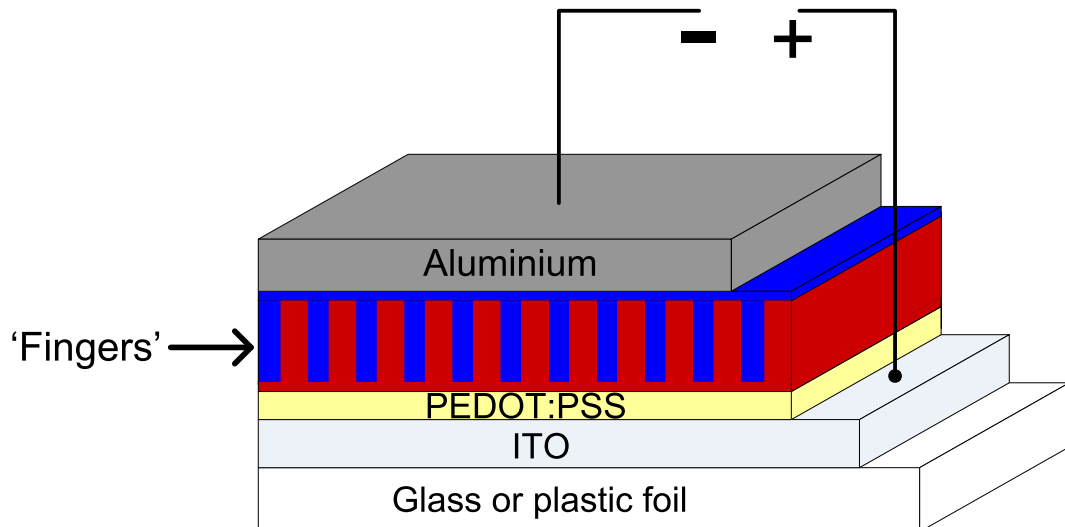


FIGURE 2.10: Interdigitated device architecture.

- every exciton created is within reach of a heterojunction yielding high exciton dissociation efficiency
- there are uninterrupted pathways to the appropriate electrode reducing charge carrier recombination
- electrodes are only in contact with the desired material, resulting in selective contacts

The width of the fingers should be optimised as to decrease charge recombination, but still allow for efficient exciton dissociation. Dynamical Monte Carlo modelling shows that an ordered checkered morphology is 1.5 times more efficient than the maximum efficiency of a disordered blend [101]. However, an ordered structure is even more sensitive to minor variations in the domain size and thus morphology optimisation is even more crucial in these ordered morphologies. The fabrication of an optimal interdigitated structure require a relative large area to be structured on the nanoscale which has proven to be a challenging task [102]. This difficulty, together with the inherent sensitivity to domain size, makes this structure less suitable for cheap large scale production unless self-assembled systems can be fabricated [102].

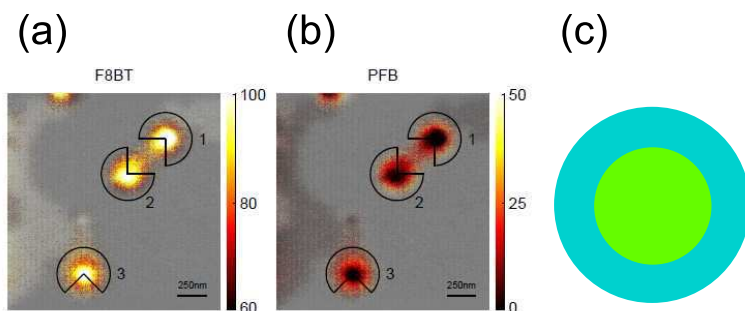


FIGURE 2.11: (a) and (b) STXM F8BT and PFB composition maps of PFB:F8BT nanoparticles, obtained from [107]. (c) a schematic representation of core-shell nanoparticles, blue indicates a mixture of PFB and F8BT and green indicates the F8BT core.

2.3.4 Nanoparticle structures

In addition to BHJ and interdigitated structures there is a third way of achieving a large heterointerface area of the two photoactive moieties in organic solar cells. Semiconducting nanoparticles consisting of two organic materials can be prepared through a miniemulsion process [103]. This approach provides a means to control the domain size while using a water based solvent, which is environmentally friendlier than organic solvents. As a result, aqueous dispersions of polymer nanoparticles have received considerable attention [104]. The size of these nanoparticles can be tuned over a wide range (nm to μm) [105]. For organic solar cells, particle sizes on the order of the exciton diffusion length (i.e. 10-50 nm) are required and have been successfully fabricated [106]. Figure 2.11 shows scanning transmission x-ray microscopy (STXM) images of poly(9,9-dioctyl-fluorene-2,7-diyl-co-bis- N,N' -(4-butylphenyl)-bis- N,N' -phenyl-1,4-phenylenedi-amine) (PFB) poly(9,9-dioctylfluorene-2,7-diyl-co-benzothiadiazole) (F8BT) nanoparticles together with a schematic picture of their structure. Burke et al. [104] showed that PFB:F8BT nanoparticles have a core-shell morphology, where the core consists of F8BT and the shell consists of a mixture of PFB and F8BT. The performance of such a nanoparticle system is investigated in Chapter 8.

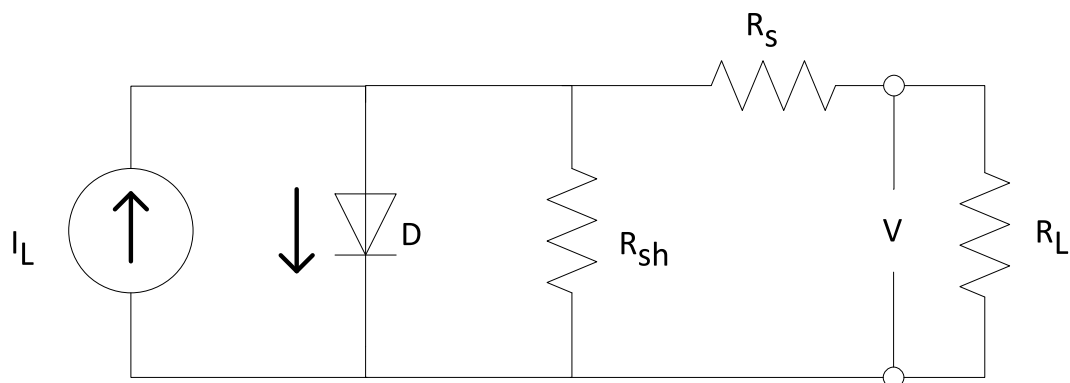


FIGURE 2.12: The classical one diode model

2.4 Modelling organic photovoltaic devices

2.4.1 Electrical equivalent circuit model

Solar cells have been described using an electrical equivalent circuit model, which consists of a network of ideal electrical components. As shown in Figure 2.12, this model comprises

- a current source, I_L , representing charge creation in the device. Exciton dynamics are not considered in this model.
- a shunt resistance, R_{sh} , representing recombination of charges.
- a series resistance, R_s , representing resistance charge carriers encounter when moving through the various layers of the device, which includes the mobility of the organic layer(s), resistance of electrodes and resistance associated with barriers at the organic-electrode interfaces.
- a diode, D , accounting for asymmetry in the current-voltage behaviour of the semiconductor junction. An ideality factor is associated with the diode.
- an externally applied voltage, V .
- a load resistance, R_L , representing components in the external circuit.

Inorganic photovoltaic devices have been accurately described using the classical one diode model [108] shown in Figure 2.12. However, this model does not describe OPV devices adequately [109] and diode ideality factors commonly takes on values that do not have a physical meaning. Various modification have been made to the circuit in an attempt to describe OPV devices [110, 111]. However, an electrical circuit modelling approach lacks an evident link to physical molecular processes in organic solar cells. Hence, it cannot fully account for morphology or allow for an easy investigation of the impact of material properties on PV performance or model the detailed intricacies of the different types of recombination processes in organic solar cells. As such, electrical equivalent circuit modelling is not adequate for the research purposes of this project. Nonetheless, the electrical circuit model is useful for describing OPV devices in terms of known electrical parameters such as R_s and R_{sh} and is also useful for modelling modular architectures, where several cells are connected in series and/or parallel.

2.4.2 Drift-diffusion based modelling

A different approach that does account for physical processes in OPVs is a 1D device model that involves a set of differential equations to calculate the current density (usually as a function of voltage). This system of equations contains the Poisson equation, drift-diffusion equations and continuity equations and can be numerically solved when appropriately choosing boundary conditions [112, 113]. These models can differ in terms of their choice of boundary conditions and treatment of recombination mechanisms. However, the 1D/2D nature of this model means that every layer is treated as an homogeneous layer. Hence, this model cannot account for a complex 3D morphology, which is known to have a major impact on device performance. Exciton dissociation and subsequent CT-state separation is a multi-step process [66], but a drift-diffusion approach does not consider multi step dynamics for each exciton/CT-state on molecular scale. Instead Onsager theory [80] or adaptations thereof (e.g. Braun's model [86]) are used to determine the separation of the CT state [112]. Onsager provided a theoretical description of the dissociation dynamics of ion pairs by considering Brownian motion and their Coulomb interaction [80]. In 1984, Braun modified the Onsager

model and incorporated the finite lifetime of the CT state in a more realistic manner [86]. Braun also proposed that for disordered organic semiconductors a distribution of nearest neighbour distances exists and thus one has to integrate over this distribution. Further modifications have been proposed as discrepancies between theory and experiment were identified. For example, the Onsager model has been modified to account for high charge mobility [114] and to consider a finite distance-dependent intrinsic recombination rate [115]. Also, the Langevin expression that underpins Onsager theory has been shown not to hold in polymer:fullerene solar cells [116]. So, while the original Onsager theory is relatively easy to implement and provides a theoretical framework to increase the understanding of geminate recombination, its use must be carefully considered for OPV systems. In drift-diffusion type models, photon absorption is assumed to immediately yield CT states [113], i.e. the interplay between the exciton dissociation efficiency and morphology is ignored even though it has been shown that morphology plays a critical role in the dissociation efficiency [101]. For the purpose of creating a virtual organic solar cell a more complete model has been chosen that is capable of accurately modelling all OPV processes on a molecular scale.

2.4.3 Dynamic Monte Carlo model

In order to take into account all relevant physical process in an organic solar cell, modelling on the molecular level is necessary. Dynamic Monte Carlo models treat excitons and charge carriers as particles and use established theories to model their hopping behaviour in organic materials while accounting for 3D morphology and energetics. These type of models have already proven to be valuable in understanding OPV operation [70, 101, 117]. Since all relevant OPV processes can be modelled in a 3D fashion, it has the potential to provide an all inclusive model that is able to accurately describe any OPV system. The only downside of the Monte Carlo approach is its computational burden. In this thesis, Monte Carlo type modelling will be used to develop a virtual organic solar cell. The development of this model is discussed in detail in Chapter 4.

2.5 Stability

An increased understanding of OPV behaviour will help fabricate high performance OPV modules. However, for practical and commercial purposes they need to be durable as well. Degradation occurs via a number of pathways. These include photooxidation of the organic active materials in the presence of O₂ and/or H₂O; electrochemical reactions between organic active layers and metallic electrodes; and physical effects, such as delamination [118]. In most devices, several degradation modes can occur concurrently, making it difficult to attribute the observed performance decay to any one cause. The primary degradation mechanism in devices with an aluminium cathode is investigated in Chapter 9. Long-lived OPV devices may be realised by utilising stable materials and encapsulation techniques.

3

Experimental

3.1 Device fabrication

Most devices were fabricated and characterised by the author of this thesis. Wherever this is not the case, the appropriate acknowledgements are clearly made. Devices were fabricated both at CSIRO and University of Newcastle. Three different lateral architectures were used throughout this project and are shown in Figure 3.1. The active area of the device is defined by the overlap of the cathode and anode. The active area of each of the 4 devices using architecture I is 2 mm x 10 mm. Architecture II has four square devices with different sizes: 2 mm x 2 mm, 4 mm x 4 mm, 6 mm x 6 mm and 10 mm x 10 mm. Device architecture III comprises 6 devices with an active area of 2 mm x 2.5 mm. Nanoparticle device fabrication and characterisation were conducted

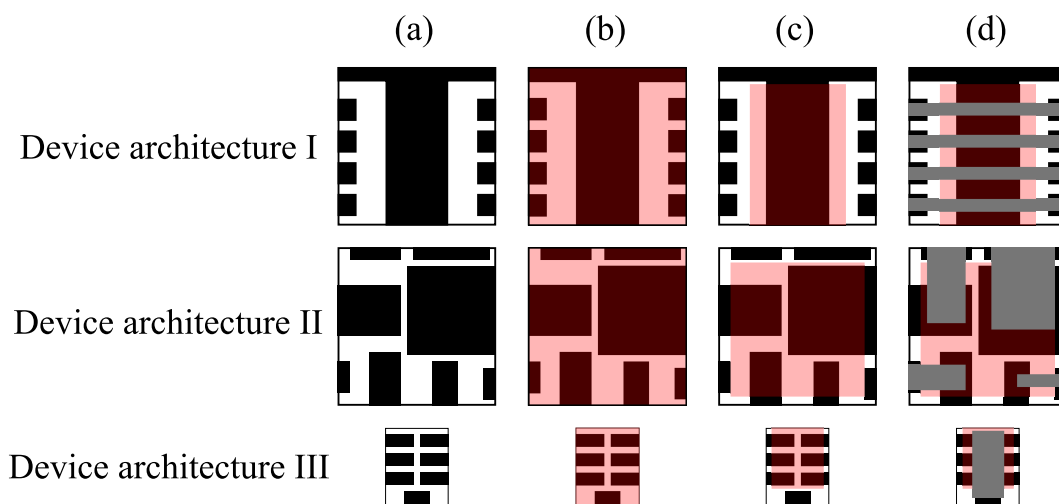


FIGURE 3.1: Rows indicate the three device architectures used in this project. Columns indicate the various stages of device fabrication: (a) cleaned pre-patterned ITO coated glass substrate, (b) after deposition of organic layer(s), (c) after removal of organic material at the edges so contact can be made to the underlying electrode, (d) complete device after cathode deposition.

by Natalie Holmes and Syahrul Ulum.

3.1.1 Substrate preparation

Patterned ITO coated glass substrates are purchased from Kintec Company. They undergo a series of cleaning steps to ensure consistent results:

- Substrates are rinsed with deionised water and undergo a visual inspection.
- Substrates are rinsed with and undergo sonication for 30 minutes in acetone.
- Substrates are rinsed with and undergo sonication for 30 minutes in isopropyl alcohol.
- Substrates are rinsed with water and undergo blow-drying with nitrogen.
- Substrates are plasma cleaned for 15 minutes using a mixture of air and pure oxygen.

The last cleaning step is always done immediately before thin film deposition.

TABLE 3.1: Spin parameters for materials used in this thesis.

| Material(s) | Solvent | Acceleration (rpm/s) | Speed (rpm) | Duration (s) |
|-------------|---------------|----------------------|-------------|--------------|
| P3HT:PCBM | chlorobenzene | 500 | 1000 | 30 |
| PEDOT:PSS | water | 1680 | 5000 | 60 |
| TTP | chloroform | 1680 | 2000 | 60 |

3.1.2 Spin-coating thin films

Thin organic films are deposited through spin coating. Substrates are held in place by vacuum and sufficient solution is deposited on the substrate to cover it entirely. Then, the substrate is spun with acceleration, speed and duration as presented in Table 3.1. All solutions were filtered prior to deposition using a 0.2 μm filter. PEDOT:PSS is commercially available as an aqueous dispersion (Clevios P VP Al 4083) and does not need further addition of a solvent. PEDOT:PSS films were 40 nm thick. P3HT (Reike) and PCBM (Solenne B.V.) were spun from chlorobenzene. Tetra(p-tolyl)porphine (TTP) was synthesised by Nathan Cooling and was spun from chloroform. Both spin acceleration and spin speed affect the film thickness. However, these parameters also affect the quality of the film. In general, more non-uniformities are found when decreasing spin speed and increasing acceleration [119]. Therefore, when aiming to vary thickness, it is best to keep the spin speed and acceleration fixed at values that give high quality films and vary the concentration of the solution instead. It is known that film thickness linearly increases with concentration for certain materials [120]. This relation indeed holds up for a P3HT:PCBM blend with a 1:1 weight ratio, as shown in Figure 3.2. The linear fit is used as a look up guide when depositing layers of a desired thickness. Measurements presented in Figure 3.2 were mostly gathered by Lynn Rozanski and some data points were gathered by me.

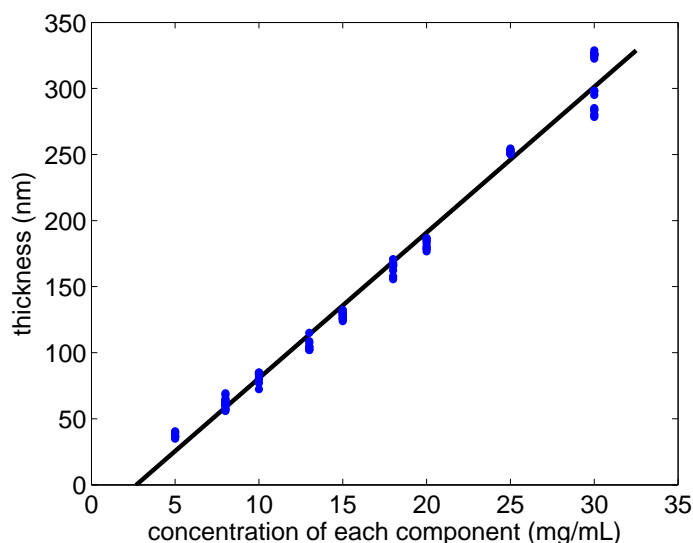


FIGURE 3.2: P3HT:PCBM thickness after annealing for 4 min. at 140 °C as a function of blend concentration. Since a 1:1 weight ratio is used the concentration of each component is the same.

3.1.3 Evaporative deposition

Metal cathodes were deposited by thermal evaporation. High purity (99.99 %) pellets of aluminium or silver were used. The substrate rotates during deposition to minimise shadowing effects (thickness non-uniformities near the edge of the mask caused by a finite mask thickness). These effects are further discussed in Chapter 9. Thin interface layers at the internal side of the cathode, either LiF or Ca, were also deposited through physical evaporation resulting in film thicknesses of 1.5 nm or 20 nm respectively. A thin layer (~ 1.5 nm) of LiF does not provide complete coverage, but instead consists of island clusters [121]. Small organic molecules, such as TTP, can also be deposited without fragmentation through evaporative deposition. TTP started to sublime at 250 °C. Good agreement is found between evaporated TTP absorption spectra and spin casted TTP spectra (see Section 5.3.2) which confirms that deposition occurred at a temperature below that for pyrolysis.

3.1.4 Encapsulation

In order to exclude degradation effects during measurements, devices were encapsulated using a custom cut cover glass and UV-cured epoxy (Lens Bond, Emsdiasum). The encapsulation was conducted in the glove box under inert atmosphere (dry nitrogen). Only the edge of the electrodes were not covered by the cover glass so contact could be made to the encapsulated device.

3.2 Device and materials characterisation

3.2.1 UV-VIS absorption spectroscopy

Transmission and reflection spectra were measured using a Varian Cary 6000i UV-Vis-NIR spectrophotometer. Quartz substrates were used when the wavelength region of interest was <350 nm as microscope slide glass absorbs light in this region. From transmission and reflection spectra, absorption spectra could be plotted, which were used for optical modelling and to estimate Gaussian energy disorder. UV-VIS measurements were conducted both at CSIRO and University of Newcastle.

3.2.2 Photoluminescence measurements

Photoluminescence (PL) measurements were captured using a Cary Eclipse fluorescence spectrophotometer at University of Newcastle. PL is a measure of exciton recombination as discussed in Chapter 5.

3.2.3 Profilometry

Film thickness was measured using a Veeco Dektak 150 surface profilometer at CSIRO. The thin layer was purposely scratched in several places and multiple linescans were taken across these scratches to determine the average film thickness. Care was taken to ensure that the underlying glass substrate was not damaged by the scratching process.

3.2.4 Atomic Force Microscopy

Surface roughness and morphology were investigated using a Cypher Atomic Force Microscope (AFM). AFM tips were purchased from BudgetSensors and AsylumResearch. AFM measurements were conducted at University of Newcastle.

3.2.5 X-ray photoelectron spectroscopy depth profiling

In order to gain vertical compositional information of an OPV device, X-ray photoelectron spectroscopy (XPS) depth profiling was conducted by Dr Bill B. Gong at the Mark Wainwright Analytical Centre, University of New South Wales, Australia using a Thermo Scientific Escalab 250 Xi XPS system. Depth profiling was made possible by using an argon sputtering source. A thin layer of material would be removed with the sputter gun and an XPS scan of relevant parts of the spectra were taken. This process was repeated many times until the bottom of the device was reached, thus providing vertical compositional information. The etching area was 2.5×2.5 mm and the diameter of the X-ray spot was 0.5 mm. Figure 3.3 shows individual XPS spectra that were used to identify material concentrations throughout the OPV device. The composition as a function of depth was tracked by measuring the change in the area of the elemental XPS peak relevant to the component of interest. The markers used to identify molecules are presented in Table 3.2. PEDOT:PSS, P3HT and PCBM all contain carbon, but in different quantities relative to sulphur. Consequently, the combination of tracking carbon and sulphur allows to differentiate between these three materials and by extension the relative P3HT:PCBM ratio in the active layer [122].

3.2.6 Current-voltage characteristics

The global standard for testing PV devices, is the measurement of current-voltage (I-V) curves under simulated solar illumination. The solar simulator is designed to approximate the reference solar spectrum defined in IEC60904, commonly referred to as 'AM1.5'. Part of the AM1.5 spectrum is shown in Figure 2.4. To further comply

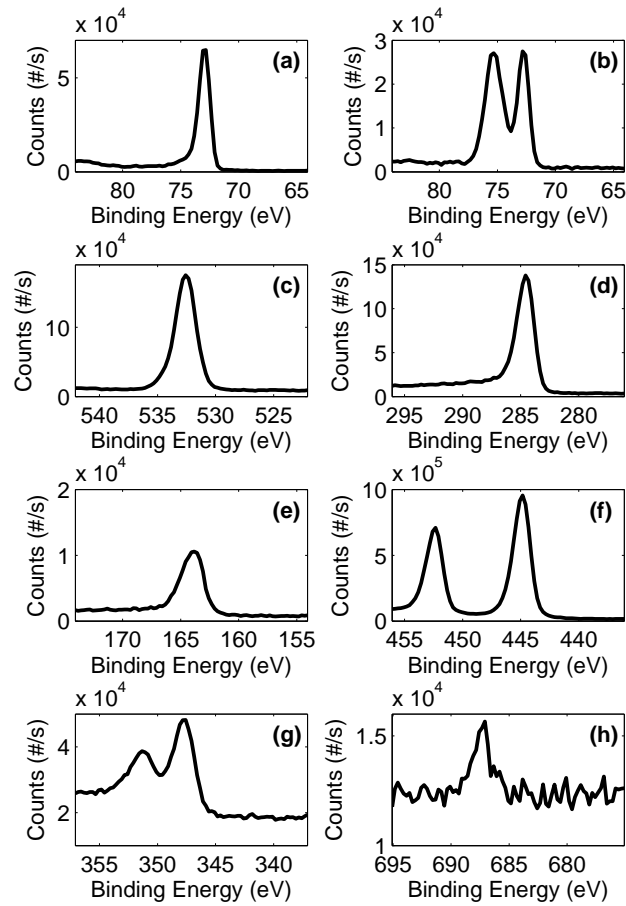


FIGURE 3.3: XPS spectra of elements of interest. (a) shows the spectrum of Al 2p in its metal state, (b) shows the Al 2p metal (right peak) and oxidised state (left peak), (c) shows the O 1s state, (d) the C 1s state, (e) the S 2p state, (f) the In $3d_{5/2}$ state, (g) the Ca 2p state and (h) the F 1s state.

with the standard, the irradiance was set at 1000 Wm^{-2} , which was determined using a calibrated reference cell. AM1.5 illumination is simulated using a Newport Oriel class AAA solar simulator (model 91160A). Current is measured as a function of voltage using a Keithley SourceMeter (model 2400), resulting in a typical plot such as the one shown in Figure 3.4. Voltage is swept over a range that at least covers the fourth quadrant (when photocurrent is plotted as being negative). Four probe measurements were made to eliminate contact resistance and the resistance in the probe wires. In this thesis, I-V curves measured under AM1.5 are referred to as light I-V curves and

TABLE 3.2: XPS markers

| Component | State |
|--------------------|----------------------|
| aluminium | Al 2p |
| oxidised aluminium | Al 2p |
| ITO | In 3d _{5/2} |
| Calcium | Ca 2p |
| LiF | F 1s |
| PCBM | C 1s |
| P3HT | C 1s and S 2p |
| PEDOT:PSS | C 1s and S 2p |

I-V curves measured with no illumination at all are referred to as dark I-V curves. The light I-V curve in addition to the device area provides enough information to calculate common performance indicators: short circuit current (I_{SC}), short circuit current density (J_{SC}), open circuit voltage (V_{OC}), Fill Factor (FF) and power conversion efficiency (η). I_{SC} is the generated current at $V = 0$, V_{OC} is the voltage at $I = 0$ and FF is given by

$$FF = \frac{I_{mpp}V_{mpp}}{I_{SC}V_{OC}} \quad (3.1)$$

where I_{mpp} and V_{mpp} are the current and voltage at the point of maximum power. Power conversion efficiency is calculated as

$$\eta = \frac{I_{SC}V_{OC}FF}{P_{in}} \quad (3.2)$$

where P_{in} is the total power of the light hitting the solar cell. I-V measurements were conducted at CSIRO and University of Newcastle. In most instances in this thesis, current density (J) is plotted against voltage instead of current. I-V Measurements were conducted without a mask, which may introduce an error in current density due to deviations from the intended photoactive area. The real photoactive area is discussed in more detail in Chapter 9. As discussed in Chapter 6, external quantum efficiency measurements correspond to J_{SC} measurements indicating that J_{SC} correctly measured.

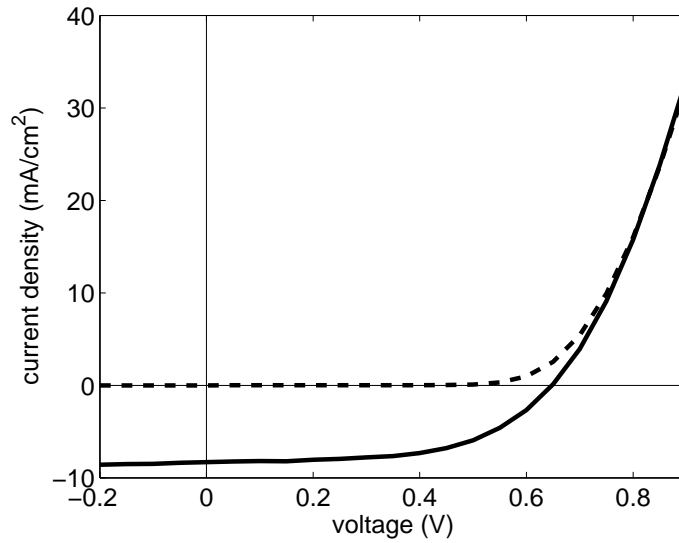


FIGURE 3.4: A typical light I-V curve (solid line) and dark I-V curve (dashed line)

3.2.7 External Quantum efficiency measurements

External quantum efficiency (EQE) is the percentage of electrons extracted from a PV device compared to the total number of photons hitting the surface of the device and is thus expressed in number of electrons per photon. Internal quantum efficiency (IQE) is the ratio of the number of electrons extracted from the device to the number of photons absorbed by the active layer. EQE can be converted to IQE by taking into account reflected light, transmitted light, absorption coefficients of the various components and interference effects. In order to determine light absorption in the device as a function of depth, the internal optical field in our devices has been determined using transfer matrix techniques as described previously, [30, 123] using optical models similar to those used by others [124, 125]. The coding of the optical model and determination of optical constants of materials were conducted by Nicolas Nicolaidis. In this thesis, IQE is normalised to the absorbed light by the active layer (not the entire device). Additionally, IQE is used to refer to the total IQE, i.e. integrated over the entire spectrum. The same is true for EQE, unless indicated as $\text{EQE}(\lambda)$ (as in Equation (3.3)). A tungsten halogen lamp was used in combination with a monochromator and chopper to give modulated monochromatic light of variable wavelength. Light of known

intensity (and wavelength) hits the device and the resulting I_{SC} was measured. The measured current can be converted EQE using

$$EQE(\lambda) = \frac{\#electrons}{\#photons} = \frac{hcI_{SC}}{e\lambda P_{light}} \quad (3.3)$$

where λ is the wavelength of incident light, h Planck's constant, c the speed of light, e the charge of an electron and P_{light} the power of incident light. EQE measurements were carried out at CSIRO.

4

Monte Carlo modelling

4.1 Introduction

This chapter describes the dynamic Monte Carlo (DMC) model that I developed and put to use in Chapters 5 - 8. Figure 4.1 gives an overview of the model and lists all processes in a modular way and shows the possible options after each step. In the DMC model, excitons are created upon light absorption and these can either immediately recombine, dissociate if adjacent to a heterointerface or hop to a nearby site. The exciton may hop around for a while, but eventually it can either recombine or dissociate. Once the exciton is dissociated an electron and a hole are created at the heterointerface. These charge carriers can hop or recombine another charge carrier of the opposite polarity. If recombination does not occur in the lifetime of the charge carrier, it will eventually hop towards the cathode or anode where it may be extracted.

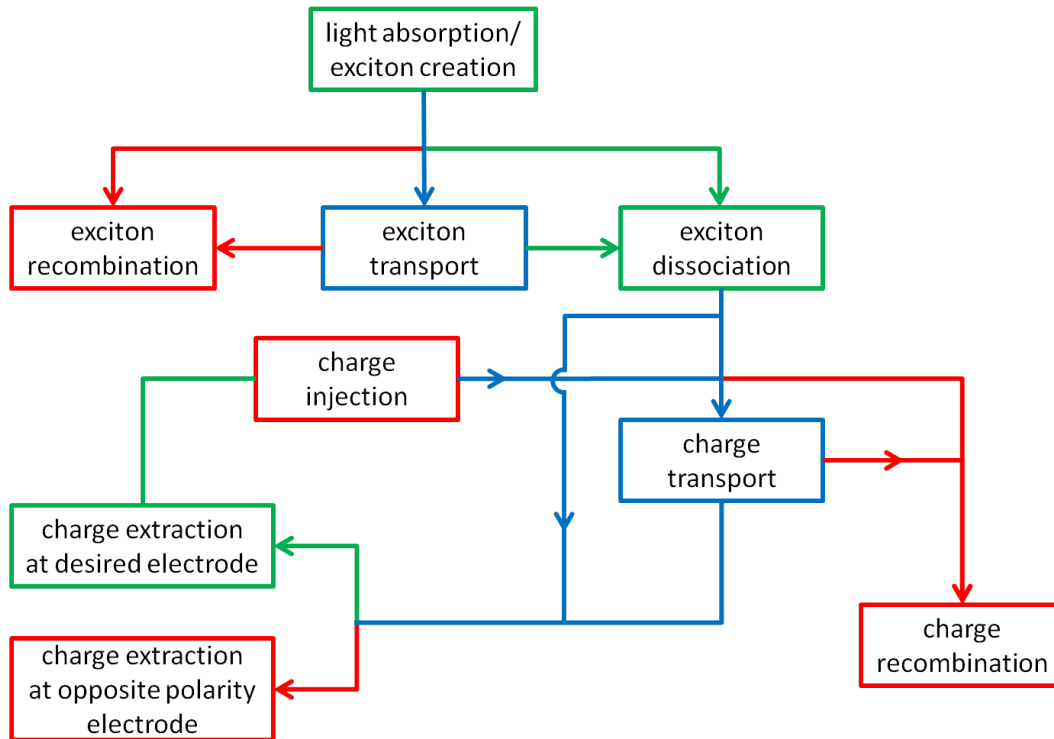


FIGURE 4.1: Overview of processes included in the DMC model. All events considered in the model are captured by the boxes shown. Green boxes and arrows indicate processes necessary to generate photocurrent and red boxes and arrows are loss mechanisms. The blue boxes and lines are neutral and do not directly lead to a loss or gain mechanism.

Charge carriers are also injected at the electrodes and these charge carriers may undergo the same steps as a charge carrier created via exciton dissociation. As shown in Figure 4.2, a three dimensional lattice is set up, where each voxel (volume element) has x-, y- and z-coordinates, an associated energy and may be occupied by an exciton and/or electron or hole. The lattice represents the photoactive layer of an organic solar cell and each voxel is either associated with the electron donor material or electron acceptor material. The physical processes of exciton creation, exciton transport, exciton dissociation, charge transport and extraction are discussed, but before a discussion of the modelling details of each process takes place, the general Monte Carlo approach is presented. After introducing the Monte Carlo method, the approach taken to create the morphology is treated. In this thesis morphology is used to refer to the arrangement

of donor and acceptor in the photoactive layer. Finally, the determination of performance parameters, such as J_{SC} or IQE, from the simulations is presented. OPV Monte Carlo models offer more advantages, information and the possibility of a full virtual solar cell compared to other modelling methods (see section 2.4). However, the price paid for this level of detail is a very computationally intensive program. Consequently, supercomputers made available through CSIRO were used to run the computationally time intensive simulations. I wrote the code for the simulations in Matlab and Fortran.

4.2 Monte Carlo method

The DMC model simulates the time evolution of a system by finding all possible events (reactions), which are listed in Figure 4.1, and calculating their associated kinetic rates, k . The calculation of k is different for each type of event and a section is devoted to explain each of these. Rates of individual events are converted to a 'waiting time', τ , which is the time until the event occurs. The system state changes slightly every time an event occurs. The transition of the system state from the present to the immediate future can be calculated when the present state is known and does not depend on the history of the system. This 'memoryless' property is called a Markov property. Models that possess the Markov property are called Markov chains. When considering a particular system state, the average rate of an event may be fixed, but individual events will not follow each other up with a fixed time step, as depicted in Figure 4.3. For example, consider radioactive decay of a system of N particles, where the rate of decay is given by

$$\frac{dN}{dt} = -\lambda_d N \quad (4.1)$$

and λ_d is the decay constant and t is time. Given that N at $t = t_0$ and λ_d are known, the decay rate can be exactly calculated at any time t . The average lifetime (or waiting time) is given by

$$\tau = \frac{1}{\lambda_d} \quad (4.2)$$

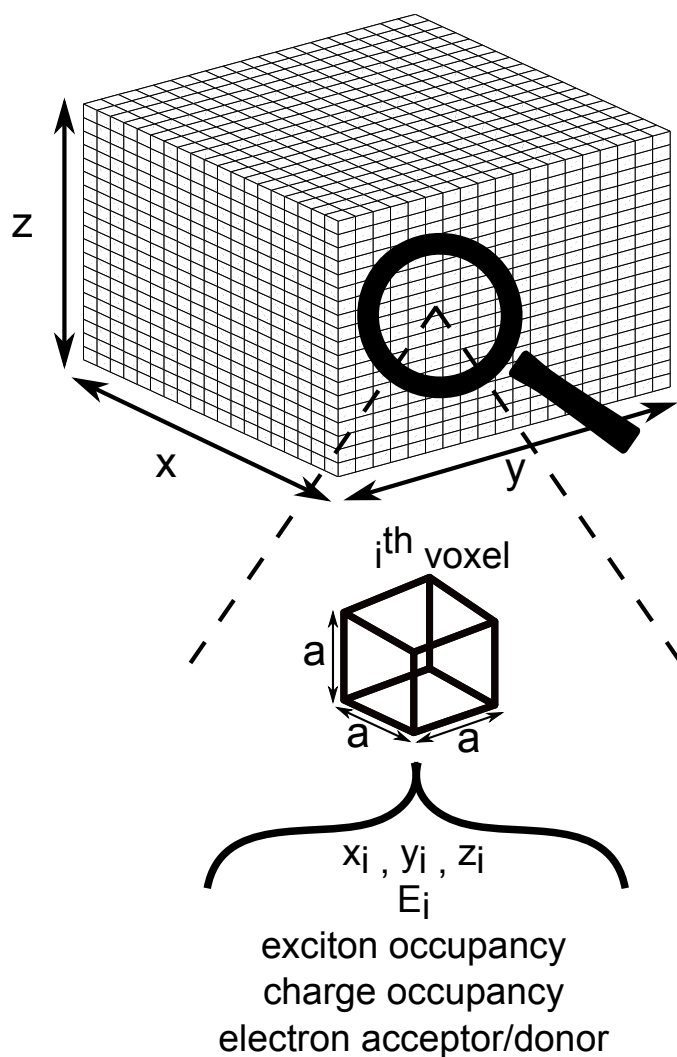


FIGURE 4.2: Three dimensional lattice, where each voxel has associated with it x -, y - and z -coordinates, energy (E), exciton occupancy, charge carrier occupancy and type of organic semiconducting material (electron donor or acceptor).

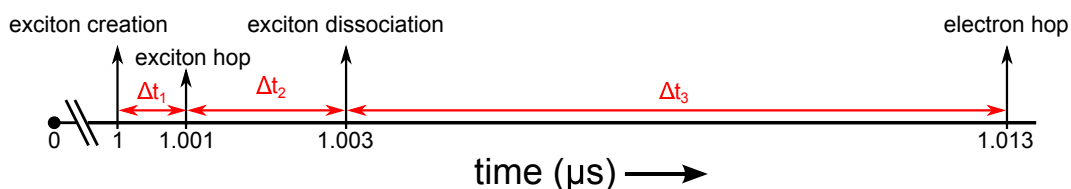


FIGURE 4.3: Event time line showing 4 events that occur at various moments in time. The time difference between consecutive events (Δt_1 , Δt_2 and Δt_3) is not constant and in theory may take on any positive real number.

however the exact time of an individual decay event is still random as it is a probabilistic process. In other words, the entire ensemble of particles will on average obey equation (4.2) and the probability distribution as given by equation (4.1), but the exact time at which an individual decay event occurs is still a random process. The same general principle is true for all reaction kinetics simulated in the DMC model. Gillespie [126] has shown that the time it takes (waiting time) for the system to transition from state Y_1 to state Y_2 (e.g. an exciton recombines and changes the system from state Y_1 to state Y_2) is defined by the following probability density function, P ,

$$\frac{dP_{Y_1}}{dt} = -kP_{Y_1} \quad (4.3)$$

, where k is the reaction rate of the associated event. Equation (4.3) essentially says that the rate of change of the probability of the system remaining in state Y_1 is proportional to the probability of being in state Y_1 . The solution to equation (4.3) is

$$P_{Y_1}(t) = e^{-kt} \quad (4.4)$$

A noteworthy feature of equation (4.4) is that if no events occur, the probability density function retains its shape. This is a unique property of an exponential function and is in accordance with a Markov chain Monte Carlo model. If no events occur the system state has not changed and the probability of it changing is still the same as this probability depends on the present system state only (not the past). We are interested in the time needed for an event to occur, i.e. the time needed for the system to transition from state Y_1 to state Y_2 , which is given by 1 minus the probability of remaining in state Y_1

$$P_{Y_2}(t) = 1 - e^{-kt} \quad (4.5)$$

In other words, since we are dealing with a probabilistic process, we would like to generate a random number that obeys equation (4.4). In order to achieve generate this number, it is important to realise that Equation (4.5) is the cumulative distribution function of equation (4.4). Probability integral transform states that a random number obeying (4.4) is generated by solving

$$F(t) = X \quad (4.6)$$

where X is a random number with a uniform distribution between 0 and 1 and F the cumulative distribution function. Solving equation (4.5) and (4.6) for t gives [127]

$$t = -\ln(1 - X) \frac{1}{k} \quad (4.7)$$

Since X is a random number between 0 and 1, $1 - X$ will also be a random number and thus equation (4.7) can be written as

$$t = -\ln(X) \frac{1}{k} \quad (4.8)$$

Using equation (4.8), the waiting time (time until the event occurs), τ , can easily be calculated once the corresponding rate is known. All events are stored in a list (queue) which is sorted according to their respective waiting time. The event with the smallest waiting time is executed first. This methodology is referred to as the First Reaction Method (FRM) and was devised by Gillespie in 1976 [127]. As a result of event execution new events may be inserted in the list and others may disappear. When a particular event waiting time is calculated, the present time is added to it before inserting in the queue of waiting times. In this way newly generated events will occur at the appropriate time relative to all other events. This approach is computationally more efficient than updating all waiting times as the simulation proceeds.

The FRM utilises a variable time step, which means that after every iteration the system changes, no time is wasted calculating event rates that do not lead to a system change as would be the case if the virtual time progresses with a fixed time step. k is calculated at the time of event generation and not at the time of event execution. The system may have changed slightly during this small period of time and the previously calculated rate may not be correct. In order to calculate the rate correctly, one would have to recalculate τ for each event after each event execution. This more exact approach would be computationally extremely time consuming. Groves et al. [128] evaluated the accuracy of the FRM approach and has shown that the FRM simplification is justified, because the FRM agrees with the exact model to better than 2 %. Before an event is executed, the program does check whether that particular event is still possible. For example, since electrons are fermions, only one electron is

allowed to occupy a site. If the destination site of a charge hop is found to be occupied, the charge hopping rates are re-evaluated to prevent violation of the single occupancy rule imposed on the system.

The flow diagram of the code written in Matlab and Fortran is presented in Figure 4.4. After the system is initiated, the first events are determined by calculating the respective waiting times. Each event may have multiple possible outcomes, e.g. an electron may hop in 6 directions, and thus multiple waiting times are calculated. Only the outcome with the shortest waiting time is added to the queue as it excludes the other possible outcomes. Then the virtual time is incremented with τ of the first event and the first event is executed. As a result of this, new events may be added to the queue and others may be deleted (e.g. charge recombination deletes all events associated with the electron and hole in question). Depending on the purpose of the simulation the time evolution of certain variables are of interest and they are frequently recorded. Also, the entire workspace (all variables) is saved after t_{save} seconds has passed to prevent data loss in the case something goes wrong with the supercomputer. If t_{max} seconds has passed, the simulation is ended and the workspace is saved for analysis, otherwise the simulation keeps running and events are continuously executed.

An OPV device is represented by a three dimensional Cartesian lattice with a lattice constant, a (see Figure 4.2). The z-coordinate is perpendicular to the electrodes and thus points in the direction of the electric field set up by the work function difference of the electrodes. The z-direction is thus constrained by the thickness of the device. Periodic boundary conditions are invoked in the y- and x- directions, which means that particles hopping out of the right of the lattice will enter on the left of the lattice. The program not only contains the queue of events with associated τ , event number (identifying event type), particle number (identifying particle involved in event), y-, x- and z-coordinates (destination site of particle hop), a variable comprising lattice occupancy, but also a variable comprising site energy and a variable indicating morphology are also part of the program. In the program, the latter three variables all have the same dimension as the three dimensional lattice. The morphology variable

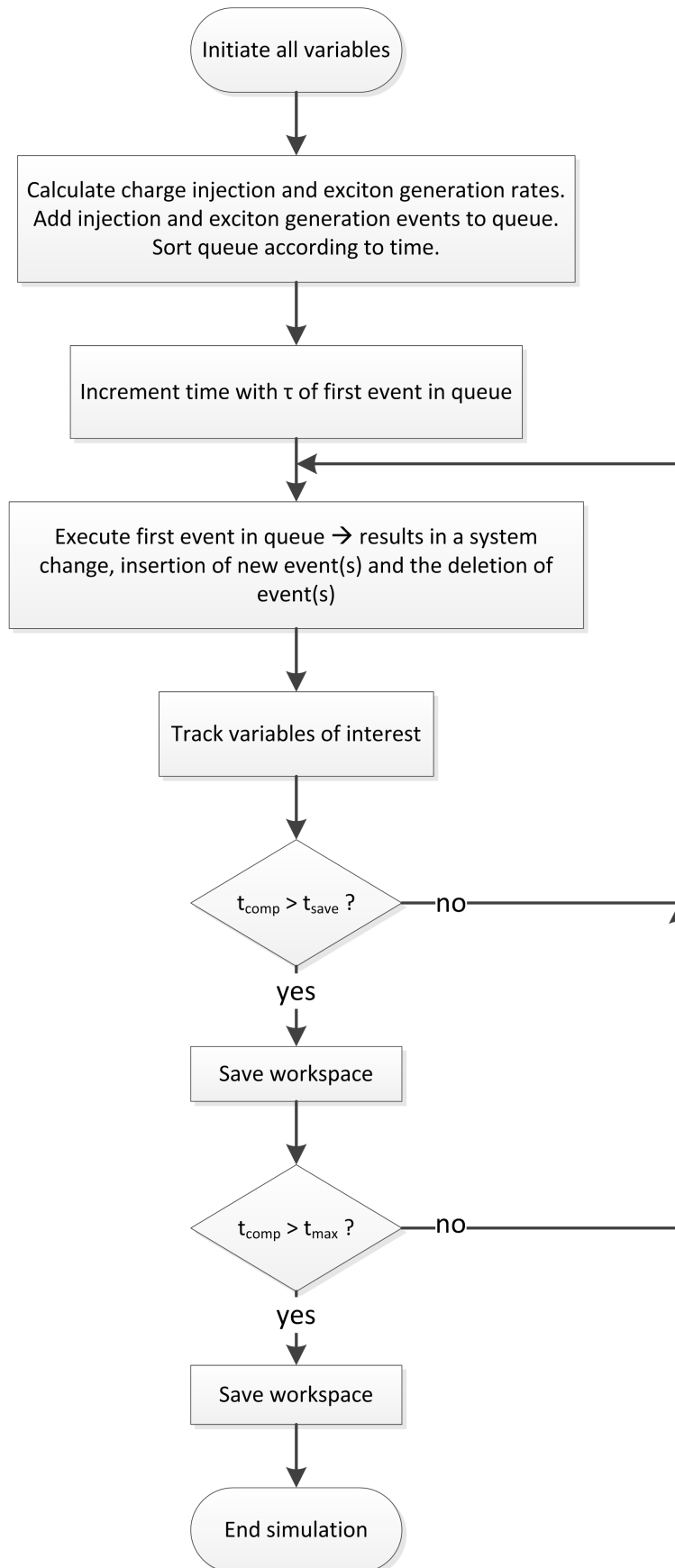


FIGURE 4.4: Flow diagram of FRM approach

contains zeros where electron donating material (e.g. P3HT) is found and ones where electron accepting material (e.g. PCBM) is located. Morphologies are defined and in theory any type of morphology could be created. Each point in the lattice is a point of localisation for both excitons and charge carriers. Knupfer et al. [37] investigated the spatial extent of excitons on molecular units used in OPV devices and found it to be 0.7 nm for C_{60} . Also the excited state wave function is generally restricted to monomer units [129], which is in the order of 1 nm. In light of these results, a voxel size of $1 \times 1 \times 1$ nm has been chosen. The simplification of a constant voxel size means that anisotropy causing different intra- and inter-chain hopping rates are not taken into account. Quantum chemical calculations would be needed to resolve anisotropy, which would increase the computational burden by orders of magnitude. An approach to include anisotropy with a fixed voxel size would be to assign two sets of charge carrier properties to voxels of the same moiety. One set of properties would correspond to intra-chain hopping and the other to inter-chain hopping. Here, however, we assume that hopping within a single moiety can be captured by a single set of charge carrier properties. Furthermore, we are mainly interested in effects that occur on a device level and these detailed effects are assumed to average out on a large scale. The success of drift-diffusion models where morphology is not taken into account, also shows this simplification is justified.

4.3 Setting up the morphology

As mentioned before, any morphology could be generated simply by defining where electron accepting and donating voxels are located in a three dimensional lattice. In this thesis, two types of morphologies are investigated: BHJ and nanoparticle morphologies. Nanoparticle morphologies were elucidated using STXM composition measurements. Due to the novelty and lengthy discussion of the approach together with the fact that Chapter 8 is dedicated to nanoparticles, the generation of nanoparticle morphologies is discussed in Chapter 8. As for the generation of BHJ morphologies, a cellular automata method [130] is initially used. It is important to realise that we are not trying to

simulate the exact phase separation process as a result of annealing, rather we are trying to generate a final BHJ morphology that represents a real BHJ morphology. While, the optimum weight ratio somewhat differs between research groups, a 1:1 P3HT:PCBM weight ratio is most often used as the optimal ratio [131]. Thus, for simplicity a 1:1 ratio is also assumed in the morphology lattice. First, the lattice is randomly filled with moiety identifiers (zero for electron accepting material and one for electron donating material) while ensuring a 1:1 ratio. Attempts are made to swap neighbouring pairs of sites. Swaps are accepted based on the resulting change in total site energy in a similar way to spin exchange in the Ising model [101]. The energy of site i is calculated using

$$E_i = -\frac{J}{2} \sum_j (\delta_{s_i, s_j} - 1) \quad (4.9)$$

where s is the moiety identifier, δ is the Kronecker delta function and J the exchange interaction between neighbouring moiety identifiers, which was chosen as 1. The summation over j indicates a summation over all nearest neighbours of site i . s_i is 1 for the electron donor (e.g. P3HT) and 0 for the electron acceptor (e.g. PCBM). The exchange interaction between two neighbouring sites can take on two values

$$\delta_{s_i, s_j} - 1 = \begin{cases} = 0 & \text{if } s_i = s_j \\ = -1 & \text{if } s_i \neq s_j \end{cases} \quad (4.10)$$

The energy corresponding to likewise sites is lower than that of dissimilar sites and equation (4.9) essentially reduces to

$$E_i = \frac{J}{2} [\# \text{ of dissimilar neighbouring sites}] \quad (4.11)$$

The total energy of the system is a measure for the interface area between electron donor and acceptor. Hence, lowering the system energy effectively increases the feature size, which is defined as [70]

$$\text{feature size} = \frac{3 \times \text{volume}}{\text{interface area}} \quad (4.12)$$

A bilayer structure will have a total energy that is much lower than that of completely random BHJ morphology. The swap probability may be calculated through a number

of spin exchange formalisms (even though we are not swapping spin, we are swapping moiety identifiers). We choose to start with a typical cellular automata approach [130] and then switch to a cluster algorithm. The swap probability is chosen to follow Kawasaki spin-exchange dynamics and is given by

$$P(\Delta E) = \frac{e^{-\frac{\Delta E}{k_B T}}}{1 + e^{-\frac{\Delta E}{k_B T}}} \quad (4.13)$$

where ΔE is the total system energy difference between the state after the swap and before the swap. Only the site energies of nearest neighbours of the two sites involved in the swapping process are needed to calculate ΔE , as the rest of the lattice remains unaffected. However, this approach becomes very slow once a larger feature size is reached, because large correlated regions are hardly affected by single swaps. This critical slowing down may be improved using a cluster method [132]. As the name suggests the method proceeds by swapping clusters as opposed to single sites. A cluster is formed by first randomly choosing a starting point, site i . If neighbouring sites are of the same moiety and they have not been added to a cluster before, then they will be added to the new cluster with a fixed probability, $P_{cluster} = 0.6$. This particular probability is chosen as 0.6, because it was found to lead to the desired feature size fastest. Next the newly added sites will undergo the same procedure and its neighbours are also evaluated, which may lead to new additions to the cluster. In this way, the cluster grows. After the entire lattice is divided into clusters, clusters with equal volume (to preserve the 1:1 ratio), but with different moiety identifiers are swapped. If the swap leads to an increase in the feature size it is accepted otherwise it is rejected. Since large groups of sites are swapped at once, this method only slows down after a sufficiently large feature size is reached. Another advantage of the cluster method is that small islands (one or two voxels) are quickly avoided. The cellular automata method sometimes produces morphologies with single site islands which do not cluster rapidly. Lyons et al. [133] argues that these small islands are non-physical since they do not correspond to observed PL quenching and polymers are longer than 1 nm (voxel size). They manually swapped these small one or two voxel islands to the moiety of its surroundings. Figure 4.5 shows the evolution of a morphology at

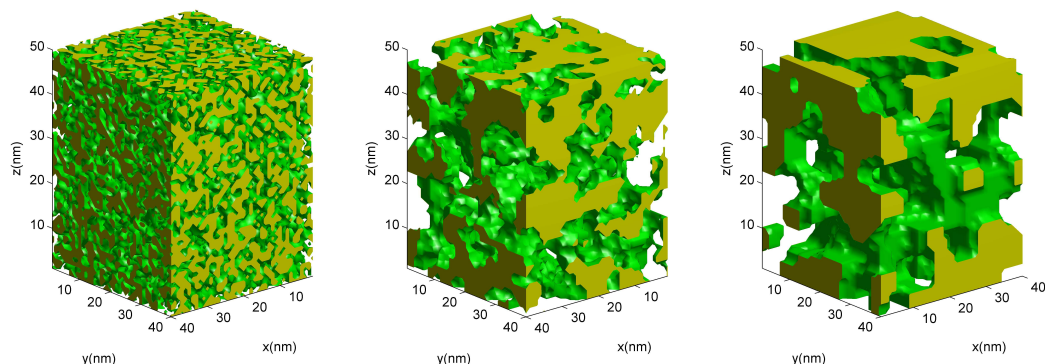


FIGURE 4.5: BHJ morphologies at various stages in the swapping algorithm. The feature size increases from left to right.

different stages of the swapping algorithm. The morphology displayed on the right in Figure 4.5 has a feature size of 14.2 nm, which corresponds to feature sizes of annealed BHJ films as determined via AFM phase images [134]. This particular morphology did not have any isolated islands which is in accordance with expectation since the donor and acceptor phase volumes of a blend with a 1:1 mixing ratio exceed the percolation threshold of $\sim 31\%$ [135]. The percolation threshold is defined in such a way, that below this threshold many isolated islands are expected, but when the phase volumes are significantly above it a fully connected network is expected.

It should be noted that the morphologies generated using the Ising model is only an approximation of the real morphology, which in the case of P3HT:PCBM devices has been shown to be complex and consisting of P3HT crystallization, PCBM aggregation and P3HT:PCBM mixed zones [136]. This approximation of the real morphology could lead to discrepancies between simulated and measured PV performance.

Now that the simulation methodology and morphology generation have been discussed, the physics behind each type of event (see Figure 4.1) is examined.

4.4 Light absorption

A photovoltaic process starts with the absorption of light (see Figures 2.7 and 4.1). Each absorbed photon is assumed to yield an exciton. As mentioned in Section

2.2.2, interference effects are prevalent in thin film devices. Optical modelling for a ITO/PEDOT:PSS/P3HT:PCBM/Al BJJ system was conducted by Nicolas Nicolaidis, University of Newcastle, Centre of Organic Electronics. Excitons were generated according to the absorption profile (as a function of depth). An exciton generation event with its associated rate is created for each z-coordinate and when one of these events is executed an exciton is generated at a random x- and y-location. Consequently, the number of exciton generation events are equal to the thickness of the device expressed in lattice constant units. This approach ensures an exciton generation profile that corresponds to the known true absorption depth profile.

4.5 Energy considerations

As will become clear in Section 4.6 and 4.7, the site energy plays an important role in exciton and charge hopping transport. The total 'energy landscape' comprises several effects:

- Gaussian energetic disorder
- Built-in electric field
- Coulomb interaction between charge particles
- Surface charge induced at the electrode interface (image charges)

Exciton transport only takes into account Gaussian energetic disorder, since the exciton is a charge-neutral species. Electrons and holes on the other hand are not. Hence, the other three aspects need to be considered in order to take into account the full electric field in the active layer. All effects are expressed in energy (as opposed to for example force or voltage) and are superimposed to give the total energy landscape. These energy values are used to calculate hopping rates. Two energy lattices are created: one containing only Gaussian energetic disorder for excitons and the other contains all four effects for charge carriers.

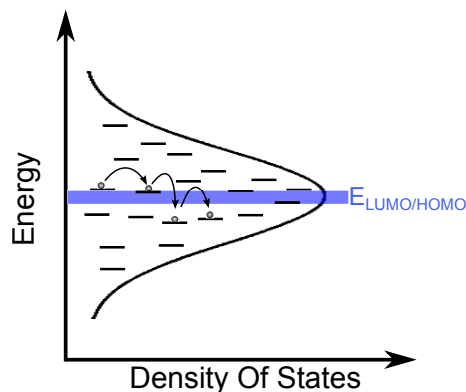


FIGURE 4.6: Particle hopping in the intrinsic DOS. The HOMO and LUMO levels are assumed to have a Gaussian distribution. The energy of the HOMO/LUMO is indicated in blue.

4.5.1 The Gaussian energetic disorder model

Gaussian energetic disorder arises from inhomogeneous broadening of the intrinsic density of states (DOS), which is essentially a result of an imperfect conjugated system due to chemical defects, kinks and twists in polymer chains, variation in conjugation length etc. The shape of this disorder is approximated to be Gaussian, because absorption spectra are found to have this shape as well [137]. Particle hopping occurs within the Gaussian energetic disorder associated with the HOMO and LUMO levels as depicted in Figure 4.6. Electrons are assumed to reside in the LUMO and holes in the HOMO irrespective of the excitation wavelength. This assumption can be made because vibronic relaxation (relaxation from higher energy states down into the LUMO) occurs on a femtosecond time scale [138] which is smaller than any of the processes considered in the DMC model (particle hopping and recombination). Particle motion (exciton hopping or charge hopping) generally occurs faster than any other process considered in the DMC model and since the Franck-Condon principle states that energetic changes are instantaneous compared with nuclear motion, the assumption to only consider the HOMO and LUMO levels is reasonable. The absorption cross section is a measure of the probability of an absorption process at a particular wavelength, which can be used as an approximation for the DOS. Since the absorption cross section linearly relates to the absorption coefficient, which is directly measured in an UV-VIS spectrum, the

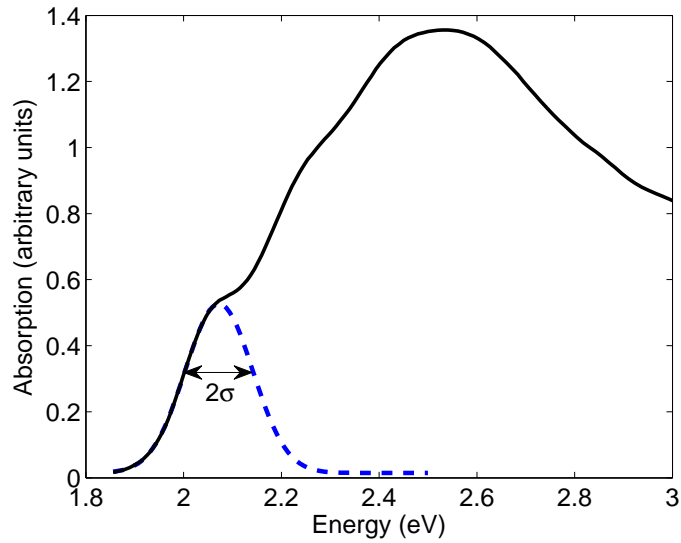


FIGURE 4.7: Measured absorption spectrum of a P3HT film (solid black line) and a Gaussian fitted against the absorption edge (dotted blue line)

TABLE 4.1: σ for some materials

| Material | σ (eV) |
|-----------------|---------------|
| 6T | 0.05 |
| C ₆₀ | 0.09 |
| P3HT (annealed) | 0.06 |

standard deviation of the Gaussian energy distribution, σ , is estimated by fitting a Gaussian function to the edge of the measured absorption spectrum [137, 139]. Provided that the absorption mechanism does not vary with thickness, the energy width of the absorption peaks does not change with thickness. Figure 4.7 shows the absorption spectrum of an annealed P3HT film with a Gaussian fitted against the absorption edge. The corresponding σ is tabulated in table 4.1 along with those corresponding to C₆₀ and sexithiophene (6T). The influence of the deposition method and thermal annealing treatment on energetic disorder and in particular σ is discussed in Section 5.3.2.

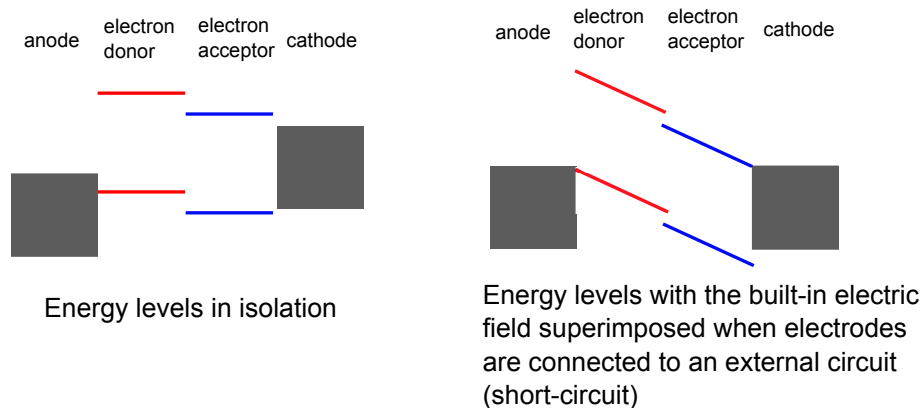


FIGURE 4.8: HOMO and LUMO levels are shown for the electron donor (red) and acceptor (blue) together with the work functions of the cathode and anode. On the left side of the diagram the isolated energy levels are depicted, whereas on the right they are shown when the device is under short-circuit conditions.

4.5.2 Built-in electric field

The cathode has a Fermi level that is closer to vacuum level than the anode. When both electrodes are electrically in contact with each other (through the external electric field), the Fermi levels will equalise and charge transfer will occur which sets up a potential across the active layer (similar to a parallel plate capacitor, see Figure 4.8), which is termed the built-in electric field. Since the active layer is generally ~ 100 nm thick and the potential difference between electrodes is ~ 0.8 eV, electric fields in the order of 10^7 V/m are common in OPV devices. When measuring IV characteristics, an external voltage is applied. The external voltage produces an electric field that opposes the built-in electric field. For an efficient OPV device, the external electric field nullifies the built-in field at roughly V_{OC} . The potential difference between the electrodes affects V_{OC} [25, 140, 141], but many other factors, such as the HOMO and LUMO of both donor and acceptor [24, 25, 142], device structure [141, 143], charge recombination [144, 145], electron traps at the electrodes (see Chapter 7) and the Ohmicity of the semiconductor/electrode contacts [25, 84], do as well. As such, the electric field in the device cannot be assumed to be exactly 0 V/m at V_{OC} , especially for low efficiency devices.

4.5.3 Coulomb interaction

Coulomb interaction between charge carriers will dominate charge behaviour at short distances. Coulomb interaction at site i due to all other j is given by [146]

$$E_{ij} = \frac{q_e q_h}{4\pi\epsilon_0\epsilon_r} \sum_{j=1}^n \frac{1}{r_{ij}} \quad (4.14)$$

where n is the total number of charges in the vicinity of site i , q_e/h the charge of an electron/hole, ϵ_0 the permittivity of free space and ϵ_r the relative permittivity. Coulomb interaction between electrons and electrons or holes and holes is repulsive and coulomb interaction between charges with dissimilar polarity is attractive. Coulomb interaction is calculated for all charges within the ceiling of the thermal capture radius (expressed in lattice constants) +1 lattice constant (i.e. $\text{ceil}(r_c)+1$ nm). The thermal capture radius, r_c , is also termed the coulomb capture radius. r_c is defined as the distance where Coulomb interaction is equal to thermal energy $k_B T$ and is thus given by

$$r_c = \frac{q^2}{4\pi\epsilon_0\epsilon_r k_B T} \quad (4.15)$$

r_c is essentially defined by ϵ_r , which is 2–4 depending on the organic material used. Unless stated otherwise, in my model I assume ϵ_r to be 3.1 appropriate for a P3HT:PCBM system [147], which means all charges within a radius of 20 nm are taken into account. If the coulomb capture radius is chosen too small, IQE and J will be underestimated [148]. However, it has been shown that using r_c as the cut-off radius corresponds extremely well with the exact treatment of electrostatic interactions (Ewald sum) under short-circuit conditions and only has an error of 5 % under open-circuit conditions [148]. This error will even be smaller in my model since the chosen cut-off radius is larger than r_c . Care was taken to not include the non-physical scenario of Coulomb interaction of a particle with itself. Calculating coulomb interaction is the most time consuming part of the program and has to be done for all sites that are considered when calculating hopping rates. Instead of doing calculations for every hop that is considered, a new approach is taken where the coulomb potential energy field is calculated once. This field is then added to the energy landscape for each charge particle.

As the charge moves the field is updated accordingly. In this way, the energy sites for charges automatically include Coulomb interaction.

4.5.4 Surface charge induced at the electrodes

The electric field inside perfect metals is always 0, because they have an infinite amount of free electrons that can move with no resistance and are thus able to oppose any external electric field. As charge carriers approach a metal electrode surface charge is induced to compensate for this external (metal electrode's point of view) electric field. The method of image charges is used to incorporate this effect [146]. Essentially an equal and opposite image charge inside the metal is created, which results in a lowering of the potential energy at the electrode interface. As soon as a charge carrier is within the cut-off radius of the metal electrodes, an image charge is created, which ensures that the electric field in the metal remains zero.

4.6 Exciton transport and recombination

The performance of an OPV device is a function of the efficiency of both exciton dissociation and charge extraction. The exciton dissociation efficiency depends upon the morphology and the exciton transport properties associated with the materials of interest. However, exciton dissociation at the heterointerface is assumed to have an efficiency of unity, which follows from previous reports of fast and efficient charge separation in blends [54]. A two-step dissociation mechanism has been reported for material systems with efficient energy transfer to the fullerene moiety [149]. This proposed mechanism consists of energy transfer (i.e. exciton transfer) from the polymer to fullerene followed by fast hole transfer from the fullerene back into the polymer. Irrespective of the exact mechanism, exciton dissociation at the heterointerface occurs at near unity efficiency.

The preferred method for modelling exciton hopping transport may be either Förster Resonance Energy Transfer (FRET) theory or Dexter theory, depending on the dominant type of exciton (triplet or singlet) [43]. Dexter's approach treats exciton transport

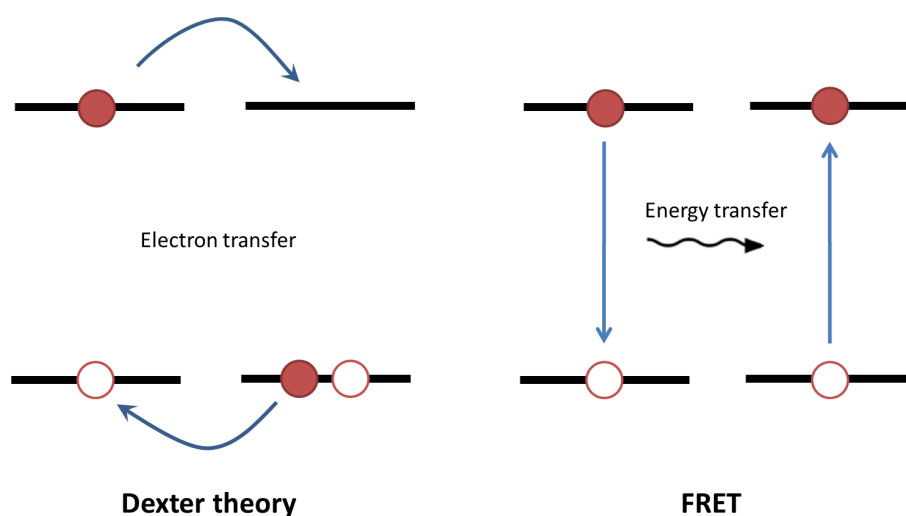


FIGURE 4.9: Left: exciton transport through charge transfer. Right: exciton transport through energy transfer.

as electron transfer as opposed to energy transfer and predicts that the exciton transfer rate decays exponentially with the distance between the exciton donor and acceptor sites. However, when a triplet exciton is located near a phosphorescent organometallic donor it has been shown it may undergo Förster transfer [150]. Figure 4.9 depicts the fundamental difference between the Dexter and FRET mechanism for exciton transport.

Singlet excitons have short lifetimes on the order of nanoseconds [47, 151–153] while triplet excitons have lifetimes on the order of microseconds [46, 154–156]. While triplet excitons tend to have longer lifetimes, they also tend to have lower diffusivities (as predicted by the difference in transfer rates calculated from FRET and Dexter theory) and thus travel slower, which results in similar diffusion lengths for both types of excitons [43].

In contrast to excitons that are created through charge injection, light absorption in organic semiconductors yields only singlet excitons and thus triplet excitons can only be formed through intersystem crossing [157, 158]. However, these triplet excitons slowly decay to the ground state since they lie in an energy state that is too low for dissociation [158]. An example of this process is shown in Figure 4.10 for an F8BT:PCBM solar cell. Thus, intersystem crossing does not generally contribute to

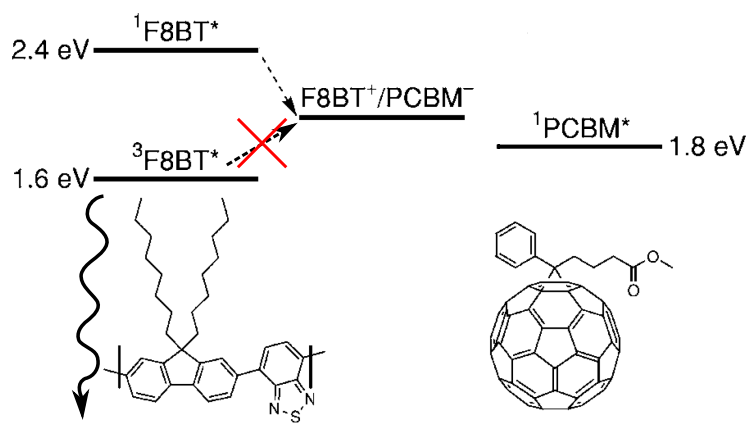


FIGURE 4.10: Modified from [155]. The singlet and triplet F8BT states are shown together with the F8BT/PCBM CT state (in the middle) and the PCBM LUMO. While conversion of the F8BT singlet state to the CT state is energetically favourable, the same is not true for the F8BT triplet state. As a result, the triplet state is more likely to decay to the ground state instead of dissociating.

charge generation and may be viewed as a (delayed) recombination mechanism. There are two exceptions to this statement: upconversion [159] and singlet fission based OPV devices. Photochemical upconversion is achieved by utilising a sensitizer with efficient singlet-triplet intersystem crossing. Triplet excitons are passed on to a second species (referred to as the emitter [160] or acceptor/annihilator), where two triplet excitons annihilate to form a singlet exciton with more energy than the original singlet exciton generated in the sensitizer. The resulting high energy singlet exciton may be emitted and absorbed by photoactive materials. Upconversion can thus be utilized to absorb light in the long wavelength region where common OPV materials do not absorb well. Upconversion is an advanced concept and as yet enhancements have not been significant, but future improvements are expected [160].

Singlet fission is the process of converting a single singlet exciton into two triplet excitons through coupling with a nearby molecule in the ground state [161]. As a consequence, the number of extracted charges (i.e. photocurrent) could potentially be doubled, while halving the maximum achievable voltage as the triplet excitons have at most half the energy of the singlet exciton. Quantum efficiencies have been shown to increase by 45 % [162], but as yet the PCE of systems that use this advanced concept

remain low [163, 164].

Notwithstanding these exceptions, intersystem crossing is irrelevant for certain material systems, including the commonly used P3HT:PCBM system, as the overall rate covering singlet diffusion and subsequent exciton dissociation at the hetero-interface is much higher than the intersystem crossing rate [165]. Consequently, singlet excitons are the dominant exciton species and thus FRET is the preferred theory to describe exciton behaviour in organic solar cells. In Chapter 5 FRET is compared to a random walk and thus both the implementation of FRET and a simple three dimensional random walk are treated below.

In my model, single occupancy (only one exciton is allowed to occupy a single site) is imposed for excitons as they are found to behave like fermions for short range interactions and at high enough concentrations [166, 167]. Since OPV materials have high absorption coefficients, the exciton population is assumed to be high enough for fermionic behaviour. Also, in the DMC model, single occupancy only plays a role if exciton density is high and thus fermionic behaviour is ensured in cases that matter [168]. For exciton densities under operating conditions (1000 W/m²) exciton-exciton annihilation can be ignored [169].

An exciton always has two events associated with it: an exciton hopping event and an exciton recombination event. If the latter is executed the exciton is deleted from the system (including its hopping event) and a record is made of the recombination event along with the time and location of recombination. The exciton recombination rate is simply determined by the fluorescence lifetime, t_0 :

$$k_{exrec} = \frac{1}{t_0} \quad (4.16)$$

Lifetimes together with measured diffusion length, L , for excitons in some materials are shown in table 4.2.

4.6.1 Förster Resonance Energy Transfer

Now that FRET has been identified as the appropriate theory to model exciton transport in the DMC model, a closer look at FRET is taken at the theory and how hopping

TABLE 4.2: t_0 and L for some materials

| Material | $t_0(s)$ | $L(nm)$ | Reference |
|----------|-----------------------|--------------|-------------------------|
| 6T | 1.8×10^{-9} | 100 ± 20 | [152], [47] & Chapter 5 |
| PCBM | 1.25×10^{-9} | 5 | [170] |
| P3HT | 4×10^{-10} | 8.5 | [153] |

rates are calculated. In 1948 Förster published a quantum-mechanical treatment of transfer of electronic excitation energy between similar molecules (oscillators) [171]. These oscillators effectively behave like dipoles and their interaction governs the energy transfer rate. Energy must be conserved, which means that the acceptor must have energy states available such that the gain in energy of the acceptor is equal to the loss in energy of the donor. As argued before, the available energy states can be experimentally determined by measuring the absorption spectrum and fluorescence spectrum. Förster determined that the energy transfer rate, k_{FRET} , is given by

$$k_{FRET} = \frac{1}{\tau_0} \left(\frac{R_0}{r} \right)^6 \quad (4.17)$$

where τ_0 is the fluorescence lifetime of the exciton, r the distance between donor and acceptor and R_0 the Förster radius which is the critical distance at which the fluorescence probability is equal to the energy transfer probability and is given by

$$R_0^6 = \frac{9000 \ln(10) \phi \kappa^2}{128 \pi^5 N_A n^4} \int_0^\infty \epsilon(\nu) F(\nu) \frac{d\nu}{\nu^4} \quad (4.18)$$

where κ is the orientation factor between donor and acceptor, ϕ the fluorescence quantum yield, n the index of refraction, N_A Avogadro's number, ν is the frequency of light, ϵ the peak-normalised fluorescence spectrum of the donor and F the absorption spectrum of the acceptor. The integral is referred to as the overlap integral and experimentally quantifies the dipole-dipole interaction of donor and acceptor. κ is difficult to measure directly, which is why R_0 is treated as a fitting parameter. However, R_0 can be determined in a separate experiment by fitting against photoluminescence (PL) measurements as will be discussed in Chapter 5 where the relation between R_0 and the diffusion length is also discussed. The distance dependence of the exciton hopping rates

is captured by equation (4.17), but exciton transport is also influenced by the energy landscape as determined by Gaussian energetic disorder. A downward hop in energy is taken to occur with the maximum rate while the rate of hops upwards in energy will decrease exponentially with the energy difference. This dependence on relative site energy is captured by the so called f -function or Boltzmann factor:

$$f(E_i, E_j) = \begin{cases} e^{-\frac{E_j - E_i}{k_B T}} & E_j > E_i \\ 1 & E_j < E_i \end{cases} \quad (4.19)$$

where k_B is the Boltzmann constant, T temperature, E_i is the energy of the current site and E_j is the energy of a possible destination site, j . The total hopping rate is thus given by

$$k_{FRET} = \frac{1}{\tau_0} \left(\frac{R_0}{r} \right)^6 f(E_i, E_j) \quad (4.20)$$

All possible sites within 3 nm (121 sites in total when the lattice constant is 1 nm) are considered and the site with the shortest waiting time is taken as the destination site of the next hop and is added to the event queue.

4.6.2 Random Walk

A simple random walk (RW) is independent of the energy landscape. Only nearest neighbours are considered and there is an equal hopping probability for each of the six directions. A random walk is simulated using the same FRM approach of calculating rates. The diffusion length, L , scales with the number of steps taken, N , through

$$N = L^2 \quad (4.21)$$

See Appendix A for the derivation of this equation. Since we set N to whatever diffusion length is desired and we also know the exciton lifetime, the average hopping time, τ_{RW} , is related to N through

$$N = \frac{\tau_0}{\tau_{RW}} \quad (4.22)$$

and thus the hopping rate is given by

$$k_{RW} = \frac{L^2}{\tau_0} \quad (4.23)$$

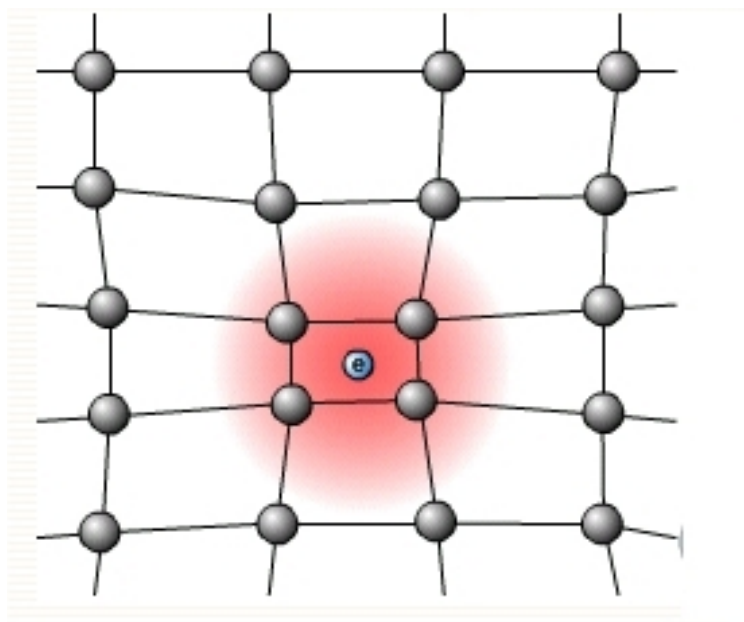


FIGURE 4.11: Depiction of an electron and the lattice deformation it causes, i.e. a polaron.

4.7 Charge Transport

One of the most crucial parts of modelling an organic solar cell is modelling charge transport. Charges enter the system either through exciton dissociation or charge injection. As described before, charges in organic semiconductors are localised on conjugated segments. The local atoms have to accommodate the charged particle and thus the network of atoms become deformed through electron-phonon interaction (see Figure). This coupling is relatively strong in organic semiconductors and the complex of a charge and its deformed surroundings is termed as a polaron. Polaron transport has been modelled in a number of ways [172], the most frequently used established theories in the context of DMC models are Marcus theory and Miller-Abrahams type expressions. Both theories will be discussed as both are used to describe charge transport in the bulk and charge injection respectively.

4.7.1 Miller-Abrahams expression

Miller and Abrahams investigated polaron rate equations in 1960 [173]. Just like with most tunnelling processes, the polaron hopping probability is assumed to decay exponentially with the distance between localised states. The hopping rate is given by

$$k_{MA} = k_0 e^{-2\gamma r} f(E_i, E_j) \quad (4.24)$$

where k_0 is the attempt to hop frequency, f is as described previously (equation (4.19)) and γ the localisation constant. γ essentially indicates to what extent the charge particle is localised [139]. γ is usually in the order of 1 nm^{-1} [101, 139]. However, when only considering nearest neighbours, r is not variable and the exponential reduces to a constant. While equation (4.24) has been shown to accurately model charge transfer rates [172], it lacks a comprehensive theoretical derivation, i.e. it is an empirical equation.

4.7.2 Marcus theory

Arguably, the most successful theory in molecular charge transfer dynamics, Marcus theory was developed by R. H. Marcus in 1956 [174]. Marcus' contribution to electron transfer theory was rewarded with the 1992 Nobel Prize in Chemistry. Hush developed a similar theory, which is referred to as Marcus-Hush theory [175, 176]. Unlike Miller-Abrahams expression, Marcus theory has a strong theoretical background and is therefore the preferred theory for electron transfer in the organic active layer, which is why it is frequently used in Monte Carlo simulations of OPV devices [70, 128, 177, 178].

Classical derivation

In the derivation of classical Marcus theory, the initial and final states are approximated with harmonic oscillators:

$$\begin{aligned} U_i &= \frac{1}{2} m \omega x^2 + E_i = \alpha x^2 + E_i \\ U_j &= \frac{1}{2} m \omega (x - r)^2 + E_j = \alpha (x - x_j)^2 + E_j \end{aligned} \quad (4.25)$$

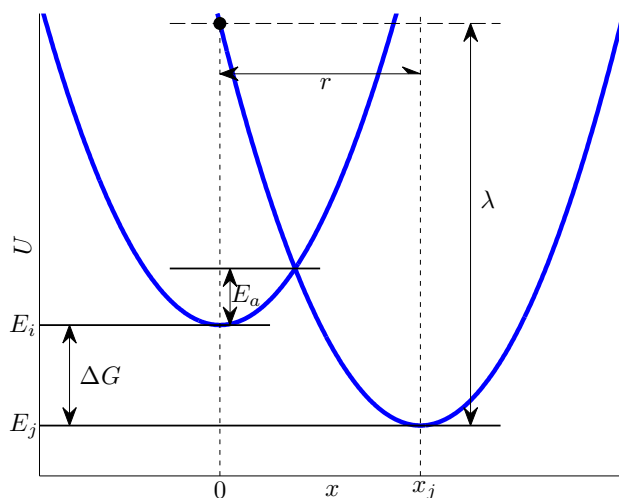


FIGURE 4.12: Initial (left curve) and final state (right curve) are approximated with harmonic oscillators. The dashed vertical lines go through the minimum of their respective parabolas. The relevant quantities in equation (4.28) are indicated as well. The horizontal dashed line goes through the point corresponding to the potential energy of the final state at the position of the initial state (indicated with a black dot).

where x is the reaction coordinate, U the potential energy, m and ω oscillator mass and angular frequency, which are captured by a single constant α . Subscripts i and j refer to the initial and final states respectively. For algebraic ease, x is defined in such a way that the initial harmonic oscillator is centred around 0. This may be done since only the relative reaction coordinate (between initial and final state) is of importance. Both equations are plotted in Figure 4.12. The Franck-Condon principle states that an energetic transition is much faster than nuclear motion, i.e. transition in the y -axis in Figure 4.12 are faster than transitions in the x -axis. In order to satisfy both energy conservation and the Franck-Condon principle charge transfer must occur at the intersection of the parabolic curves. The intersection of the two parabolic curves thus determines the energy barrier, E_a , which determines the transfer rate through the Arrhenius equation:

$$k = k_0 e^{\frac{-E_a}{k_B T}} \quad (4.26)$$

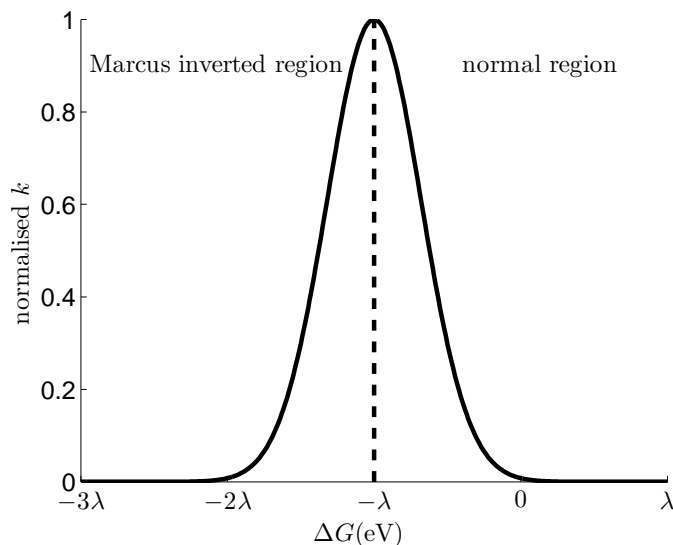


FIGURE 4.13: Marcus rate as a function of site energy difference (solid line). The dashed line acts as a divider for the Marcus inverted and normal regions.

E_a can be determined by equating and solving the harmonic oscillator equations (equation (4.25)), which gives

$$E_a = \frac{(\alpha r^2 + \Delta G)}{4\alpha r^2} \quad (4.27)$$

where ΔG is the Gibbs free energy, i.e. $E_j - E_i$. E_a is normally expressed in terms of the reorganisation energy, λ , which is the energy needed to bring the charge and its surroundings to the equilibrium geometry of the final state [63], i.e. the energy of the final potential curve at the atomic coordinate of the initial state, as can be seen in Figure 4.12. Combining $\lambda = \alpha r^2$ with equation (4.27) and equation (4.26) gives us the Marcus equation:

$$k_{Marcus} = k_0 e^{\left(\frac{-(E_j - E_i + \lambda)^2}{4\lambda k_B T} \right)} \quad (4.28)$$

The most striking part of this equation is the quadratic response to ΔG , because it means that the hopping probability to sites that are energetically much lower than the present energy state is very small, which is in contrast to the Boltzmann factor (equation (4.19)), where downward hops proceed with the maximum rate. Figure 4.13 shows the charge hopping rate as a function of ΔG . k_{Marcus} peaks at $-\lambda$. The part of the function to the left of $-\lambda$ is called the Marcus inverted region and has

been experimentally confirmed for many organic materials [179] including derivatives of the commonly used electron acceptor, C₆₀, and electron donor, porphyrin [64]. This experimental evidence further justifies the use of Marcus theory instead of Miller-Abrahams type expressions. Charge recombination must occur in the Marcus inverted region, otherwise recombination will be extremely dominant and EQE values of well over 50 % (Figure 9.2) would not be possible. Thus, HOMO_{donor}-LUMO_{acceptor} provides an upper limit for λ . In DMC models λ is generally taken to be in the order of 0.2 eV [70, 79]. λ has been measured to be 0.66 eV for C₆₀-porphyrin electron transfer [180]. For this complex, the reaction centres were separated by ~ 1 nm, which corresponds to our lattice constant. Furthermore, Coffey et al. [181] determined λ for poly[9,9'-dioctyl-fluorene-co-bithiophene] and Poly[(9,9-di-n-octylfluorenyl-2,7-diyl), which are polymers that have been used in OPV devices. For these polymers λ was found to be 0.8 and 0.4 eV respectively. In light of these results, a value for λ of 0.5 eV has been chosen for DMC simulations.

Semi-classical equation and distance dependence of Marcus rate

Classical Marcus theory works well for diabatic electron transfer [182]. Electron transfer may be regarded as a radiationless transition between two potential energy curves and is in general given by Fermi's golden rule (FGR)

$$k_{FGR} = \frac{2\pi}{\hbar} J^2 FC \quad (4.29)$$

where J is the electronic coupling matrix element i.e. wavefunction overlap of donor and acceptor sites and FC the Franck-Condon Factor. A classical analysis of FC yields

$$k_{Marcus} = \frac{J^2}{\hbar} \sqrt{\frac{\pi}{\lambda k_B T}} e^{\left(\frac{-(E_j - E_i + \lambda)^2}{4\lambda k_B T} \right)} \quad (4.30)$$

Equation (4.30) corresponds to a semi-classical analysis, where the electronic coupling is treated quantum mechanically, but nuclear motion is treated classically. It is clear that equation (4.30) is equivalent to equation (4.28) with

$$k_0 = \frac{J^2}{\hbar} \sqrt{\frac{\pi}{\lambda k_B T}} \quad (4.31)$$

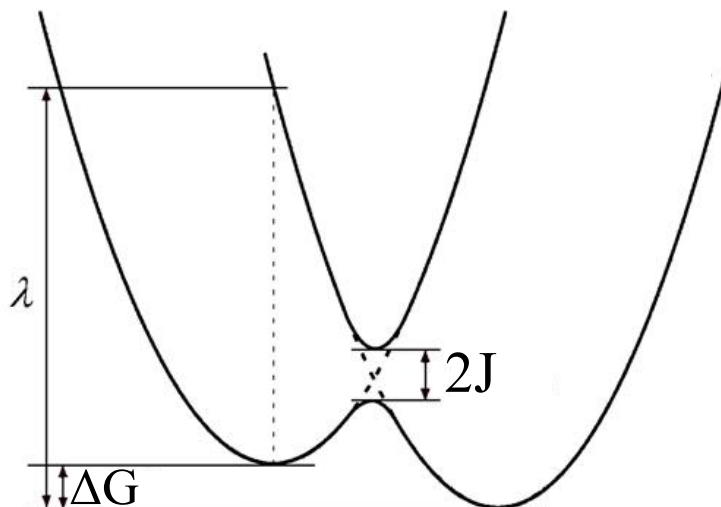


FIGURE 4.14: Splitting of potential curves occurs when electronic coupling between the two states is sufficiently large. The electron follows the lowest potential curve that connects the two states.

Electron transfer can be regarded to take place in adiabatic, nonadiabatic or intermediate regions depending on the magnitude of J [176]. If J is small (coupling between the two states is weak), the initial and final state retain their potential curves. However, if J is large (significantly larger than $k_B T$), the two states interact at the crossing of their potential energy curves and they effectively split into a lower and upper one as illustrated in Figure 4.14. This coupling between the two states may allow for faster electron transfer as the energy barrier is lower than predicted by Marcus theory. The splitting of these potential curves is not taken into account in semi-classical Marcus theory and for full adiabatic electron transfer, a quantum chemical approach must be taken. In the DMC model J is assumed to be sufficiently small, so Marcus theory may be used to calculate charge transfer rates. J decreases with distance and may be approximated with

$$J^2 = c_0 e^{-\beta r} \quad (4.32)$$

where c_0 is a constant and β is a damping factor. This exponential decay with distance shows excellent agreement with many single hop electron transfer experiments [183]. In literature, only nearest neighbours are considered when using Marcus theory in DMC

models [70, 177, 178, 184]. Imahori et al. [180] shows that for a C₆₀-porphyrin system (both C₆₀ and porphyrins are common OPV materials) k decays exponentially with distance, which means the distance dependence of k is dominated by equation (4.32) rather than λ . They determined β to be 0.6 Å⁻¹. Using this value and integrating equation (4.32) from 0 to 1 nm shows that 99.75 % of hops to any site is captured by nearest neighbour hops, which justifies the approach we take of considering the six nearest neighbours only. In addition, Wolf et al. show that there is hardly any statistical difference between including nearest neighbours only and including second-nearest neighbours as well. They used the Miller-Abrahams expression, which has a similar exponential form to equation (4.32) and conclude that long-range hopping is unimportant [185]. However, if modelling polymers with a high discrepancy between intra- and inter-chain hopping probabilities, long range hopping may need to be considered using Equation (4.32). We assume this is not the case for the virtual organic solar cells that we model. In the rare case that no sites are available for hopping for morphological reasons or occupancy by other charges, an event is added to the end of the event queue after which hopping rates for the particle in question are recalculated.

4.8 Charge extraction and injection at electrodes

Charge extraction (organic-metal hop) is treated in the same way as an organic-organic hop i.e. extraction rates are calculated using Marcus theory [70, 178]. The energy level of the electrodes are assumed to have no energetic disorder (i.e. perfect metal). In addition, they are assumed to be pinned throughout the simulations, i.e. they are not affected by the flow of charge. Image charges ensure that the Coulomb electric field of the charges does not affect the energy level of the electrodes at the organic-electrode interface. The energy barrier at this interface may not be simply defined by using measured energy levels of isolated materials. When the organic layer comes into contact with an electrode the actual barrier may be quite different than expected due to the existence of a dipole layer at the interface [186], an oxide barrier due to electrode corrosion [187, 188] or another chemical reaction giving rise to different interface species

[82] and Fermi level pinning effects [186]. As such, the energy barrier is somewhat arbitrary and is treated as a fitting parameter to within a reasonable deviation from the energy barrier as dictated by measured isolated energy levels. The effect of an energy barrier at the electrode on IV characteristics is investigated in more detail in Chapter 7. The physical contact between organic layer and electrodes are assumed to be perfect, since surface roughness induced disorder has been evaluated and was found to be too weak to give a noticeable difference in charge injection [189].

In order to generate full IV curves from DMC simulations, dark current has to be modelled as well, which is achieved by adopting a thermionic injection method. This has been shown to adequately model dark current injection in organic semiconductors [185]. The small polaron model (Marcus theory) may not be appropriate for metals and thus the empirically valid and conventional Miller-Abrahams expressions are used. We thus take the same approach as Meng et al. [178] and use Marcus theory for charge extraction and the conventional Miller-Abrahams expression for charge injection. The same energy barrier that applies to charge extraction also applies to charge injection, but with an opposite sign. Electrons are injected from the cathode into the electron accepting material and holes are injected from the anode into the electron donating material. Unless there is a significant extraction barrier, charges that are injected into the layer closest to the electrode are likely to be extracted immediately as the site energy at the interface is dominated by the coulomb potential of the image charge [190]. This interaction with the induced surface charge in the metal electrode reduces the probability of successful charge injection and is referred to as the Schottky effect [187]. Figure 4.15 shows the combined potential of the image charge and the electric field as a function of the distance to the image charge, r at $F=10^7$ V/m (approximately J_{SC}), $F=0$ V/m (roughly V_{OC}) and $F=-1.25 \times 10^7$ V/m (forward bias). The points associated with the first and second layer of the organic lattice are indicated with a blue and red dot respectively. For electric fields within the normal range of a typical IV curve, an injected charge carrier has to overcome an energy barrier to hop into the active layer. This energy barrier is greatly reduced when the charge carrier is in

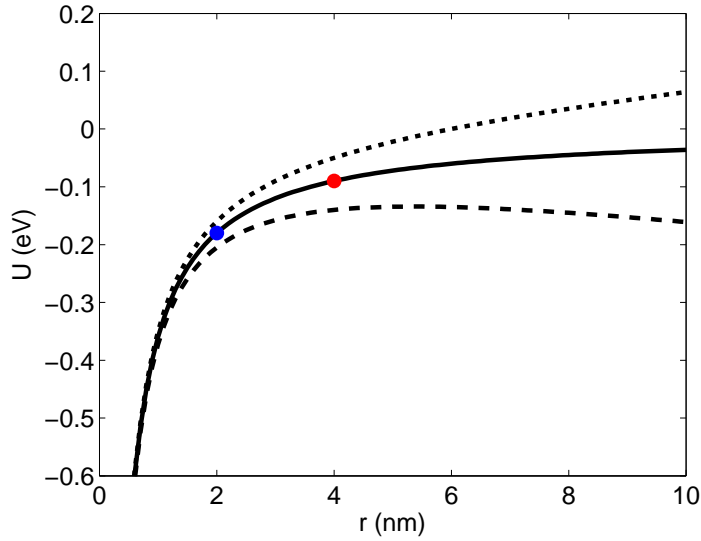


FIGURE 4.15: The potential energy, U , due to Coulomb interaction with the image charge and the electric field. The dotted line corresponds to $F=10^7$ V/m (approximately J_{SC}), solid line to $F=0$ V/m (roughly V_{OC}) and the dashed line to $F=-1.25 \times 10^7$ V/m (forward bias). The blue dot indicates the position of a charge that is injected in the first layer of the organic lattice and the red dot is the situation associated with the a charge in the second layer.

the second layer and the device is in forward bias. Continuously injecting charges, that are immediately extracted again wastes computational time. To diminish this computational waste, injected charges are forced to hop once into the active layer with the rate associated with that hop before allowing the freshly injected charge to be extracted. This approach is in accordance with Meng et al. [178]. All simulations that included charge injection reached an equilibrium, which provides confidence that detailed balance is not violated by Meng et al.'s charge injection approach. As an example, the number of charge carriers in the active layer as a function of simulated time is shown in Figure 4.16 for a virtual organic solar cell in the dark (no exciton generation) for a voltage of 0.3 V, 0.6 V, 0.75 and 0.9 V. The charge carrier density would always equilibrate if simulations ran long enough. The injection rate constant (k_0 in equation (4.24)) is treated as a fitting parameter and is determined by fitting against experimental dark IV curves. By appropriately choosing the energy barrier and the injection rate constant good fits can be obtained, which also justifies the approach taken. The injection rate does not vary with thickness as it is an interface process and

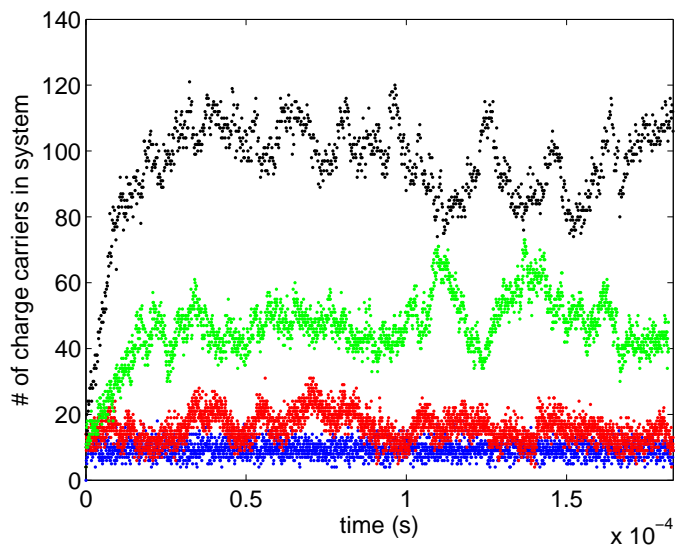


FIGURE 4.16: Charge carrier population in the active layer as a function of time for a simulation in the dark at a voltage of 0.3 V (blue), 0.6 V (r), 0.75 V (green) and 0.9 V black.

not a bulk process such as light absorption. A thicker active layer would result in a longer pathway for injected charges, which in turn results in a lower current for the same voltage. Hence, a decrease in the apparent rectifying strength is expected as the active layer thickness increases. Figure 4.17 shows dark IV curves of the first device (smallest ITO pathway to common electrode) on architecture I substrates (see section 3.1) for active layer thickness varying from 23 nm to 308 nm. It is clear that the rectifying strength decreases with increasing active layer thickness, which is consistent with the theory that the charge injection rate does not scale with thickness and only depends on the electrode-organic interfaces. When matching experimental dark IV curves to modelled dark curves, one has to be conscious of series resistance in the electrodes, which is not considered in the DMC model. The model only considers the processes in the photo-active layer and not in the electrodes. Figure 4.18, shows dark IV curves of four devices on the same architecture I substrate. Since these devices are located on the same substrate and have undergone the same fabrication steps, they should produce the same IV curves. However, the ITO pathway to the common electrode is different and thus extra series resistance will decrease the apparent rectifying behaviour. Compared to the finger closest to the common electrode, the second closest has an extra resistance

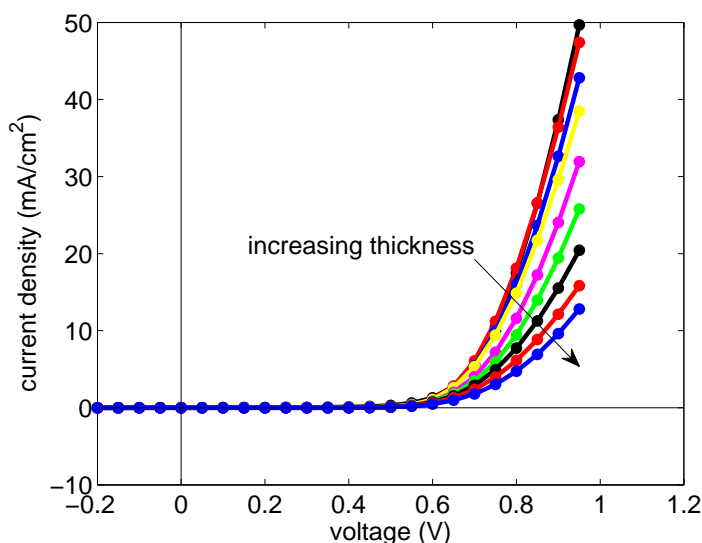


FIGURE 4.17: Measured dark curves for the following thickness: 23 nm, 57 nm, 80 nm, 114 nm, 137 nm, 171 nm, 194 nm, 251 nm and 308 nm. The rectifying strength decreases with increasing thickness, which indicates that charge injection is an interface process.

of 8Ω , the third closest 18Ω and the furthest finger 26Ω . In order to diminish the effect of external electrode series resistance, modelled results should only be compared to devices with the shortest ITO pathway. In Chapter 7, full I-V curves are simulated and a good fit is found for the dark I-V curve (see Figure 7.3).

The rectifying behaviour mainly results from charge injection. However, charge particles in the organic bulk also exhibit a rectifying behaviour in the fourth quadrant, as seen in the voltage dependence of photocurrent (the difference between dark and light I-V curves) [191, 192]. In order to quantify the behaviour of bulk charges, a simulation was set up where excitons are created according to the optical field (as usual), but charges are not injected. In other words, all processes in an organic solar cell except for charge injection were simulated. The result of these simulations are shown in Figure 4.19 for $\lambda = 0.1$ eV and $\lambda = 0.5$ eV. The maximum V_{OC} , as defined by the work function difference of the electrodes (0.8 eV), is achieved. An interesting result is that charge transport alone (i.e. charge extraction efficiency is unity) gives rise to a fill factor < 1 . The behaviour is symmetrical in V_{OC} , because this is the point where the electric field changes direction. Consequently recombination is largest at 0.8

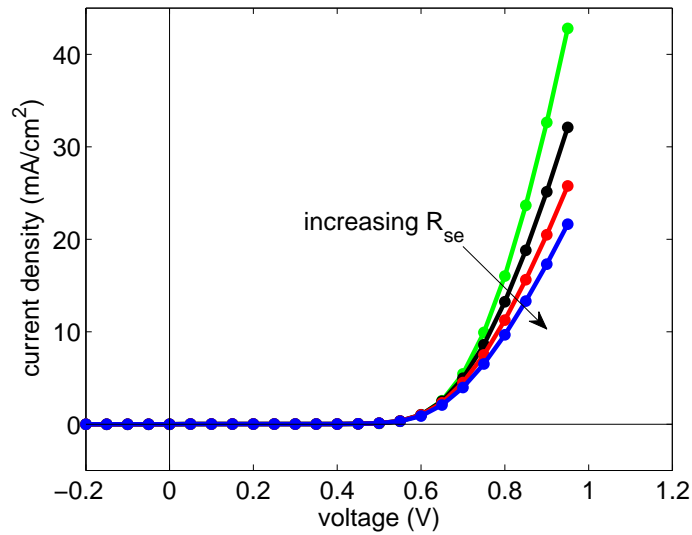


FIGURE 4.18: Dark IV curves of architecture I devices on the same substrate. The only difference between these devices is the ITO path length and thus R_{se} . Green corresponds to the device that is closest to the common ITO contact and blue the one that is furthest away from the common electrode.

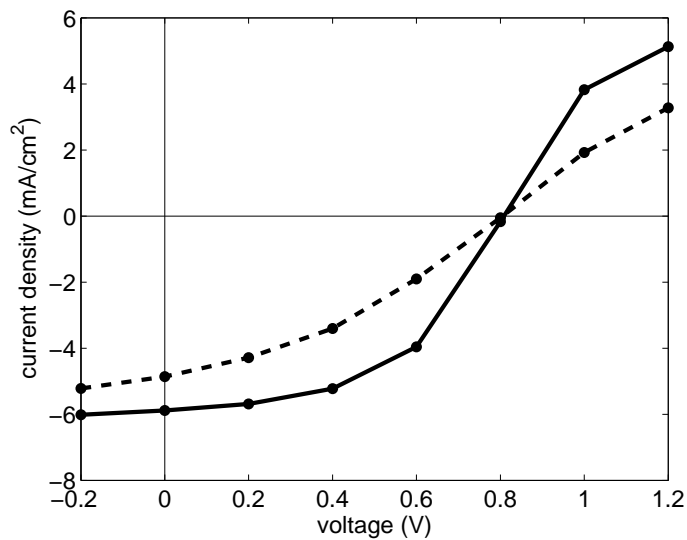


FIGURE 4.19: IV response of BHJ devices, while ignoring thermionic charge injection. The dashed line corresponds to $\lambda = 0.5$ eV and the solid line corresponds to $\lambda = 0.1$ eV.

V. An active layer of 100 nm was simulated, which means that the energy difference between adjacent sites due to the electric field at J_{SC} is only 0.008 eV. Even though this value is very small compared to the other energetic effects, it is the only effect with a consistent direction. As such, the average charge flow is heavily affected by the built-in electric field. Hence, the rectifying behaviour of IV curves does not only originate from thermionic injection, but also the built-in field.

4.9 Charge recombination

When an electron and hole are adjacent to each other, they may recombine with a certain probability. This type of recombination is referred to as charge recombination. Generally, we distinguish between two types of charge recombination: geminate recombination and bimolecular recombination. Geminate recombination refers to charge recombination where both electron and hole originate from the same charge-transfer complex i.e. exciton. Bimolecular recombination refers to charge recombination between charges originating from different excitons. The overall charge recombination probability is defined by two competing rates: the charge hopping rate and the charge recombination rate. Charge recombination is essentially the hopping of an electron from the LUMO of the electron acceptor into an available state (hole) in the HOMO of the electron donor. Hence, Marcus theory may be used to calculate this hopping probability. The recombination rate, is then defined by the gap between the LUMO of the acceptor and HOMO of the donor ($\text{HOMO}_{donor}\text{-LUMO}_{acceptor}$ gap). Considering equation (4.28), λ is the fitting parameter to tailor charge recombination to experimental data. Figure 4.20 shows the percentage of charge transfer complexes (newly dissociated excitons that are still coulombically bound at the heterointerface) that separate for two cases: a heterointerface defined by a 1 eV $\text{HOMO}_{donor}\text{-LUMO}_{acceptor}$ gap and a heterointerface defined by a 1.5 eV $\text{HOMO}_{donor}\text{-LUMO}_{acceptor}$ gap. A charge pair is considered separated when the distance between them is larger than the coulomb capture radius. In these simulations charge hopping was simulated using equation (4.30), where the distance dependence is given by equation (4.32) with $\beta = 0.6 \text{ \AA}^{-1}$. Other chosen

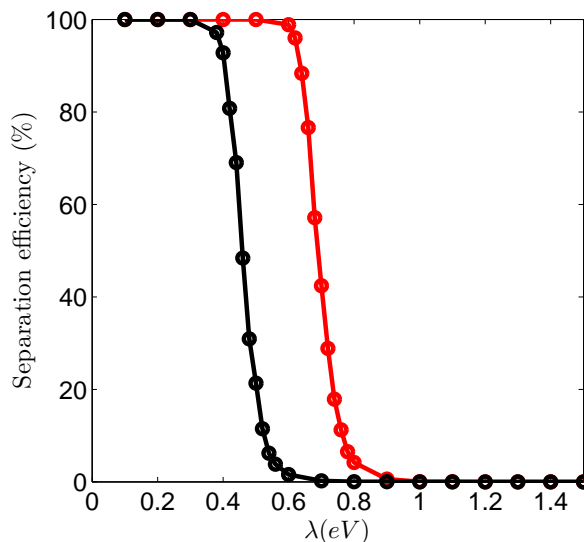


FIGURE 4.20: Geminate separation efficiency of charge pairs as a function of λ for a HOMO_{donor} - $\text{LUMO}_{acceptor}$ gap of 1 eV (black) and 1.5 eV (red)

parameters were $\sigma = 0.05$ eV, k_0 is 2×10^{14} Hz and an electric field of 8×10^6 V/m. A bilayer morphology was employed and periodic boundaries were invoked in all directions effectively creating an infinite lattice. Charge pairs were created one at a time to exclude bimolecular recombination. Both functions drop off in the same manner, but the larger HOMO_{donor} - $\text{LUMO}_{acceptor}$ gap pushes the point where geminate recombination becomes dominant towards larger values of λ , because charge recombination is pushed deeper into the Marcus inverted region. It is clear, that lowering λ would lead to larger separation efficiencies as would increasing the HOMO_{donor} - $\text{LUMO}_{acceptor}$ gap. Obviously the drawback of a large HOMO-LUMO gap is the loss in light absorption. Viewing from the other side, Marcus theory predicts that low band gap polymers are inherently more prone to charge recombination. This relation has been experimentally observed in a oligo(p-phenylene vinylene)/ C_{60} system [193]. Since V_{OC} depends on charge recombination [145], this result is also consistent with the observation that the maximum V_{OC} as dictated by energy levels alone, is difficult to achieve in OPV devices [68].

In light of Figure 4.20, λ values < 0.6 eV seem reasonable for a 1 eV HOMO_{donor} - $\text{LUMO}_{acceptor}$ gap system (e.g. P3HT:PCBM). In this simulation we treated λ as

the fitting parameter to yield expected recombination rates as could be determined from fitting to experimental data. Instead of fitting λ , we directly choose the desired recombination rate, in correspondence with literature [101, 178, 184]. This approach may also include charge recombination mechanisms that are facilitated by triplet states [67, 69] or impurities in the HOMO-LUMO gap [194] and does not purely rely on direct HOMO_{donor}-LUMO_{acceptor} gap recombination. It is thus a more general, simple and perhaps more inclusive model for charge recombination. Now, it is important to investigate the relation between recombination efficiency, η_{rec} , and recombination rate, k_{rec} , relative to hopping rate constant, k_0 . Recombination efficiency does not depend on the absolute value of k_{rec} , but it depends on k_{rec} relative to k_0 , because recombination efficiency quantifies the competition between recombination and charge separation (directly influenced by charge carrier mobility). A full simulation was run with a BHJ morphology at $V=0$, where $\lambda=0.5$ eV, $k_0 = 3 \times 10^{11} \text{ s}^{-1}$. The results in Figure 4.21 will serve as a 'look-up' Figure for simulating a particular system, as is done in Chapter 6. We note that charge carrier mobility depends on k_0 , λ and energetic disorder. There may be several combinations of these parameters that would give the same charge carrier mobility and recombination efficiency. Figure 4.21 only serves as a 'look-up' figure to tune charge recombination for the specific combination of k_0 ($3 \times 10^{11} \text{ s}^{-1}$), λ (0.5 eV) and energetic disorder ($\sigma = 0.05$ eV) used in this simulation. The charge recombination efficiency is shown together with the chosen hopping rate constant.

4.10 Determining performance parameters from simulations

A simulation starts with the creation of an exciton or the injection of a charge. As a result, the system starts off with 0 charges, which in most cases is not the average charge population of a system in steady state. The performance of a system in the transient regime may be quite different from the performance of a system in steady

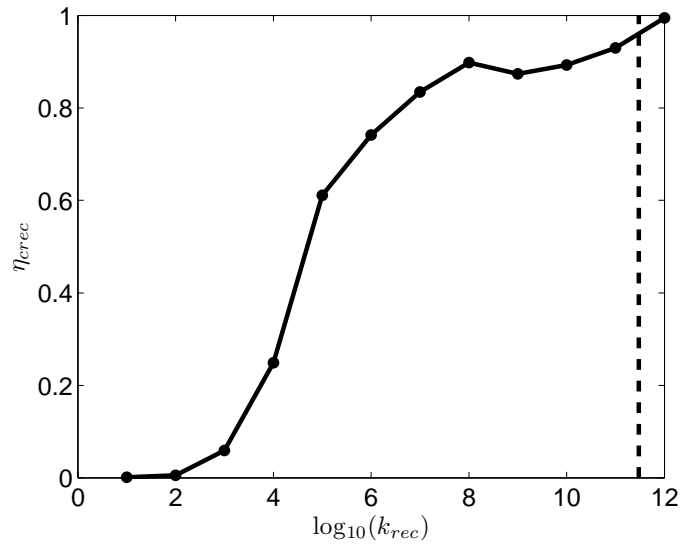


FIGURE 4.21: Charge recombination (η_{rec}) as a function of the recombination rate constant (k_{rec}). The vertical dashed line indicates the hopping rate constant.

state. Hence, before any information is extracted from the simulations, the simulations have to run long enough to reach a steady state. The exciton population is usually relatively small and reaches steady state very quickly. The charge population, on the other hand, can be much larger and is usually the bottleneck in reaching a steady state. The average number of charges in the system at steady state depends on the injection rate, recombination rates, exciton generation rate, dissociation efficiency, extraction efficiency, hopping rates, system size and morphology. Figure 4.22 shows the evolution of the charge population for five different simulations. Some systems may contain such a small number of charges that they virtually start in steady state (yellow curve). A larger steady state charge population generally requires more virtual time (simulated time), but also more computational time. Once a steady state is reached, the input (generation, injection) and output (dissociation, recombination, extraction) of excitons and charges are tracked to determine performance indicators. At least 5 separate simulations are executed for each set of parameters, so an average and a standard deviation may be determined. The standard deviation in the simulated performance parameters is generally smaller than that seen in experimental data corresponding to a set of devices that are nominally the same. Many performance indicators may be extracted from

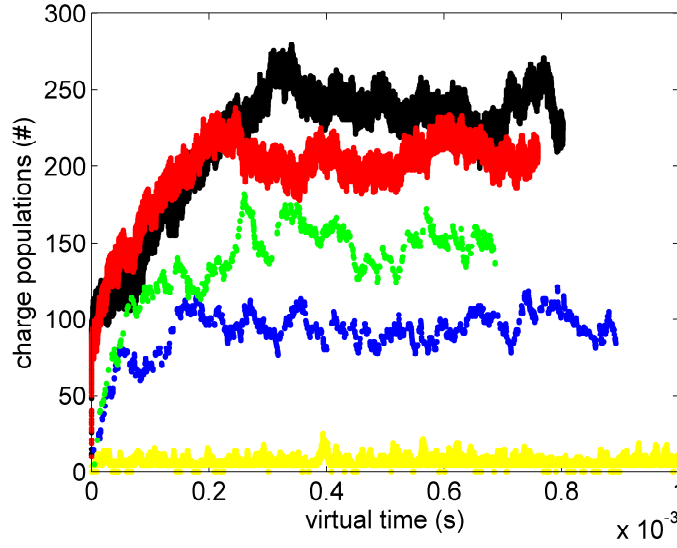


FIGURE 4.22: Charge population as a function of virtual time for five different simulations.

each simulation. However, to reduce computational time only the relevant variables were tracked. In this thesis, we mainly look at exciton recombination/dissociation, charge recombination, internal quantum efficiency and current density. Exciton recombination and dissociation events are simply tracked during the simulation. The same goes for charge recombination and charge extraction events. The polarity of the electrode (cathode or anode) of each charge extraction event was also recorded. The following equations explicitly show how all performance parameters are calculated.

$$\eta_{exdis} = \frac{\# \text{ dissociated excitons}}{\# \text{ generated excitons}} \quad (4.33)$$

where η_{exdis} is the exciton dissociation efficiency.

$$\eta_{exrec} = \frac{\# \text{ recombined excitons}}{\# \text{ generated excitons}} \quad (4.34)$$

where η_{exrec} is the exciton recombination efficiency (= 1-dissociation efficiency).

$$\eta_{crec} = 1 - \frac{\Delta \text{charges extracted at electrodes}}{2 \times \# \text{ dissociated excitons} + \# \text{ injected charges}} \quad (4.35)$$

where η_{crec} is the charge recombination efficiency and Δ charges extracted at electrodes is the difference between charges that are extracted at electrodes of the same polarity and the number of charges extracted at opposite polarity electrode. In other words,

the sign and direction of the charge carriers are taken into account.

$$\text{IQE} = \frac{\Delta \text{charges extracted at electrodes}}{2 \times \# \text{ generated excitons}} \quad (4.36)$$

IQE is determined at $V=0$, which means that injected charges can be ignored as they do not influence the current (dark current at $V=0$ is 0). IQE, η_{exrec} and η_{crec} add up to 100 %.

$$J = \frac{\Delta \text{charges extracted at electrodes} \times q}{2 \times \text{time} \times \text{active area}} \quad (4.37)$$

where q is the charge of an electron and 'time' refers to the time needed to extract the charges. The factor of 2 takes into account that an electron that flows through the external circuit needs to enter the solar cell at the other electrode (i.e. hole extraction) to satisfy overall charge neutrality.

5

Förster resonance energy transfer theory compared to a simple random walk

5.1 Introduction

The work presented in this chapter has been published as Feron et al. in the Journal of Applied Physics [79].

The performance of organic photovoltaics (OPVs) is highly susceptible to morphology variations on the nanoscale and consequently there have been a number of studies modelling the structure-function relationship in these devices [101, 117, 195]. Monte Carlo modeling is a common computational approach for investigating morphological effects on the properties of organic semiconductors at the nanoscale and their impact on device performance [148]. The performance of an OPV device is a function of the

efficiency of both exciton dissociation and charge extraction [101]. The exciton dissociation efficiency depends upon the morphology and the exciton transport properties associated with the materials of interest [156]. Exciton diffusion is usually modelled using Förster resonance energy transfer theory (FRET) [101, 117, 139, 195], although other theories such as Dexter theory have been used depending on the dominate type of exciton (triplet or singlet) [43].

In FRET, the exciton hopping rate decreases as r_{ij}^6 , where r_{ij} is the distance between the two lattice sites, i and j . As such, in order to model exciton transport with FRET, the Förster radius, R_0 , has to be determined for the materials in question. The exciton diffusion length, L , is often the variable used and reported to quantify the ability of excitons to move in an organic material and not R_0 . However, there exists a cubic relationship between L and R_0 and once this relationship is exactly known the two can be easily inter-converted [196]. This cubic relationship becomes visible when seeing how the diffusion constant, D , relates to R_0 . Förster derived the following equation [171]

$$D = \frac{s}{t_0} (Nc)^{4/3} R_0^6 \quad (5.1)$$

where N is the number of chromophores per millimole, c is the chromophore concentration, t_0 the exciton lifetime and s is a constant that relates to the molecular distribution of the molecules. It immediately follows from Equation (5.1) and the relation between D and L that a cubic relation exists between L and R_0 [196]

$$L = \sqrt{6Dt_0} = \sqrt{6s(Nc)^{4/3}R_0^3} \quad (5.2)$$

Athanasopoulos et al. [197] have shown that energetic disorder in the material diminishes L , which means that there is an interplay between L , R_0 and energetic disorder. Once two of these variables are known the third one can be determined. In the context of Monte Carlo modelling of OPV devices it is desirable to eliminate R_0 as a fitting parameter and determine it in an independent measurement. Determining R_0 can be achieved using photoluminescence (PL) measurements, which have previously been used to determine L for a variety of materials [43, 46, 198, 199]. PL is the simplest

method to determine L , because one only needs to consider excitons and charge transport intricacies [148] can be ignored. In addition, the interfaces (substrate-material, material-air) are well defined, allowing good agreement between the model and experiment to be achieved since perfect interfaces are assumed in Monte Carlo models. As mentioned before, interference effects must be considered as well when dealing with thin films. It is noteworthy that even though the measurement technique is simple for many organic materials, it may be more complex for others. There are two prerequisites for a successful PL experiment. First of all, the organic material needs appreciable PL so it may be easily detected with a PL measurement setup. Secondly, since L is usually determined by measuring PL as a function of thickness [46, 198], the growth mechanism of the material must be consistent and provide full coverage for all thicknesses investigated. The PL-thickness relation may be significantly affected in the case of island growth. Most organic films do behave consistently when layer thickness increases and consequently diffusion lengths have been determined for many materials using PL measurements [46]. However, PL results of C_{60} and its derivative PCBM have been found to be rather complex and probably provides the worst case scenario in terms of facile interpretation of its PL measurements. Not only does the C_{60} growth pattern change with thickness, but the growth mechanism is also highly influenced by choice of substrate and deposition temperature [200–202]. On top of that, the PL signal of C_{60} degrades when exposed to light and oxygen [203, 204]. Since its PL degrades following a double exponential [203], the original PL signal may be determined by tracking the exposure time to air and light, monitoring the degradation rate and fitting a double exponential to back-cast the PL signal to its maximum. To make things more difficult, C_{60} and PCBM are weak emitters [205] and either thick layers or a sensitive PL setup is required. All these factors, make the determination of L for excitons in C_{60} much more challenging than most other organic semiconductors [46, 170].

The main drawback of using a DMC model to model an organic solar cell is the time needed to conduct the calculations. A gain in terms of computational efficiency is therefore most welcome. In terms of modelling exciton transport, FRET is widely used. In this model, all sites within the R_0 should be taken into account when calculating

exciton hopping rates. Usually all hopping rates up to a radius of 3 lattice constants are calculated [101]. The same is done in my DMC model, which means for every exciton hop 122 sites are considered. Calculating the f -function (contains an exponential) for 122 sites for each exciton hop can be relatively time consuming, especially for large systems (thick active layers) and large exciton diffusion lengths (e.g. 6T). If DMC models are to be used in OPV devices, a fast method of determining fitting parameters such as L is crucial. Hence, in this chapter the possibility of using a simple random walk (RW) in 3 dimensions instead of FRET, is considered. Since only 6 sites are considered in a RW and no exponentials have to be calculated, computational efficiency for exciton hopping is 2 orders of magnitude larger compared to FRET. Furthermore, a simpler model is such as RW is more attractive, because it is easier to implement and interpret even in modelling approaches other than dynamic Monte Carlo. Initially, we show that a computationally fast alternative can be used to fit PL measurements and results in exciton diffusion lengths that are indistinguishable (considering the noise inherent in the measurements) from those obtained using the FRET methodology. In addition to PL fitting, we also explore the option of using RW in Monte Carlo models that describe OPV devices. In contrast to FRET, a RW does not consider energy relaxation during the hopping process, energetic disorder or long-range hopping. The consequence of using the simpler model are analysed and quantified. Finally, we take advantage of the gain in computational efficiency from using RW to investigate the impact that the diffusion length has on the exciton dissociation efficiency, which could not be done within a reasonable amount of time using FRET.

5.2 Simulation Methodology

In the simulations presented, the photoluminescent material is modelled as a cubic lattice of $100 \times 100 \times d$ sites sitting on a quartz substrate, where d is the thickness of the photoluminescent film (see Figure 5.1). The voxel size is set at $1 \times 1 \times 1$ nm. Excitons are then created within this model proportionate to the optical field in the

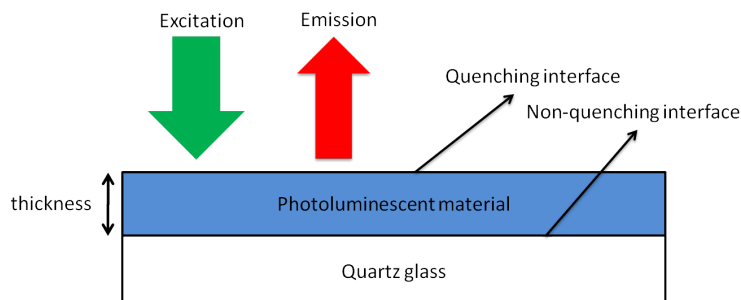


FIGURE 5.1: Schematic of a PL measurement.

layer. Two methods were used to simulate exciton transport in this model system. The first one uses FRET, where the hopping rate given by (4.20). All hopping rates within a 3 nm radius (i.e. 122 sites) are considered and the site with the highest hopping probability is chosen to be the next destination of the exciton. The second method uses a simple random walk in 3 dimensions. There the hopping rate is given by (4.23). The interface of the photoluminescent layer with the quartz substrate is treated as an inert interface [198] while the air interface is treated as a quenching interface, since molecular oxygen is known to be an efficient collisional quencher [206]. A quenching probability is assigned when an exciton reaches this interface. If an exciton is successfully quenched, it is deleted from the system. If an exciton is not quenched within its lifetime, it will recombine and emit a photon. BHJ morphologies with a feature size of 14.2 nm were used to explore the applicability of RW in OPV models.

As opposed to the PL experiment, OPV devices have two active components and excitons are dissociated with a set dissociation probability at the interface between the two moieties, giving rise to a charge pair. To investigate the effect of using RW instead of FRET on subsequent processes in an OPV device, charge transport was also simulated as described in Section 4.7. The electric field was set to 10^7 V/m, which approximately corresponds to the field in an OPV device under short-circuit conditions. ϵ_r was chosen as 4, charge hopping rate constant 10^9 s⁻¹, recombination rate 10^7 s⁻¹. Charge pairs are considered fully separated when the distance between the two respective charges is larger than the thermal capture radius. The lattice size used for the charge transport simulations was $50 \times 50 \times 50$ nm, but periodic boundary

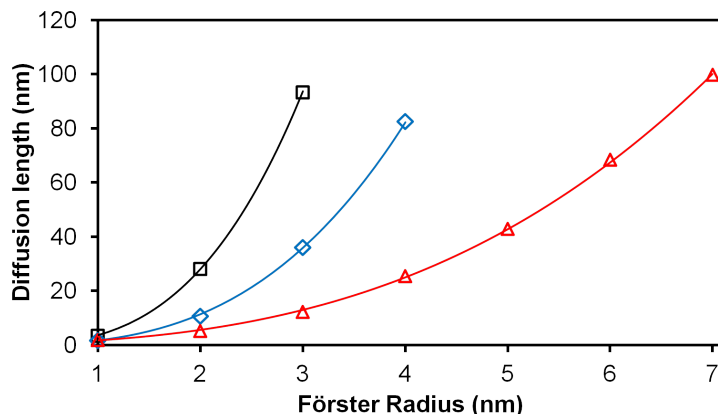


FIGURE 5.2: Cubic relationship between L and R_0 for $\sigma = 0.09$ eV (black squares), 0.05 eV (blue diamonds) and 0 eV (red triangles). The solid lines are cubic fits used to interpolate between points.

conditions were used in each direction resulting in an effectively infinite volume.

5.3 Results and Discussion

5.3.1 Validation of the implementation of FRET

A validation of the Monte-Carlo simulation is provided by Figure 5.2, which shows the variation in calculated exciton diffusion length as a function of Förster radius for three values of energetic disorder, σ , corresponding to 0.09 eV, 0.05 eV and a perfect energy landscape (no energetic disorder). As energetic disorder increases, the exciton diffusion length decreases and, importantly, in all three cases the expected cubic relationship is observed between the Förster radius and diffusion length [196] as per equation 5.2. The prefactor of the cubic relationship depends on energetic disorder. Small molecules generally exhibit larger L than polymers [46, 207, 208], which is a result of small energetic disorder [197].

5.3.2 Impact of fabrication process on energetic disorder

When comparing L of small molecules to those of polymers, it is important to consider the deposition technique used to deposit these films. Small molecules are generally

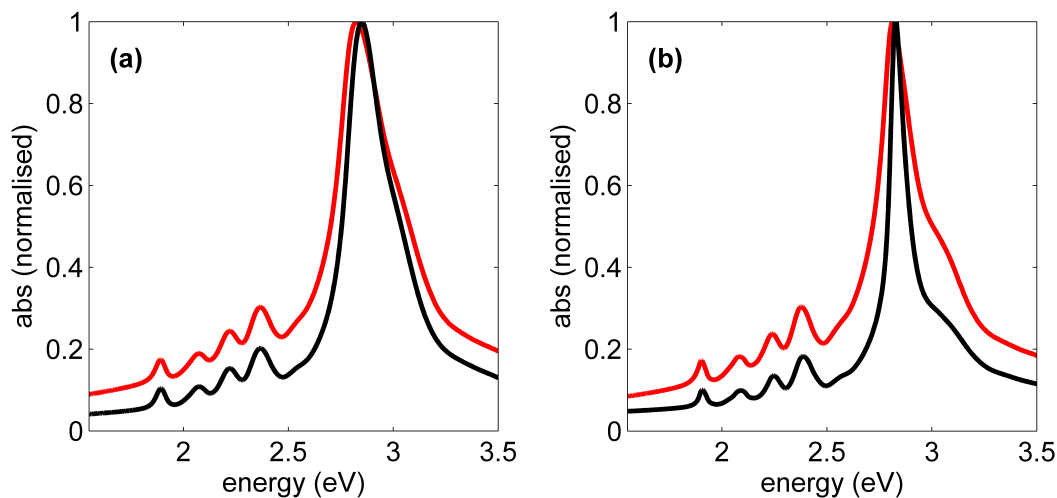


FIGURE 5.3: Normalised absorption spectra of TTP films prepared by evaporative deposition (black) and spin-coating (red). (a) shows the spectra before annealing and (b) after annealing.

evaporated and yield high quality films with potentially increased structural order and thus decreased energetic disorder. Polymers on the other hand are too large to be evaporatively deposited; the polymer will decompose before it sublimates or evaporates. In order to show the effect that deposition techniques may have on energetic disorder, TTP was both evaporated and spin-cast on quartz substrates. Figure 5.3 shows the absorption spectra of these films before and after a thermal anneal treatment of 140 °C for 4 minutes. Evaporated absorption curves are slightly red shifted compared to the spin-cast ones. Both films had approximately the same thickness (40 nm) and AFM indicates that the evaporated films are smoother. Annealing causes a slight red-shift in both the spun and evaporated films. Energetic disorder is estimated by fitting a Gaussian to the main absorption peak at roughly 2.8 eV. The standard deviations are listed in table 5.1. Evaporated TTP has sharper peaks both before and after annealing. The difference is small for the as-deposited films, but after annealing there is a significant difference as the energetic disorder in the evaporated film is less than half that of the spin-cast film. This result indicates that the observation of larger L in small molecules is at least partly related to the deposition technique. So, while small molecules are likely to form more crystalline films than polymers, the effect of

the deposition technique should not be overlooked when comparing these two types of organic molecules.

TABLE 5.1: σ of TTP

| Deposition technique | Thermal anneal treatment? | σ (eV) |
|----------------------|---------------------------|---------------|
| Thermal evaporation | no | 0.057 |
| Spin coating | no | 0.060 |
| Thermal evaporation | yes | 0.020 |
| Spin coating | yes | 0.042 |

5.3.3 FRET compared with a random walk: exciton diffusion

In order to compare the two models used in the Monte-Carlo simulations we define the effective distance travelled by an exciton as the distance between the point of exciton creation and exciton recombination. Figure 5.4 shows the distribution of these effective distances obtained using the FRET and RW models and demonstrates that both models give almost identical distributions. In FRET the hopping probability decreases rapidly with distance and thus hopping to nearest neighbours is dominant. Therefore, if hops to sites further away than one lattice constant occur rarely, implementing FRET simply becomes a computationally more time consuming way of performing a random walk in 3 dimensions. For σ values typically found for organic materials (10 – 90 meV) [70, 117, 139, 209] the most frequent hop will be a nearest neighbour hop. Only for σ values significantly larger than $k_B T$ will the energy landscape dominate the diffusion behaviour in such a way that the modelled exciton transport will no longer behave like a RW. In this case, the hopping behaviour will closely follow low energy pathways in the energy landscape.

Other approaches used to describe triplet excitons, such as Dexter theory [43, 210] and Miller-Abrahams tunnelling [211], also involve the possibility of hops to non-adjacent lattice sites. However, in both of these cases, the probability of hops to sites that are more than one lattice site away decreases exponentially with distance.

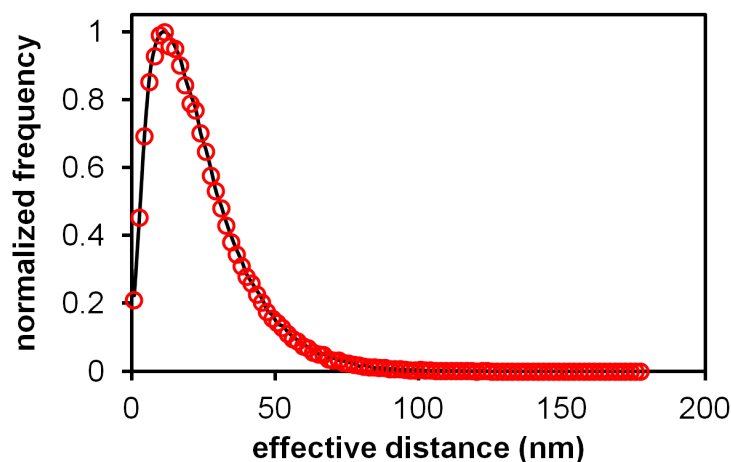


FIGURE 5.4: The distance between the point of exciton creation and exciton recombination is the effective distance travelled. The distribution of the effective distances travelled by excitons for FRET and RW are indicated with red open circles and a black solid line respectively. The FRET simulation was executed with $R_0 = 2.75$ nm and $\sigma = 0.05$ eV. These parameters give a corresponding value of $L = 28$ nm, which was used for the RW simulation. The lifetimes were the same in both simulations (10^{-6} s).

Therefore, it seems reasonable to suggest that the RW model will be equivalent to these approaches as well.

5.3.4 FRET compared with a random walk: photoluminescence

Given that both the FRET and RW models display the same effective distance distribution, we might expect that calculating the PL as a function of layer thickness for these two models should also produce the same result. However, two possible sources of discrepancy between the two models are the effect of exciton generation rate and interface quenching probability on the calculated PL.

It is possible for the exciton diffusion behaviour to change if the exciton density is extremely large, because many sites will be occupied and thus the number of available sites for each hop will be diminished. In order to test the sensitivity of the simulation to this parameter, the exciton generation rate was varied up to 10 excitons/s/nm³ for the RW model, which is well beyond the light intensity used in obtaining the experimental data in Figure 5.6. However, no change in the exciton diffusion behaviour with exciton

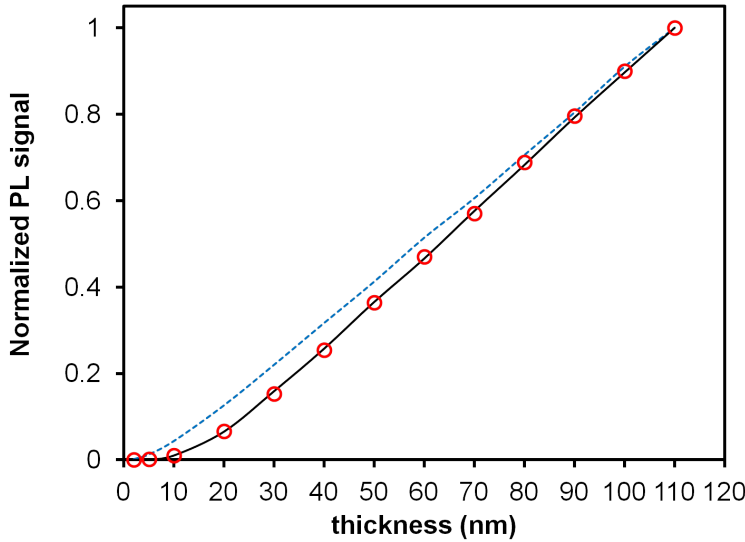


FIGURE 5.5: PL as a function of thickness for quenching probabilities of 1% (blue dashed line), 50% (red open circles) and 100% (black solid line). L was set to 40 nm for all three simulations.

generation rate was observed. As such, the PL signal is independent of the exciton generation rate (< 10 excitons/s/nm³) and thus we can normalise the PL signal relative to that of the thickest modelled system.

Figure 5.5 shows the effect of the quenching probability on the normalised PL signal as a function of thickness for the RW model. It is apparent from Figure 5.5 that there is hardly any statistical difference between the normalised PL results observed for a quenching probability of 50% and that for 100%. Indeed, reducing the quenching probability to only 1% still results in only a small change in normalised PL signal. The reason for this observation is that once an exciton is in the vicinity of the quenching interface it is likely that it hits the interface several times, thus significantly increasing the chances of quenching. Moreover, given that molecular oxygen is known to be a very efficient quencher [206] and that the simulation has a low sensitivity to quenching probability it seems reasonable to model the quenching probability at the air interface as 100 %. To further demonstrate the validity of the RW model, we have compared calculated PL measurements as a function of thickness to experimental data from the literature. Figure 5.6 shows a plot of normalised PL as a function of thickness for

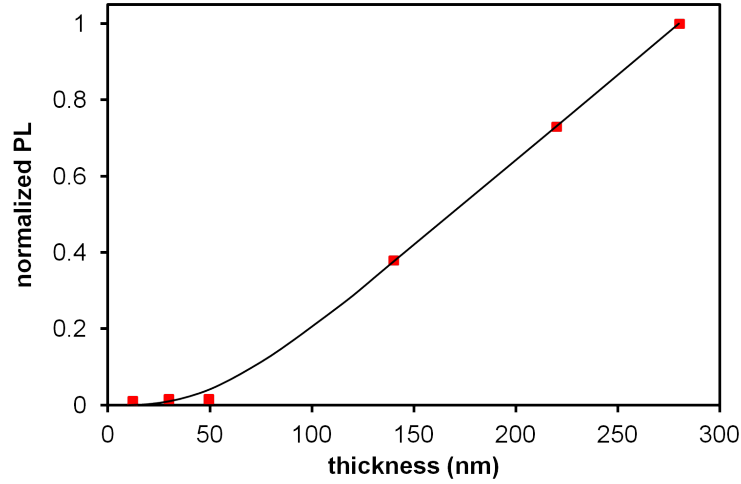


FIGURE 5.6: Normalised PL signal as a function of 6T layer thickness. The solid line is obtained from the simulation using the RW model for a fitted diffusion length of 140 nm. The experimental results (red filled squares) are obtained from Mani et al. [198]. Two vertical dashed lines have been added to distinguish between the 3 characteristic regimes associated with the measurement.

6T for both the simulation and experimental results obtained from Mani et al. [198]. In the absence of any information about the internal optical field extant during the experiment, a uniform optical field was assumed. However, regardless of the validity of this simplification, it provides a good case to compare FRET to RW in terms of L extracted from fitting and computational efficiency. Figure 5.6 can be separated into three sections. In section 1, quenching is the dominant process, because most excitons are in the vicinity of the air interface and very little PL is observed. The linear regime in section 3 arises from the fact that increasing the thickness in this regime only results in greater recombination whilst the number of excitons that are quenched does not change, while section 2 is a transitional phase between section 1 and 3. It is clear that the modelled fit is in close agreement with the experimental data across the different sections, thus providing a further confirmation of the validity of the RW approach.

The key advantage of the RW model from a computational point of view is that it is computationally 2-3 orders of magnitude faster than other approaches such as FRET. As such, the RW approach is particularly suited to modelling large lattices, i.e. thick films. The significant saving in computational time that can be gained by using RW

TABLE 5.2: Comparison of computational time cost for the FRET and RW models.

| Model | Calculated Exciton Diffusion Length (nm) | Computational time (s) |
|-------|--|------------------------|
| FRET | 140 | 2.0×10^6 |
| RW | 140 | 6.5×10^3 |

is illustrated in table 5.2, which compares the time taken to simulate the experimental data shown in Figure 5.6 for both the RW and FRET models. Both models give the same calculated three dimensional exciton diffusion length of 140 nm, which is equivalent with a one dimensional exciton diffusion length of 81 nm and corresponds well with a previously reported value in the literature of 100 ± 20 nm [47]. However, the FRET model takes more than 23 days of computational time whereas the RW model is complete in under 2 hours, more than 300 times faster. As such, RW is the preferred model for determining L from PL measurements.

5.3.5 FRET compared with a random walk: energy relaxation and long-range hopping

Now we explore the possibility of implementing RW in Monte Carlo models that describe OPV devices. There are two key differences between the RW and FRET methodologies. First, RW only considers nearest neighbours whereas in systems with small material domain sizes and low quenching probability it is necessary to consider hops to sites that are further away than one lattice constant. Figure 5.7 shows exciton dissociation efficiency as a function of L for a BHJ morphology with a feature size of 14.2 nm. While it is clear that lowering the dissociation probability will decrease the exciton dissociation efficiency, the drop-off is different for RW compared to FRET. For less efficient hetero-interfaces, RW will only match FRET if the diffusion length is sufficiently large compared to the feature size of the morphology. As mentioned before, large diffusion lengths are observed for small molecules [46, 197]. In terms of the exciton dissociation efficiency, there is no difference between FRET and RW if the

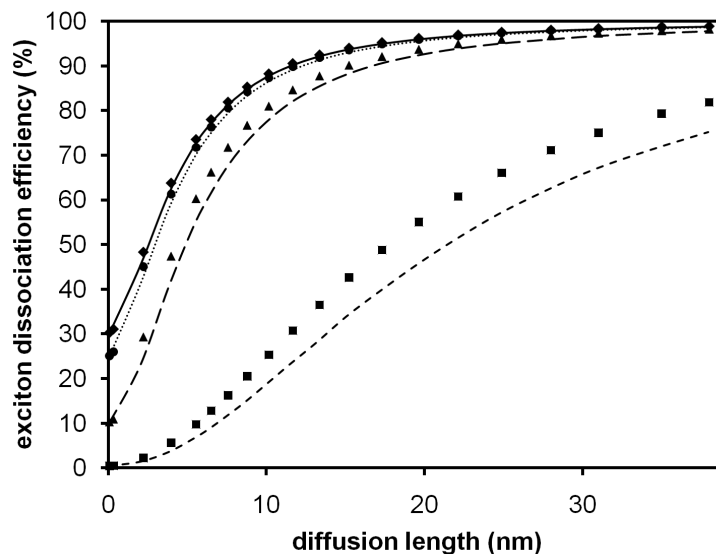


FIGURE 5.7: Exciton dissociation efficiency as a function of L for FRET (lines) and RW (markers). Graphs for the following dissociation probabilities are shown: 100% (diamonds and solid line), 75% (circles and dotted line), 25% (triangles and long dashed line) and 1% (squares and dashed line).

dissociation probability is high ($> 75\%$).

The second limitation of RW is that it does not consider energy relaxation of the exciton as it hops from site to site. Figure 5.8 shows that moderate energy relaxation occurs for systems with high exciton dissociation probabilities and substantial energy relaxation occurs for systems with low exciton dissociation probabilities. In Monte Carlo models exciton dissociation occurs at hetero-interfaces with a set dissociation probability, the energy of the exciton is not taken into account in this process. While exciton relaxation has little to no impact on the exciton diffusion process itself or even the exciton dissociation process, it will cause excitons to preferentially dissociate at interface sites with low energies. In other words, newly dissociated charges will have lower energies when using FRET instead of RW. Groves et al. [212] have shown recently that trapped charges (charges with a significantly lower energy compared to its surroundings) will have an increased probability of geminate recombination. The effect of trapping is not straight forward, since energy relaxation will cause more electrons to be trapped, but the opposite is true for holes. Groves et al. demonstrated that,

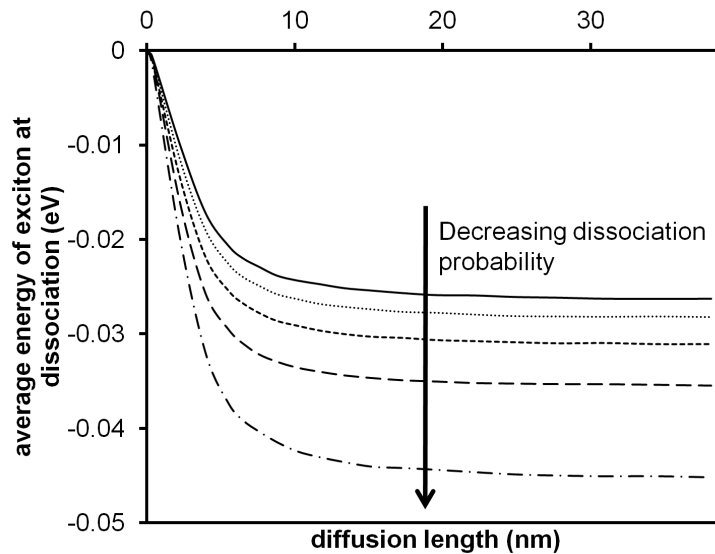


FIGURE 5.8: Average energy of an exciton at dissociation as a function of L for a BHJ morphology with a feature size of 14.2 nm when using FRET. σ was chosen to be 0.05 eV. Graphs shown are for the following dissociation probabilities: 100% (solid line), 75% (dotted line), 50% (short dashed line), 25% (long dashed line) and 1% (dash-dot line).

for a bilayer device, a decrease in geminate pair separation efficiency is observed when both electron and hole are trapped with energy of more than 0.05 eV or when either charge carrier is trapped with energy of more than 0.15 eV [212]. In order to determine the significance of this charge trapping effect, the percentage of newly created charges that satisfy these conditions has been determined for both FRET and RW (Figure 5.9(a)). In the case of RW, there is no dependency of geminate recombination on L or the exciton dissociation probability (the graphs exactly overlay) since charges are randomly created at interfaces. Here, only the roughness of the energy landscape will influence geminate recombination. Thus, for very small L values, FRET will give the same result as RW, because excitons will hardly hop between sites and thus energy relaxation cannot occur. Exciton dissociation is then mainly determined by the location of exciton creation, which is a random process for BHJ morphologies. As L increases, the probability of geminate recombination will increase until a maximum is reached when L equals roughly the feature size (10-15 nm). For $\sigma = 0.05$ eV, there is very little difference between RW and FRET especially for high dissociation probabilities.

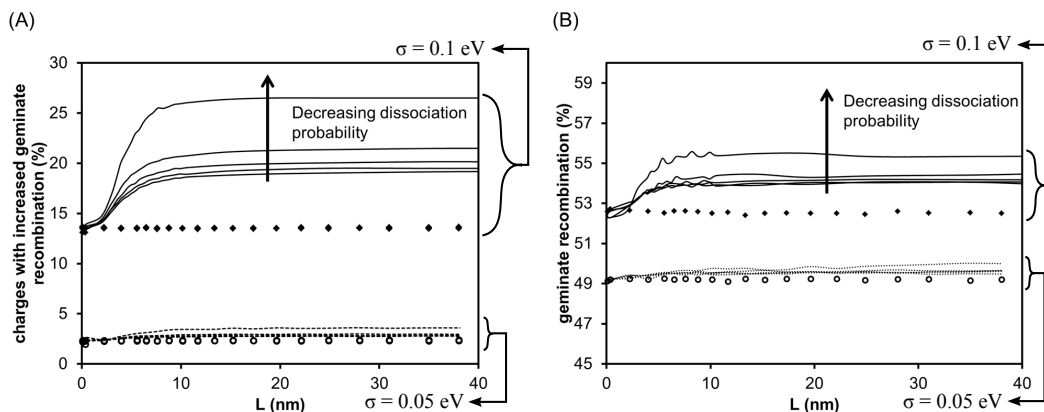


FIGURE 5.9: Percentage of charges meeting the conditions of reduced geminate separation efficiency (i.e. when both hole and electron are trapped with energy > 0.05 eV or either charge is trapped with energy > 0.15 eV,) [212] as a function of L for RW (circles and diamonds) and FRET (solid and dashed lines). (b): Geminate recombination as a function of L for RW (circles and diamonds) and FRET (solid and dashed lines). In both (a) and (b) the dissociation probability was varied (100%, 75%, 50%, 25% and 1%) for both RW and FRET. In both (a) and (b) the solid lines and diamonds correspond to $\sigma = 0.1$ eV whereas the dashed lines and circles correspond to $\sigma = 0.05$ eV. The bottom plot of each series corresponds to a dissociation probability of 100% and the top plot corresponds to 1%. There are 20 plots in each graph, however, the 10 plots for RW condenses to 2 plots, because the dissociation probability and diffusion length do not influence the geminate separation efficiency.

For material systems with high exciton dissociation probabilities (> 50 %), FRET predicts that 2.8 % of dissociated charges will have an increased geminate recombination probability due to trapping effects compared to 2.35 % for RW. This is an insignificant difference and RW is readily applicable in this situation. However, larger differences are noticeable for materials with large energetic disorder. For $\sigma = 0.1$ eV, increased geminate recombination is found for 19 – 20 % of all charges when using FRET compared to 13.6 % for RW. It is noteworthy that geminate recombination is mainly caused by both charges being trapped as opposed to single trapped charges. For $\sigma = 0.05$ eV, only 0.1 % of all charges have a trap energy of 0.15 eV or higher. Even for large energetic disorder (e.g. 0.1 eV) this value is only 4.4% since energy relaxation decreases the occurrence of trapped holes, which partially compensates for the increased number of trapped electrons. Given that charges that meet the conditions of increased geminate recombination do not necessarily recombine, the data in Figure 5.9(a) therefore provides an overestimation of the total recombination. To determine the exact effect

of exciton energy relaxation on geminate recombination, charge transport has been modelled; see Figure 5.9(b). To isolate the effect of geminate recombination on bulk geminate recombination periodic boundaries were invoked in all 6 directions, which effectively means that image charge effects are not included. This approach is similar to Groves et al. [212] as they modeled a bilayer where the hetero-interface is too far away from the electrodes for image charges to have a significant influence. Image charge effects are expected to increase geminate separation and thus the choice of not looking at edge effects near the electrode provides an upper limit. The graphs in Figure 5.9(a) and 5.9(b) are similar in shape, which indicates that our simulations give similar results to Groves et al. In both cases, geminate recombination increases as the dissociation probability decreases due to a decrease in the average exciton energy at dissociation (Figure 5.8). The difference between RW and FRET is smaller in Figure 5.9(b) compared to Figure 5.9(a). This is consistent with the fact that the data in Figure 5.9(a) is not geminate recombination, but the percentage of charges with an increased probability of geminate recombination. The maximum underestimation of geminate recombination when using RW is 3 % and only 1.5 % if the dissociation probability is 100 %. Therefore, the overall effect of using RW instead of FRET on the simulated current is minimal. If we consider the worst case that we investigated (dissociation probability of 1 % and L is such that the difference in exciton dissociation efficiency (Figure 5.7) is maximised (10 %)), the simulated current will be overestimated by 13 %. However, these extreme values of σ and dissociation probability are actually outside the range of what is normally accepted. The dissociation probability is generally taken as 100 % and σ generally ranges from 0.01 to 0.09 eV [70, 101, 117, 139, 213]. For values within the usual range, the overestimation will not be greater than 2 % and negligible in most cases. This deviation is an acceptable error considering the typical variability in the performance of OPV devices. It has to be noted that the gain in computational efficiency is less significant in Monte Carlo models that simulate OPV devices, because charge transport is the bottleneck in these simulations.

5.3.6 Exciton diffusion and sensitivity to domain size variations

It is widely recognised that domain size is a key factor in determining the performance of OPV devices [214]. Monte-Carlo simulation of exciton diffusion is one of the few techniques available for determining *a priori* the optimum domain size. Figure 5.10(a) shows the distribution of distances that excitons travel, i.e. the distance between the location of exciton generation and the location of recombination, calculated for a range of exciton diffusion lengths. This distribution gives an indication of the optimal phase separation for a given diffusion length in the active layer of OPV devices. Figure 5.10(b) shows the minimum interface distance required to collect a certain fraction of excitons as a function of diffusion length. Here, the interface distance is defined as the absolute distance that an individual exciton has to travel to reach a hetero-interface and is analogous to the concept of domain size in a bulk heterojunction morphology. Figure 5.10(b) suggests that only approximately 30% of all excitons are able to reach an interface that is one diffusion length away. This value is likely to be an upper limit since, for a given structure, not all excitons will travel directly to the closest interface. For example, in a columnar structure, two out of the six hopping directions will not lead to an interface.

The number of excitons that reach an interface drops off rapidly as the interface distance increases. The derivative of Figure 5.10(b) has been calculated to determine at what distance most excitons are lost as the interface distance increases and is shown in Figure 5.10(c). The minimum of the derivative is located at the same distance as the peak of the corresponding distribution of effective distances (Figure 5.10(a)). It is therefore desirable for optimal exciton dissociation to design the morphology so that the average interface distance is smaller than the peak of the effective distance distribution. Figure 5.10(c) also shows that the minimum is deeper for shorter diffusion lengths and, as such, materials with shorter diffusion lengths are more susceptible to deviations from the optimum domain size. Conversely, the exciton dissociation efficiency of organic solar cells based on materials with longer diffusion lengths (i.e. less energetic

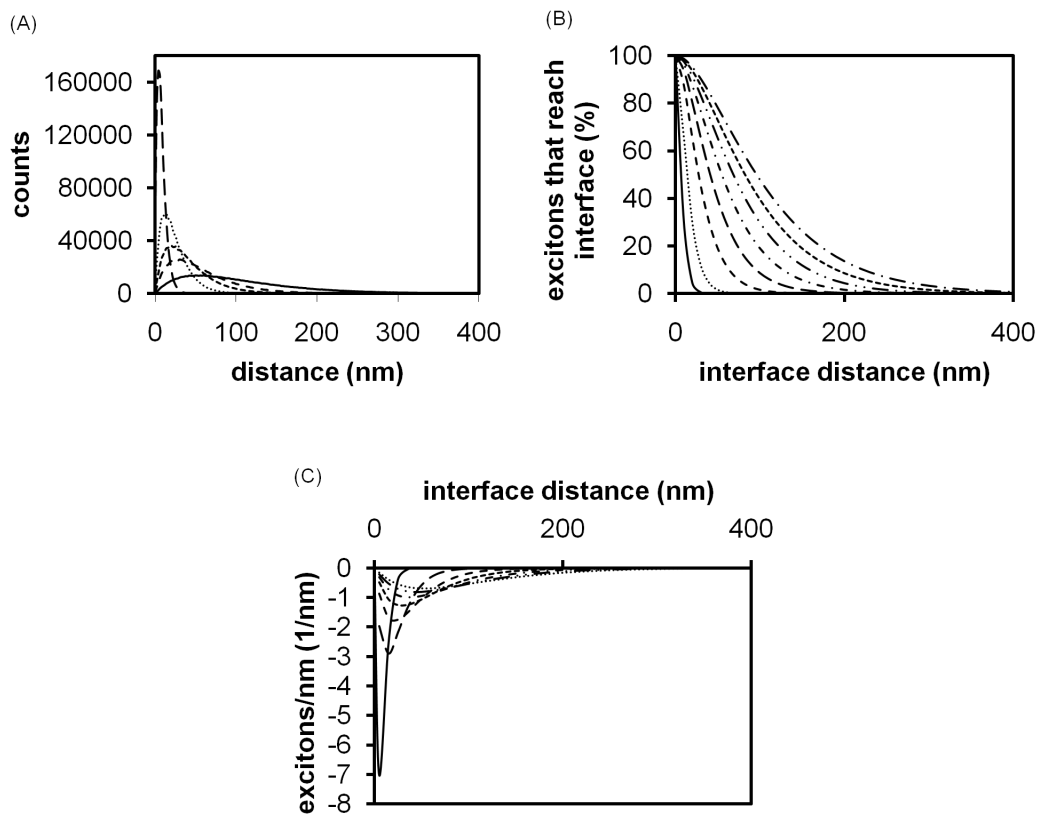


FIGURE 5.10: (a): plots of effective distance travelled for a range of diffusion lengths. Traces are shown for $L = 10$ nm, 30 nm, 50 nm, 70 nm and 130 nm. Smaller L exhibit narrower and higher peaks. (b): The percentage of excitons collected at an interface as a function of interface distance. Traces are shown for $L = 10$ nm, 20 nm, 40 nm, 60 nm, 80 nm, 100 nm, 120 nm and 140 nm. A shorter L exhibits a quicker drop off. Graph (c) shows the derivative of (b) and this gives the same distribution as (a) with a sign change. Traces are shown for $L = 10$ nm, 30 nm, 50 nm, 70 nm, 90 nm, 110 nm and 130 nm. A narrower and deeper minimum correspond to a smaller L .

disorder) will be more forgiving to variations in domain size. This work highlights the effectiveness of the RW approach in Monte Carlo simulations of exciton diffusion in OPV devices. The simulations presented in Figure 5.10 required approximately one day of computational time using the RW approach. By contrast, the same simulations would have required almost half a year of computational time using the FRET model.

5.4 Conclusion

We have shown that a simple RW model gives the same hopping behaviour as FRET when modelling single component systems. Thus the process of determining exciton diffusion lengths by fitting against PL measurements can be made less computationally expensive by using the RW model, since RW is typically 2 – 3 orders of magnitude faster than FRET. This saving is especially significant for large systems i.e. thick layers and materials with large exciton diffusion lengths such as 6T. The quenching efficiency has been shown to have little impact on the PL signal when efficient quenchers are used. Using the RW model, the exciton diffusion length of 6T has been calculated to be 140 nm, which is in good agreement with literature. Once L is known, R_0 can be determined using the cubic relationship between L and R_0 . In this manner, RW can be used to determine R_0 , which is an essential parameter when using FRET. Energetic disorder affects this cubic relation and has been shown to depend on the deposition technique, i.e. evaporative deposition generally yields films with less energetic disorder than spin-cast films. Despite the fact that RW does not account for non-nearest neighbour hopping or energy relaxation, the resulting overestimation of the simulated current does not exceed 2 % for common OPV parameters. In addition, simulation results highlight that materials with large exciton diffusion lengths are less susceptible to structural variations that arise in fabrication processes.

6

Experimental validation of the dynamic Monte Carlo model: thickness dependence of organic photovoltaic performance and the impact of charge blocking layers

6.1 Introduction

The work in this chapter has been published as Feron et al. in Applied Physics Letters [215].

The DMC approach allows for a full treatment of the relevant processes in an organic solar cell (including light absorption and subsequent transport, dissociation and

recombination of excitons and free charges) while accounting for the blend morphology of the photoactive layer. In principle, the DMC approach allows for the development of a virtual solar cell whereby, for a known morphology, OPV performance could be predicted by modelling these internal processes. Once it has been established that such an extensive model correctly predicts device performance, it can be used to test new materials and optimise systems. More importantly, initial testing and optimisation can be conducted without having to actually fabricate devices and will consequently lower the costs of device fabrication for the purpose of research. Although DMC simulations have been shown to describe experimental observations qualitatively [70, 117, 178], a direct quantitative comparison of modelled and experimentally measured OPV performance indicators such as total IQE and J_{sc} for a specific OPV system is still lacking. Here, we report a quantitative description of BHJ OPV devices with the conventional structure ITO/PEDOT:PSS/(P3HT:PCBM)/Aluminium using a dynamic Monte Carlo approach.

6.2 Experimental and modelling aspects

Conventional values for the energy levels and other relevant parameters were used (see Table 6.1). Koster et al. [116] had to use a charge carrier recombination rate, k_{rec} , of $1 \times 10^4 \text{ s}^{-1}$ to reproduce experimental results for P3HT:PCBM devices when using their drift-diffusion type model. We use the same value in our DMC model and also find an excellent match with experimental results. It should be noted that photo-physical studies show a decay rate of the CT state of roughly $10^8 - 10^9 \text{ s}^{-1}$ [216, 217]. This discrepancy could be explained by considering the difference between the meaning of the experimentally observed decay rate and k_{rec} in the DMC model. k_{rec} refers to the recombination rate when an electron and hole are immediately adjacent to each other without interference from other charge carriers and does not depend on the number of electron-hole encounters, which is influenced by mobility, morphology and film thickness. The measured decay rate, on the other hand, is influenced by mobility, morphology, film thickness and other factors [217]. Furthermore, these photo-physical studies

often cannot distinguish between geminate and bimolecular recombination [218]. Even though the term 'recombination rate' is used in experimental studies and DMC models, they refer to different meanings/situations. Hence, one cannot expect k_{rec} to be the same as the recombination rate as measured in photo-physical studies. Morphologies

TABLE 6.1: Simulation parameters used to describe ITO/PEDOT:PSS/P3HT:PCBM/Al devices.

| Property | Value | Reference |
|-------------------------------------|--|---|
| Temperature | 300 K | |
| Relative dielectric constant | 3.1 | [147] |
| σ P3HT and PCBM | 0.05 | as determined from absorption spectra |
| Förster radius PCBM | 3.65 nm (equivalent to 1D L of 40 nm) | [46] (PCBM L is assumed to be the same as C ₆₀) |
| Förster radius P3HT | 2.15 nm (equivalent to 1D L of 8.5 nm) | [153] |
| Exciton lifetime PCBM | 11 μ s | [155] |
| Exciton lifetime P3HT | 400 ps | [153] |
| Charge hopping rate constant PCBM | $3 \times 10^{12} \text{ s}^{-1}$ | [70, 195] |
| Charge hopping rate constant P3HT | $3 \times 10^{12} \text{ s}^{-1}$ | [70, 195] |
| Charge carrier recombination rate | $1 \times 10^4 \text{ s}^{-1}$ | |
| Reorganisation energy (λ) | 0.5 eV | [181] Section 4.7 |
| Lattice constant | 1 nm | Chapter 4 |
| PEDOT:PSS energy level | -5.1 eV | [219] |
| Aluminium work function | -4.3 eV | [219] |
| P3HT HOMO | -5.3 eV | [219] |
| PCBM LUMO | -4.3 eV | [219] |

with a feature size of 14.2 nm were generated. The feature size used here is comparable to domain sizes used in other Monte Carlo models [70, 101, 117] and is in accordance

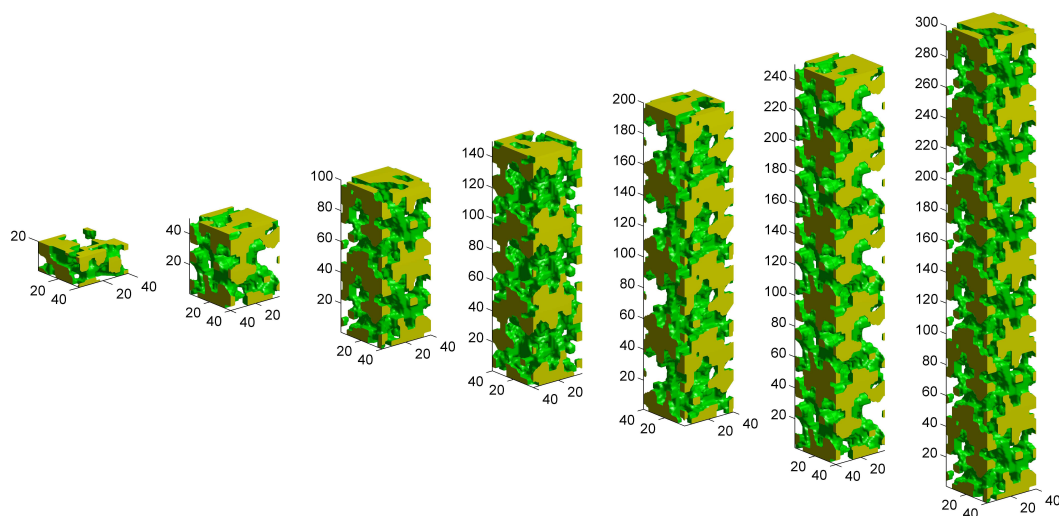


FIGURE 6.1: Morphologies with a feature size of about 14.2 nm and thickness of (from left to right) 20 nm, 50 nm, 100 nm, 150 nm, 200 nm, 250 nm and 300 nm.

with an estimation of P3HT:PCBM domain sizes based on atomic force microscopy phase imaging [220]. At this feature size exciton dissociation is efficient ($\sim 95\%$), which correlates with the almost complete quenching of photoluminescence observed in these devices [94, 97, 221]. The BHJ morphologies did not contain isolated islands and formed an interpenetrating network from one electrode to the other. A depiction of the morphologies used can be seen in Figure 6.1. Approximately 50 % of the anode was covered by P3HT and 50 % of the cathode was covered by PCBM unless blocking layers were simulated, in which case the perfect blocking layer ensures 100 % electrode coverage by the desired material (i.e. a perfect capping layer).

The internal optical field in our devices has been determined using transfer matrix techniques as described previously, [30, 123] using optical models similar to those used by others [124, 125]. The coding of the optical model and determination of optical constants of materials were conducted by Nicolas Nicolaidis. Figure 6.2 shows the imaginary and real dielectric constant of P3HT:PCBM. The entire optical system of a real device was modelled. PEDOT:PSS films were 40 nm thick, the aluminium cathode was 100 nm, the glass substrate 1 mm, and the ITO layer was 140 nm thick. The P3HT:PCBM layer thickness was varied. Figure 6.3 shows a contour plot of light

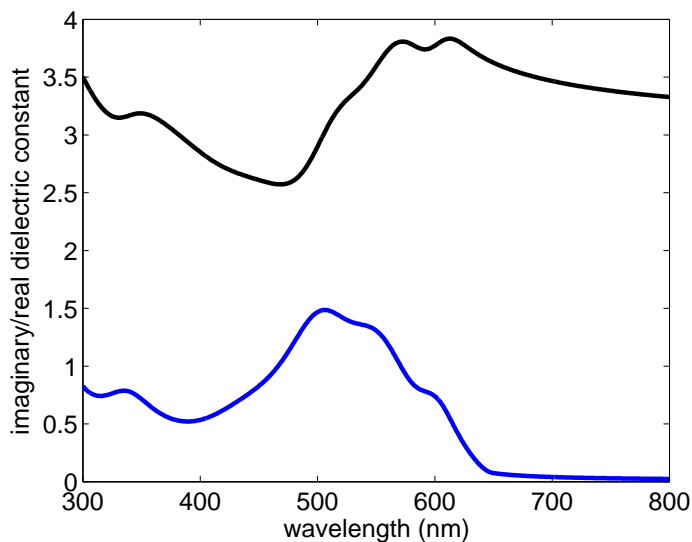


FIGURE 6.2: The imaginary (blue) and real (black) dielectric constant of P3HT:PCBM (1:1 weight ratio) as a function of wavelength.

absorbed in the photoactive layer as a function of depth (z) and wavelength for a P3HT:PCBM film thickness of 200 nm. The exciton generation rate as a function of depth (and wavelength) in the photoactive layer was determined by overlaying the absorption spectrum with the AM1.5 spectrum followed by an integration over the entire spectrum while accounting for photon energy at different wavelengths. Figure 6.4 shows the exciton generation rate for various photoactive layer thicknesses. In this figure, light enters from the right (ITO side) and a 100 nm aluminium cathode is located at $z=0$ nm. It is clear that the number of absorbed photons increases rapidly as the thickness of the photoactive layer increases and that for thin layers most excitons are created near the anode. For thicker layers (>100 nm) a second absorption peak is seen (as also seen in Figure 6.3), which is a result of cathode reflection and interference effects. Even though thickness variations in the PEDOT:PSS and Al layer will influence the optical field in the photoactive layer, the optical field is most sensitive to variations in the active layer thickness itself. Table 6.2 shows the maximum change in the exciton generation rate profile (Figure 6.4) when changing the PEDOT:PSS thickness from 30 nm to 50 nm, while keeping all other layers the same. The same

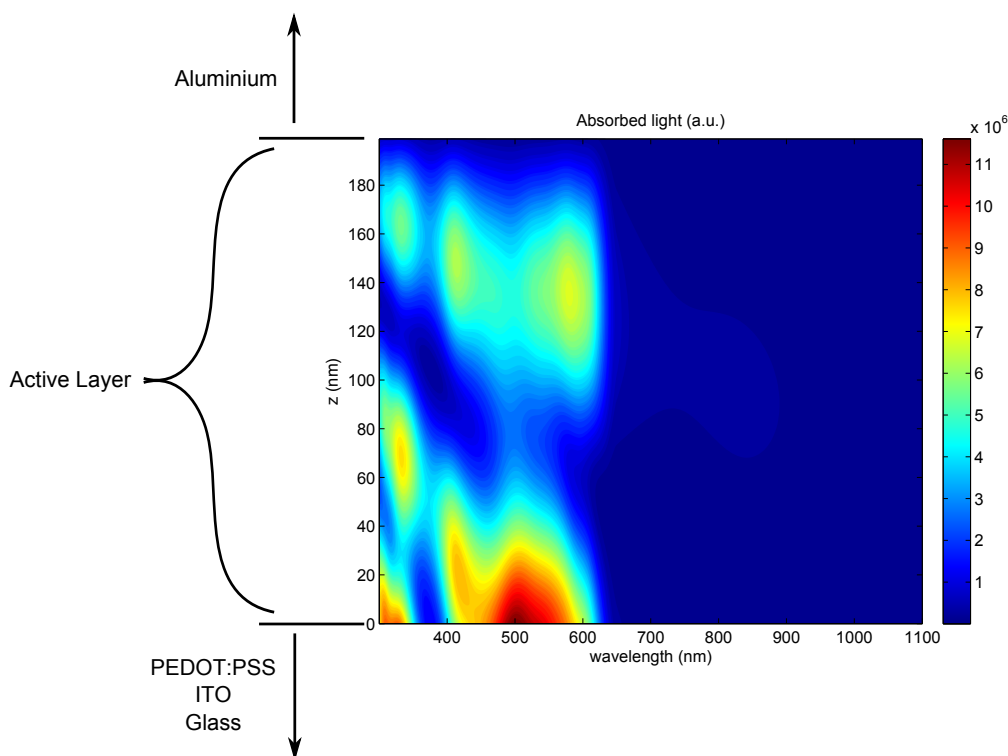


FIGURE 6.3: Contour plot of light absorption in the photoactive layer as a function of depth (z) and wavelength. In this figure $z=0$ corresponds to the PEDOT:PSS interface and $z=200$ corresponds to the aluminium interface.

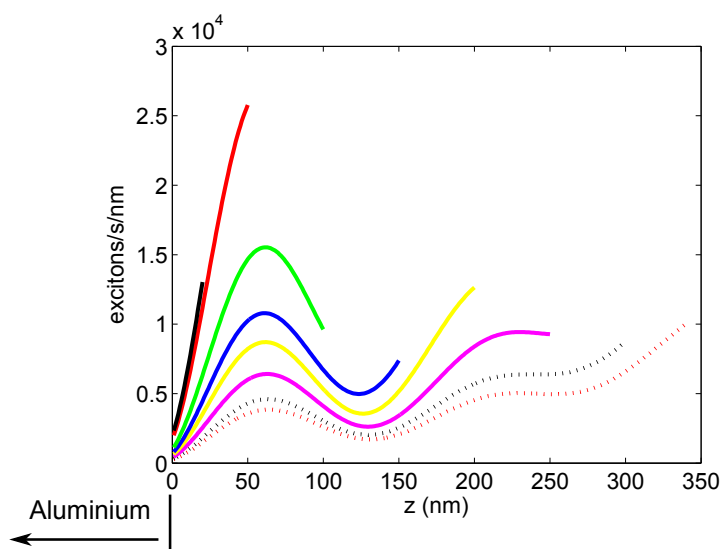


FIGURE 6.4: Exciton generation rate (integrated over wavelength) for a $40 \text{ nm} \times 40 \text{ nm}$ area as a function of depth in the P3HT:PCBM photoactive layer (z) for a thickness of 20 nm (black, solid), 50 nm (red, solid), 100 nm (green, solid), 150 nm (blue, solid), 200 nm (yellow, solid), 250 nm (magenta, solid), 300 nm (black, dashed) and 340 nm (red, dashed). In this figure $z=0$ corresponds to the aluminium interface and the PEDOT:PSS interface starts where the graph stops.

was done for aluminium (a 50 nm film was compared to 100 nm film). The exciton generation profile (as a function of depth, i.e. absorbed excitons/s/nm) is not very sensitive to fluctuations in either of these films. On the other hand, when changing the P3HT:PCBM layer by 20 nm (from 20 nm to 40 nm), a change of 82 % was observed, highlighting the importance of accurately controlling and optimising the photoactive layer thickness. From a measurement point of view, it is important to accurately

TABLE 6.2: Maximum change in the exciton generation profile (excitons absorbed/s/nm) when changing thickness. A 30 nm PEDOT:PSS film was compared to a 50 nm PEDOT:PSS film while keeping all other layers constant. A 50 nm aluminium cathode was compared to a 100 nm film thickness while keeping all other layers constant

| Active layer thickness | max. change due to PEDOT:PSS thickness change of 20 nm | max. change due to Al thickness change of 50 nm |
|------------------------|---|--|
| 40 | 0.43 % | 0.04 % |
| 90 | 3.83 % | 0.03 % |
| 140 | 3.50 % | 0.03 % |
| 190 | 2.39 % | 0.04 % |
| 240 | 3.31 % | 0.04 % |
| 290 | 3.90 % | 0.04 % |
| 340 | 2.38 % | 0.04 % |

determine the photoactive layer thickness and to average over several devices to smooth out small thickness variations in the photoactive layer. J_{SC} was obtained from the device I-V curves measured under AM1.5 conditions. Since the devices were small ($< 1 \text{ cm}^2$), the real J_{SC} in the absence of edge-effects was established following an established method [222], i.e. by measuring devices of different sizes and extrapolating to large area. Larger cells are progressively less influenced by extra current due to light scattered inward from outside the cell edge, since they have a lower ratio of perimeter length to cell area. Since the test cells are all square, the perimeter-to-area ratio can be represented by the term $4\sqrt{A}/A$, where A is the cell area. On this basis the measured J_{SC} values can be fitted to equation 6.1, where $J_{SC}^{edgefree}$ represents the short circuit current density that would be observed in the absence of macroscopic edge effects that

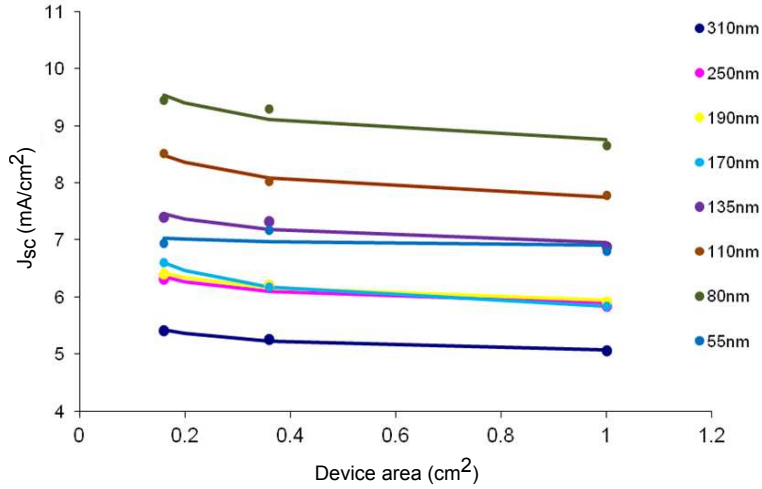


FIGURE 6.5: Measured J_{SC} (dots) for nine OPV devices with different layer thickness, each fabricated at three different sizes; $4\text{ mm} \times 4\text{ mm}$, $6\text{ mm} \times 6\text{ mm}$ and $10\text{ mm} \times 10\text{ mm}$. The solid lines represent fits based on equation 6.1.

are not taken into account in the nano-scale model.

$$J_{SC} = k \frac{4\sqrt{A}}{A} + J_{SC}^{edge\ free} \quad (6.1)$$

Total internal quantum efficiency (IQE) was calculated by modelling the absorption of the photoactive materials to determine the total number of absorbed photons and by calculating the total number of extracted electrons from the J_{SC} measurements. 12 different devices were fabricated at each thickness and the average IQE and J_{SC} values together with the corresponding standard deviations were calculated. Device fabrication and I-V measurements for these solar cells were conducted by Dr. Lynn J. Rozanski. EQE spectra were also measured for a select number of devices. J_{SC} measurements were determined from these spectra by overlaying the solar simulator spectrum with the EQE spectrum and integrating over wavelength. J_{SC} values as determined by these two methods matched to within 5.3 %, which is smaller than the standard deviation of the measurements. Since the illumination area is smaller than the photoactive area, it is not necessary to accurately determine the actual photo-active area. The good match between integrated EQE and edge-corrected J_{SC} shows that the edge-effect elimination approach is valid.

In order to determine directly the vertical composition of the P3HT:PCBM devices, XPS depth profiling measurements were conducted on annealed and unannealed devices. The aluminium layer is directly identified by measuring the Al 2p peak, the active layer is identified from the carbon 1s peak and the anode is tracked by looking at the indium 3d_{5/2} peak. In addition, by monitoring the sulphur 2p signal and the carbon:sulphur (C:S) ratio, it is possible to monitor both the relative P3HT:PCBM concentration and to differentiate between the active and PEDOT:PSS layers [122, 223]. XPS depth profiling measurements were conducted by Bill B. Gong at the Mark Wainwright Analytical Centre, University of New South Wales.

The Ar ion beam used in the XPS measurements induces ion beam mixing effects that lead to interface broadening, such as atomic mixing, preferential etching and ion implantation. In order to estimate interface broadening due to these mixing effects, the TRIDYN simulation package [224] was used. TRIDYN simulates dynamic change of thickness and composition during ion-beam etching and uses the binary collision approximation model for ballistic transport [225, 225, 226]. These simulations were carried out by Professor Bruce King.

6.3 Results and Discussion

6.3.1 Thickness dependence of IQE and J_{SC}

As shown in Figure 6.6(a) and (b), there is excellent agreement between the experimental and modelled results, with the data generated for the virtual organic solar cell corresponding to the measured values to within the statistical error of the measurements.

6.3.2 Charge blocking layers

For an optimal device, holes are transported to the ITO anode and electrons to the metal cathode exclusively and subsequently extracted into the external circuit. However, in the absence of a selective electrode or a blocking layer, it is possible for charge

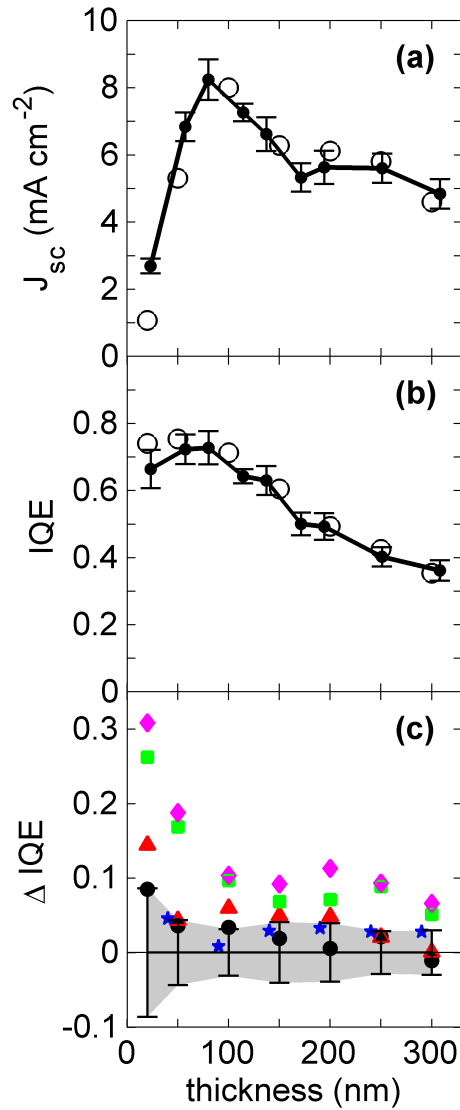


FIGURE 6.6: J_{sc} (a) and IQE (b) as a function of thickness. Dots are measured results and open circles are modelled data. A line is drawn through the experimental results as a guide to the eye. Discrepancy between modelled data and measured IQE data (c) is shown as a function of thickness for the four virtual device structures initially modelled: (i) Black dots correspond to a device without blocking layers, (ii) red triangles to a device where a perfect blocking layer is used at the cathode (i.e. PCBM capping layer) only, (iii) green squares to a device where a perfect blocking layer is used at the anode (i.e. PEDOT:PSS) only and (iv) magenta diamonds to a device where two blocking layers are used. Also shown (blue pentagrams) is the discrepancy between modelled data and measured IQE data for the actual annealed device structure with partial P3HT (58 % anode coverage) and PCBM (60 % cathode coverage) blocking layers as subsequently determined by XPS measurements. Error bars and shading indicate the statistical error (standard deviation) of the measured values.

carriers to hop into the opposite polarity electrode (albeit with a smaller probability) resulting in reduced device efficiency. For the P3HT:PCBM system, it is well known that thermal annealing affects the vertical composition of the active layer [227], leading to enrichment of the components at the electrode interfaces [228]. Indeed, previous work has indicated that annealed P3HT:PCBM devices should contain P3HT-rich and PCBM-rich blocking layers at the anode and cathode, respectively, resulting in improved electrode selectivity [227]. It is noteworthy that studies based on the active layer – air interface are not representative of what occurs at the active layer – cathode interface, which explains the distinct change in performance when annealing with or without a cathode [130].

In order to establish the theoretical effectiveness of these potential blocking layers, we initially modelled 4 different solar cell configurations: (1) blocking layers at both electrodes, (2) one blocking layer at the anode, (3) one blocking layer at the cathode, and (4) no blocking layers. Figure 6.6(c) shows the difference between the modelled and experimental IQE values (ΔIQE) for each of the initial 4 configurations, with the error bars and shaded region showing the standard deviation in the experimental measurement. It is clear that ΔIQE is minimised for the model with no blocking layers and that, surprisingly, the addition of blocking layers at the electrodes results in a progressively poorer fit to the data. As such, the DMC model suggests that, contrary to expectation, there are no effective blocking layers present in this experimental system.

6.3.3 Recombination mechanisms

In order to gain further insight into the dominant recombination mechanisms that are operating for each model, we have calculated separately the total bulk recombination efficiency (η_{bulk}), which consists of bimolecular, geminate and exciton recombination) [194], and the interface recombination efficiency (η_{int}). Interface recombination consists of charge carriers that are collected at the opposite polarity electrode, i.e. electrons at the anode and holes at the cathode. This recombination mechanism essentially represents a loss of charge at the electrode interfaces. Bulk recombination is defined as the total recombination minus interface recombination. The way these recombination

types are defined means that all recombination is accounted for when adding bulk and interface recombination, i.e. $\text{IQE} + \eta_{\text{bulk}} + \eta_{\text{int}} = 1$.

Figure 6.7 shows the bulk and interface recombination efficiency as a function of thickness for each model and reveals that, in the absence of any blocking layers, interface recombination is significant for all thicknesses and increases for thinner films. The optimal device efficiency is obtained for an active layer thickness of ~ 80 nm, which correlates well with the intersection point of the bulk and interface recombination efficiencies. Interestingly, although interface recombination efficiency is lowered in the presence of a cathode blocking layer, the reduction is moderate compared to the presence of an anode blocking layer, which leads to a large increase in performance. This difference in performance gain is related to the difference in the number of excitons generated near the cathode and anode. When the system contains blocking layers at both electrodes, interface recombination is necessarily eliminated for all thicknesses. In order to quantify the relative importance of the two mechanisms, the ratio of interface to bulk recombination (for the model of best fit) is plotted in Figure 6.8. As might be expected, for thin layers (< 100 nm), recombination is substantially influenced by the electrode interfaces, but for thicker layers interface recombination has a minimal impact on device performance.

6.3.4 XPS analysis of interfaces

In order to investigate the cathode and anode interfaces of the real devices, XPS depth profiling was conducted. Figure 6.9(a) and (b) show the XPS depth profiles for the unannealed and annealed devices respectively. Whereas the unannealed device exhibits a constant PCBM:P3HT ratio throughout the active layer, it is clear that in the annealed device the carbon concentration is higher at the cathode than in the middle of the active layer suggesting that PCBM has segregated to the top electrode. In fact, from the C and S XPS signals we can calculate the PCBM concentration near the cathode relative to the PCBM concentration in the bulk of the layer (middle of

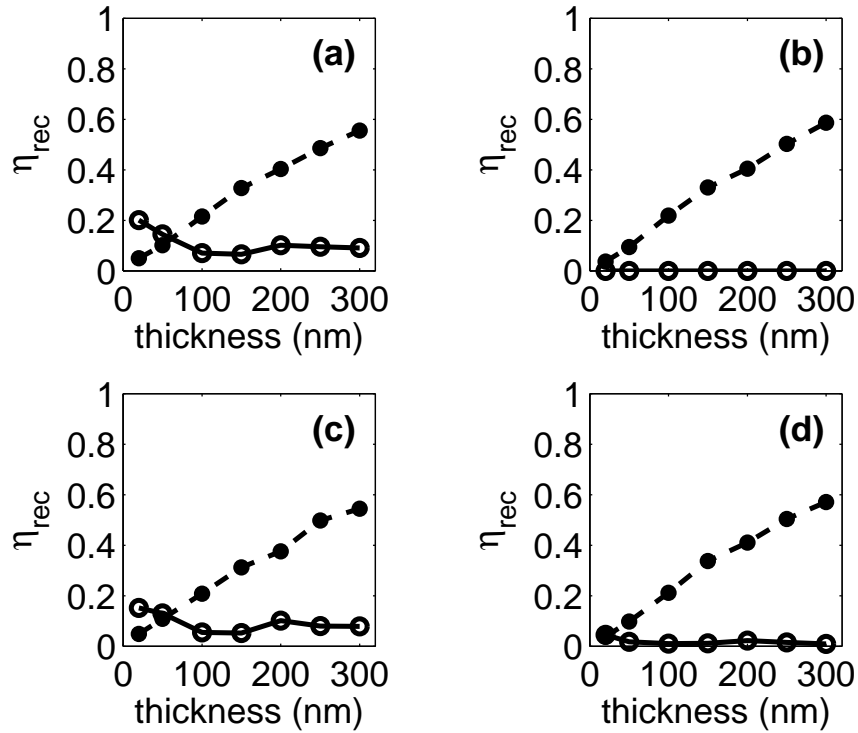


FIGURE 6.7: Interface recombination efficiency (open circles) and bulk recombination efficiency (filled circles) as a function of thickness for a virtual device with (a) no blocking layers, (b) blocking layers at both electrodes, (c) only one blocking layer at the anode and (d) only one blocking layer at the cathode.

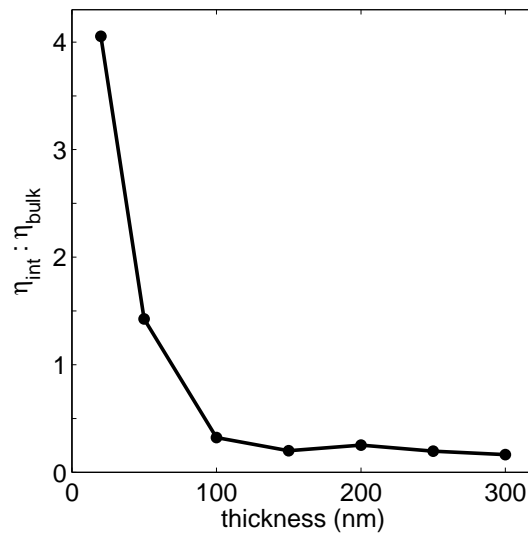


FIGURE 6.8: This figure shows the ratio between interface recombination and bulk recombination and indicates to what degree interface recombination dominates.

the active layer). If the C:S ratio is 1.5 times higher, it could be that the S content has decreased, the C content has increased or a combination of both. The C:S ratio for a single P3HT unit or PCBM molecule is constant and known. Consequently, the C:S ratio can be converted to a PCBM:P3HT ratio. Furthermore, there is only one possible solution, i.e. PCBM:P3HT ratio, for a given C:S ratio. As such, the above three situations are equivalent in terms of the relative PCBM:P3HT ratio. The C:S ratio near the cathode is approximately 1.5 times larger than in the bulk of the active layer. It is easy to determine the resulting PCBM:P3HT increase when considering the situation, where the S content has decreased by a factor of 1.5. Since in the active layer, S is only present in P3HT the PCBM:P3HT concentration must increase by a factor of 1.5 as well. Since, the other situations, where either the C content increases or the C content increases and S content decreases simultaneously, give equivalent PCBM:P3HT ratios, we can immediately see that the PCBM concentration is 1.5 times higher near the cathode than in the bulk of the layer. In both the annealed and unannealed case, the C:S ratio is constant in the middle of the active layer and then decreases to a lower plateau before reaching the substrate interface; consistent with the presence of a P3HT:PCBM layer atop a PEDOT:PSS layer. Thus, the XPS data supports the prediction that, upon annealing, PCBM migrates to the cathode. In principle, therefore, the presence of a PCBM-rich region at the top electrode, coupled with a PEDOT:PSS layer at the substrate interface, should result in blocking layers at both interfaces; contrary to the conclusions of the DMC modelling shown in Figure 6.6.

However, there are a number of possible explanations for the apparent inconsistency between the observation of interface layers in the device and the fact that the best fit DMC model contained no blocking layers. Firstly, interdiffusion is known to occur between the metal electrode and the blocking layer resulting in an incomplete blocking layer [229]. The broad cathode and anode interface widths shown in Figure 6.9 arise from interdiffusion during device fabrication and from ion beam mixing effects induced by the incident 3 kV Ar ion beam [230]. The etch rate was the same for both

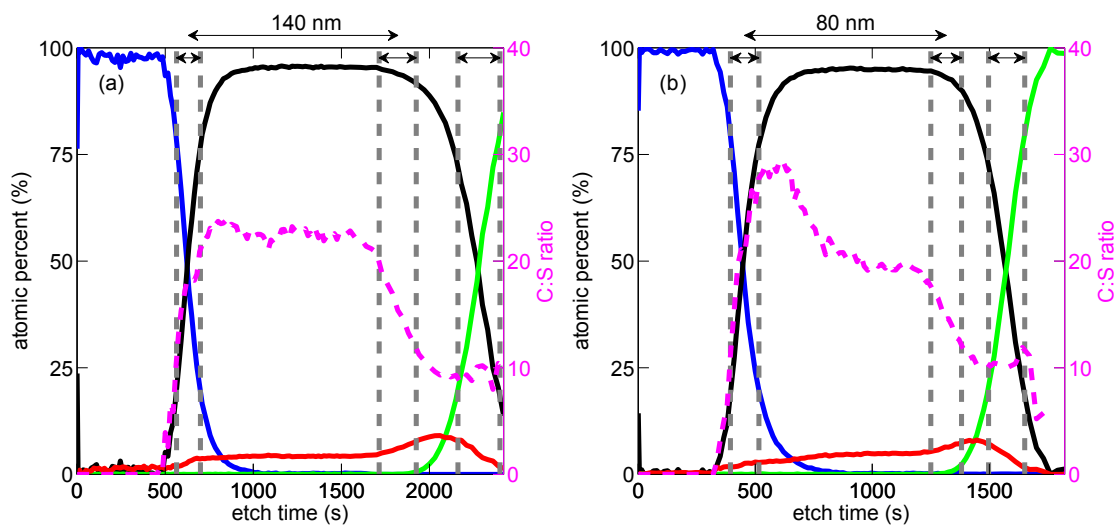


FIGURE 6.9: XPS depth profiling results for: (a) an unannealed OPV device (active layer thickness of 60 nm) and (b) an annealed OPV device (active layer thickness of 80 nm). Blue indicates Al 2p (i.e. aluminium cathode), black C 1s (i.e. active layer and PEDOT:PSS layer), red S 2p (i.e. active layer and PEDOT:PSS layer), green In 3d_{5/2} (i.e. ITO anode) and magenta indicates the C 1s : S 2p ratio. Gray dashed lines indicate the interface widths, which have been conventionally defined [224] using the etch time difference between the 80 % and 20 % signal intensity levels for each interface component.

depth profiles and the relative etch time corresponds to the relative active layer thickness. The interface widths have been conventionally defined [230] using the etch time difference between the 80 % and 20 % signal intensity levels for each interface component. The widths of the Al/P3HT:PCBM (cathode) and PEDOT:PSS/ITO (anode) interfaces were measured to be 11.1 nm and 14.4 nm respectively. These widths are marginally larger than the interface width due to ion beam mixing (10.7 nm), which we have calculated to a first approximation using the TRIDYN-FZR simulation package [224], see Figure 6.10 for the Ar⁺ fluence. As such, the depth profiling measurements indicate that interpenetration of aluminium into the PCBM rich layer and indium into the PEDOT:PSS layer occurs within 10 – 20 nm of the interface, consistent with previous reports [229]. Secondly, the measured PCBM enrichment (1.5 times the P3HT concentration by weight) at the cathode would only lead to a 60 % PCBM coverage and hence result in an incomplete PCBM interface layer. Thirdly, P3HT itself has been shown to possess poor electron blocking properties [231] and does not form a

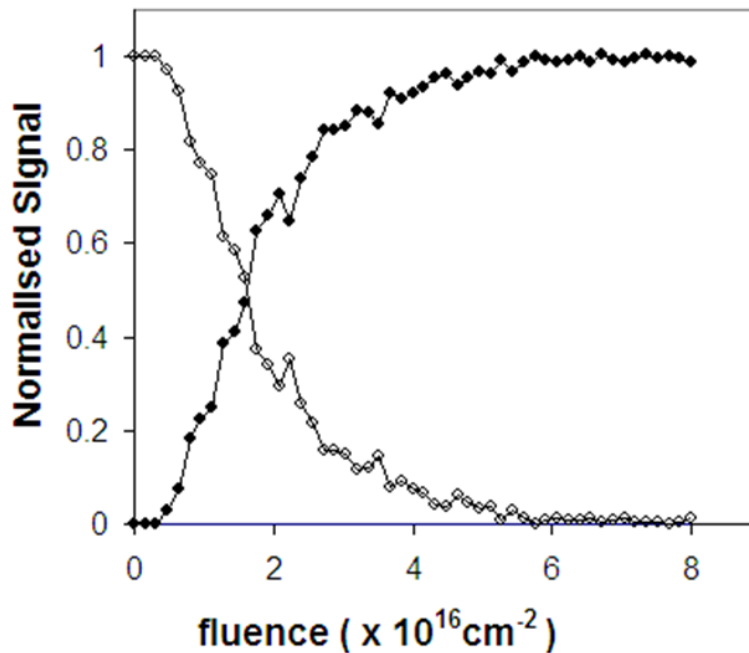


FIGURE 6.10: TRIDYN-FZR [224] simulation of depth profile of a 10 nm Al layer on an Al substrate sputtered by 3 keV Ar+ at 39° incidence. The normalised yield of the surface layer (open circles) and the normalised yield of the substrate layer (closed circles) are plotted as a function of Ar+ fluence. The depth scale is determined by defining the fluence at the crossover point between the two yields as the thickness of the surface layer (10 nm).

continuous capping layer at the PEDOT:PSS interface [232]. Finally, PEDOT:PSS has also been shown to have relatively poor electron-blocking properties [233, 234]. This combination of: (a) interdiffusion at the electrodes, (b) incomplete PCBM layer formation at the cathode, (c) incomplete P3HT layer formation at the anode, and (d) poor electron blocking capability of P3HT and PEDOT:PSS at the anode would eliminate any blocking effect of these interface layers; consistent with the significant interface recombination and poor electron/hole blocking properties that are predicted by the Monte Carlo simulations and explaining why the best fit is obtained when assuming no blocking layers at all. In order to test this hypothesis, a fifth set of simulations were run using the electrode coverage indicated by the XPS measurements, i.e. 58 % of the anode is in contact with P3HT and 60 % of the cathode is in contact with PCBM. As shown in Figure 6.6(c) the performance of this fifth virtual device structure agrees with the experimental data to within the statistical error of the measurements, thus demonstrating that the device performance as a function of active layer thickness is

consistent with the absence of effective blocking layers.

Thus, a consistent picture has emerged, with the simulation indicating that there are no perfect blocking layers present, in agreement with the observed intermixing at the electrode interfaces. The excellent agreement between the modelled and experimental photocurrent data, supported by the conclusions from the XPS analysis provides confidence that the simulation is indeed accurately representing real device performance. Returning then to the simulation results, we see that the model predicts that OPV devices with blocking layers are actually more efficient for all thicknesses (Figure 6.6) and that interface recombination is the dominant loss mechanism (Figure 6.8 and 6.7). Possible interfacial recombination mechanisms include reverse diffusive recombination at contacts [190, 194] or recombination through defects or impurity states at the interface for thin devices [85]. As such, the simulation suggests that improving the selectivity of the electrodes will lead to an increase in device performance.

6.4 Conclusion

In conclusion, we have shown that dynamic Monte Carlo models are not only useful from a qualitative point of view, but also correspond well with experimental data from a quantitative perspective. We have quantified the effect of interface recombination on device performance as a function of thickness and have shown that electrode interfaces dominate the performance of P3HT:PCBM devices for thin active layers (< 100 nm) and remains significant until a thickness of ~ 150 nm. Furthermore, XPS depth profiling reveals the presence of substantial interface mixing at both electrodes. This observation, combined with the fact that the PCBM rich region at the cathode interface cannot provide complete coverage and that PEDOT:PSS has poor electron blocking properties, leads to the significant interface recombination that is predicted by the Monte Carlo simulations. Modelling suggests that a substantial performance gain may be achieved by improving charge selectivity at the anode, while charge selectivity improvements at the cathode result in a smaller performance increase. Overall, this work highlights the effectiveness of Monte Carlo simulations as a predictive tool and,

in doing so, emphasizes the need to understand and control interface processes in OPV devices.

7

Anomalous current-voltage behaviour

7.1 Introduction

Many organic solar cell models, such as drift-diffusion type models or electrical equivalent circuit models, provide a good fit against experimental data [109, 112], when OPV devices with well-behaved I-V curves are used to gather the experimental data. However, models may arguably provide the most valuable insight if they can model anomalous behaviour, because then the model could be used to understand and ultimately prevent anomalous I-V behaviour.

A typical anomaly in I-V curves organic solar cells is the appearance of a 'kink' or s-shape [235, 236]. Two examples of such an anomaly are shown in Figure 7.1. As a comparison an I-V curve with no kink is shown as well. Generally, J_{SC} is not much affected by the s-shape effect, in contrast to FF which is severely reduced. V_{OC} is

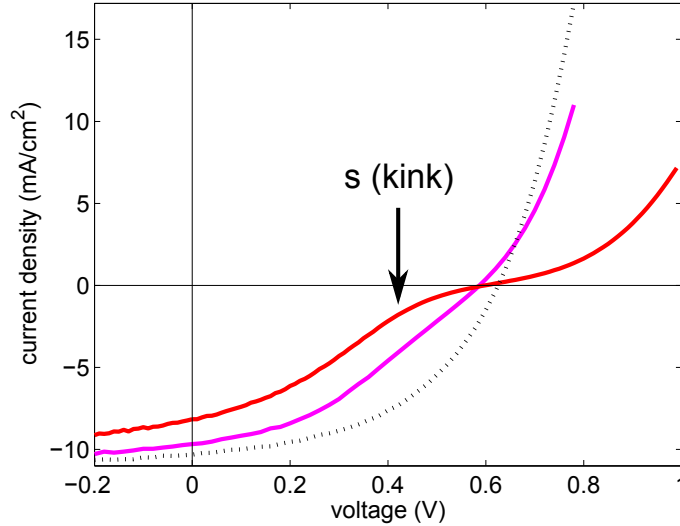


FIGURE 7.1: Three I-V curves. The dotted black line is a normal I-V curve, while the red and magenta solid lines are s-shaped I-V curves. The red curve shows a much more severe kink than the magenta curve.

only considerably affected if the s-shape effect is severe. While devices that exhibit s-shaped I-V curves can be purposely fabricated [237], the opposite is not always true. Even though the same fabrication recipe is used, a device that exhibits s-shaped I-V behaviour is observed from time to time [238].

In order to understand the s-shape effect, existing models had to be modified. The standard electrical equivalent circuit model (one-diode or two-diode model) cannot produce s-shaped curves [239] and it had to be changed by introducing an extra diode in reverse bias with an associated parallel resistance [240]. An exact analytical solution to this circuit has only recently been determined [239]. Ecker et al. [236] performed impedance spectroscopy measurements and proposed a different equivalent circuit model, but do not demonstrate in a satisfactory manner that their model produces s-shaped I-V curves.

Different adaptations to the drift-diffusion type models have been made in order to generate s-shaped I-V curves. Kumar et al. [241] proposed a model where the s-shaped behaviour is induced by interface dipoles with a corresponding electric field that points in the opposite direction to the built-in field due to the work function difference of the

electrodes. Wagenpfahl et al. [237] took a more general approach to charge extraction and introduced a semiconductor-electrode surface recombination term, which models restrictions on the charge-extraction process. Both the adaptation by Kumar et al. and Wagenpfahl et al introduced modifications that are related to the active layer-electrode interface and were able to successfully model s-shaped curves.

DMC simulations have, to the best of our knowledge, not been used to investigate s-shape behaviour. In order to model this anomalous s-shape I-V behaviour and see whether the DMC model can reproduce this effect, its origin must be understood.

The occurrence of s-shape behaviour is linked to vertical phase segregation. In fact, Tremolet de Villers et al. [238] have shown that the deposition of a thin PCBM layer on top of the BHJ active layer (cathode side) effectively prevents s-shaped behaviour from occurring. AFM images and I-V measurements show that the metal-organic interface is especially important, as devices with a P3HT dominated cathode-active layer interface are much more prone to s-shape behaviour [238]. S-shape behaviour commonly arises in pristine devices and often disappears after thermal annealing treatments [242]. Since annealing treatments are known to modify the vertical distribution of PCBM [122, 228, 243], it is possible that the disappearance of the kink in I-V curves after annealing is simply a result of an increased PCBM concentration at the cathode interface.

Castro et al. have shown that the insertion of a thin bathocuproine (BCP) layer in between active layer and cathode prevents s-shape behaviour. However, if high aluminium deposition rates are used, s-shape behaviour is still observed despite the thin BCP layer. Certain interface layers, such as BCP, are believed to prevent physical destruction of the organic layer when the cathode is vacuum deposited [85, 235, 244]. Castro et al. propose that isolated aluminium nanoclusters are formed as a result of the aggressive evaporative deposition process. These clusters are believed to act as trap sites. The authors also propose that these aluminium clusters coalesce at elevated temperatures (thermal annealing) and merge with the bulk cathode, thus removing trapping sites. Wagner et al. [235] showed that samarium, as opposed to aluminium, does not penetrate into the underlying organic layer and forms a continuous film already after a few monolayers. When using samarium, BCP is not needed to prevent s-shaped

I-V curves. This observation provides further evidence that the s-shape behaviour is likely to relate to aluminium diffusion into the organic layer.

While different mechanisms have been proposed to describe the anomalous I-V behaviour as a result of interface effects (i.e. vertical segregation of PCBM vs aluminium diffusion into the organic layer), they both share a common aspect. S-shaped I-V behaviour is controlled by the electrode-organic interface. In the case of P3HT:PCBM devices, the aluminium-P3HT:PCBM interface is of particular importance. It is difficult to experimentally prove either theories, as annealing treatments induces both vertical diffusion and diffusion of aluminium nanoclusters. Furthermore, both theories are not mutually exclusive. In this chapter, both theories are explored using DMC modelling.

It is not only the electrode-organic interface that gives rise to s-shaped behaviour, but impurities in the bulk of the active layer have also been shown to correlate to this anomalous behaviour. Wagner et al. [235] argued that impurity-induced hole traps give rise to s-shape I-V curves. Tress et al. [245] showed that materials systems with a large mobility mismatch (larger than a factor of 100) that were fabricated in the bilayer architecture are prone to s-shaped behaviour. When both the hole and electron mobility are low, no s-shaped curves were seen. Interestingly, if the same large-mobility-mismatch materials were used in a BHJ architecture, no s-shaped curves were observed. In a BHJ device the asymmetric electric field distribution due to charge build-up is averaged out, because both donor and acceptor are located throughout the device resulting in a spatial averaging of the space charge.

Wagenpfahl et al. [237] showed that the s-shape around V_{OC} is essentially the transition phase from Ohmic conductivity to a space-charge limited current and is influenced by the extraction rate at the electrode-organic interface. Irrespective of the s-shape triggering mechanism, the mechanism always involves a disruption of the electric field in the device. In this chapter, mobilities of both donor and acceptor materials are modelled to be the same and thus we do not investigate the origin of s-shaped curves as seen by Tress et al. [245]. Another origin of electric field disruption, i.e. space charge, are small isolated islands of P3HT and/or PCBM which effectively

act as charge trapping regions [246]. However, in this chapter we do not focus on this effect either. Instead, we focus on the effect of impurities or defects, either at the interface or in the bulk. Such defects are hard to control and may be the result of poor fabrication procedures, interface materials (e.g. LiF, Ca) penetrating into the device, electrode (e.g. Al, ITO) penetration into the device [240, 247], the use of insufficiently pure material [235] or degradation of any of the components in an OPV device [246]. It is likely that impurities or defects act as charge trapping sites [55, 241]. Hence, in this chapter defects are modelled by creating charge trapping sites in the energy landscape of the DMC model. No modifications were made to the underlying principles of the DMC model.

While the existence of traps is well known, its simulated impact on the shape of the I-V curves is only briefly discussed in literature. Mandoc et al. [248] investigated electron traps in MDMO-PPV devices using a 1D drift-diffusion based modelling approach and did not report evidence for s-shaped curves, they did show that V_{OC} , J_{SC} , FF and thus power conversion efficiency (PCE) is negatively influenced by electron traps due to increased charge recombination. On the other hand, Giebink et al. [192] used drift-diffusion based modelling to show that electron traps can cause s-shaped I-V curves.

In this chapter, it is demonstrated that the DMC model, not only describes good devices (Chapter 6), but also is able to simulate inefficient devices that exhibit s-shaped I-V curves. This demonstration further establishes the all around capability of DMC models to describe OPV devices.

7.2 Simulation methodology

Mobility studies of P3HT:PCBM systems have found evidence for the existence of deep energy traps leading to trapped electrons and holes [249]. Energy traps may represent defects in the film or deep energy states in the tail of the DOS. Activation energies associated with these traps are found to be in the range of 0.05 to 0.4 eV with total trap densities in the range of $10^{22} - 10^{24} \text{ m}^{-3}$ [192, 246] which

equates to one trap for every $10^3 - 10^5 \text{ nm}^3$. Electron transport in organic materials is frequently hindered by electron traps, while hole transport generally shows trap-free behaviour [250]. P3HT seems to be an exception, as evidence for trapped holes has been reported [251, 252], but is much lower than what is usually found for the electron trap density [246]. Considering the apparent dominance of electron traps over hole traps, only electron traps are taken into account in the DMC model, consistent with common materials like poly[2-methoxy-5-(2-ethylhexyloxy)-p-phenylenevinylene] (MEH-PPV), poly[9,9-didecanefluorene-alt-(bis-thienylene) benzothiadiazole] (PF10TBT), poly[2,6-(4,4-bis-(2-ethylhexyl)-4H-cyclopenta[2,1-b;3,4-b]-dithiophene)-alt-4,7-(2,1,3-benzothiadiazole)] (PCPDTBT) [250]. These electron traps are introduced by creating energy traps in the energy landscape associated with the electron donor material (e.g. PCBM). As shown by [246] Schafferhans et al. the trap depth distribution looks neither purely Gaussian nor purely exponential. Traps could come from various sources that are not inherent to the electron acceptor material, as previously mentioned. One cannot expect that the distribution of traps is the same for these different sources. The distribution of traps is therefore hard to predict. Here a simple approach is taken and traps with a fixed depth, d_{trap} , are added to the system with a particular density, n_{trap} . The definition of d_{trap} is depicted in Figure 7.2. A spatially random distribution in the x- and y-directions was used. However, in order to evaluate the impact of traps at the electrode interfaces compared to traps in the bulk, the distribution was confined in the z-direction, i.e. the direction perpendicular to the electrode interfaces.

Thermionic injection is used to simulate dark current injection as described in Chapter 4. In this chapter a general investigation of modelling s-shaped I-V curves with a DMC model is conducted and parameters were not fitted against any specific device. However, since the balance between injected and photo-generated charges plays a role in the severity of the s-shape effect (discussed in Section 7.3.3) it is important to use accurate parameters for current injection. The simulated dark I-V curve parameters were chosen such that they match a P3HT:PCBM device. The built-in field due to

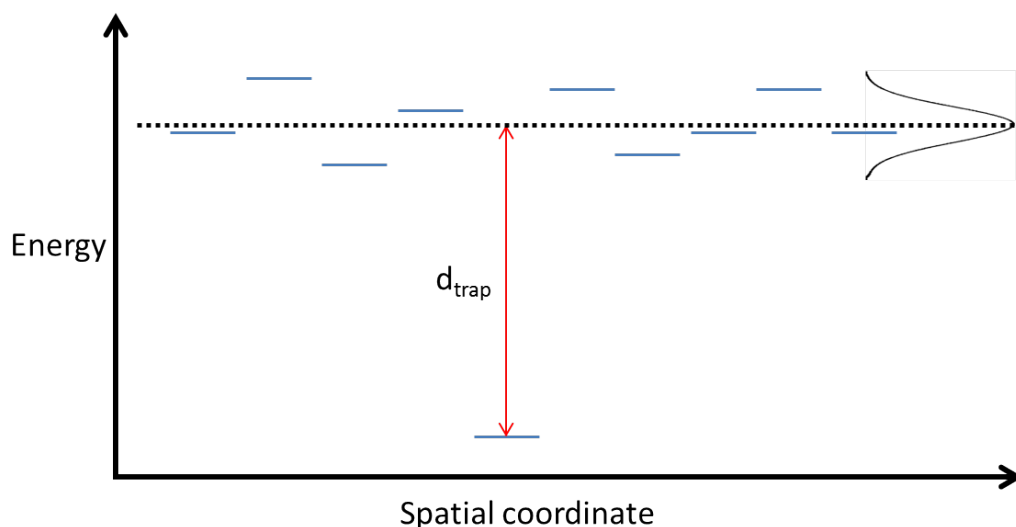


FIGURE 7.2: d_{trap} is the depth of the energy trap with respect to the mean of the Gaussian energetic disorder (in absence of traps).

the work function difference of the electrodes was assumed to be the result of a 0.72 V voltage drop across the thickness of the device, consistent with the work functions of aluminium and ITO. The thermionic charge injection rate was chosen to be $1.111 \times 10^8 \text{ s}^{-1}$. With these values a good fit was obtained for a P3HT:PCBM device, as the measured and simulated values agree to within the experimental error, except for the measurement at 0.9 V (see Figure 7.3). The discrepancy of the last point is not surprising considering that the series resistance of the electrodes is not taken into account in the DMC model. In Chapter 4 it has already been established, that ignoring series resistance will decrease the apparent rectifying behaviour. Even though the measured curve in Figure 7.3 corresponds to the device architecture that has the least series resistance (out of the three architectures described in section 3.1 and considered in this thesis, architecture II devices have the least series resistance), there is still a finite resistance due to a significant pathway through the ITO electrode. As a result, the measured curve is expected to have a slightly lower current value at high voltages, where the resistance has a larger impact on the measured value.

Only BHJ morphologies were explored in this chapter. The morphologies were created following the procedure explained in Chapter 4.

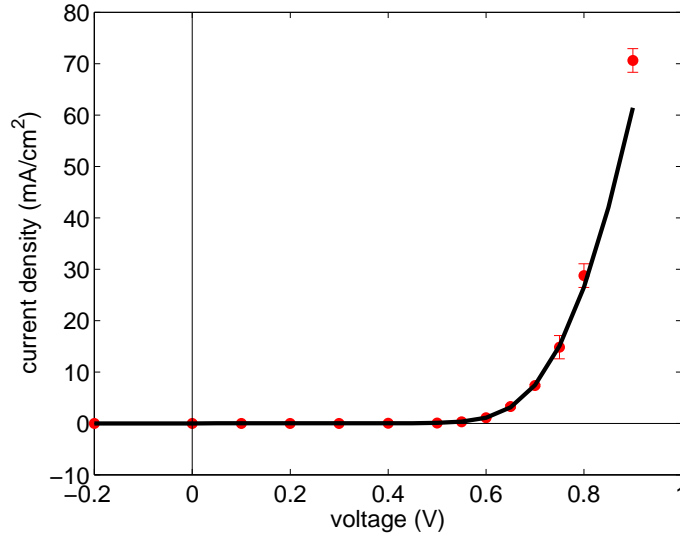


FIGURE 7.3: A measured dark I-V curve (black) and simulated dark I-V curve (red dots) with corresponding standard deviation. The thickness of the device was approximately 55 nm and the modelled system had a thickness of 50 nm. An architecture I device was used, because this architecture has the least series resistance.

The DMC simulations are computationally intensive. In order to reduce the computational load, the number of virtual data points were limited. In most cases, 0.1 V steps were taken when simulating I-V curves as opposed to 0.02 V for experimentally measured I-V curves. The reduced number of points were sufficient for the purposes of this chapter. V_{OC} values were estimated by linear interpolation of the two nearest data points, which only introduces a minor error that does not affect direct comparisons of I-V curves. FF , on the other hand, is more crudely determined, because the maximum power point cannot be linearly interpolated (linear interpolation of a peak is not possible). No other interpolation method was used and thus the maximum power point is restricted by the step size in the voltage. Nevertheless, the error in FF and by extension PCE does not affect the conclusions drawn from the data.

DMC simulations were run with parameters as presented in Table 7.1 unless stated otherwise.

In order to evaluate whether the Coulomb capture radius is sufficiently large to capture long-range interaction effects, a series of simulations were run where the Coulomb capture radius was varied from 10 to 25 nm. Long-range Coulomb interaction may

TABLE 7.1: DMC simulation parameters.

| Property | Value | Reference |
|--|------------------------------------|--|
| Temperature | 300 K | |
| Relative dielectric constant | 3.1 | [147] |
| σ energy landscape | 0.05 | as determined from absorption spectra |
| Exciton lifetime acceptor moiety | 11 μ s | [155] |
| Exciton lifetime donor moiety | 400 ps | [153] |
| Charge hopping rate constant acceptor moiety | $3 \times 10^{12} \text{ s}^{-1}$ | [70, 195] |
| Charge hopping rate constant donor moiety | $3 \times 10^{12} \text{ s}^{-1}$ | [70, 195] |
| Charge carrier recombination rate | $1 \times 10^4 \text{ s}^{-1}$ | |
| Charge injection rate | $1.111 \times 10^8 \text{ s}^{-1}$ | |
| Reorganisation energy (λ) | 0.5 eV | [181] Section 4.7 |
| Lattice constant | 1 nm | Chapter 4 |
| ITO work function | -4.8 | [219] |
| Aluminium work function | -4.08 eV | [219] |
| HOMO Donor moiety | -5.2 eV | |
| LUMO acceptor moiety | -4.48 eV | |

be more important in s-shaped I-V curves, which is why a virtual device that exhibits s-shaped behaviour was chosen as the test case. The results are shown Figure 7.4. When the Coulomb capture radius is smaller than 15 nm the current density is not correctly simulated. However, there was no statistical difference found for simulations with a Coulomb capture radius of 15 nm or higher. All simulations were run with a Coulomb capture radius of 19 nm, the distance at which Coulomb interaction equals thermal energy.

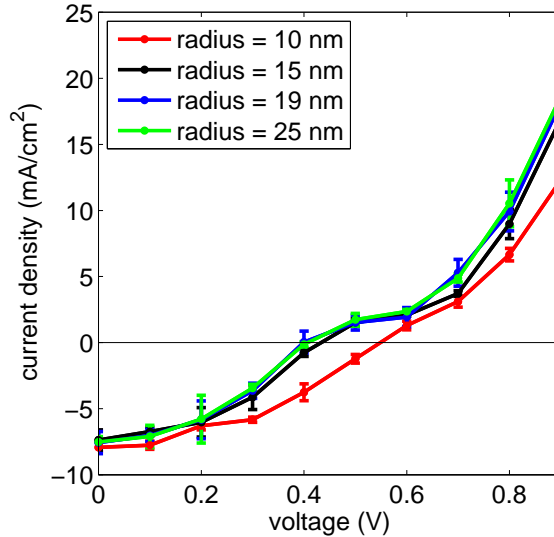


FIGURE 7.4: A virtual device that exhibits s-shaped I-V behaviour was simulated with different Coulomb capture radii.

7.3 Results and discussion

7.3.1 Effect of energy traps on exciton transport

Energy traps in the energy landscape will not only affect charge carriers, but also excitons. In Chapter 5, the exciton diffusion length was seen to decrease with increasing energetic disorder, which affects the number of excitons that reach the heterointerface and thus decreases the exciton dissociation efficiency. Therefore, energy traps are expected to slow down exciton hopping. It is important to quantify the impact of energy traps on exciton transport, in order to delineate excitonic effects from charge related issues.

Excitons either dissociate or recombine. Dissociation at the heterointerface is very efficient (near unity), which is why the exciton dissociation has been defined as the number of excitons that reach the heterointerface divided by the total number excitons created in the same amount of time. If the trap density is high, many traps will be situated at the heterointerface. Dissociation at the heterointerface involving a trap site may not occur with unity efficiency, as the energy levels at such a site is likely not to be conducive towards exciton dissociation, since electron injection from donor

to acceptor or hole injection from acceptor to donor is not efficient. Therefore, in the following a new term, η_{exint} , is introduced to distinctly differentiate between actual exciton dissociation and the probability for excitons to reach the heterointerface. η_{exint} is defined as the number of excitons that reach the heterointerface divided by the total number of excitons created. Thus, η_{exint} is synonymous with exciton dissociation efficiency when dissociation at the heterointerface is unity, i.e. when the trap density is low. Simulations indicate that the diffusion length and thus η_{exint} decreases with increasing trap density and depth, see Figure 7.5(a) and (b). Figure 7.5(a) shows η_{exint} as a function of d_{trap} . As traps become deeper than ~ 0.4 eV, the diffusion length does not decrease any more and η_{exint} levels off. This plateau exists because the escape rate for traps deeper than ~ 0.4 eV is smaller than $1/\text{lifetime}$. Not only the lifetime will dictate at what point the curve levels off, but also the exciton diffusion length, because the diffusion length influences the escape rate of excitons out of traps. In these simulations exciton hopping parameters associated with P3HT and PCBM were used i.e. $L_{P3HT} = 8.5\text{nm}$ [153] and $L_{PCBM} = 5\text{nm}$ [170], see table 6.1. Another set of simulations were run where L of excitons in the acceptor was changed to 40 nm, corresponding to C_{60} [46]. η_{exint} increased for all values of d_{trap} and a trend similar to that shown in Figure 7.5 was seen. In accordance with expectations, the point at which the curve levels off is shifted towards deeper traps for larger L . For the range of trap densities and depths presented in Figure 7.5 the relative drop in η_{exint} does not exceed 5 %. Since exciton transport is assumed not to be influenced by the electric field, exciton trap effects cannot produce s-shaped I-V curves. However, an overall drop of 5 % in current across the voltage range may be expected. L associated with the electron donor sites was not changed, because there are no energy traps in this moiety and thus no change would be seen as a function of d_{trap} or n_{trap} .

Not considering a distribution of energy levels for the energy trap population removes two extra variables (type of distribution and standard deviation of distribution). This approach is adequate for a general consideration of the effect of energy traps on I-V curves as modelled for the first time with an OPV DMC model, since s-shaped

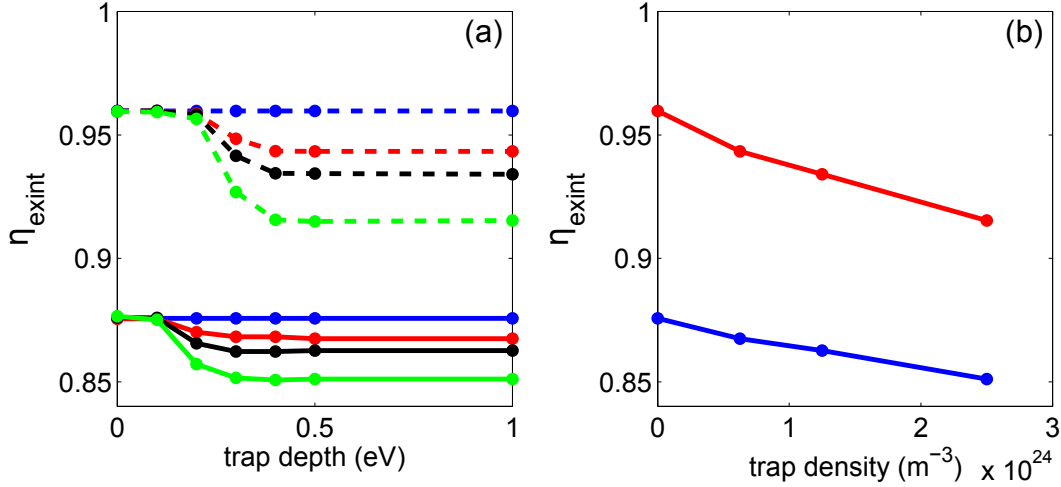


FIGURE 7.5: (a) η_{exint} as a function of trap depth for a trap density of 0 (blue), 6.25×10^{23} (red), 1.25×10^{24} (black) and 2.50×10^{24} m⁻³ (green). The dashed and solid lines correspond to $R_0 = 3.65$ nm (1D L = 40 nm) and $R_0 = 1.8$ nm (1D L = 5 nm) for excitons in the electron acceptor material respectively. In both sets of simulations, $R_0 = 2.15$ nm (1D L = 8.5 nm) for excitons in the electron donor material. (b) η_{exint} as a function of trap density for traps with an energy depth of 1 eV. The blue line corresponds to $R_0 = 1.8$ nm (i.e. PCBM) and the red line corresponds to $R_0 = 3.65$ nm (i.e. C₆₀).

curves similar to experimental data could be generated as is shown in the next sections. However, this simplification may give rise to unrealistic effects at high trap density as the addition of many traps essentially removes energetic disorder. At high trap densities, the standard deviation, σ , of the energetic landscape is significantly affected. In this case, the trap population can no longer be considered a minority and within the model excitons could even hop between traps. In order to assess what trap densities are needed to see these effects, the same exciton simulations were run with trap densities of 6.25×10^{25} , 1.25×10^{26} and 2.50×10^{26} m⁻³. To put these values into perspective, at these densities 12.5 %, 25 % and 50 % of the available electron acceptor sites are occupied by energy traps respectively as opposed to 0 %, 0.125 %, 0.25 % and 0.5 % for the data presented in Figure 7.5. Figure 7.6 shows the results corresponding to the high trap density simulations. Here, the counteracting effects of slowing down of excitons due to traps and the effect of an increase in exciton mobility due to a decrease in energetic disorder are seen. These two effects almost nullify each other for $L_{C60} = 40$ nm (dashed lines) as there is not much variation with d_{trap} or n_{trap} . For the results corresponding to $L_{PCBM} = 5$ nm it is seen that η_{exint} even consistently increases for

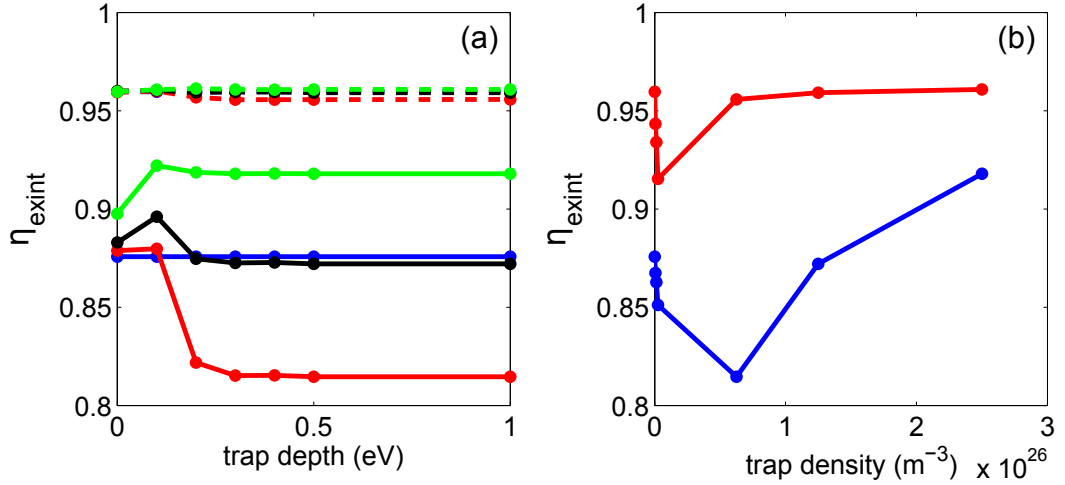


FIGURE 7.6: (a) η_{exint} as a function of trap depth for a trap density of 0 (blue), 6.25×10^{25} (red), 1.25×10^{26} (black) and $2.50 \times 10^{26} \text{ m}^{-3}$ (green). The dashed and solid lines correspond to $R_0 = 3.65$ nm (1D L = 40 nm) and $R_0 = 1.8$ nm (1D L = 5 nm) for excitons in the electron acceptor material respectively. In both sets of simulations, $R_0 = 2.15$ nm (1D L = 8.5 nm) for excitons in the electron donor material. (b) η_{exint} as a function of trap density for traps with an energy depth of 1 eV. The blue line corresponds to $R_0 = 1.8$ nm (i.e. PCBM) and the red line corresponds to $R_0 = 3.65$ nm (i.e. C₆₀).

the highest trap densities. The results corresponding to $n_{trap} < 6.25 \times 10^{25} \text{ m}^{-3}$ do not deviate much from the trend as seen for the low trap densities. For trap densities that are reported in literature ($10^{22} - 10^{24} \text{ m}^{-3}$ [192, 246]), which equates to 0.001 % and 0.1 % of all voxels respectively, no anomalous behaviour is seen and thus the simplified approach is justified for this experimentally determined trap density regime. At these low trap densities, the traps can be considered a perturbation to the energy landscape, which is illustrated by the histograms shown in Figure 7.7. Here, the energy scale is relative to the average HOMO/LUMO before the addition of traps. Figure 7.7(a) shows the histogram corresponding to a trap density of 10^{22} m^{-3} , while Figure 7.7(b) histogram corresponds to a trap density of 10^{24} m^{-3} . In both cases, a trap depth of 0.2 eV was used. The traps are not even visible for the low trap density and only a slight bump is seen at -0.2 eV for the higher trap density. In both cases, the Gaussian character of the energy landscape remains dominant.

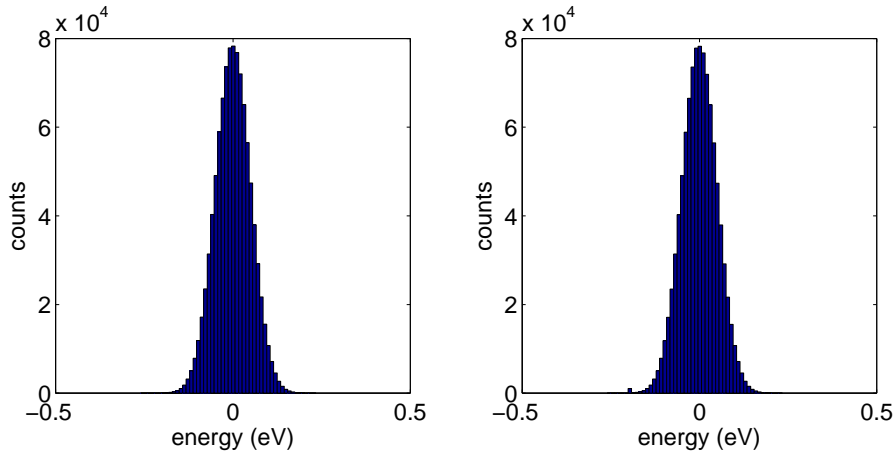


FIGURE 7.7: Histograms of the energy landscape due to energetic disorder and traps with a density of (a) 10^{22} m^{-3} and (b) 10^{24} m^{-3} . The traps had a trap depth of 0.2 eV.

7.3.2 Traps in the bulk compared with traps at the electrode interfaces

First it is important to establish whether s-shaped I-V curves can be generated using DMC models. In literature, electrode interface effects have been identified as the source of s-shape behaviour [235, 238, 240–242, 253]. As such, initially electron traps were only introduced (with a certain density) to electron acceptor sites that were immediately neighbouring either electrode. These traps are referred to as ‘interface traps’ and we distinguish between interface traps and bulk traps (trap sites that are not in contact with either electrode). A range of energy trap depths and densities were investigated and Figure 7.8 shows J,V curves for various combinations of trap depth and density. Figure 7.8(a) shows the evolution of the J,V shape as the trap density increases from 0 m^{-3} to $2.2 \times 10^{24} \text{ m}^{-3}$ while keeping the trap depth fixed at 0.2 eV. The black curve is the J,V curve corresponding to a device without any traps and it performs best

in terms of J_{SC} , V_{OC} , FF and consequently also PCE. It can be seen that interface traps indeed give rise to s-shaped curves. Arrows indicate how the J,V curves changes with increasing trap density and indicates that the severity of the s-shape anomaly becomes worse as the trap density increases. Likewise, the arrows in Figure 7.8(b) indicate the J,V curve evolution when the trap depth is increased and the trap density is fixed at $6.1 \times 10^{23} \text{ m}^{-3}$. Increasing the trap depth also increases the severity of the s-shape anomaly. However, there is only a minor difference between the J,V curves corresponding to a trap depth of 0.4 eV and 1 eV, which indicates that electrons are already efficiently trapped at the trapping sites for a trap depth of 0.4 eV. This saturation effect was also seen in the evolution of η_{ext} with trap depth (see Figures 7.5 and 7.6). Trap depths greater than 1 eV in absolute value were not investigated. However, Marcus theory predicts that when the trap depth is much larger in absolute value than the reorganisation energy, i.e. $\Delta G < -\lambda$, charge carriers will not be trapped as hopping to these deep traps will occur in the Marcus inverted region. While FF is affected the most by electron traps, a decrease in J_{SC} and V_{OC} is also seen, which agrees with experimental observations as shown in Figure 7.1.

Having thus established with DMC modelling that interface traps give rise to s-shaped I-V behaviour, we investigate the influence that bulk electron traps have on the J,V shape. Bulk traps were randomly created in the energy landscape, but in order to avoid interface traps, electron traps were not added to sites that were within 10 nm of either electrode. Since the chosen photoactive layer thickness was 100 nm, traps were only added to sites with a z-coordinate (spatial direction perpendicular to the electrode interface) larger than 10 nm or smaller than 91 nm. Various trap densities and depths were investigated and the results are shown in Figure 7.9. Again, the black curves correspond to I-V behaviour of a device without traps, but with all other simulation parameters being the same. In Figure 7.9(a) the trap depth was fixed at 0.2 eV and the trap density was varied. The average amount of charge carriers in steady state conditions increases with trap density. As the number charge carriers in the devices increases the computational load increases as well. For very large trap densities the

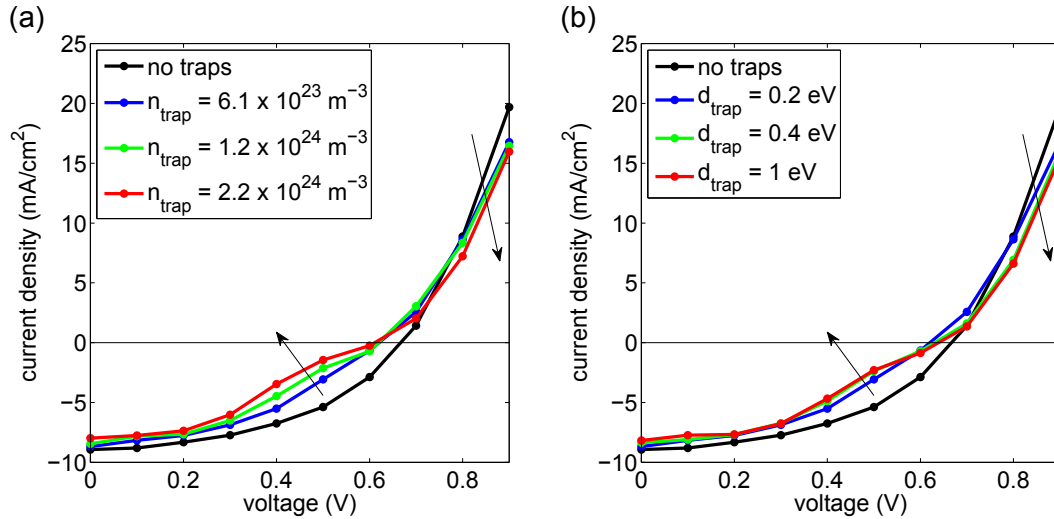


FIGURE 7.8: (a) current density as a function of voltage for various trap densities while the trap depth was fixed at 0.2 eV. (b) shows J,V curves for various trap depths, while keeping the trap density fixed at $6.1 \times 10^{23} \text{ m}^{-3}$. Arrows indicate the trend of the J,V curves when increasing trap density (a) or trap depth (b). In both (a) and (b) the J,V characteristics of a virtual device without electron traps is shown in black. All virtual BHJ devices had an electron donor electrode coverage of 50 % and active layer thickness of 100 nm. All other simulation parameters were also the same for these simulations.

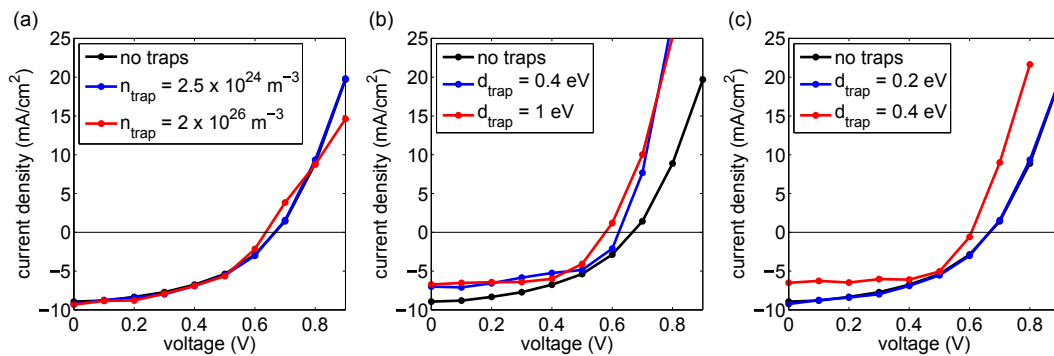


FIGURE 7.9: (a) current density as a function of voltage for various trap densities. The trap depth was fixed at 0.2 eV. (b) shows J,V curves for trap depths of 0.4 and 1 eV while keeping the trap density fixed at $6.25 \times 10^{23} \text{ m}^{-3}$. (c) shows J,V curves for trap depths of 0.2 and 0.4 eV while keeping the trap density fixed at $2.5 \times 10^{24} \text{ m}^{-3}$. In both (a), (b) and (c) the J,V characteristics of a virtual device without electron traps is shown in black. All virtual BHJ devices had an electron donor electrode coverage of 50 % and active layer thickness of 100 nm. All other simulation parameters were also the same for these simulations.

computational load reaches an impractical level and consequently trap densities were explored up to a certain limit. For a trap depth of 0.2 eV, J,V curves were obtained up to a trap density of $2 \times 10^{26} \text{ m}^{-3}$, which is two orders of magnitude larger than trap densities reported in literature for PCBM:P3HT devices [192, 246], and no s-shaped I-V behaviour was seen. In fact, the J,V curve with a density corresponding to previous reports could not be distinguished from the J,V characteristics of a device without traps. Even for a trap density of $2 \times 10^{26} \text{ m}^{-3}$, only a slight change around V_{OC} was observed. On the other hand, for devices with interface traps, that had the same depth of 0.2 eV, severely s-shaped I-V curves could be obtained with trap densities corresponding to those reported literature (see Figure 7.8(a)). Hence, DMC modelling suggests that for realistic trap densities, no s-shape I-V behaviour can be induced by bulk traps.

The trap depth was also varied, while keeping the trap density fixed at either $6.25 \times 10^{23} \text{ m}^{-3}$ (Figure 7.9(b)) or $2.5 \times 10^{24} \text{ m}^{-3}$ (Figure 7.9(c)). For deep traps (0.4 and 1 eV) a reduction in J_{SC} and V_{OC} is observed, but FF is hardly affected. Thus, while bulk traps do not induce s-shapes, they certainly lower PCE and should be avoided.

7.3.3 Injected charge carriers vs photo-generated charge carriers

The total I-V characteristic describes the current flow in a device. These moving charge carriers are either photo-generated or injected. I-V curves measured in the dark (no photo-generated charges) never exhibit s-shaped I-V behaviour and thus the cause of the s-shape is related to photo-generated charges and not injected charges. The ratio of photo-generated and injected charges can be directly manipulated by controlling the light intensity. Consequently, for a device that exhibits s-shaped I-V behaviour, the severity of the inflection at V_{OC} is expected to change with light intensity as well. Figure 7.10 I-V curves of the same architecture III device measured at various light intensities. The current was normalised for J_{SC} . The severity of the anomalous behaviour at V_{OC}

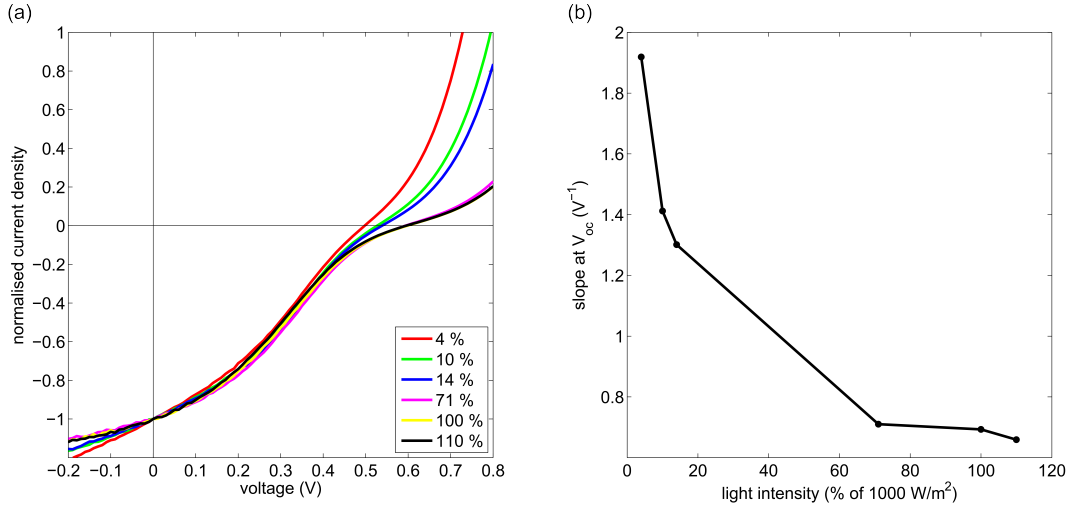


FIGURE 7.10: (a) normalised measured (not modelled) current as a function of voltage for various light intensities (indicated in legend as a percentage of 1000 W/m^2) as measured for an s-shaped device. (b) slope at V_{OC} of the normalised measured I-V curves shown in (a) as a function of light intensity.

can clearly be seen to increase with light intensity. In order to quantify how pronounced this inflection is (i.e. the severity of the s-shape), we determined the slope at V_{OC} for J_{SC} normalised I-V curves, $S_{V_{oc}}$. $S_{V_{oc}}$ should not be confused with the inverse series resistance ($1/R_{se}$). R_{se} is used in the context of an electrical equivalent circuit model, where R_{se} is distinguished from the shunt resistance. R_{se} can be approximated by calculating the inverse slope at V_{OC} , but this is only true for an I-V curve that can be fitted with the one- or two- diode model. The latter two models cannot account for a kink in the I-V curve and other electrical elements need to be added to account for this kink. These elements influence the slope at V_{OC} and thus $S_{V_{oc}}$ is not simply determined by $1/R_{se}$. The smaller $S_{V_{oc}}$ is, the more pronounced the s-shape anomaly is. $S_{V_{oc}}$ decreases with light intensity and levels off at approximately 7100 W/m^2 , which further confirms that the s-shape is caused by photo-generated charges. From a modelling point of view, it is thus important to correctly estimate the charge injection and exciton generation rates.

Similar to the real experiment, a virtual experiment was conducted where the light intensity, i.e. exciton generation rate, was varied. A virtual device was chosen with interface traps that had a density of $1.2 \times 10^{24} \text{ m}^{-3}$ and a depth of 0.2 eV. The resulting

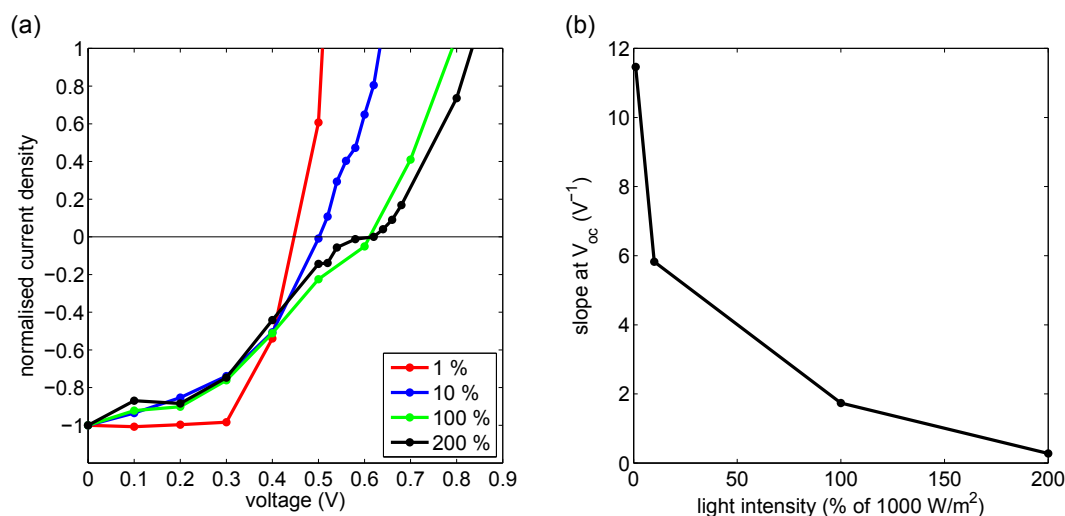


FIGURE 7.11: (a) normalised modelled current as a function of voltage for various light intensities (indicated in legend as a percentage of 1000 W/m^2) as simulated using the DMC model. Interface traps with a density of $1.2 \times 10^{24} \text{ m}^{-3}$ and a depth of 0.2 eV were used. (b) slope at V_{OC} of the normalised modelled I-V curves shown in (a) as a function of light intensity.

I-V curves are shown in Figure 7.11. V_{OC} decreases with decreasing light intensity, but FF improves, since the s-shape becomes increasingly less pronounced and is not visible for a light intensity of 10 W/m^2 . $S_{V_{oc}}$ was also determined for the simulated data. Even though there are fewer data points compared to Figure 7.10, the same $S_{V_{oc}}$ trend is observed with light intensity (Figure 7.11(b)), which provides confidence in the correctness of modelled trends.

7.3.4 Charge recombination and s-shape severity

We have seen that s-shape behaviour is readily influenced by light intensity. Depending on the morphology and material system, bimolecular recombination may also significantly be influenced by light intensity, because the light intensity determines the electron and hole density, which in turn affects bimolecular recombination [70, 144, 191]. As such, the severity of an s-shaped device is investigated with the DMC model by changing the charge recombination rate, which is the recombination rate associated with an electron-hole pair when they are adjacent to each other. In previous simulation a charge recombination rate, k_{rec} , of $1 \times 10^4 \text{ s}^{-1}$ was used. Figure 7.12 presents

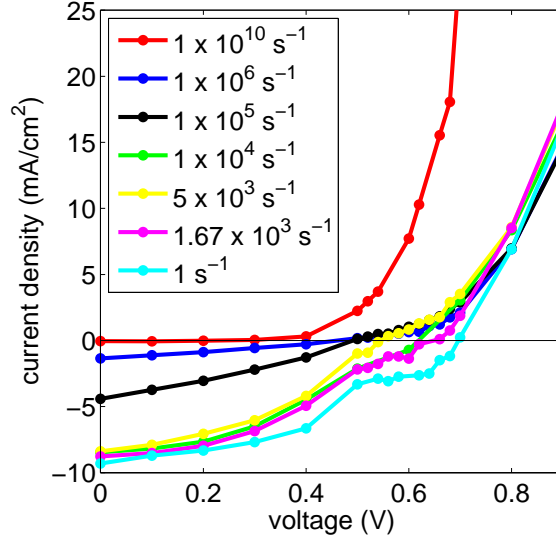


FIGURE 7.12: Series of devices where k_{crec} was changed. The legend indicates the corresponding k_{crec} values for each J,V curve.

I-V curves for a series of virtual devices where k_{crec} was varied from 1 s^{-1} to $1 \times 10^{10} \text{ s}^{-1}$. As expected, J_{SC} decreases as k_{crec} increases due to more efficient charge recombination. When $k_{crec} = 1 \times 10^{10}$ almost all photogenerated charges recombine and J_{SC} is almost 0. From the series it can be seen that the centre of the inflection (voltage, where S_{Voc} is smallest) is not constrained by V_{OC} , i.e. for the low charge recombination devices, the centre of the inflection is not located at V_{OC} . This location difference has also been observed experimentally. Figure 7.13(a) shows measured I-V curves for three P3HT:PCBM OPV devices, that are nominally the same (that is the same fabrication recipe, as outlined in chapter 3, was used). One device performed as expected (black curve), one device had an I-V curve with an inflection that coincided with V_{OC} and another that had an inflection that did not coincide with V_{OC} . To illustrate the location of the inflection with respect to V_{OC} , the derivative of the three curves are shown in Figure 7.13(b). Only derivatives of s-shaped I-V curves have a minimum and this minimum corresponds to the centre of the inflection. The V_{OC} of the blue curve approximately coincides with the centre of the inflection, but this is clearly not the case for the red curve. As such, models that assume that the centre of the s-shape coincides with V_{OC} (such as [242]) are not adequate to describe all I-V curves. Figure

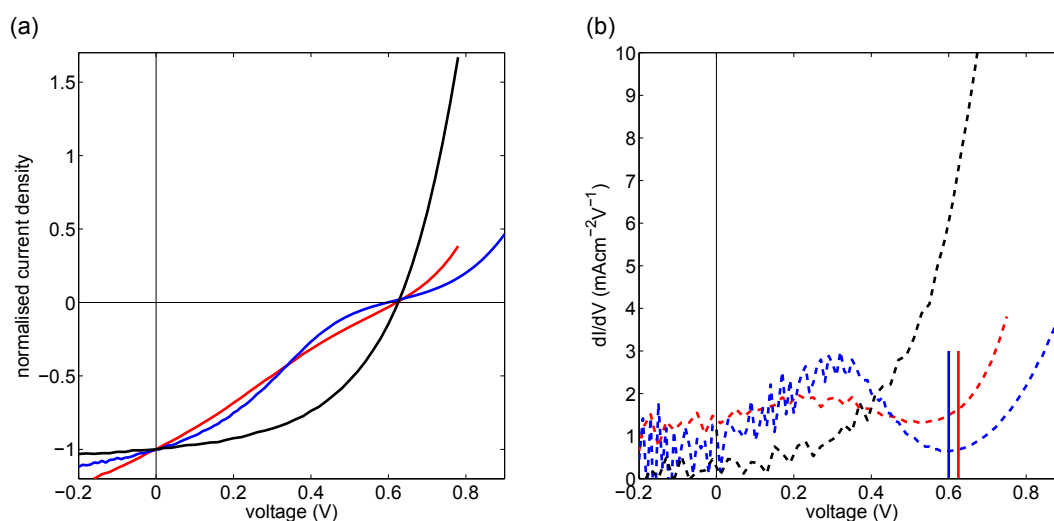


FIGURE 7.13: (a) (real) normalised current as a function of voltage for three P3HT:PCBM devices. The corresponding derivative of the J,V curves (dashed curves) are shown in (b). (b) also includes solid lines to indicate the V_{OC} of the red and blue curves. Colours are used to refer to each of the three devices, i.e. blue graph in (b) corresponds to the blue curve in (a) etc.

7.12 clearly shows that the DMC model is capable of shifting the centre of the anomaly with respect to V_{OC} . Similar to the simulated results, the experimental curve for which the centre of inflection did not coincide with V_{OC} , had a higher V_{OC} than the other s-shape curves.

V_{OC} has been shown to decrease with increased charge recombination strength [144, 145]. The DMC simulations corroborates this relationship as the V_{OC} can clearly be seen to increase with decreasing k_{rec} . The built-in field of the simulated devices would permit a maximum V_{OC} of 0.72 V and is almost achieved for the device with the lowest k_{rec} . Unlike V_{OC} , the s-shape severity seems to decrease with increasing k_{rec} . In other words, the s-shape is much more pronounced in the low recombination devices and is not or barely visible for devices that exhibit a lot of charge recombination. As is shown in section 7.3.2, in these DMC simulations s-shape behaviour is caused by trapped charge carriers. The only way to remove the kink in the I-V curves is by removing trapped charge carriers. When the recombination rate is high the recombination probability of these trapped electrons is also high. In low k_{rec} devices, trapped charge carriers do not recombine quickly and their presence disrupts the electric field

causing s-shape behaviour. This disruption may be less pronounced in a system where trapped charge carriers disappear (recombine) rapidly. DMC modelling thus indicates that while charge recombination itself reduces PCE, it does not cause s-shaped I-V behaviour. Rather, trapped charge carriers that disrupt the electric field in the device causes the anomaly. DMC modelling predicts, somewhat counter-intuitively, that a system with very little bimolecular recombination is more prone to exhibit s-shape behaviour.

In order to understand better how charge recombination influences anomalous I-V curves, we analyse the two types of charge recombination that occur in a device: interface recombination and bulk recombination. As described in chapter 6, interface recombination refers to charge carriers that are extracted at the opposite polarity electrode, while bulk recombination refers to recombination that occurs in the active layer (exciton, geminate and bimolecular recombination). Figure 7.14 shows bulk recombination efficiency η_{bulk} , interface recombination efficiency η_{int} and total charge recombination efficiency (η_{rec}) for a device with an s-shaped I-V curve and a non-anomalous I-V curve. η_{int} and η_{rec} can exceed unity, because injected charge carriers that are extracted are not distinguished from photo-generated charge carriers. η_{rec} can be seen to have the same shape as the I-V curve, i.e. they both have a kink for the s-shape exhibiting device, which the non-anomalous curve does not have. η_{bulk} , on the other hand, is not significantly different between the two virtual devices and certainly does not have a shape that resembles the s-shape for either devices. A comparison of η_{int} and η_{bulk} as a function of voltage (Figure 7.14(a) and (b)) reveals that the s-shape of the total recombination finds its origin in interface recombination. Despite the fact that injected charges, that are created at the interface, do not induce anomalous I-V behaviour and photo-generated charge carriers, that are created in the bulk, are needed to observe an inflection in the I-V curve, Figure 7.14 demonstrates the importance of controlling electrode interface processes in order to prevent s-shape I-V behaviour.

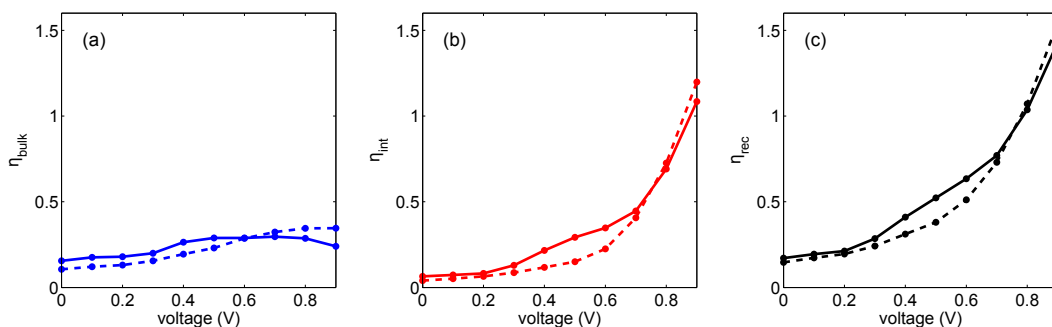


FIGURE 7.14: (a) η_{bulk} , (b) η_{int} and (c) η_{rec} as a function of voltage for a virtual device with no traps and thus no s-shape I-V behaviour (dashed lines) and a virtual device with interface traps that exhibits an s-shaped I-V curve (solid lines).

7.3.5 Isolating the effect of the compositional donor-acceptor distribution at electrodes on I-V curves

In Chapter 6 it is shown that the electrode coverage by donor and acceptor materials can certainly affect IQE and J_{SC} . Furthermore, it was shown that thermal annealing changes the P3HT:PCBM composition at the electrode interfaces. Previous reports show that the vertical phase distribution is linked to the occurrence of s-shapes. However, de Castro et al. [240] proposed that isolated aluminium clusters that effectively act as charge trapping centres are the cause of s-shape I-V behaviour. Since both the vertical phase and aluminium cluster distribution are simultaneously affected by annealing treatments, it is difficult to distinguish between the two. In the previous sections, we have shown that the DMC model predicts s-shape behaviour when charge traps are present at the electrode interface. Charge trapping sites may be induced by aluminium clusters or even be inherent to the donor-acceptor structure, since isolated islands of donor (or acceptor) material could act as charge trapping sites. Now, we explore the effect of electrode coverage only. In order to remove the effect of charge trapping clusters, morphologies were used that do not contain any isolated islands, i.e. the morphology consist of an continuous inter-penetrating network of donor and acceptor material. In figure 7.15, simulated I-V curves are presented for three virtual devices that had morphologies with the same feature size, but different compositional phase distributions at the electrodes. For device 1, 50.31 % of the cathode was in contact with

PCBM (49.69 % of the cathode was covered by P3HT) and 51.5 % of the anode was in contact with P3HT (thus 48.5 % of the anode was covered by PCBM). Device 2 had perfect capping layers at both electrodes (also referred to as p-i-n structure), i.e. 100 % of the anode is on contact with P3HT and 100 % of the cathode is covered by PCBM. Thus, device 1 has the same compositional distribution as an unannealed device (see Figure 6.9) and device two represents a device that is perfectly charge selective. Virtual devices 1 and 2 both had an active layer thickness of 100 nm, while device 3 had an active layer thickness of 85 nm. Device 3 had a PCBM-cathode contact percentage of 31.69 % and a P3HT-anode contact percentage of 25.37 %. The donor-acceptor composition at the electrodes of device 3 is such that only a relatively small fraction of the cathode/anode surface is available for electron/hole extraction. Consequently, device 3 might exhibit s-shape behaviour. However, modelling results show no signs of s-shaped I-V curves (black curve in Figure 7.15). Hence DMC modelling indicates that s-shape behaviour cannot be induced by solely 'bad' electrode coverage. It seems that the only way morphology can cause s-shape behaviour is through isolated islands of semiconductor material near the electrodes. The simulations thus agree with de Castro et al.'s aluminium nanocluster explanation for s-shape behaviour, where these nanoclusters act as charge traps. Furthermore, Wagenpfahl et al. developed a model that indicates that s-shape behaviour cannot be induced by an energy barrier (as would be expected for the donor-cathode and acceptor-anode interfaces) alone.

Even though J_{SC} peaks at approximately 85 nm (see Figure 6.6), device 3 exhibits the lowest J_{SC} out of the 3 virtual devices due to a P3HT:PCBM composition at the electrodes that is not beneficial towards charge extraction. Hence, while electrode coverage cannot induce s-shapes, it does affect J_{SC} , V_{OC} , FF and PCE. Since the thickness of device 1 and 2 are the same, they can be directly compared. The morphology of the bulk is exactly the same for device 1 and 2 and the only difference between the two devices is the existence of thin capping layers. As a result of the capping layers, J_{SC} increased by 8.6 %, V_{OC} increased by 4.8 %, FF increased by 81 % and PCE increased by 106 % compared to the corresponding values of the device without capping

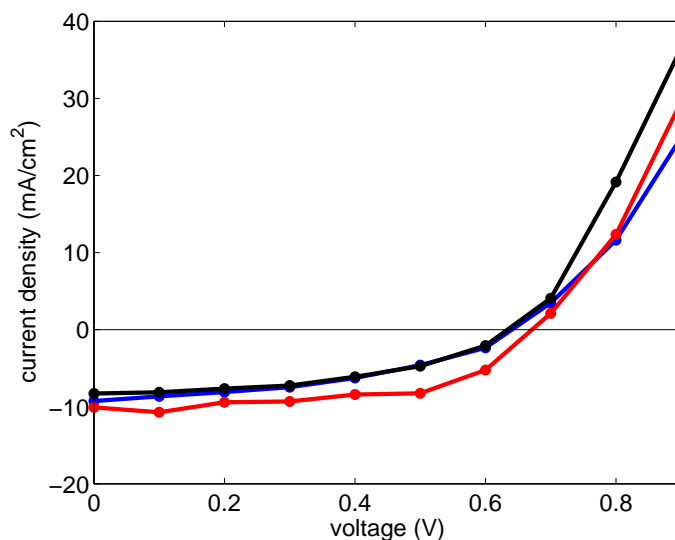


FIGURE 7.15: Simulated I-V curves for a device with (red) an active layer thickness of 100 nm and perfect blocking layers (blue) an active layer thickness of 100 nm where 50.31 % of the cathode is in contact with PCBM and 51.5 % of the anode is in contact with P3HT, and (black) an active layer thickness of 85 nm where 31.69 % of the cathode is in contact with PCBM and 25.37 % of the anode is in contact with P3HT.

layers. Thus, the DMC model predicts that thin continuous capping layers at both the electrodes considerably improves power conversion efficiency, which corresponds to the substantial performance increase experimentally seen in p-i-n structures compared to structures without capping layers [44, 85, 254, 255].

It is noteworthy, that we do not consider the thermodynamics of the annealing process and its impact on vertical composition throughout the device. Lyons et al. [133] used Cahn-Hilliard theory to show that a capping layer is often immediately neighbouring a peak composition of the other moiety (i.e. not the capping layer moiety). This subsurface layer of the 'wrong' material negatively impacts charge extraction. So while, the surface blocking layer itself is shown to improve performance, capping layers obtained through annealing procedures may inadvertently induce a subsurface layer of the non-capping layer material [133] as also indicated by depth profiling measurements [256]. A capping layer with no detrimental subsurface layers may be achieved through modification of surface energies [257], the use of interlayers [85], nanoimprint lithography [102] or phase-directing agents [258].

7.4 Conclusion

For the first time, DMC modelling has been used to investigate the nature of s-shape anomalies in I-V curves. First, the effect of energy traps on exciton transport was investigated. It was found that the exciton diffusion length and consequently η_{exint} decrease with increasing trap depth and density. At a certain energy depth excitons are stuck for their entire lifetime and deeper traps do not affect η_{exint} any further. Energy traps were added to the energy landscape with a fixed depth since the distribution of energy trap depths is unknown. Such an approach is shown to give realistic η_{exint} trends when realistic trap densities as reported in literature ($10^{22} - 10^{24} \text{ m}^{-3}$) are used. Since excitons are charge neutral, they are not affected by an external voltage as applied in an I-V measurement (0.2-1 V regime). Consequently, trap induced exciton transport effects cannot produce s-shape I-V curves.

In order to simulate I-V curves, thermionic injection was included in the simulations and s-shaped I-V curves be readily produced when sufficient energy traps are present near the active layer-electrode interface. The s-shape becomes more pronounced with increasing trap density and depth. The ability to reproduce inefficient devices (in addition to good devices, as seen in Chapter 6) further highlights the all-around capability of DMC models to describe OPV devices.

Electron traps in the bulk negatively affects J_{SC} , V_{OC} and consequently PCE, but hardly affects FF and was not found to induce s-shaped I-V behaviour (unlike interface traps). As such, the electrode-active layer interface was identified as being crucial in preventing s-shape effects. Interestingly, charge carriers that are injected at the electrode-active layer interface cannot induce an s-shaped I-V curve. Instead, photo-generated charge carriers that are created in the bulk are necessary to observe the s-shape. As such, the s-shape becomes more pronounced with increasing light intensity as shown by both simulated and experimental data. While it is known that charge recombination increases with light intensity, the DMC simulations indicate that charge recombination alone does not cause s-shaped I-V characteristics. In fact, the s-shape becomes less pronounced with increasing bulk charge recombination, which suggests

that efficient OPV materials systems that exhibit little charge recombination are more sensitive to electrode-active layer interface effects that induce anomalous I-V behaviour. By tuning bulk charge recombination, the centre of the inflection (s-shape) could be changed with respects to V_{OC} . While in most cases the inflection centre approximately coincides with V_{OC} , experimental and simulated evidence shows that this is not always the case. The DMC model allows us to distinguish between bulk recombination and interface recombination. Interface recombination is shown to induce s-shape I-V curves, again highlighting the importance of the electrode interface.

Annealing procedures influence several film properties including vertical phase segregation and clustering of isolated aluminium domains (that are created upon physical deposition of the aluminium cathode). These latter two effects have been proposed to induce s-shaped I-V characteristics. It is difficult to distinguish between the two effects, because they both occur at the same time, i.e. during annealing treatments. DMC modelling allows us to investigate these two effects separately. Electron traps, that could be formed by isolated aluminium clusters, can certainly induce s-shapes. Morphologies with no charge traps, but with different vertical phase compositions were investigated. While phase composition at the electrodes (electrode coverage) affects J_{SC} , V_{OC} , FF and PCE and is thus important to control, electrode coverage is not observed to induce s-shaped I-V curves. The only way that morphology can induce s-shaped I-V behaviour is when isolated islands of donor or acceptor material are present near the electrodes. Thus DMC modelling supports the idea that s-shaped I-V behaviour is induced by aluminium nanoclusters as opposed to phase composition at electrodes.

8

Assessing nanoparticle morphologies

8.1 Introduction

One of the major advantages of a DMC approach is the ability to analyse morphological effects. Indeed, a variety of morphologies such as BHJ, interdigitated, columnar, bilayer and gyroid structures have been investigated using DMC models [70, 101, 177, 195].

Aqueous nanoparticle morphologies offer inherent advantages of direct control of domain size while eliminating the need for organic solvents. [103–105, 259]. Scanning transmission X-ray microscopy (STXM) compositional analysis of F8BT:PFB nanoparticles revealed that they can form a so-called core-shell structure, where the core predominantly consists of F8BT and the shell of PFB. Such a structure is different to the standard successful BHJ structure. As discussed in Chapter 2, morphology can have a profound impact on device performance. In the case of a core-shell structure,

very poor charge extraction is expected. In fact, if the core consists of pure PCBM and the shell of pure P3HT, electrons would not be able to get out of the device. However, P3HT:PCBM nanoparticle device are found to work [260]. This is partly explained by STXM measurements, that indicate that the shell of these structures is not pure, but is P3HT rich [260]. However even with a donor rich shell, charge extraction is expected to be severely limited. In this chapter, the DMC model is utilised to investigate the performance of core-shell nanoparticle structures. In order to do this, a realistic virtual 3D structure must be created. STXM measurements are used to help construct a 3D structure that approximates the structure as found in a real device. The virtual 3D structures are then used as an input in the DMC simulations and the modelled performance of core-shell structures is compared to that of BHJ structures. Finally modelled results are compared to measured results.

8.2 Experimental and modelling aspects

8.2.1 Device fabrication and characterisation

P3HT:PCBM nanoparticle devices were fabricated by Syahrul Ulum and Natalie Holmes. For an extensive description of the fabrication procedure, the reader is referred to the PhD thesis of Dr Andrew Stapleton [106]. In short, P3HT and PCBM were dissolved in an organic solvent and introduced to an aqueous SDS solution. The solution is stirred to form a macroemulsion and then sonicated to form a miniemulsion, as depicted in Figure 8.1. A heating treatment removes the organic solvent and a centrifuge is used to remove excess surfactant from the suspension. The resulting suspension in water forms the active solution and can be spin coated onto a substrate. All subsequent steps of the fabrication process are the same as for a BHJ device and is described in Chapter 3. The architecture III lateral design (see section 3.1) was used in the fabrication of the devices presented in this chapter. Nanoparticle size could be varied by changing the SDS concentration. The size of the nanoparticles in the miniemulsion were measured using dynamic light scattering (DLS). In the chapter the term nanoparticle size is used

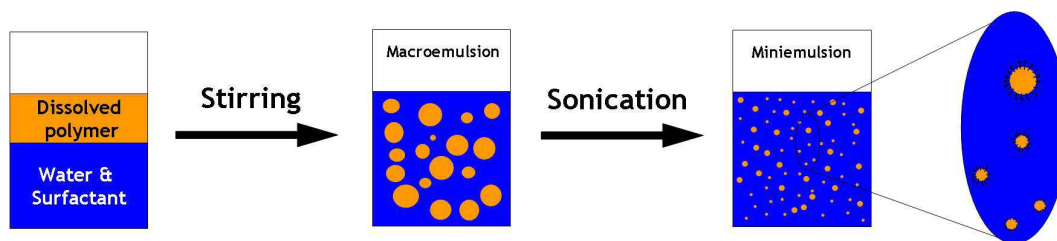


FIGURE 8.1: Schematic of the miniemulsion fabrication procedure. This diagram is reproduced from Dr Andrew Stapleton’s thesis [106].

to refer to the diameter of the nanoparticle, which encompasses both the core and shell. DLS measurements were conducted by Syahrul Ulum. STXM measurements were conducted by Kerry Burke and Natalie Holmes at the Advanced Light Source on beamline 5.3.2 [261]. The reader is referred to Kerry Burke’s thesis for more information on the STXM measuring and post-processing procedure [107]. The molecular weight of the P3HT that was used for the fabrication of nanoparticles OPV devices was 17932 Dalton and the P3HT that was used for STXM analysis was 14000 Dalton.

8.2.2 Simulation parameters

DMC simulations were run with parameters as presented in Table 8.1. These parameters largely correspond to P3HT:PCBM BHJ devices, in order to ensure that reasonable parameters are used. However, parameters were not fitted against any particular material system or device. In this chapter, we simply describe our general analysis of core-shell structures and do not attempt to quantitatively simulate a particular photovoltaic device. Modelled trends are used to describe experimentally measured behaviour of P3HT:PCBM nanoparticle devices.

8.3 Results and discussion

8.3.1 STXM imaging

While STXM is a very powerful technique, its theoretical resolution is limited to approximately 25 nm [104]. Optimised P3HT:PCBM nanoparticle devices have domain

TABLE 8.1: DMC simulation parameters.

| Property | Value | Reference |
|--|-----------------------------------|--|
| Temperature | 300 K | |
| Relative dielectric constant | 3.1 | [147] |
| σ | 0.05 | as determined from absorption spectra |
| Exciton lifetime electron acceptor | 11 μ s | [155] |
| Exciton lifetime electron donor | 400 ps | [153] |
| Charge hopping rate constant electron acceptor | $3 \times 10^{12} \text{ s}^{-1}$ | [70, 195] |
| Charge hopping rate constant electron donor | $3 \times 10^{12} \text{ s}^{-1}$ | [70, 195] |
| Charge carrier recombination rate | $1 \times 10^4 \text{ s}^{-1}$ | |
| Reorganisation energy (λ) | 0.5 eV | [181] Section 4.7 |
| Lattice constant | 1 nm | Chapter 4 |
| PEDOT:PSS energy level | -5.1 eV | [219] |
| Aluminium work function | -4.3 eV | [219] |
| HOMO (P3HT) | -5.3 eV | [219] |
| LUMO (PCBM) | -4.3 eV | [219] |

sizes smaller than the resolution of STXM. As such, nanoparticle films were fabricated with large nanoparticle sizes, that could be resolved with STXM. Figure 8.2(a)(c)(d) shows P3HT composition mass maps of unannealed P3HT:PCBM nanoparticles that were drop cast on a silicon nitride window. Yellow indicates a high P3HT concentration and orange/red a low P3HT concentration. The black and white pattern corresponds to areas with no P3HT or PCBM and is simply background noise that should be ignored. The PCBM composition map is simply the inverse of the P3HT composition map and is not shown. The composition maps shows core-shell type structures (introduced in Section 2.3, in particular Figure 2.11 shows a schematic of a core-shell structure). In order to estimate the diameter of the cores and the width of the shells radially averaged composition profiles were determined. These profiles were obtained

for several nanoparticles by averaging across arcs that were clear of neighbouring particles to give an average composition as a function of distance from the centre of the particle, r . The rotational profiles of three nanoparticles are shown in Figure 8.2(b,d,f). The corresponding nanoparticles are shown in the left column of Figure 8.2. In each of these composition maps, the arc corresponding to the largest value of r as shown in the radial composition profiles are drawn in blue. Since STXM is a transmission technique, this composition profile represents both the rotationally and vertically averaged P3HT composition, which is why the P3HT composition increases with r until the edge of the spherical core is reached. The shell surrounding the core appears to have a constant P3HT composition and consists of 68-80 % P3HT (and thus 20-32 % PCBM). As r increases the number of data points used in calculating the average composition increases as well. The centre consists of one data point and is consequently relatively noisier. However, on average the centre of nanoparticles showed a vertically averaged composition of 52 ± 2 % P3HT. On average the cores had a diameter, d , of 260 nm and a shell width, s , of 50 nm. The diameter of these nanoparticles is about 7-9 times larger than the experimentally observed optimal nanoparticle size, which is approximately 30 nm as determined using DLS. The core-shell ratio of the larger nanoparticles ($d : s$ ratio) was 3.5-7. This ratio is of importance, because we assume that the relative dimensions of the smaller nanoparticles as used in OPV device are the same as the larger nanoparticles and is used to construct virtual 3D core-shell morphologies.

Nanoparticles are not always exactly spherical in shape, but may be elliptical. Transmission electron microscopy (TEM) imaging conducted by Natalie Holmes show that many particles better resemble ellipsoids than spheres. In these cases, a radial average that assumes particles to be spheres is less appropriate for determining the size of the core and shell. In an OPV device, a continuous nanoparticle layer is formed and the distance between neighbouring cores (i.e. shell) may be different. In order to estimate the distance between cores, linear line profiles were extracted from the STXM composition map. Lines were chosen such that they connect the centres of neighbouring cores. In this way, it does not matter if particles are ellipsoidal. However, the STXM

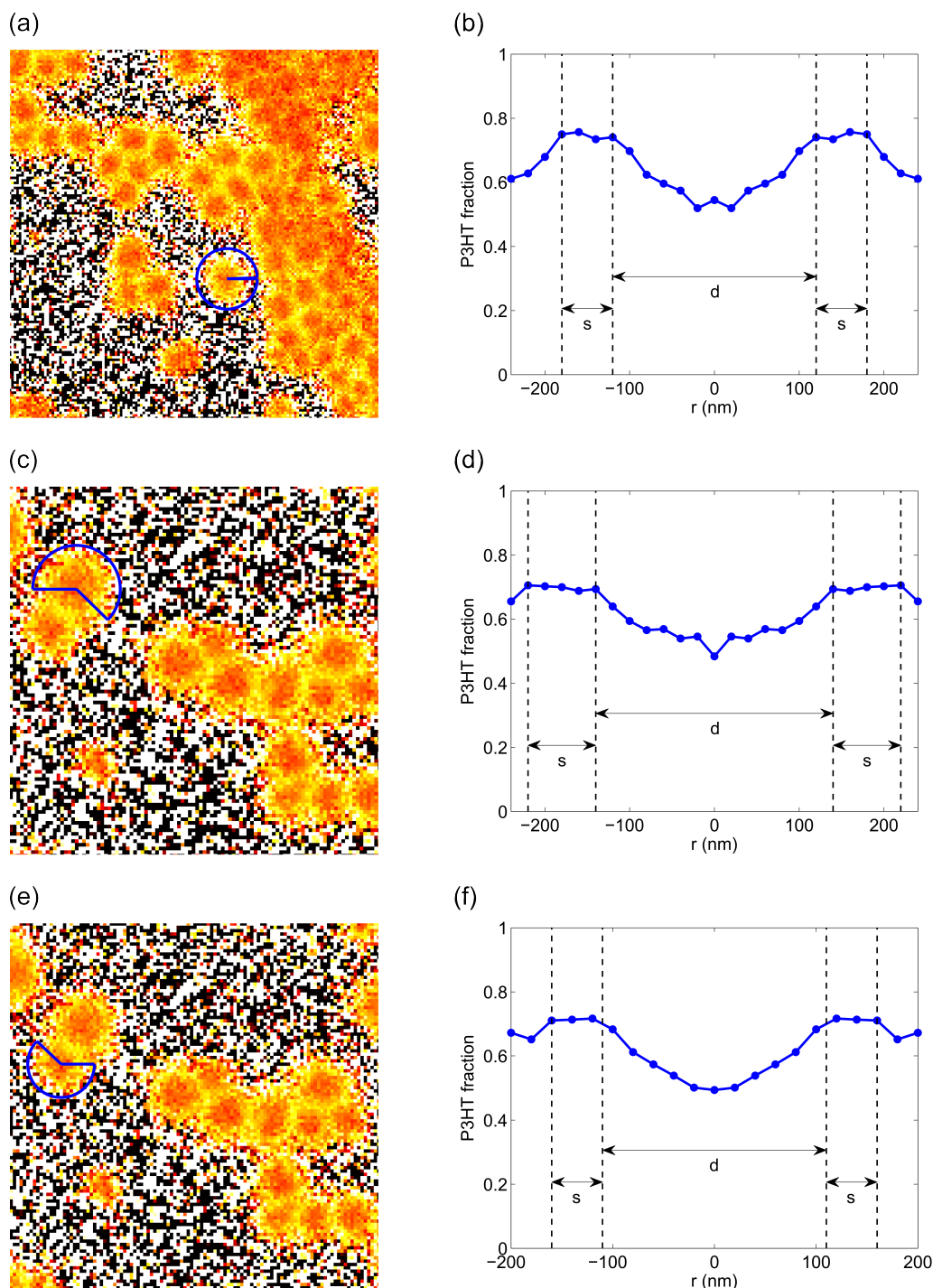


FIGURE 8.2: (a), (c) and (e) show the P3HT composition maps corresponding to the radial composition mass profiles, which are shown in (b), (d) and (f). Arcs drawn in blue indicate where rotational averages have been calculated. The arcs not only indicate the position, but also the angle of the radial average. s indicates the width of the shell and d the diameter of the core.

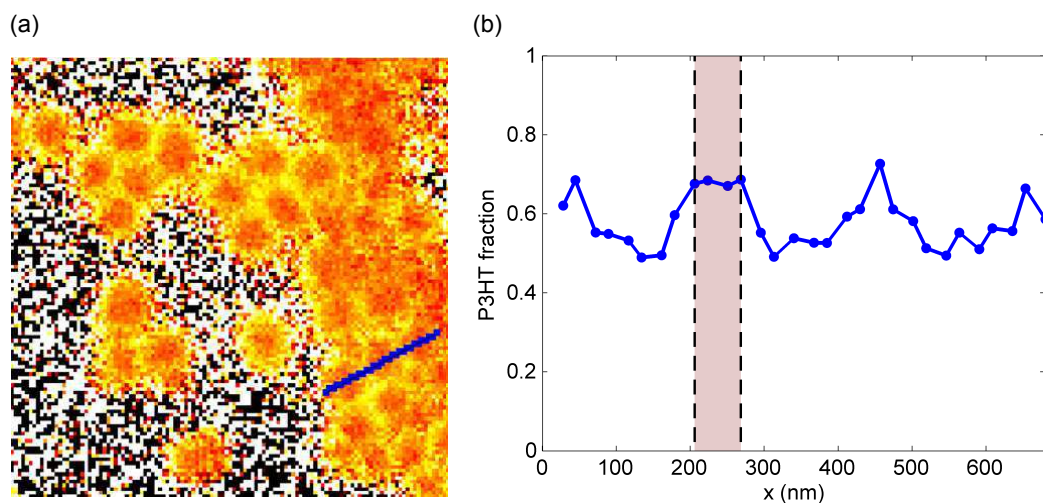


FIGURE 8.3: (a) P3HT composition map with blue line indicating the location of the line profile as shown in (b). The width of twice the shell is also indicated for the two neighbouring particles on the left of the linescan.

measurements are relatively noisy and this becomes more pronounced in line profiles, because no averaging takes place. A combination of radial average profiles and line profiles can provide sufficient information to estimate the 3D core-shell morphology. An example of a line profile is shown in Figure 8.3. The d:s ratio was seen to vary from 3.5 to 10. To within the error of the measurements, the d:s ratio of single nanoparticles and nanoparticles that are immediately surrounded by other nanoparticles are approximately the same.

8.3.2 Constructing the 3D morphology

Based on the STXM observations, a 3D morphology was created by placing a sphere of pure electron acceptor material in a random mix of donor and acceptor with a 75:25 ratio. Unlike the STXM sample, an OPV device contains a continuous film of nanoparticles. The aforementioned 'shell' then dictates the distance between neighbouring cores. In other words, the $d : s$ ratio is used to calculate the distance between cores for a known core diameter. To a first approximation, the virtual morphology was compared to experimental STXM results by determining the vertically averaged

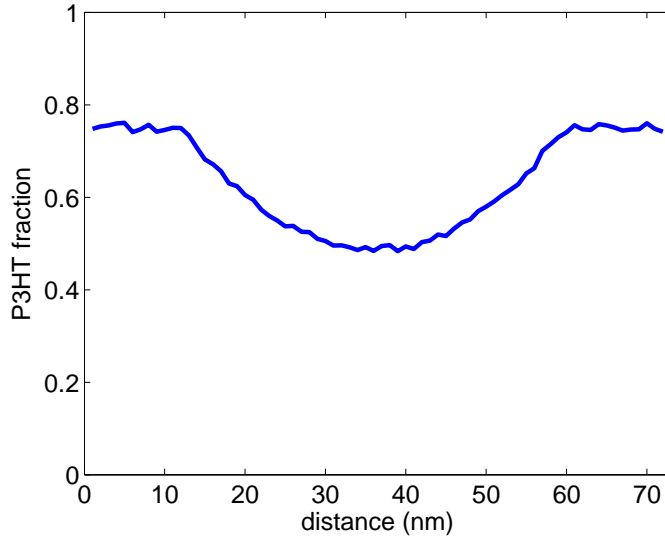


FIGURE 8.4: Vertically averaged composition profile of a virtual morphology with $d = 48$ nm and $s = 12$ nm. The shell donor concentration fraction was set to 75 %.

composition as a function of distance. Figure 8.4 shows a vertically averaged composition profile of a virtual morphology with a $d : s$ ratio of 4, where d was 48 nm. The shape matches the measured STXM profiles shown in Figure 8.2, which provides confidence in the approach taken to construct the 3D morphology. Since STXM is a transmission technique, it is difficult to decouple the true composition of the core. Here we assume 100 % core purity, which is in accordance with Burke et al.'s [104] work done on PFB:F8BT nanoparticles and Ulum et al.'s [260] work done on P3HT:PCBM nanoparticles.

As may be viewed in Dr Andrew Stapleton's thesis [106] and is also seen in the STXM composition maps shown in Figure 8.2 a film of nanoparticles contains a range of different sizes. The nanoparticle diameter exhibits a Gaussian distribution with a typical polydispersity index (PDI) of 0.1-0.3 [106], where PDI is defined as

$$PDI = \frac{\sigma^2}{\langle d \rangle} \quad (8.1)$$

The measured distribution is relatively narrow and thus for simplicity only morphologies are constructed that consist of nanoparticles of the same size (i.e. PDI=0). Figure 8.5 shows film thickness as a function of nanoparticle size. A linear fit, that was forced

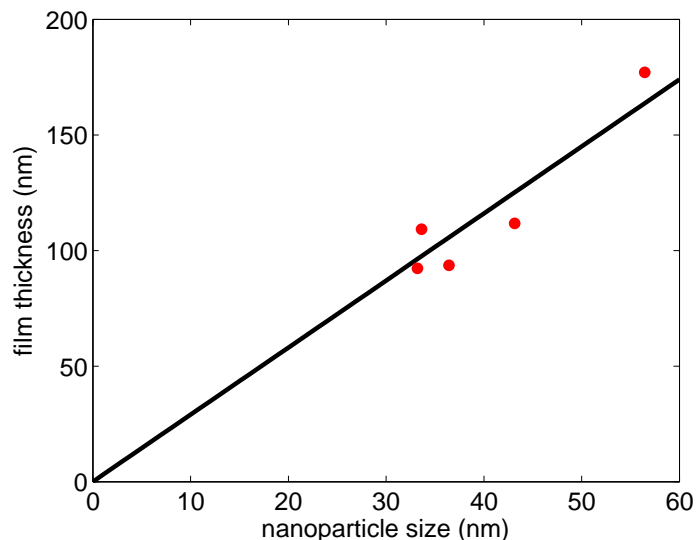


FIGURE 8.5: Film thickness (as determined from profilometry measurements) as a function of nanoparticle size (as determined using DLS). The red dots correspond to measured results and the black line is a linear fit that is forced to go through the origin.

to go through the origin, was obtained and its slope was 2.9 ± 0.14 . Hence, films as used in OPV devices are likely to consist of three layers of nanoparticles and consequently virtual morphologies were created that consist of three stacked nanoparticle layers. We assume that they stack in a primitive cubic fashion. This assumption allows for the use of smaller morphologies, which is desirable from a computational efficiency point of view.

The mixed zone surrounding the pure cores initially has a random distribution. Akin to the generation of BHJ morphologies, a modified swapping algorithm (as discussed in Section 4.3) is used to increase the feature size of the nanoparticle morphologies. Care was taken to make sure that the morphology after the swapping procedure still has a composition profile that was similar to the initial one. For very large feature sizes, the core becomes so distorted by the swapping algorithm it cannot be regarded as spherical any more. For a feature size of ~ 14.2 nm, which is the feature size used in virtual BHJ devices and the highest feature size investigated in virtual nanoparticle devices, the profile was slightly affected, as shown in Figure 8.6. The core still resembled a spherical shape, but the shell donor concentration increased. In order to quantify the

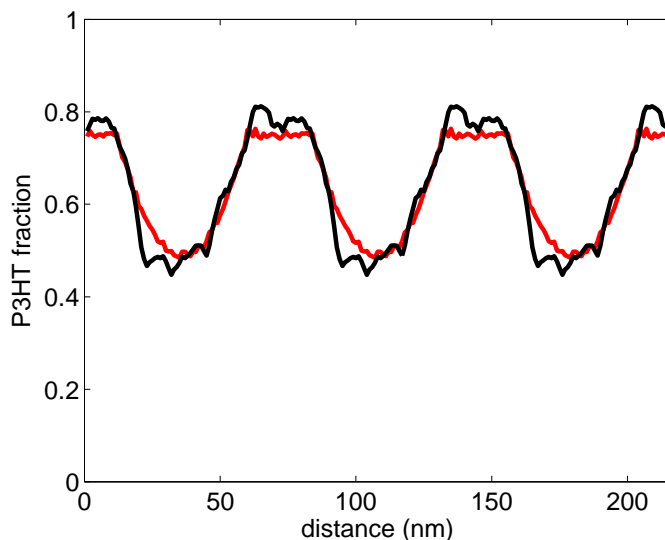


FIGURE 8.6: Vertically averaged composition profile of three nanoparticles with $d = 48$ nm and $s = 12$ nm, that are adjacent to each other. The red graph corresponds to the morphology before the swapping algorithm was executed, the feature size was 3.1149 nm. The black corresponds to a morphology after the swapping algorithm was run and had a feature size of 14.1945 nm. The average difference between the two curves was 4.38 %.

deviation from the initial composition profile (prior to the swapping algorithm), the z-averaged, y-averaged and x-averaged profiles were calculated. A spherical nanoparticle is symmetrical in these three directions and the composition profile of each are similar. The average absolute difference between the compositional profile of the morphology prior to the swapping algorithm and the compositional profile after the swapping process is determined for each of the three directions (y,x and z). The average of these three is take to give a single number that quantifies the distortion of the nanoparticle shape. The average deviation increases with feature size, but with a decreasing rate, as shown in Figure 8.7. Since in the measured STXM maps, the shell concentration was seen to vary between 68 % and 80 % P3HT, an average deviation from the initial composition profile (prior to the swapping algorithm) of ~ 6 % was considered acceptable. Considering the noise of the STXM measurements, using this measure, the composition profiles in Figure 8.6 still correspond to the STXM composition map.

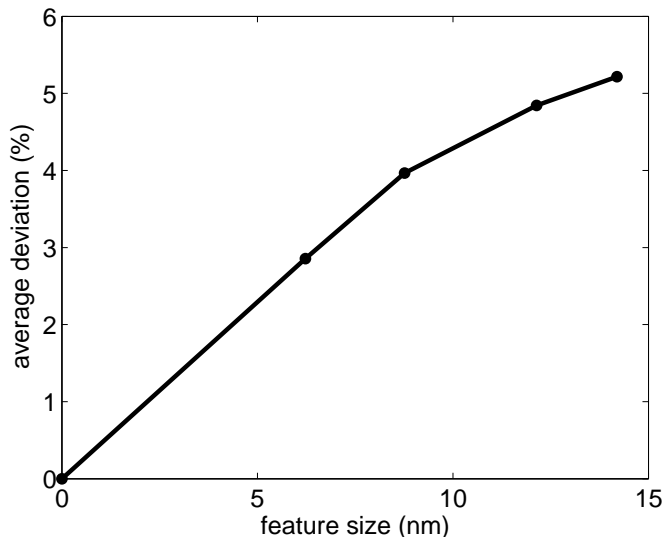


FIGURE 8.7: Average deviation (taking into account all three directions) from the composition profile prior to the swapping process as a function of feature size for a nanoparticle with $d = 48$ nm and $s = 12$ nm.

8.3.3 Photovoltaic performance and nanoparticle size

Morphologies with varying nanoparticle size and feature size were used as an input to the DMC model. First, the exciton dissociation efficiency was extracted from simulations and these results are presented in Figure 8.8. Here the Förster radii were chosen to produce exciton diffusion lengths as reported for P3HT (8.5 nm [153]) and PCBM (5 nm [170]). As expected, η_{exdis} decreases as the feature size increases for all structures. The black curve corresponds to a BHJ morphology and it clearly performs significantly better than any of the other morphologies. The other curves correspond to morphologies with different nanoparticle sizes. As expected, η_{exdis} decreases with increasing core diameter. However, the $d : s$ ratio also affects η_{exdis} . The solid lines (except the black one) correspond to core-shell structures with a $d : s$ ratio of 10. To illustrate the influence of the $d : s$ ratio, a core-shell structure with a $d : s$ ratio of 4 is also included in the figure (broken magenta line). Exciton dissociation for the latter structure is more efficient than the structure associated with the red curve, even though the core-diameter associated with the red curve is smaller (30 nm vs 32 nm). Essentially, a BHJ structure very efficiently dissociates excitons and consequently the

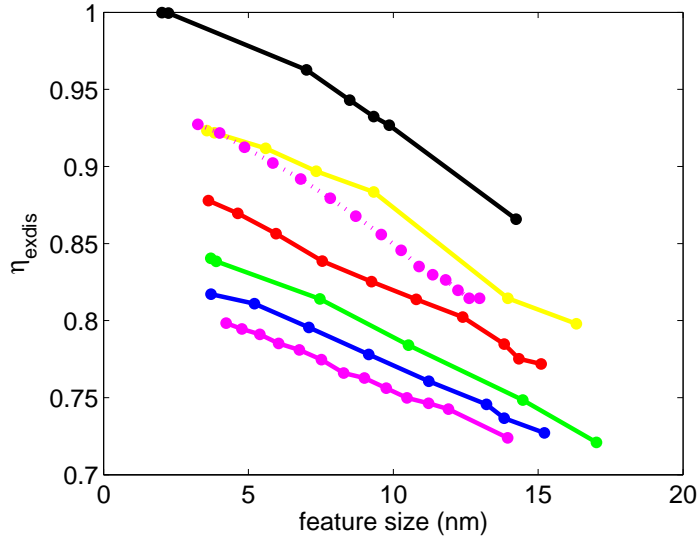


FIGURE 8.8: Exciton dissociation efficiency as a function of feature size for a (black) BHJ morphology and nanoparticle morphologies. The nanoparticle morphologies had characteristic sizes as follows (yellow) $d = 20$ nm and $s = 2$ nm, (red) $d = 30$ nm and $s = 3$ nm, (green) $d = 40$ nm and $s = 4$ nm, (blue) $d = 50$ nm and $s = 5$ nm, (magenta, solid line) $d = 60$ nm and $s = 6$ nm and (magenta, broken line) $d = 32$ nm and $s = 8$ nm.

better a nanoparticle morphology resembles a BHJ morphology (small core diameter and high $d : s$ ratio), the higher η_{exdis} is. Even though, BHJ morphologies exhibit more efficient exciton dissociation, η_{exdis} in core-shell structures are still high enough to yield efficient OPV devices.

Exciton dissociation is only part of the photoconversion mechanism and thus we also investigated how IQE and J_{SC} change with nanoparticle size. For the following simulations, Förster radii of 2.15 nm for the donor material and 3.65 nm for the acceptor were used. Since no information on the exact optical field in these nanoparticle devices was available, a uniform exciton generation profile was assumed. This simplification allows for a more straightforward comparison of the different morphologies, because interference effects are excluded. However, the downside of such an approach simulated is that J_{SC} values cannot be quantitatively compared to measured J_{SC} values. Figure 8.9 presents modelled IQE and J_{SC} as a function of nanoparticle size for nanoparticles with a $d : s$ ratio of 10. Since film thickness is simply three times the nanoparticle size, a thickness scale was added as well, which allows direct comparison with a BHJ

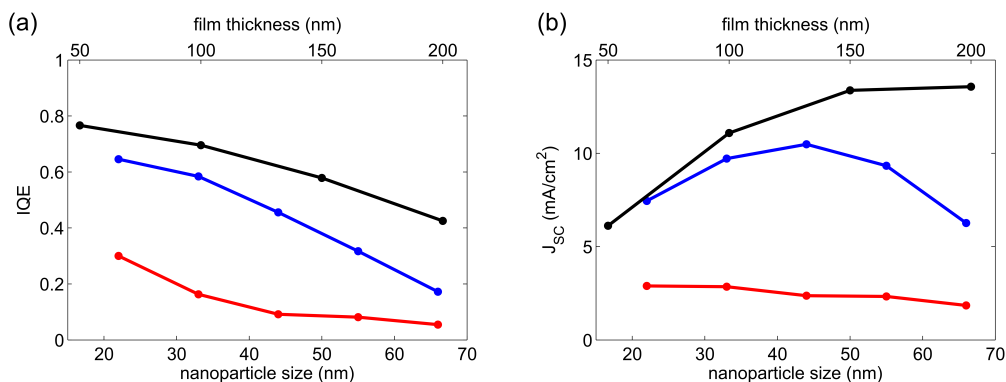


FIGURE 8.9: (a) IQE and (b) J_{SC} as a function of nanoparticle size for simulated devices. Film thickness is three times the nanoparticle size and is also shown. Black corresponds to a BHJ morphology with a feature size of 14.2 nm, blue corresponds to a nanoparticle morphology with a feature size of ~ 14.1 nm, and red corresponds to a nanoparticle morphology with a feature size of ~ 3.6 nm. Both nanoparticle morphologies had a $d : s$ ratio of 10.

morphology using the same modelling parameters. The blue curve and black curve exhibit approximately the same feature size. Nevertheless, the BHJ morphology (black curve) has a higher IQE across the entire thickness range. As film thickness increases, the number of absorbed photons (and thus generated excitons) increases, while IQE decreases. As a result, an optimum film thickness and nanoparticle size exists, which can be clearly seen to be 132 nm and 44 nm respectively for the nanoparticle morphology with a feature size of ~ 14.1 nm. In these simulations a diffusion length of 40 nm was used for excitons in the acceptor and since the largest domain (the core) consists of pure acceptor material, a J_{SC} peak shift towards smaller core diameter is likely. A nanoparticle morphology with a very small feature size was simulated as well and results in the red curve. The latter morphology performs very poorly across the entire film thickness range and continuously decreases with thickness. The feature size is influenced by annealing conditions. Thus, the simulations indicate that if the annealing conditions are not optimal, core-shell structures perform poorly. However, if annealing conditions are such that the feature size of the nanoparticle structures is the same as that of a well-performing BHJ structure, good performance can be achieved. In fact, for films < 100 nm in thickness, the J_{SC} for both nanoparticle and BHJ structures are almost the same. So, despite a donor rich shell, core-shell structures can be quite

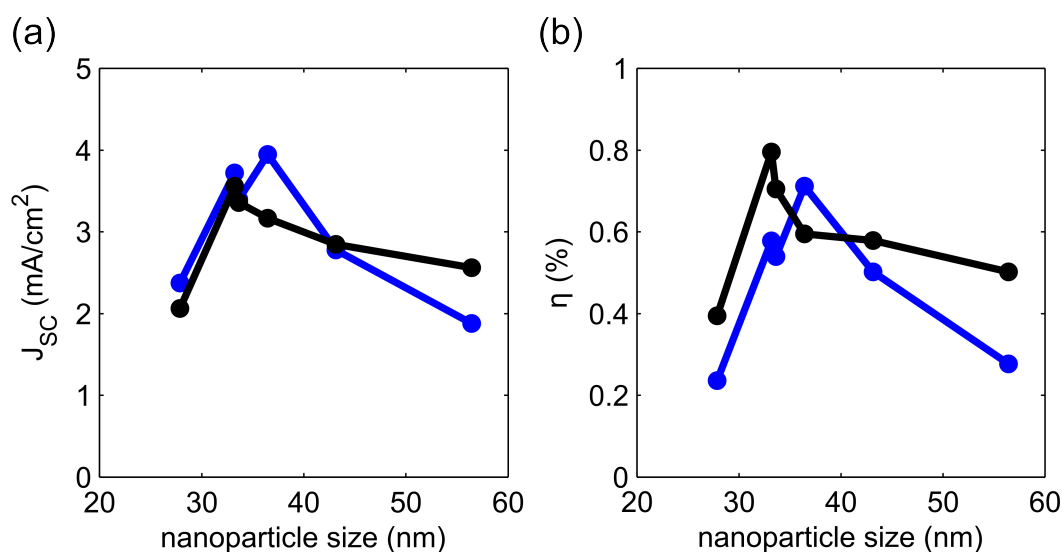


FIGURE 8.10: (a) J_{SC} and (b) PCE as a function of nanoparticle size for real P3HT:PCBM nanoparticle devices. Blue curves show the performance prior to annealing and black the performance after annealing for 4 minutes at 140 °C.

efficient.

I-V curves were (experimentally) measured for (real) devices with various nanoparticle sizes. For each nanoparticle size, 6 devices were fabricated and the average J_{SC} and PCE are shown in Figure 8.10. These devices were annealed using the standard recipe for BHJ devices (140 °C, 4 min.) and both performance prior to annealing and after annealing is shown. Similar to the simulated devices with a $d : s$ ratio of 10 an optimum nanoparticle size exists. However, Figure 8.9 shows that J_{SC} of the morphology with a feature size of 14.1 nm is almost symmetrical about the optimum, while experimental measurements show that J_{SC} initially rises rapidly with nanoparticle size before slowly decreasing on the right side of the optimum. The optimum nanoparticle size of the simulated data does not exactly match the experimental data. This discrepancy could be explained by the chosen exciton diffusion length. In the simulations an exciton diffusion length of 40 nm was assumed for the acceptor moiety. A smaller exciton diffusion length is expected to decrease the optimum nanoparticle size. Figure 8.9 shows that the feature size affects the position of the optimum as well. For the nanoparticle morphology with a feature size of 3.6 nm (red curve) the optimum was not seen and it must thus be equal to or smaller than the smallest nanoparticle size

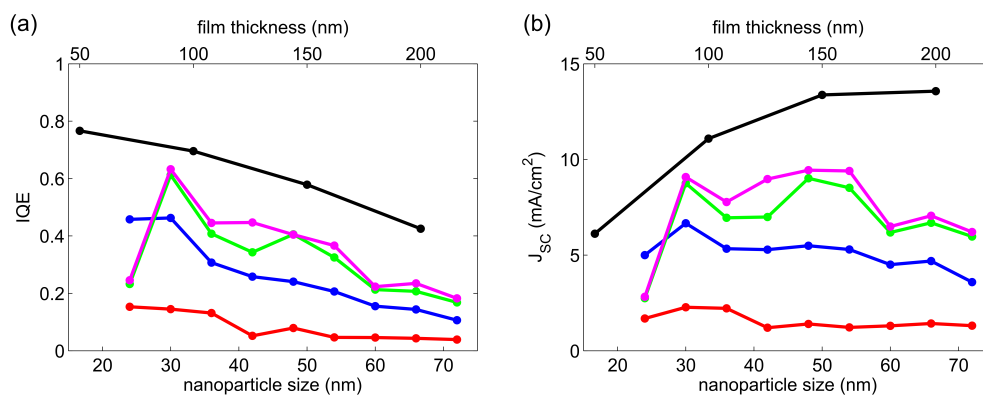


FIGURE 8.11: (a) IQE and (b) J_{SC} as a function of nanoparticle size for simulated devices. Film thickness is three times the nanoparticle size and is also shown. Black corresponds to a BHJ morphology with a feature size of 14.2 nm, the other colours correspond to nanoparticle morphologies. Red, blue, green and magenta correspond to a feature size of 3.1, 5.9, 12 and 14.1 nm respectively. All nanoparticle morphologies had a $d : s$ ratio of 4.

(22 nm) investigated. Annealing is known to affect feature size and a slight change in the optimum nanoparticle size is seen after annealing.

A series of nanoparticles morphologies with a $d : s$ ratio of 4, which better corresponds to the median $d : s$ ratio as seen in the STXM maps. These results are presented in Figure 8.11. Nanoparticle morphologies with the following feature sizes were investigated: 3.1 nm (red), 5.9 nm (blue), 12 nm (green) and 14.1 nm (magenta). Again, the BHJ morphology (black curve) performs better than the nanoparticle morphologies. The IQE of the latter morphologies peak at a nanoparticle size of 30 nm. Consequently, J_{SC} also has a maximum at 30 nm, which corresponds well with the experimental data in Figure 8.10(a). Interestingly, for a feature size of 12 and 14.1 nm, the nanoparticle morphologies approach the performance of the BHJ structure quite closely when optimised for feature size and nanoparticle size. The J_{SC} evolution of the nanoparticle morphologies with the two smallest feature sizes matches the experimental data reasonably well. This observation suggests that the real nanoparticle device has a small feature size. The DMC simulations indicate that a larger feature size results in improved IQE and J_{SC} . Indeed annealing improved peak PCE (Figure 8.10(b)). However, the shape of the curve still resembled the low feature size simulated curves. Hence, it is likely that the feature size of the real device is still relatively small

and improvements may be achieved by changing the annealing conditions as to induce a larger feature size. A larger feature size may be achieved by annealing for a longer period of time (> 4 min.). Indeed, Stapleton [106] found that PCE and J_{SC} of real P3HT:PCBM nanoparticle devices could be increased by increasing the annealing time, as suggested by the simulations. The virtual devices with a larger feature size (12 and 14.1 nm) have a second maximum at ~ 50 nm, which indicates that real nanoparticle devices must be re-optimised for nanoparticle size when changing annealing conditions.

8.4 Conclusion

For the first time, nanoparticle core-shell morphologies have been assessed using DMC modelling. As a first approximation, STXM composition maps were used to estimate and construct 3D core-shell structures. The $d : s$ ratio was extracted from STXM measurements and was assumed to remain the same for nanoparticle sizes as used in organic solar cells. In order to assess the impact of morphology alone, the same uniformly distributed optical field was assumed for all virtual devices. Nanoparticle morphologies systematically performed better as the feature size increases up to the maximum feature size that was investigated (~ 14.1 nm). Since the experimentally measured data has a similar evolution (with nanoparticle size) as the simulated morphologies with a small feature size, it is likely that significant improvements could be achieved by annealing for a longer period of time or at a higher temperature in order to induce a larger feature size. Stapleton's [106] results show that unlike the BHJ morphology, P3HT:PCBM nanoparticle device performance could indeed be systematically improved by increasing the annealing time. Unlike the core-shell morphologies with a feature size < 6 nm, J_{SC} as a function of nanoparticle size exhibited a second maximum for morphologies with a larger feature size (12 and 14.1 nm). Hence, real devices should be re-optimised for nanoparticle size when changing annealing conditions. While the BHJ morphology had a higher η_{exdis} , IQE and J_{SC} in all instances, the performance of the core-shell structure approaches that of a BHJ structure, when optimised for both feature size and nanoparticle size. Hence, the core-shell morphology need not be

severely limited by a donor-rich shell and, in theory, optimised nanoparticle devices should yield similar efficiencies as optimised BHJ devices.

9

Mapping photocurrent

9.1 Introduction

In previous chapters, the focus has been on understanding device physics on a nano-scale. The DMC model described in this thesis considers all the major processes in a perfectly fabricated photoactive layer. However, imperfect fabrication techniques or degradation give rise to lateral non-uniformities. In order to assess these non-uniformities a spatially resolved photocurrent mapping technique was developed. Spatially resolved methods for the study of photovoltaics are not new. Techniques such as conductive atomic force microscopy [262, 263] and near-field scanning optical microscopy [264] allow mapping of various performance parameters across a solar cell with very high resolution. These methods are valuable for investigating micron sized areas of the cell surface, but are less effective for tracking effects that occur over greater

length scales. Imaging techniques such as lock-in thermography [265], photo- and electroluminescence [266] and light beam induced current (LBIC) [267] are more suitable for analysing larger areas. Lock-in thermography, photo- and electroluminescence assess parts of the photo-conversion mechanism. However, we are interested in analysing non-uniformities that affect the end product of a photovoltaic device: current and voltage. As such, LBIC, which allows us to spatially map the generated current, is most suitable for our purposes. LBIC is a well known low resolution technique for observing variations in performance across larger areas of a solar cell [268] and was first introduced in the late 1970s [269]. The LBIC method works by scanning a light beam over the surface of a photovoltaic device and recording the resulting current. LBIC has been used to identify spatial features in OPV devices that vary depending on the device preparation process [270]. Krebs et al. [271] used LBIC to investigate printed metal electrodes, while Galagan et al. [272] looked at the impact of current collecting grids. Shunts may also be located with LBIC [273]. We are interested in analysing OPV with an active area on the order of mm^2 to a couple of cm^2 with a resolution on the order of μm . Many LBIC systems do not provide this level of resolution across the desired area. Hence, a custom-made system was developed at CSIRO, that does allow for high-resolution photocurrent mapping. In literature, LBIC systems are also referred to as scanning microscope for semiconductor characterisation (SMSC) [270] or laser beam induced current system [268]. While not listed as a PhD supervisor, Dr Tim Nagle acted as a supervisor in the development of the LBIC system. As such, he helped design the system and conducted some of the measurements. Measurements conducted by Dr Tim Nagle are clearly acknowledged. In this chapter, the photocurrent mapping technique is described and is followed by a description of applications of the technique to OPV devices.

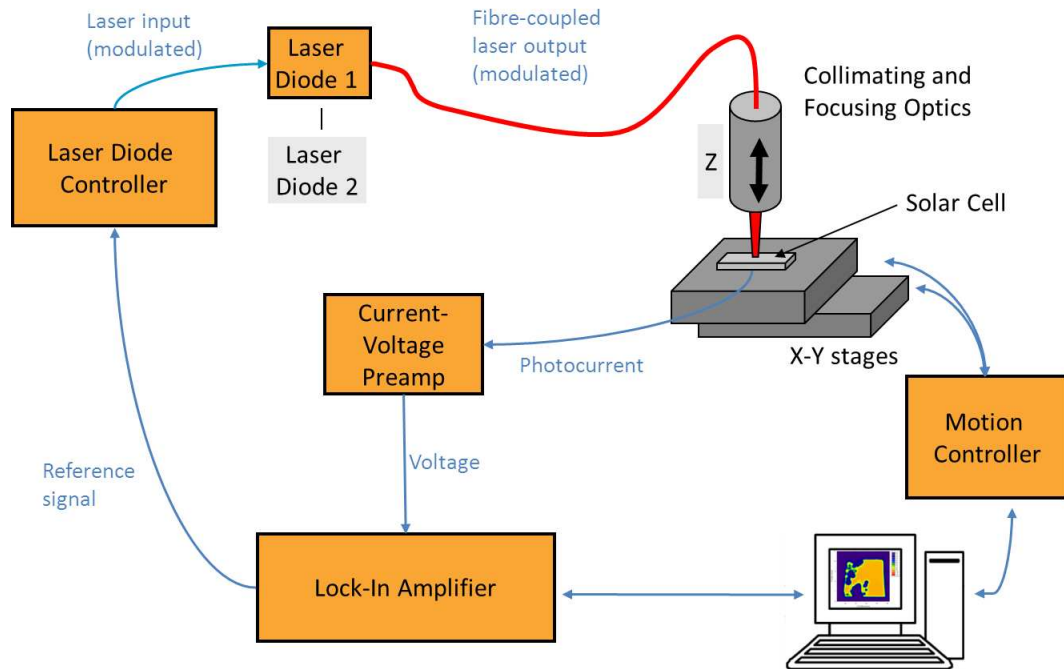


FIGURE 9.1: Schematic diagram of the photocurrent mapping apparatus

9.2 Experimental aspects

9.2.1 Light beam induced current setup

A schematic diagram of the photocurrent mapping apparatus is shown in Figure 9.1. A laser diode (635 nm or 405 nm, Thorlabs) is electronically modulated and the output is pigtailed into a single-mode fibre. The modulation frequency should not be higher than the frequency response of OPV devices, but still high enough to enable fast mapping speeds. As such, a modulation frequency of 191 Hz was chosen. The other end of the single-mode fibre is aligned with a collimating lens and a focusing lens inside a lens tube. The lens tube is attached to a manual precision translation stage (Thorlabs, PTA1/M) and may be moved along the axis of the beam to change the position of the focal plane. In this way, the spot size can be easily changed. The solar cell is mounted on a set of two orthogonal computer-controlled translation stages (Thorlabs, DRV414 DC motors with BDC102 controller) and produces a modulated photocurrent induced by the laser beam. This current is amplified by a current-to-voltage preamplifier (Stanford

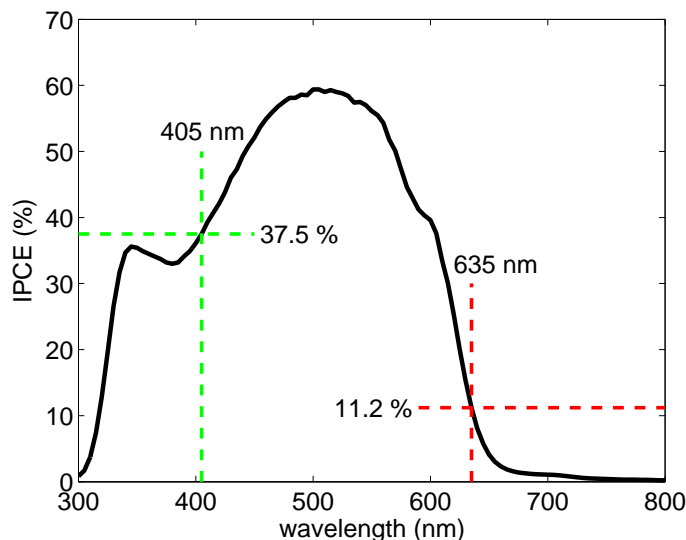


FIGURE 9.2: EQE spectrum of a P3HT:PCBM device. Performance at the wavelength of the two laser diodes used in this project are also shown.

Research, SR570) and detected with a lock-in amplifier (Stanford Research, SR830). The current-voltage preamplifier allows for measuring a wide range of photovoltaic cells, from very efficient solar cells (e.g. monocrystalline silicon reference cells) to devices with poor power conversion efficiency (e.g. a degraded OPV device). Two laser diodes with different wavelengths were used in this project: 405 nm and 635 nm. Performance of a standard ITO/PEDOT:PSS/P3HT:PCBM/Al device is shown in Figure 9.2.

9.2.2 Beam profiling

The beam radius, r , has been determined by taking one dimensional scans across a well defined edge of a solar cell for a range of spot sizes. A razor blade was used to provide the edge and optical imaging showed that the edge was straight. Figure 9.3 shows a typical line scan and its derivative when the spot crosses the edge. As the beam moves from the left, where there is no photo-active material, to the right, the photocurrent increases from non-existent to its maximum. Since the light source is a laser diode and single mode fibre optics are used, a Gaussian beam profile is expected. Good agreement of the Gaussian fit with the first derivative of the line scan also confirms that the light

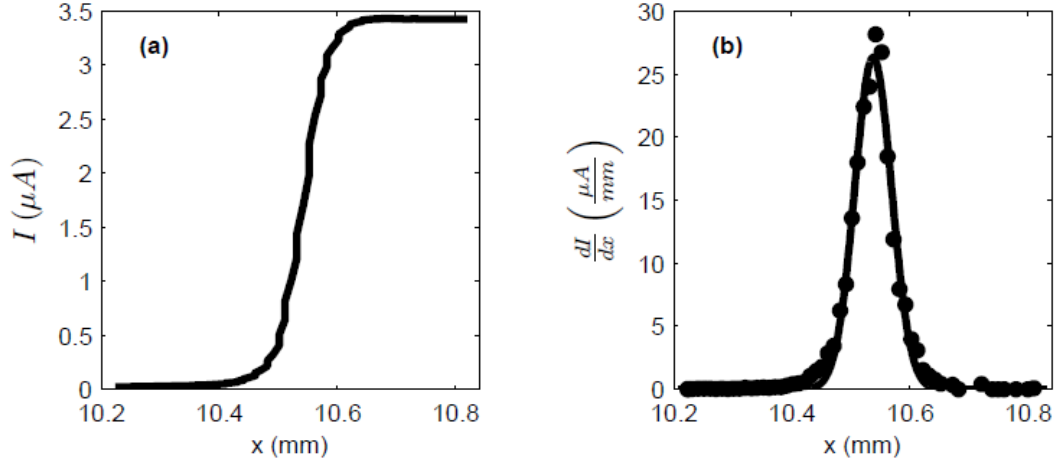


FIGURE 9.3: (a) photocurrent linescan starting at a photo inactive area and moving into a photo active area and (b) its derivative with Gaussian fit

beam has a Gaussian profile. Twice the standard deviation of the fitted Gaussian is taken to be the radius of the beam, i.e. approximately 95 % of the irradiance is captured by this definition of the beam radius. In this way, r was determined as a function of the lens position, z (see Figure 9.1), relative to the position associated with the smallest spot size, and is shown in Figure 9.4. For a Gaussian beam propagating in free space, r is given by

$$r(z) = r_0 \sqrt{1 + \left(\frac{z\lambda}{\pi r_0^2} \right)^2} \quad (9.1)$$

where z is the position along the beam (lens position) and r_0 the minimum beam radius. A good fit is found for the 635 nm laser diode when $r_0 = 3.3 \mu\text{m}$. Since photocurrent is generated in the active layer of the device, r_0 is the spot radius inside the device and not at the surface of the glass substrate, which covers the photoactive layers. Thus, the fit reveals that the smallest achievable spot radius in this system (including the pathway through the glass and transparent anode into the active layer) is $3.3 \mu\text{m}$. Since the precision and accuracy of the translation stages are better than $1 \mu\text{m}$, the resolution of a photocurrent map is defined by the spot size.

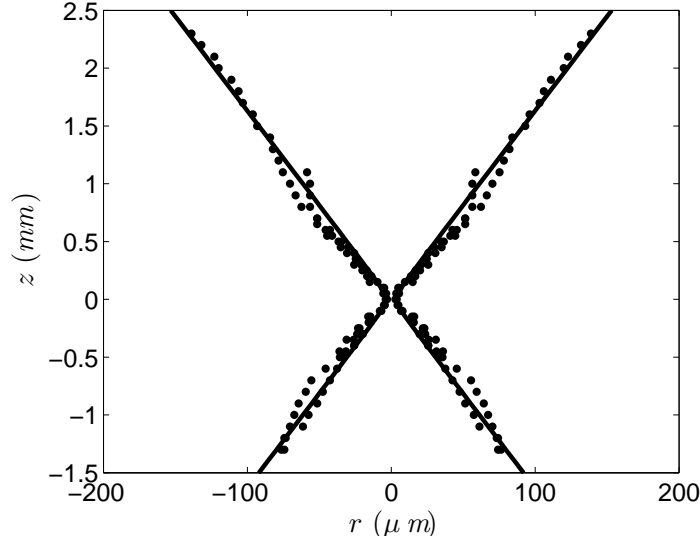


FIGURE 9.4: Beam radius, r , as a function of z -position relative the position associated with the smallest beam radius. Both the measured values (dots) and a fit to equation (9.1) (solid line) are shown

9.2.3 Intensity considerations

It is well known that OPV efficiency drops at high intensities due to increased bimolecular recombination [70], space charge issues [191], exciton-charge annihilation and possibly non-geminate exciton-exciton recombination [158]. This effect becomes apparent when decreasing the spot size (while keeping the power output of the laser diode constant). The measurements presented in Figure 9.5 were conducted by Tim Nagle and shows how the photocurrent decreases as r decreases. The missing photocurrent is lost due to increased recombination, which is caused by a large increase in irradiance. For the laser diode power levels used in this project, no significant amount of photocurrent is lost when r is larger than $90 \mu\text{m}$. Throughout this thesis two different settings were used: low resolution scans and high resolution scans. The latter corresponds to a scan taken with the smallest beam radius and a low resolution scan corresponds to beam radius of $100 \mu\text{m}$. The low resolution scans directly correlate to measured EQE spectra and thus photocurrent maps may be converted to EQE maps. However, high resolution scans operate at intensities (~ 1000 times larger than 1 Sun) where OPV devices have poor efficiency and a nonlinear photocurrent response. While

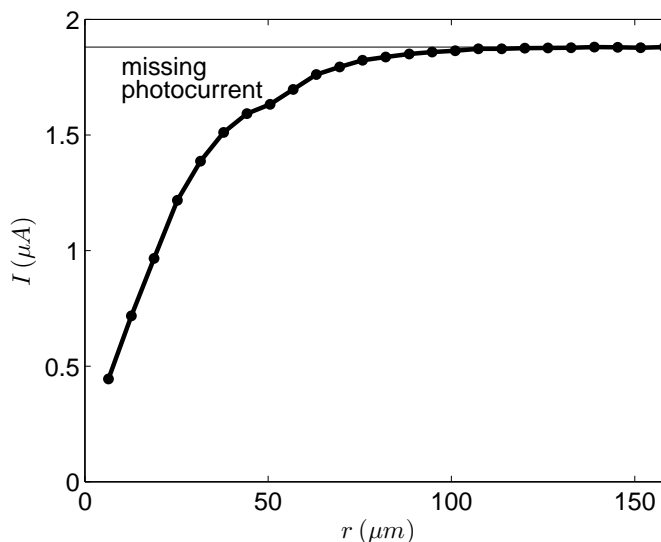


FIGURE 9.5: Photocurrent of a standard P3HT:PCBM device as a function of beam radius while the laser output is held at constant power.

features within a high resolution scan are still in proportion, photocurrent values may not be converted to EQE values in an absolute sense. The non-linear irradiance effect, as shown in Figure 9.5, is used to rapidly find the minimum spot radius as it is easy to change the lens position to minimise the resulting photocurrent. Once the minimum spot radius is found, Figure 9.4 was used to set the z-position to the height corresponding to the desired spot radius. This approach of using the non-linear irradiance effect to set the spot radius was the idea of Tim Nagle.

9.3 Results and discussion

9.3.1 Evaporative deposition: shadowing effect

The photoactive area of an organic solar cell is defined by the overlap of the cathode and the anode. While the ITO anode is purchased pre-patterned and is well-defined, the cathode is sublimed and deposited through a mask that is not as well defined. Furthermore, the mask has a non-zero thickness resulting in thickness non-uniformities near the edge as depicted in Figure 9.6. The substrate rotates during deposition, which

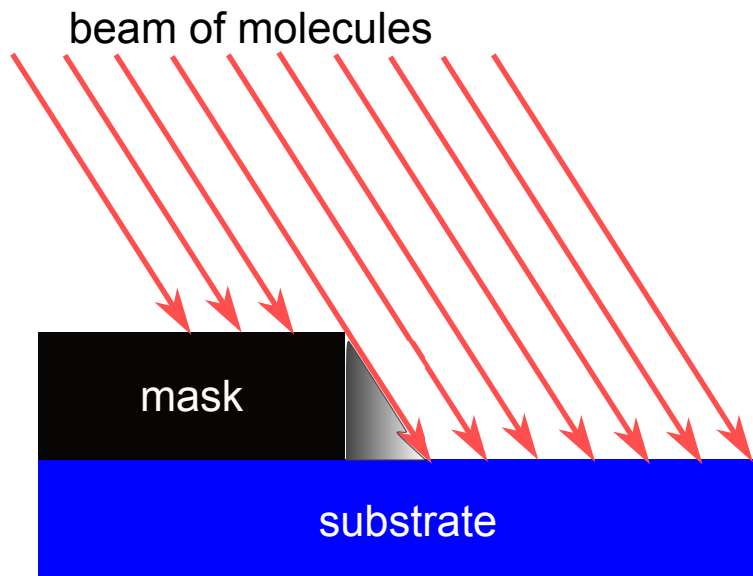


FIGURE 9.6: Diagram illustrating the shadowing effect that causes thickness non-uniformities at the edge of the mask during evaporative deposition. The grey area next to the mask indicates the shadowing effect; the thickness of the evaporatively deposited material is not uniform in this region.

reduces this shadowing effect, but does not completely eliminate it. Shadowing effects are mainly determined by the thickness of the stainless steel mask and its proximity to the surface of the substrate. The mask associated with device architecture II (see section 3.1) is positioned close to the substrate. Architecture I and III masks, on the other hand, are not perfect and sometimes there is a slight gap between mask and substrate. This gap causes noticeable shadowing effects. Line scans were taken with a profilometer to assess film thickness near the edge of the cathode. Figure 9.7 shows an extreme case where the gap between mask and substrate was large. Here, the distance associated with shadowing (the distance from the edge to the area of uniform thickness) is approximately 0.71 mm. In most cases, this value is 0.5 mm for architecture masks I and III. Device of architecture II generally have shadowing distances of 0.05 mm. However, as shown in Figure 9.7, the edge is characterised by a fast increase up to about 30 nm, after which the thickness slowly increases until the maximum thickness is reached. The impact of shadowing effects on photocurrent and the photoactive area is quantified with the LBIC system. The photocurrent generation at the two types

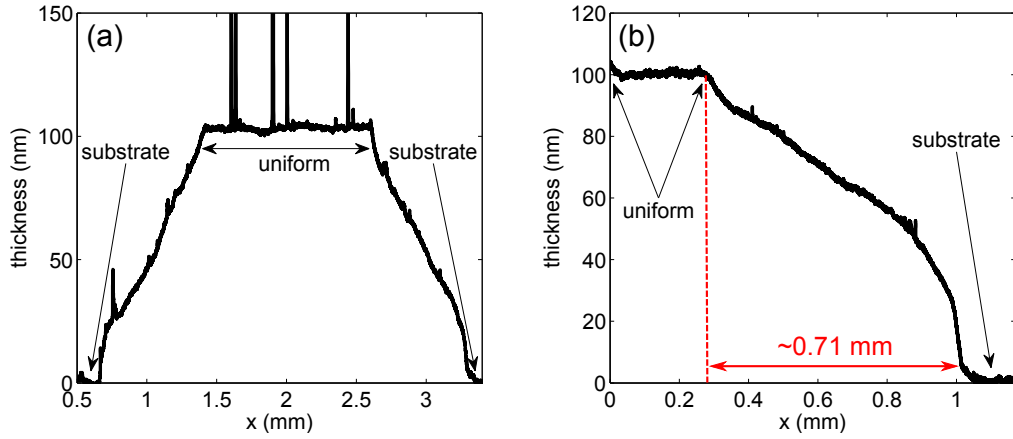


FIGURE 9.7: (a) Profilometer line scan across the width of a 100 nm thick architecture I aluminium cathode and (b) profilometer line scan starting on a 100 nm thick strip of silver, which has been deposited through an architecture I mask, and going of the edge onto the underlying glass substrate.

of edges (defined by ITO or Al) were mapped and the derivative of photocurrent line scans going off the edge are shown in Figure 9.8. Gaussian functions were fitted against the derivatives. The Gaussian corresponding to the ITO and Al edge had a standard deviation of $5.5 \mu\text{m}$ and $4.6 \mu\text{m}$ respectively, which corresponds well with half the beam radius which was set to $10 \mu\text{m}$ using the intensity relation (Section 9.2.3). Hence, the edge of the photocurrent map must be sharper than detectable with a $10 \mu\text{m}$ spot and is considered negligible. Thus the photocurrent mapping results show that shadowing effects do not have a significant impact on the sharpness of the photoactive edge even though the profilometer reveals that near the edge there is a considerable deviation in the cathode thickness compared to the thickness as found in the uniform thickness region. We can make sense of these seemingly contradictory results if we consider the magnitude of the change in resistance due to thickness variation. Using a resistivity of $2.82 \times 10^{-8} \Omega\text{m}$ for aluminium [274] the sheet resistance of an aluminium film as a function of thickness is shown in Figure 9.9. While the resistance is additive, the cathode resistance may be neglected if significantly smaller than the ITO sheet resistance of $15\text{-}20 \Omega/\square$. As shown in Figure 9.7, shadowing reduces the cathode thickness to about 30 nm. At this thickness the sheet resistance is still an order of magnitude

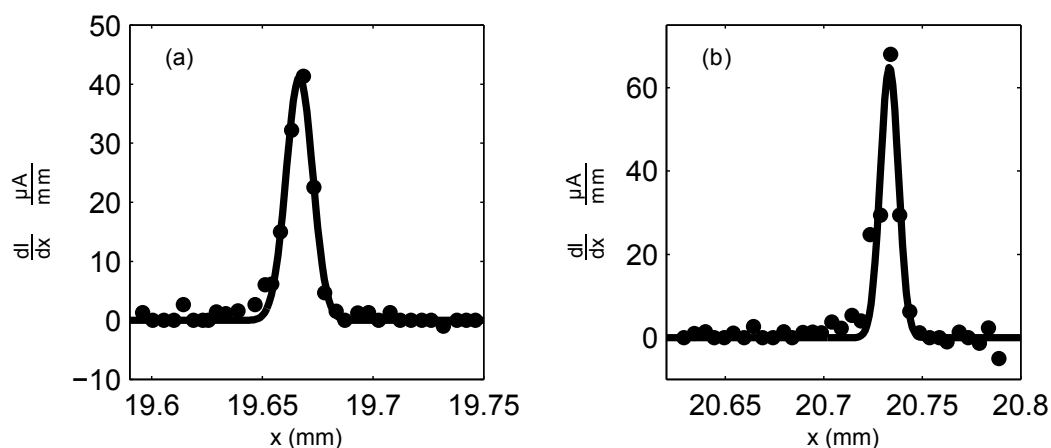


FIGURE 9.8: Derivative of a line scan going of the edge that is defined by (a) the ITO anode and (b) the Al cathode. Solid lines are Gaussian fits against the data points.

smaller than that of ITO. Hence, shadowing does not give rise to significant resistance changes at the edge as confirmed by the photocurrent mapping results. However, small molecules that are deposited via sublimation using a mask, such as BCP, Ca or LiF, are often sensitive to small variations in thickness [275, 276] and caution is still required in these situations.

9.3.2 True photoactive area

Nominal and real photoactive area: cathode mask

The masks used for cathode deposition are not well-defined laterally and as such the actual area covered by the electrode might be different than expected. Figure 9.10 shows an optical image of the cathode and it can be seen that the top and bottom edge are not exactly straight, but are wavy instead. The resulting discrepancy in photoactive area was quantified with the photocurrent mapping system. Figure 9.11 shows a photocurrent map of an architecture I device. The wavy edges of the cathode (the top and bottom edge) that is visible optically is also seen in the photocurrent map. The short edges are defined by ITO and are straight. Architecture I devices have a nominal photoactive area of 20 mm². A histogram corresponding to the photocurrent

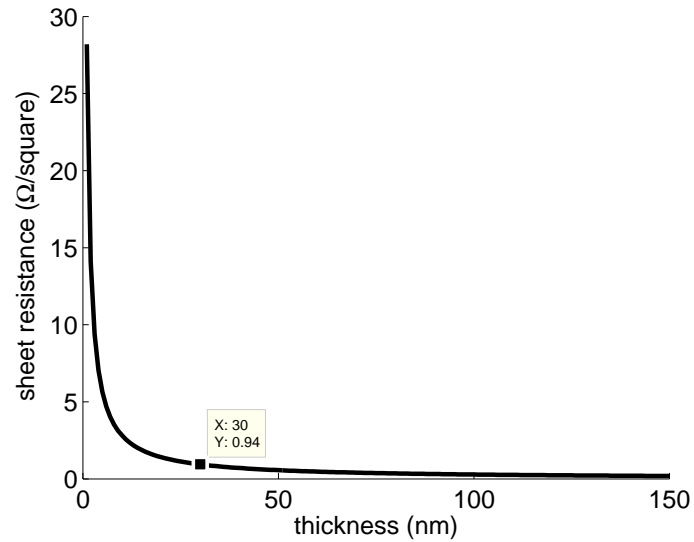


FIGURE 9.9: Aluminium sheet resistance as a function of film thickness.

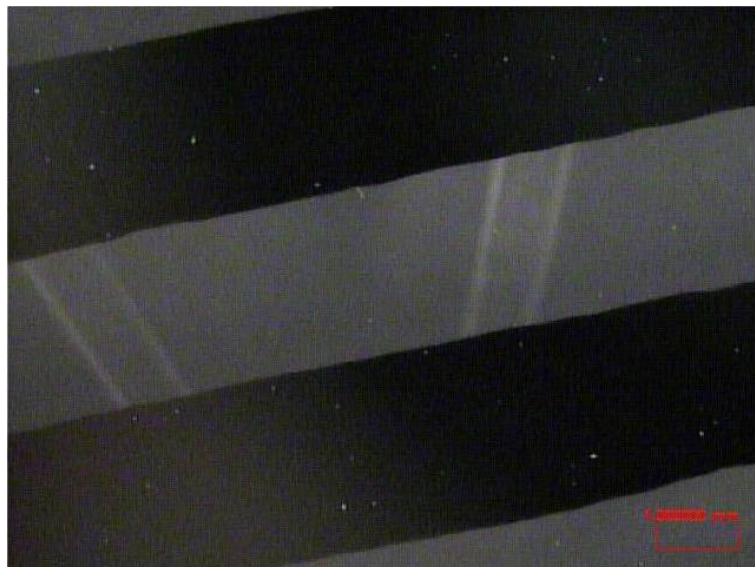


FIGURE 9.10: Optical image of a 2 mm wide aluminium cathode deposited using an architecture I mask. The black areas are regions that were covered by the mask during deposition. The 4 diagonal lines that show up in the optical image of the middle cathode finger are optical artefacts and do not represent the actual cathode.

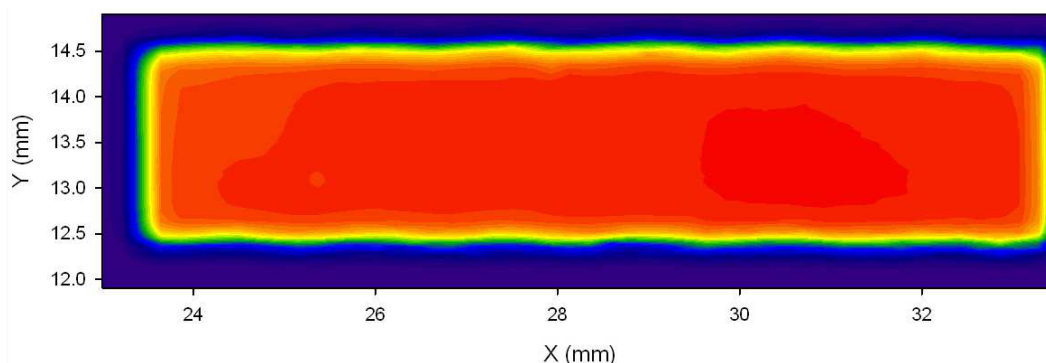


FIGURE 9.11: Photocurrent map of an encapsulated architecture I device.

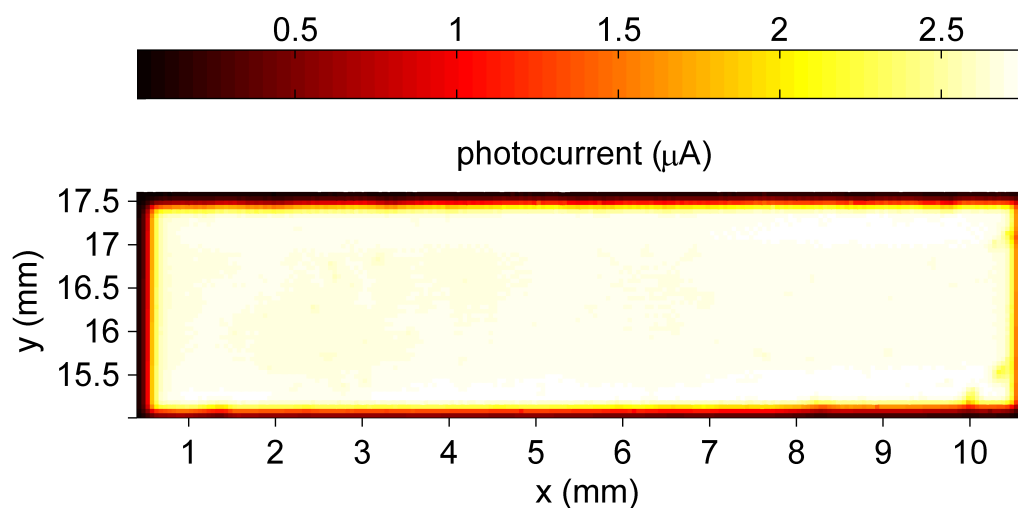


FIGURE 9.12: Photocurrent map of an encapsulated architecture I device. A histogram corresponding to these photocurrent values is shown in Figure 9.12.

map the architecture I device shown in Figure 9.12 is shown in Figure 9.13. The sharp peak is a result of the high level of uniformity that we are able to achieve. The scanned area is larger than the actual photoactive area to ensure the entire area is captured. As a result there are some counts near $0 \mu\text{A}$. The slight bump near $2.3 \mu\text{A}$ are values corresponding to areas with reduced photocurrent, which is likely a result of non-uniformities in the film. The remaining counts are due to edge roll-off. The edge of the photoactive area was determined by excluding all pixels with a photocurrent value that is less than a cut-off level of 50 % relative to the maximum photocurrent value of the entire map. The choice for 50 % stems from the fact that for a defect-free

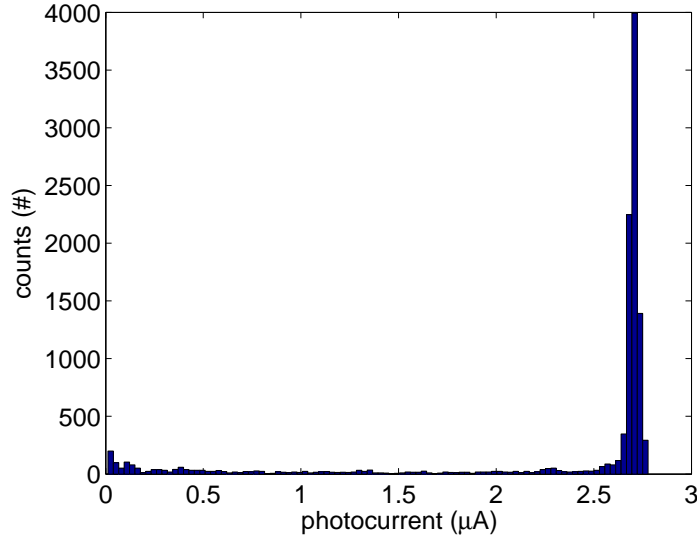


FIGURE 9.13: Histogram of the photocurrent values of a LBIC map corresponding to the photocurrent map shown in Figure 9.12. The bin size is 1 % of the maximum photocurrent, giving rise to 100 bins.

film the centre of the light spot is exactly on the edge of the photoactive area if the photocurrent is 50 % of its maximum. The area that is enclosed by the edge is taken as the actual photoactive area. Figure 9.14 shows the photoactive area as a function of the cut-off level. The photoactive area remains constant until the cut-off level reaches 75 %. Thus, the true photoactive area is not very sensitive to the cut-off level and thus the choice of cut-off level is not critical as long as it is roughly 50 %. The small drop in the photoactive area is due to local depressions in the photocurrent, as seen in the bottom and top right corners of Figure 9.12, which is related to film non-uniformities. Despite the exclusion of these depressions, the photoactive area remains larger than expected. The active area decreases only marginally until a cut-off level of $\sim 95\%$, which is when we start to cut into the main photoactive area. Obviously at a cut-off level of 100 % the photoactive area is 0. The photoactive area is thus determined to be 22.77 mm^2 , which is 13.84 % larger than nominal. Consequently, the current density and PCE measurements will be overestimated by the same percentage when not using a mask to cover a well-defined area during measurements. The discrepancy in photoactive area for architecture I mainly finds its origins in the y-width which is

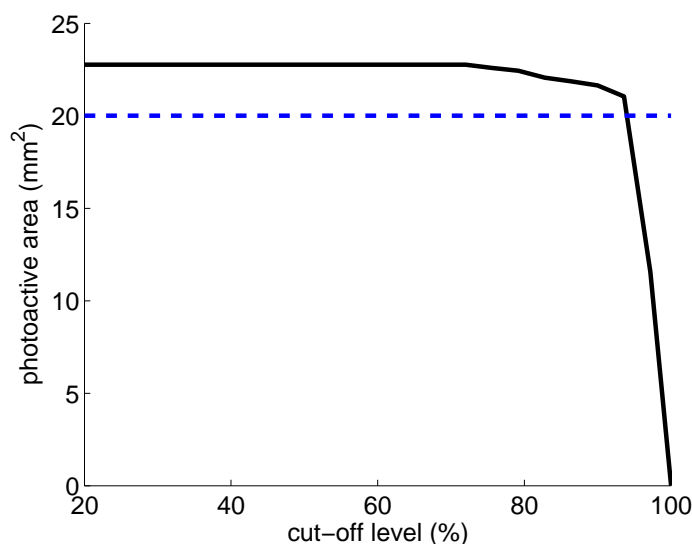


FIGURE 9.14: The calculated photoactive area as a function of cut-off level (black solid line). The nominal area is also shown (dashed blue line).

13.84 % larger than 2 mm. The x-width is exactly 10 mm, because the ITO pattern is very accurately defined. The same type of analysis was conducted for a type II device and the discrepancy was found to be 5 % due to a larger than nominal cathode, highlighting the importance of using a well-defined mask to only expose a known active area during whole-cell device characterisation.

Leakage current from neighbouring devices

Another source of 'cheat' current may be found in neighbouring devices on the same substrate, even if they are not connected to the external measuring circuit. Architecture I and II devices have extra ITO pads at positions where contact is made with external pins. These pads improve contact with pins that may otherwise pierce the thin cathode layer resulting in bad contact as the underlying glass is not conductive. However, if the active layer is insufficiently removed, these pads may act as small solar cells. Active layer removal is achieved using one of two methods. The first method involves wiping with a cotton bud that was dipped in chlorobenzene and the second method involves drawing with a marker pen that was filled with a mixture of toluene and ethanol. The first method relies on solubility whereas the latter relies more on a

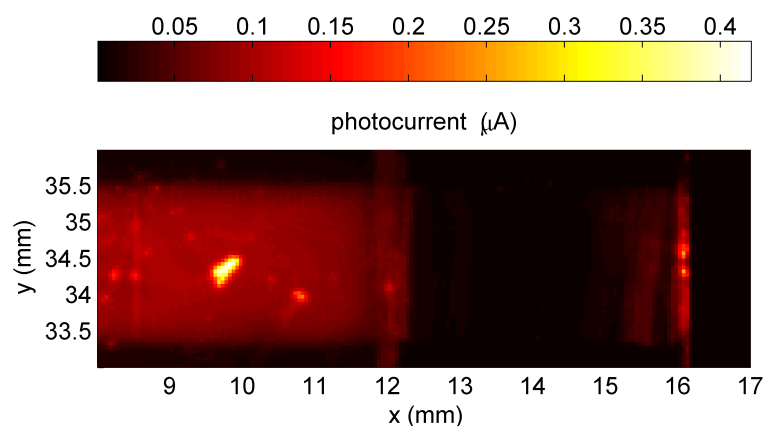


FIGURE 9.15: Photocurrent map of a device with incomplete active layer removal.

physical scraping process. In the glovebox both give the same visible result. However, LBIC measurements show that the marker method gives variable results. Since it relies on scraping, the number of passes and pressure are important parameters. Since removal is done manually in a glove box, the pressure is difficult to control. Figure 9.15 depicts an instance where the active layers was not properly removed from the extra ITO pads. Here vertical streaking is visible, consistent with the direction of the marker pen movement. The intended photoactive area is supposed to stop at ~ 12.2 mm (in the x direction), yet significant amounts of photocurrent is generated in areas to the right of this point. Especially where the extra ITO pad is located (14.5 - 16.1 mm).

While the active layer is generally removed using the organic solvent method, the underlying transparent PEDOT:PSS film is often not sufficiently removed, because it is not soluble in organic solvents. Hence, the removal of PEDOT:PSS relies on physical scraping. PEDOT:PSS is not as conductive ($\sim 1 \times 10^{-3} \text{ Scm}^{-1}$ according to the manufacturer's website) as ITO or aluminium, but contributions from neighbouring cells can still be identified. Figure 9.16(a) shows a photocurrent map that was measured across four cells on an architecture I substrate layout. The second device (from top to bottom) was directly connected to the external measuring circuit and is thus clearly visible in the photocurrent map. The trapezoidal shape is a result of degradation occurring during the measurement as this device was not encapsulated. This effect

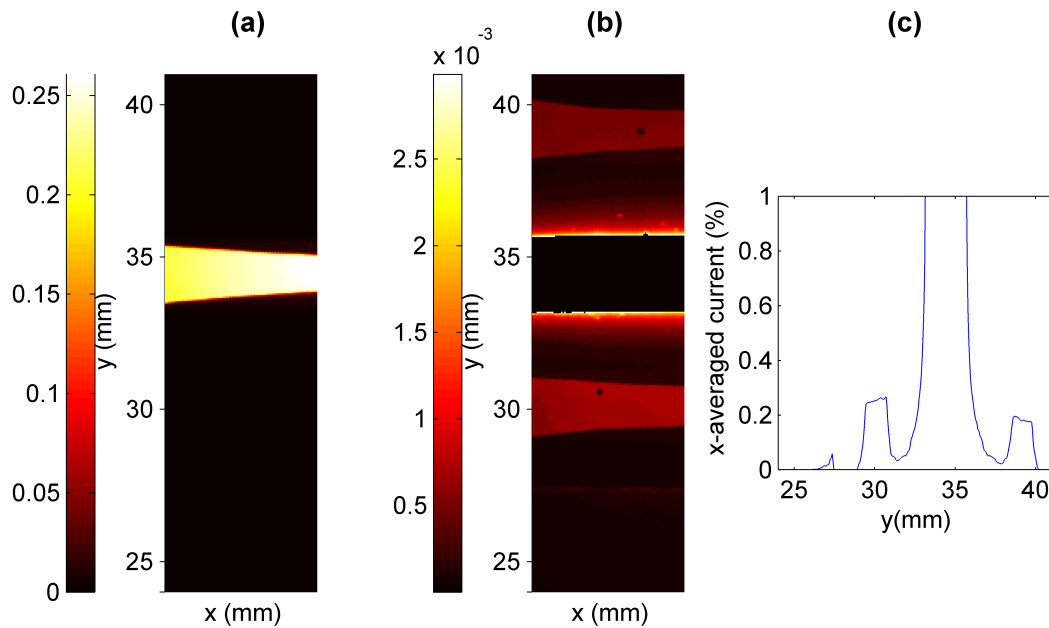


FIGURE 9.16: (a) photocurrent map of four cells while only the second device is directly connected to the external measuring circuit. (b) shows the same data with the photocurrent of the second cell eliminated, thus increasing the visual sensitivity to low photocurrent values. (c) shows the normalised x-averaged current as a function of distance.

is discussed in more detail in Chapter 10. Initially it seems that there is no current contribution from the other three cells. The colour visibility of low current values was enhanced by excluding all photocurrent values above $0.003 \mu\text{A}$, thus increasing the visual sensitivity for low current values; the result is Figure 9.16(b). Current maps of the nearest neighbour cells are now visible and even a sliver of the fourth cell is detectable. The photocurrent maps of the nearest neighbours have their own distinct features (specific trapezoidal shape and location of the largest pinholes) further demonstrating that photocurrent is gathered from areas that are relatively far away from the device in direct contact. Starting from the centre of the connected device, photocurrent is detected from areas that are up to 7 mm away. To quantify the relative current contribution of these other areas, the average of all y-line scans was calculated and is shown in Figure 9.16(c). The photocurrent within neighbouring cells exhibits a slope which is consistent with an increasing path length through a poorly conducting material. The current picked up between cells is due to light scattering into

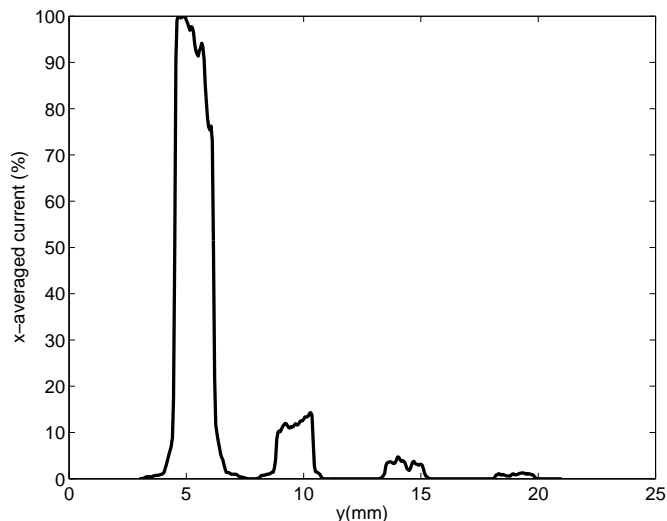


FIGURE 9.17: normalised x-averaged current as a function of distance. The left cell is directly connected to the external measuring circuit. The devices on this substrate all had poor performance due to fabrication issues with the PEDOT:PSS layer (it was dried at a temperature that was too high, which resulting in cracking of the film).

the photoactive area. Current collected in this way is negligible in these devices as it is only 0.08 % of the maximum current. The peak contribution of the neighbouring cells is less than 0.3 % and is considered negligible as well. However, in some cases the current of the nearest cell is found to be more than 10 % of the current of the average current found in the device that is directly connected to the external measuring circuit as shown in Figure 9.17. This contribution seems to be larger for poor performing devices (due to fabrication mistakes/variability or degradation) and smaller for good devices. This averaging effect would slightly decrease the apparent spread in device performance. No current from neighbouring devices is found when the PEDOT:PSS layer is properly removed from the relevant areas, confirming that PEDOT:PSS enables cross-talk between devices when not isolated from the cathode.

Unexpected small contributions can overestimate the overall power conversion efficiency of a device. Since the removal of PEDOT:PSS (or even the active layer) is very difficult to assess during fabrication, it is important to use a mask that covers the entire substrate except the area of interest during efficiency measurements to ensure

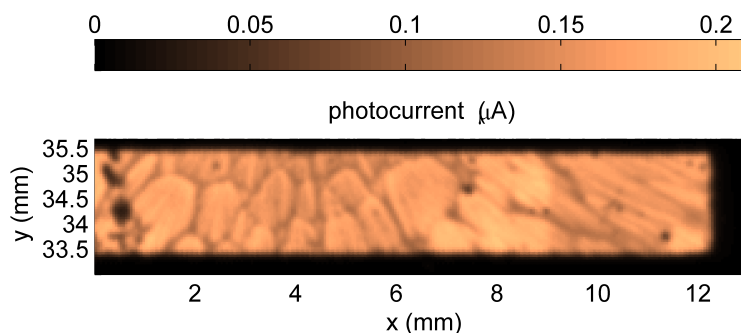


FIGURE 9.18: Photocurrent map of a device with a PEDOT:PSS film that was heated to the point where cracks were visible.

accurate assessment of device performance.

9.3.3 Identifying the impact of visual defects

Small unintentional variations and/or mistakes made in the fabrication process often result in bad performing OPV devices. However, sometimes it is found that devices that visually look non-uniform perform just as well as good uniform films. In this section two cases of visual defects are presented.

PEDOT:PSS structural defects

The first case is a somewhat straightforward case to illustrate that visual defects are also visible in the photocurrent image. PEDOT:PSS is usually dried at a temperature of 140 °C for 10 minutes immediately after it is spun. For a set of devices, PEDOT:PSS was heated at 200 °C for 20 minutes, leading to 'cracked' PEDOT:PSS films. The corresponding photocurrent map is shown in Figure 9.18. It is clear that overheating the PEDOT:PSS films should be avoided as macroscopic domains will form. Performance in the cracks is reduced leading to a reduction in whole cell current.

Comets

Particulate matter, i.e. dust or dirt, that is stuck on the substrate prior to spin coating, will give rise to so called comets (owing to their visual similarities with the celestial

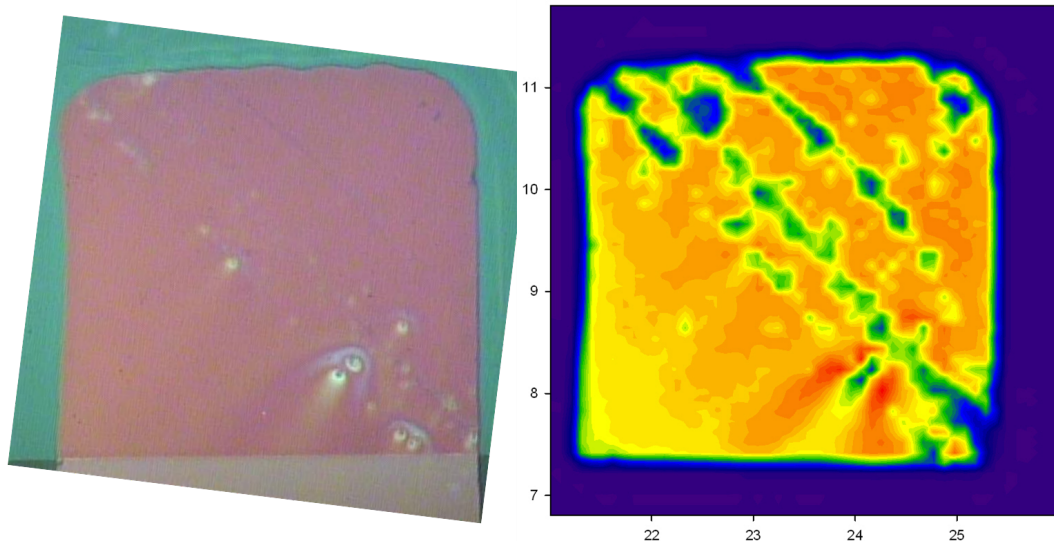


FIGURE 9.19: (left) an optical image of a 4×4 square device (architecture II) and (right) a photocurrent map of the same device. The following colours represent photocurrent values, from high photocurrent values to low photocurrent values: red, orange, yellow, green, blue and purple.

body that may form a tail that streams away from the sun). Figure 9.19 shows a side by side picture of an optical image and a photocurrent map of the same device. While most defects result in a local photocurrent depression, the big comet in the bottom right corner exhibits an increase in photocurrent, contrary to expectations. The particulate matter in the centre of the comet obviously does not generate photocurrent, but both the coma and the tail of the comet generates more photocurrent than a uniform area as shown in Figure 9.19. This is not related to film thickness as these devices are optimised for thickness. An architecture II device was fabricated to quantify the impact of comets on photocurrent generation. The corresponding photocurrent map is shown in Figure 9.20. Figure 9.20(a) is imaged in such a way that a general radial pattern is noticeable, which is likely related to small spin-induced thickness variations. Figure 9.20(b) shows that the direction of all the comets point towards the centre of the substrate consistent with the spin-coating process. Figure 9.21 depicts the same data (photocurrent has been converted to EQE) in a colour scheme that makes it easy to identify comets and dead spots. Some areas with distinctive features and uniform areas

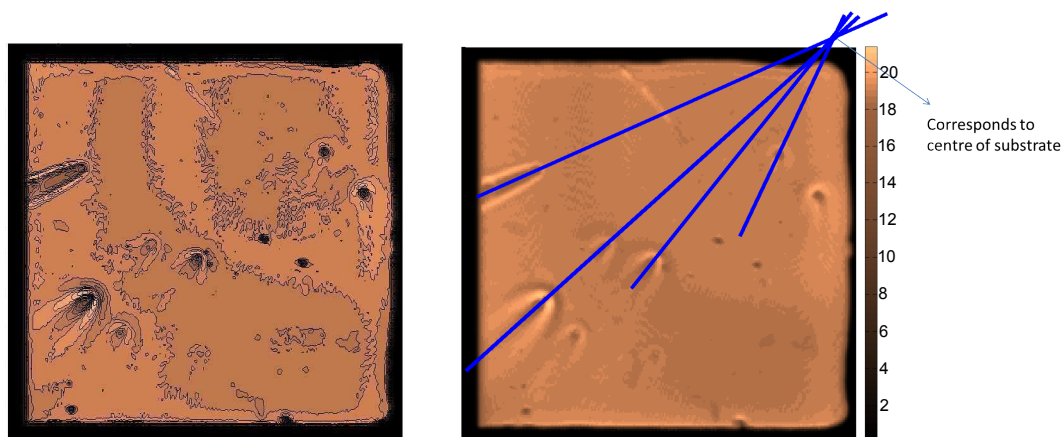


FIGURE 9.20: A low resolution ($100\ \mu\text{m}$ spot radius) LBIC scan was conducted. Photocurrent values are expressed in μA . The same photocurrent data is plotted in two different ways. (a) highlights the radial pattern and (b) the direction of the comets.

have been identified and are used to further quantify the effect these features have on EQE. Obviously a smaller area will on average exhibit a higher degree of photocurrent uniformity than a larger area. Therefore, to make a fair comparison, uniform areas of the same size were chosen for a direct comparison with their respective comet and dead spot areas. The histogram of these areas are shown side by side in Figure 9.22. The left column of plots shows the uniform areas and the right column shows areas with certain features. Uniform areas exhibit very narrow histograms, as expected. Dead spots, show an appreciable amount of pixels with reduced current. Comets on the other hand show both pixels with reduced current and pixels with enhanced current generation. In some cases, the photocurrent to the right of the histogram peak compensates for the reduced current to the left of the peak, in which case the area in question performs just as well as a perfectly uniform area. This result explains why films with many comets still perform reasonably well. Figure 9.23 shows an optical image of an unusually large comet. Comparing this to photocurrent mapping results, it is clear that the outer light brown front and the light brown 'wake' region generate less photocurrent, whereas the purple-like front and connecting tail immediately around the particulate matter exhibits increased photocurrent generation. Three typical regions

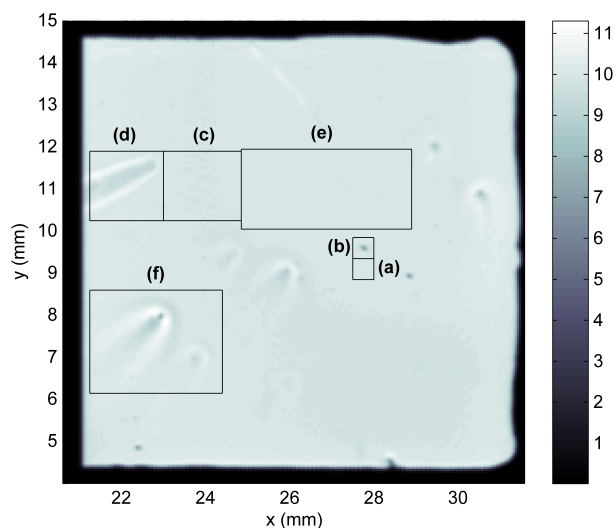


FIGURE 9.21: EQE maps of an architecture II device with several comets and circular dead spots. The areas used to plot histograms (Figure 9.22) are indicated and referenced with letters. The colour bar indicates EQE in % as opposed to photocurrent. The left and bottom edge is defined by ITO and are straight. The top and right edge are defined by the cathode, the shape exactly corresponds to the mask.

may thus be associated with comets: (1) area with no photocurrent generation, (2) area with reduced photocurrent generation and (3) an area of increased photocurrent. The sequence of these areas is further illustrated in Figure 9.24. Here, the average current is determined for a 'window' that is systematically changing. The smallest area consists of one pixel at the centre of either a comet (red graph) or a dead spot (blue graph) and thus exhibits the lowest photocurrent. The area under consideration (window) is always square and systematically increases as indicated by the arrows in Figure 9.24. For the dead spot, as the area increases the photocurrent increases as well and approaches the average photocurrent value of a uniform area (black graph). The impact of the dead spot reduces as the area under consideration increases, since we are looking at the average photocurrent of the area under consideration (i.e. for an infinite area the dead spot would not be noticeable). The response is thus straightforward, but this is not the case for a comet. Here, the photocurrent increases rapidly due to the region that exhibits enhanced photocurrent. It even exceeds the average photocurrent value, before coming down again as the poorer performing outer front starts to get

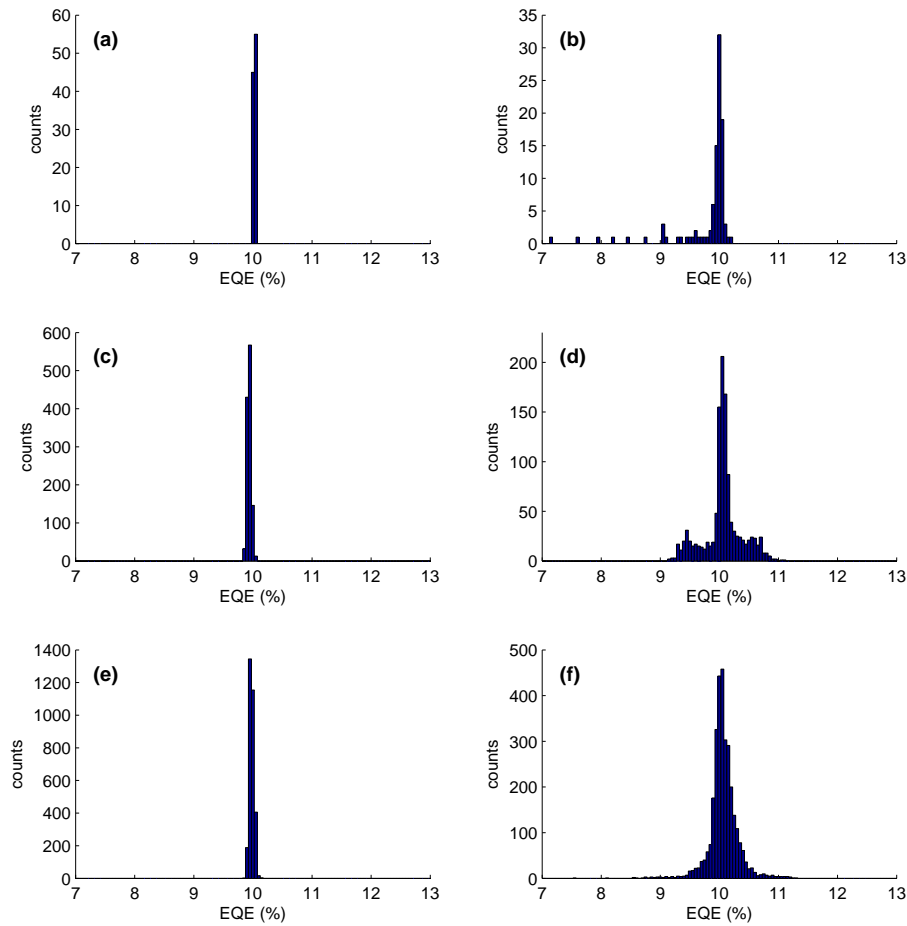


FIGURE 9.22: Histogram of the areas identified in Figure 9.21. The left column of histograms contain all the uniform areas and the right column shows the areas with distinctive features (comets or dead spots).

captured by the area under consideration. The photocurrent then climbs up again and slightly exceeds the value corresponding to a perfectly uniform area.

Figure 9.23 clearly shows a distinct (optical) colour change for the poor and more efficient areas. A photocurrent map at a different wavelength could provide valuable information, because a comparison of photocurrent maps measured at two different wavelengths combined with the expected photocurrent generation based on light absorption at these wavelengths essentially provides chemical sensitivity. In the photocurrent maps presented so far, a laser diode of 635 nm was used. At this wavelength the

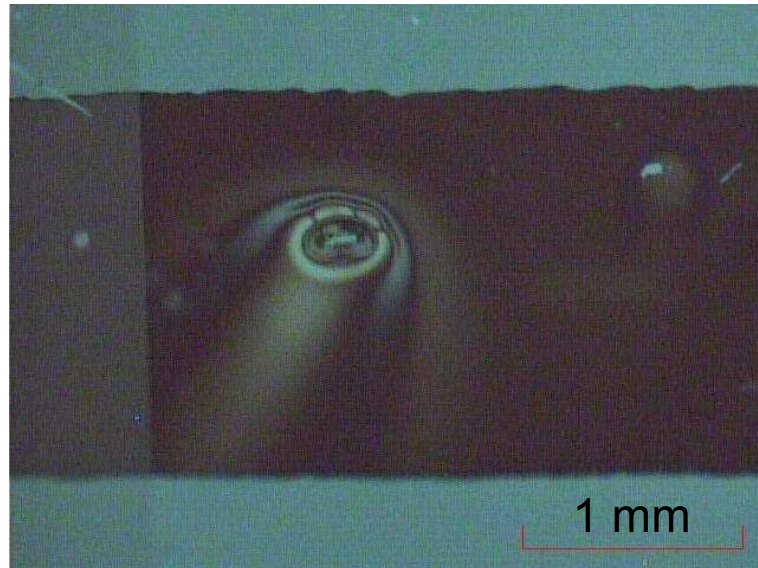


FIGURE 9.23: An optical image of an unusually large comet on the left and a small comet on the right.

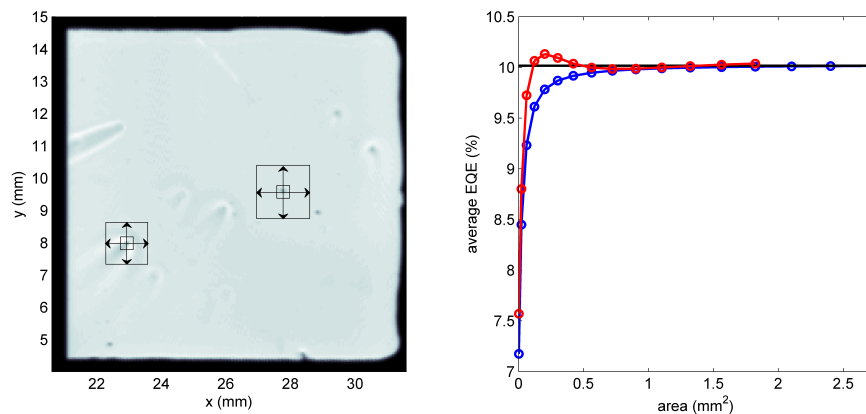


FIGURE 9.24: (right) The average photocurrent is determined for two series of areas: square areas centred around the comet (red) and square areas centred around a dead point (blue). The average current of a uniform area is also shown (black). The area under consideration is always square. Starting at the centre (1 pixel) the area is systematically increased as indicated with arrows in the left image. This is continued until another feature is reached that would influence the average current.

photocurrent contribution mainly originates from P3HT. For the thickness of standard devices (80-85 nm) over 80 % of the photocurrent originates from P3HT [277]. At 405 nm, PCBM absorbs ~ 35 % of the incoming light. The total photocurrent contribution (across the entire spectrum) is dominated by P3HT, as only up to 13 % is generated by PCBM [277]. Hence, the maps obtained at 635 nm are representative of the total photocurrent generation (across the spectrum). Figure 9.25 shows two photocurrent maps of the same area at the two different wavelengths. The specks of increased current that are scattered across both photocurrent maps are dust particles. These dust particles scatter the light of the laser causing light to spread out over a larger area which results in better charge extraction. As mentioned in Section 9.2.3, light intensities for high resolution scans are so high that considerable enhancement of recombination processes is found and scattering of light would essentially lead to lower light intensities and more photocurrent. The enhanced and decreased areas of photocurrent were not very pronounced (other than the dead spot due to particulate matter in the centre) and were hardly visible at a wavelength of 405 nm. However, the measurement system is very sensitive and small current changes can be picked up. To make these small current changes visible in the 405 nm map, an unusual colour map was used in Figure 9.25. At 635 nm, the map is much less uniform and a rapidly changing colour spectrum was not needed to visualise the changes in photocurrent. The photocurrent in areas associated with the wake and tail of the comet seem inverted when comparing the 405 nm map with the 635 nm map, i.e. an area that shows less photocurrent at 635 nm exhibits more photocurrent at 405 nm. Such an inversion is only possible if the PCBM contribution to photocurrent is slightly more than 50 % at 405 nm and much less than 50 % at 635 nm. However, as shown by Nicolaidis et al. [277], for a 1:1 P3HT:PCBM blend (as used in our devices) the current contribution of PCBM at 405 nm does not exceed 35 %. Hence, the two different photocurrent distributions could be explained through a non-uniform P3HT:PCBM weight ratio distribution. Therefore, the photocurrent mapping data suggests that the area of increased current may be related to a change in the local P3HT:PCBM composition, which may be caused by shearing of material along obstacles during the spin-casting procedure. Since the increase in photocurrent

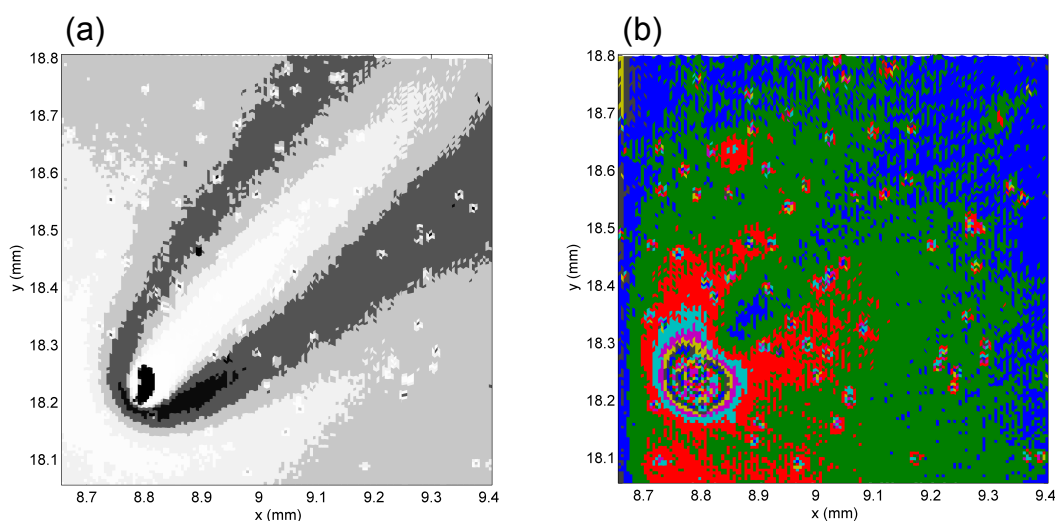


FIGURE 9.25: (a) high resolution ($10\ \mu\text{m}$ spot radius) photocurrent map taken at 635 nm and (b) at 405 nm. The 405 map shows very little non-uniformity and a rapidly changing colour map was used to visualise the small photocurrent differences. (a) dark areas indicate low photocurrent values and lighter colours indicate higher photocurrent values. (b) red indicates high photocurrent values, green lower values and blue lower still. The photocurrent distribution is inverted in (b) compared to (a).

at 635 nm is much more intense than at 405 nm, the mapping results suggest that a weight ratio in favour of P3HT will yield slightly more efficient devices, which is why ratios of 1:0.8 (in favour of P3HT) are often used in literature [131]. However, further analysis is required to undisputedly proof this hypothesis.

9.4 Conclusion

In conclusion, an LBIC system with high resolution ($\sim 3\ \mu\text{m}$) geared towards analysing OPV devices with a photoactive area of up to $25\ \text{cm}^2$ has been developed and was used to spatially resolve current non-uniformities. It is important to understand uniformities that arise from imperfect fabrication techniques, because they could potentially cause discrepancies between modelled and measured data. For example, the effect of comets and the resulting local change in the P3HT:PCBM composition is not explicitly taken into account in the DMC model.

The LBIC technique was used to measure the impact of cathode thickness variation

that occur during evaporative deposition through a mask. Both resistance considerations and photocurrent maps confirm that shadowing effects do not affect the sharpness of the edge of the photoactive area. However, since the cathode mask is not well-defined, the deposited cathode does not have the nominal physical dimensions. Furthermore, imperfect removal of the active layer or PEDOT:PSS layer may enable cross-talk between devices on the same substrate and also increase the apparent whole-cell current. As such, it is important to mask OPV devices to prevent erroneous whole-cell device performance measurements.

Certain defects can be seen with the naked eye and the photocurrent mapping technique allowed us to quantify the impact of these visual defects on photocurrent generation. In this way, cracks in the PEDOT:PSS film could be linked to a decrease in current and the impact of comets could be analysed. Comets consist of areas with increased photocurrent compared to a perfectly uniform area. Photocurrent mapping at two different wavelengths suggests that the P3HT:PCBM weight ratio is not constant in these areas, rather the weight ratio slightly in favour of P3HT as opposed to the 1:1 ratio used in our devices. The results suggest that a P3HT:PCBM weight ratio slightly in favour of P3HT could yield devices with higher overall photocurrent.

10

Diffusion limited degradation

10.1 Introduction

The study presented in this chapter has resulted in a conference paper [278], an oral conference presentation (International Organic Excitonic Solar Cells Conference, 2012) and a journal publication in *Solar Energy Materials & Solar Cells* [188]. I conducted all the experiments and data analysis unless stated otherwise.

Degradation is not explicitly taken into consideration in the DMC model, consequently, devices have to be encapsulated before performance is measured in air. It is important to understand the performance decay in devices to ensure that measured results are not clouded by degradation effects. These effects are explored in this chapter.

Degradation of OPV devices occurs via a number of pathways. These include photooxidation of the organic active materials; electrochemical reactions between organic

layers and metallic electrodes; electrode corrosion; and physical effects, such as delamination [118, 279]. These degradation modes can occur concurrently, making it difficult to attribute the observed performance decay to any one cause [280], however most of the degradation mechanisms are underpinned by the ingress of water and oxygen into the device [118].

In this chapter, we applied the photocurrent mapping technique discussed in chapter 9 to study the dominant degradation mechanism occurring when bulk heterojunction OPV devices with the conventional structure: ITO / PEDOT:PSS / P3HT:PCBM / cathode; are stored in air. If the cathode layer is made of aluminium, the primary degradation mechanism in this device type is known to be oxidation of the cathode at the internal interface [281]. The PEDOT:PSS layer promotes this reaction, since its hygroscopic nature facilitates rapid uptake of water from the atmosphere [281, 282]. The formation of an aluminium oxide layer at the cathode interface leads to locally-complete inhibition of device charge extraction [283]. Early reports suggested that the acidic nature of PEDOT:PSS (pH of 1.6–1.9) also played a role in the degradation mechanism [284, 285], but this was later shown not to affect device lifetime [286].

Since the primary degradation mechanism is diffusion limited [281], it is important to understand the diffusion process in organic solar cells. It has been previously reported [283, 287] that the diffusion of water into OPV devices occurs preferentially "through the grain structure" of the aluminium film, rather than through pinholes or at the device edge. A water-driven degradation process might therefore be expected to cause a degradation pattern that is laterally uniform across the device. Our results show that for devices with the normal aluminium cathode thickness of around 100 nm, this is not the case. We report results that instead support the observations of Voroshazi et al. [281], who conclude that water mainly diffuses via pinholes in the cathode and via the edges of the device.

Some authors have concluded that diffusion of contaminant ingress via the edge of the device is of secondary importance compared to diffusion through at pinholes [266, 287–289]. Conversely, for our architecture I devices (see section 3.1) we find that edges appear to be the principal pathway for ingress. Others have also observed this,

especially for small-area devices [266, 270, 281, 290]. Voroshazi et al. [281] concluded that the impact of the perimeter:area ratio of the device affects the device lifetime. In this work, we demonstrate the use of the LBIC technique to determine the diffusivity of water into OPV cells through pinholes and at the edges of the device. We show that not only the device lifetime but also the dominant diffusion pathway depends on the lateral design of the cell. In particular, the extent to which the photoactive perimeter is defined by the cathode can impact the cell lifetime by more than an order of magnitude and must always be considered when reporting cell durability results.

Since low work function cathode metals such as aluminium are reactive to oxygen and water [283], inverted cell geometries (transparent ITO forms the cathode instead of the anode) [291] frequently lead to improved device lifetimes as they allow for the use of more stable electrode materials, e.g. silver. Although a silver electrode is also subject to oxidation, the oxide is generally not detrimental to device performance. Nevertheless, we demonstrate that LBIC can also be used to measure diffusion in devices that use a silver electrode.

LBIC has previously been used to study degradation in organic cells. Kroon et al. observed a decline in photocurrent that decreased homogeneously across the entire cell area [292]. Rösch et al. [266] used LBIC with other imaging techniques to investigate degradation in different device structures. Small OPV modules have also been studied using LBIC [293, 294].

Although we have used non-encapsulated devices for this study, the LBIC approach is equally applicable to encapsulated devices, where it could be a valuable tool for studies of encapsulant performance.

10.2 Experimental and modelling aspects

10.2.1 Device fabrication

OPV devices with the conventional structure (ITO / PEDOT:PSS / P3HT:PCBM / cathode) were fabricated. Solar cells with the architecture I design (see figure 3.1)

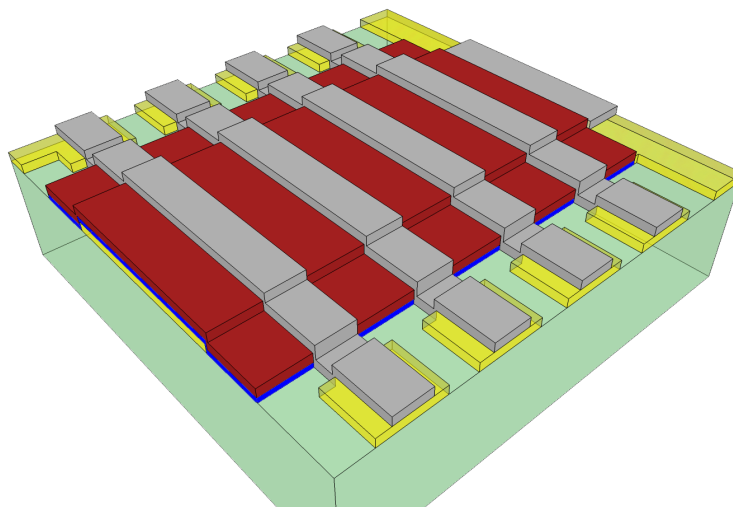


FIGURE 10.1: Layout for OPV devices used in this chapter. Yellow indicates ITO, red the active layer, blue the PEDOT:PSS layer and grey the metal cathode.

were used for most of the analysis and in some cases architecture II devices were used. The lateral design will be shown to have implications for the durability of organic solar cells. In the architecture I configuration, shown in Figure 10.1, the $2\text{ mm} \times 10\text{ mm}$ active area of each test cell is defined at the long edges by the dimensions of the metal cathode layer, and at the short edges by the width of the ITO bottom contact.

10.2.2 Environment control

In order to investigate the impact of water and oxygen, the photocurrent mapping system, which is discussed in Chapter 9, was placed in a AtmosBag (Sigma Aldrich, Z530220) to allow for measurement in an isolated and controlled environment. In addition to ambient air, the following environments were used: dry air, dry nitrogen and wet nitrogen. The dry air environment was realised by pumping compressed air through a series of drying tubes containing desiccant. The relative humidity and temperature in the Atmosbag were monitored using a hygrometer (Lambrecht) and thermometer respectively. Dry nitrogen was realised in the same fashion, even though the nitrogen was already dry to start off with. A wet nitrogen atmosphere was obtained by bubbling compressed nitrogen through deionized water. It took about half an hour to an hour

to purge the entire Atmosbag, depending on the flow rate. The incoming gas flow was located immediately underneath the solar cell. In this way, any change in the gas flow immediately had an effect on the solar cell.

10.2.3 One-diode model

In this chapter the one-diode (see Figure 2.12) is used to generate I-V curves as a function of time. The electrical circuit of this model is shown in Figure 2.12. The corresponding current-voltage relationship is given by

$$I = I_L - I_0 \left(e^{q \frac{V + IR_s}{nk_B T}} - 1 \right) - \frac{V + IR_s}{R_{sh}} \quad (10.1)$$

where n is the ideality factor of the diode and I_0 the saturation current of the diode. Even though the one-diode model has its limitations when applied to organic solar cells, it is especially useful in this chapter, because it allows for easy determination of full I-V curves and thus power conversion efficiency as a function of I_{SC} and R_s . The dependence on the latter two parameters may be determined using Equation (10.1) and the following equation:

$$I_L = I_{SC} + \frac{I_{SC}}{R_{sh}} \quad (10.2)$$

Initial parameters were determined by using the IVfit program developed by ECN (Netherlands Research Foundation) [295]. All parameters were kept constant except I_{SC} and R_s , which were varied according to a known time relation and I-V curves were generated by numerically solving Equation (10.1) in Matlab.

10.3 Results and discussion

10.3.1 General observations of encapsulated devices

Figure 10.2 presents quantum efficiency maps for an encapsulated device. Over most of the device area, the EQE is approximately 10 %, which is in agreement with whole cell measurements made at the same wavelength in a separate measurement system. This level of response reflects the relatively weak light absorption in P3HT:PCBM

OPV devices at 635 nm and is adequate for photocurrent mapping measurements. Figure 10.2(a) shows the photocurrent response over the entire 2 mm x 10 mm cell area, measured with a spot radius of 100 μm . Figures 10.2(b) and (c) show subregions of this cell, measured with a spot radius of 10 μm . All three scans indicate areas in which little or no photocurrent is generated. These areas are perfectly circular and vary in diameter from 25 to 250 μm . We observe such 'dead zones' in virtually all OPV devices we make. In non-encapsulated devices, we see them grow over time, whereas in encapsulated devices, their size does not change over a period of days. Visual inspections reveal no features that correspond to even the largest dead zone. Hence, we attribute the dead zones to the ingress of a contaminant through small pinhole defects in the aluminium electrode. The high degree of circularity of the dead zones suggests the corresponding holes in the electrode are much smaller. Otherwise, the dead zones would, on at least some occasions, retain non-circular elements of the shape of the hole in the electrode. On this basis, we estimate that the holes in this particular device must have a diameter no larger than a few micrometres, consistent with SEM imaging of pinholes in an aluminium cathode conducted by Krebs et al. [288]. The existence and behaviour of the dead zones in encapsulated devices leads us to believe that the contaminant, which we later confirm to be water, is not fully excluded during our fabrication process.

10.3.2 General observations in non-encapsulated devices

Figure 10.3 presents four EQE maps for a single device without encapsulation, collected sequentially. During each measurement, the beam moves in a raster pattern: it oscillates from top to bottom in the image, taking 60 minutes to traverse the active length of the cell from left to right. Each scan is labelled with a time axis, which represents the time since the device was first exposed to air. Immediately evident in these scans is a progressive decrease in the width of the functional cell. The width of the cell in the image decreases due to complete degradation of the active area at the long edges. While the measurement proceeds from left to right, the device degrades

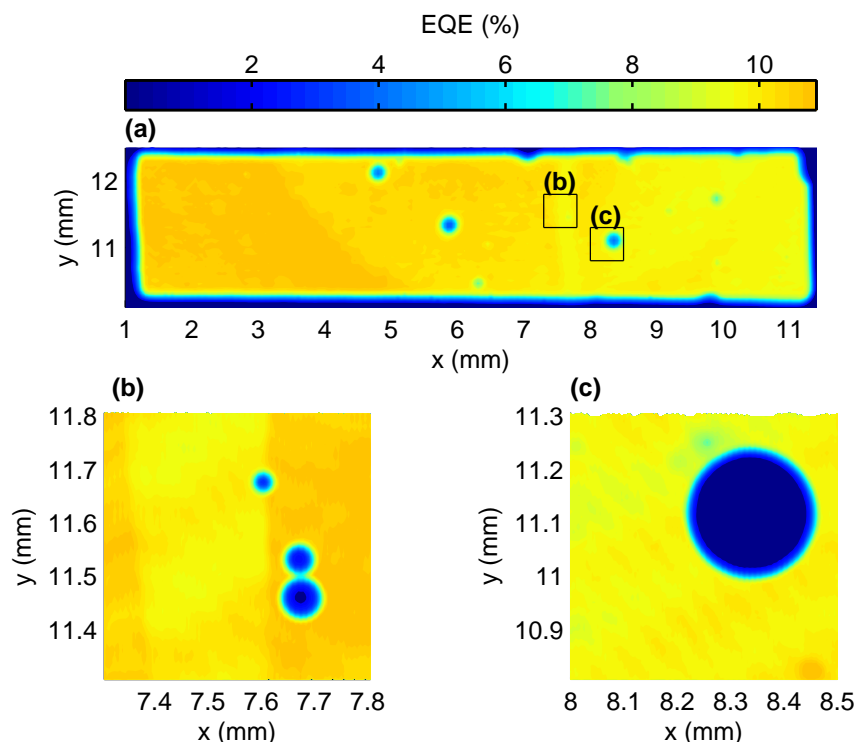


FIGURE 10.2: EQE maps of a 2 mm \times 10 mm encapsulated device measured with (a) 100 μ m spot radius, and (bc) 10 μ m spot radius.

symmetrically at the long edges (top and bottom in the images) giving rise to a trapezoidal shape. The four scans took 5 hours to complete, after which the active width of the cell was reduced to zero. No other illumination was used during the measurement, demonstrating that this degradation does not require any optical excitation, which is consistent with the observations of Kawano et al. [282]. The long dimension of the active cell remains constant throughout most of the experiment, indicating that degradation does not occur at the short edges (left and right in the image). The short edges of the device are defined by the absence of ITO, rather than by the edge of the cathode layer. In this case, the cathode layer extends laterally beyond the active edge of the device and would be expected to protect the cell from contaminant ingress at those edges. It follows that the protective nature of the aluminium cathode is of importance to the design of a stable device. Superimposed on the trapezoidal shape are a number of the circular features. These pinhole features can clearly be observed in Figure 10.3

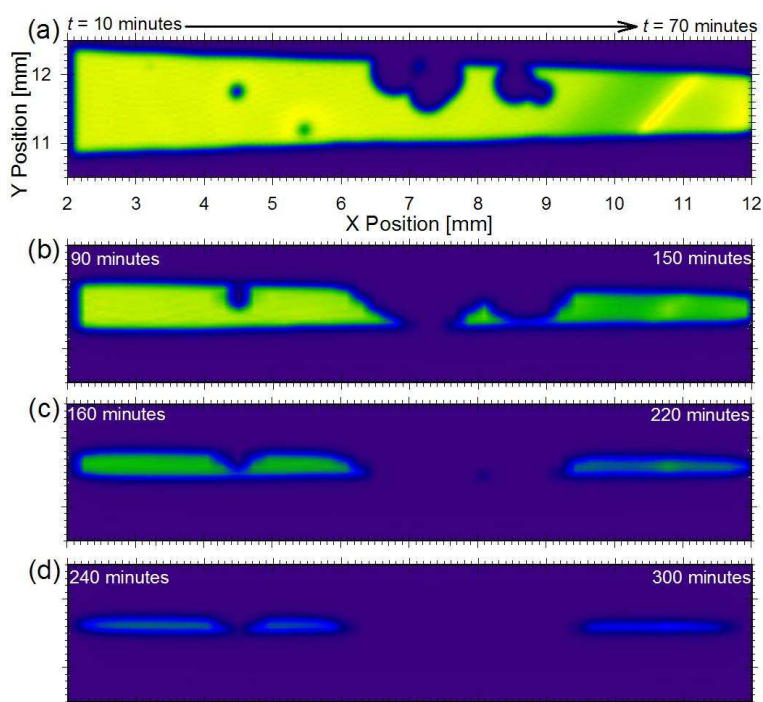


FIGURE 10.3: A sequence of four photocurrent maps for a single non encapsulated device exposed to air in the laboratory. The trapezoidal shape is due to degradation progressing as the measurement is being made.

to grow over time consistent with previous reports [283, 287–289]. In contrast to these reports and in agreement with others [266, 270, 281, 290], we observe that the impact of degradation at pinholes is less important, compared with degradation at the edges of the device. As mentioned in the previous chapter and previously reported by Voroshazi et al. [281], degradation can be seen with the naked eye, see Figure 10.4.

10.3.3 Identifying the diffusant

In order to isolate the contaminant responsible for degradation in our OPV devices we repeat the experiments in three alternate ambient environments: dry air, dry nitrogen and wet nitrogen. In addition, since PEDOT:PSS absorbs water, we repeated the experiments using devices with and without the PEDOT:PSS layer. We observed each device for 10 hours. In samples without the PEDOT:PSS layer, no significant change to the active area of the device was observed. This observation is consistent with Lloyd

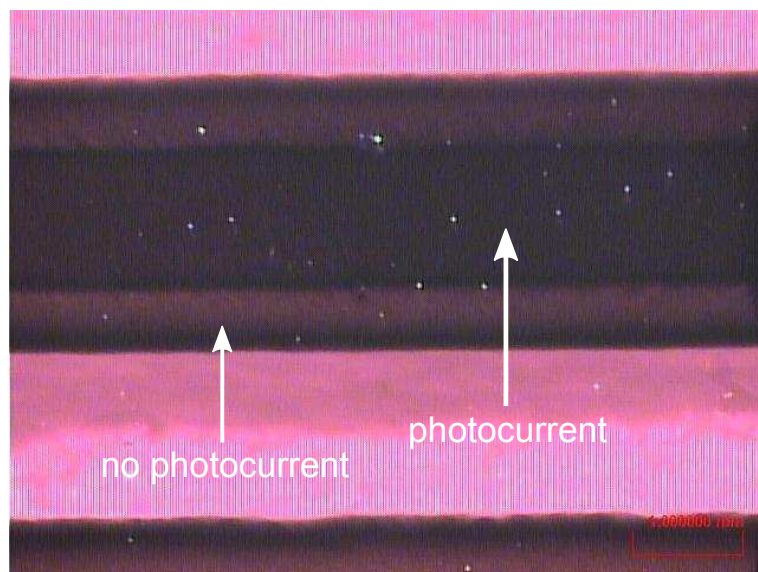


FIGURE 10.4: Optical image of a device that is partially degraded. The light pink areas are non-photoactive areas in between fingers. The top of device is seen at the bottom and the entire width of another device is seen towards the top area of the image. The area that does not exhibit a photocurrent response is slightly lighter in colour than the area that still produces photocurrent.

TABLE 10.1: Degradation of OPV devices in various environments. Devices were monitored for 10 hours.

| Environment | with PEDOT:PSS | without PEDOT:PSS |
|--------------|----------------|-------------------|
| ambient air | degradation | no degradation |
| dry air | no degradation | no degradation |
| wet nitrogen | degradation | no degradation |
| dry nitrogen | no degradation | no degradation |

et al. [296], who showed that the exclusion of PEDOT:PSS from inverted OPV devices leads to uniform device degradation, rather than localised degradation. The results in Table 10.1 show that the combination of water and PEDOT:PSS are responsible for degradation in our devices. This finding is consistent with previous reports [281, 282]. We thus confirm that the primary degradation mechanism in our devices is directly facilitated by the uptake of water by the PEDOT:PSS layer at the cell edges and through pinholes. Although this mechanism requires that water from the atmosphere must first pass down through the active layer of the device, this is not unreasonable,

given that the layer is only 80 nm thick. It has been demonstrated that degradation can be significantly slowed down by using a cathode buffer layer that has water and oxygen blocking properties [297]. It is likely that such a layer prevents rapid water uptake by the PEDOT:PSS layer.

10.3.4 Searching for an oxide layer

Photocurrent mapping results suggest that the rapid degradation of our devices occurs through damage that progresses inward from the long edges of the cell, in a way that locally destroys the charge harvesting ability of the structure. This degradation is consistent with the presence of an insulating oxide layer at the cathode interface. To confirm the presence of such a layer, we conducted XPS depth profiling measurements on two samples: one that was exposed to air as little as possible (referred to as a fresh device), and one that had fully degraded in air (i.e. $\eta=0$). The results are presented in Figure 10.5. Both profiles indicate the presence of aluminium oxide at the surface (top of the cathode), as expected. However, the profile of the degraded device reveals the presence of an aluminium oxide signal at the bottom of the cathode, inside the device, at the interface with the active layer (see Figure 10.5b), in accordance with ref. [283, 287]. An insulating aluminium oxide layer would severely inhibit both charge extraction and conductivity in this type of device. We also observed a small aluminium oxide signal in the fresh sample (Figure 10.5a), which is almost certainly due to small regions of localised degradation at pinholes in the cathode layer in the fresh sample, of the type indicated in Figure 10.2 and 10.3.

Thus we conclude that water ingress leads to the oxidation of aluminium at the internal interface, which is consistent with Voroshazi et al. [281].

10.3.5 Degradation length

Photocurrent maps such as the ones shown in Figure 10.3 allow an analysis of the rate of water ingress into the device. In the following, we make the reasonable assumption that the cathode oxidation reaction occurs very rapidly; and hence, the rate of degradation

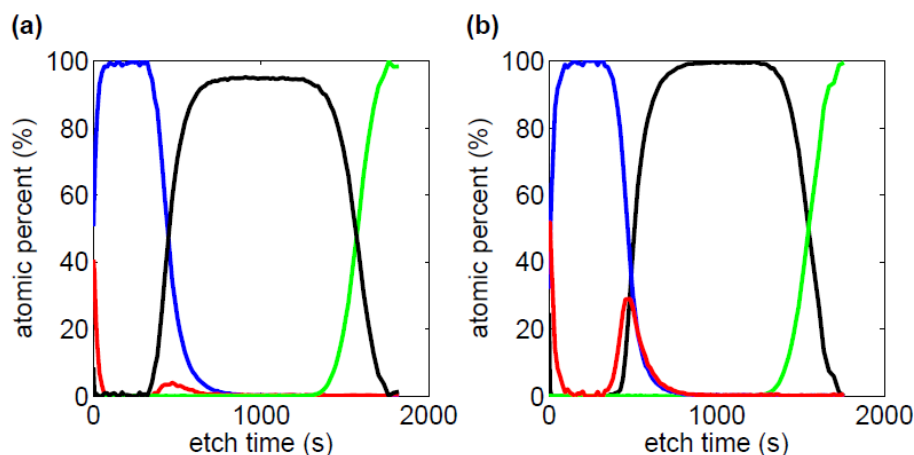


FIGURE 10.5: Normalised XPS depth profiles for (a) a fresh and (b) degraded OPV device. Blue indicates the Al 2p metal state signal; red, the Al 2p oxidised state signal; black, the C 1s signal; and green, the In 3d5 signal.

is limited only by the rate of water diffusion into the device. We also make the further assumption, that the ingress can be described by Fick's Law. In other words, we assume that the rate of diffusion at a given temperature is a function only of the difference in contaminant concentration between any two points. We define the degradation length, x , as the distance by which degradation has proceeded from the device edge; this is obtained by subtracting the width of the observed photoactive area from the width of the aluminium electrode (2 mm) and dividing the result by two. The width is determined by differentiating the measured photocurrent with respect to the y -coordinate if interested in horizontal edges (e.g. long edges in Figure 10.3) or with respect to the x -coordinate if interested in vertical edges (e.g. left edge in Figure 10.11). Figure 10.6 shows a photocurrent map, its spatial derivative with respect to y and an excerpt extracted from the derivative map. Clear maxima and minima are found and thus the photoactive width can easily be determined.

Figure 10.7 shows the degradation length as a function of time, extracted from the series of photocurrent maps shown in Figure 10.3. Points for which the cell width is affected by degradation through pinholes have been discarded for clarity. If we assume the region outside the cell boundary contains the contaminant at a constant

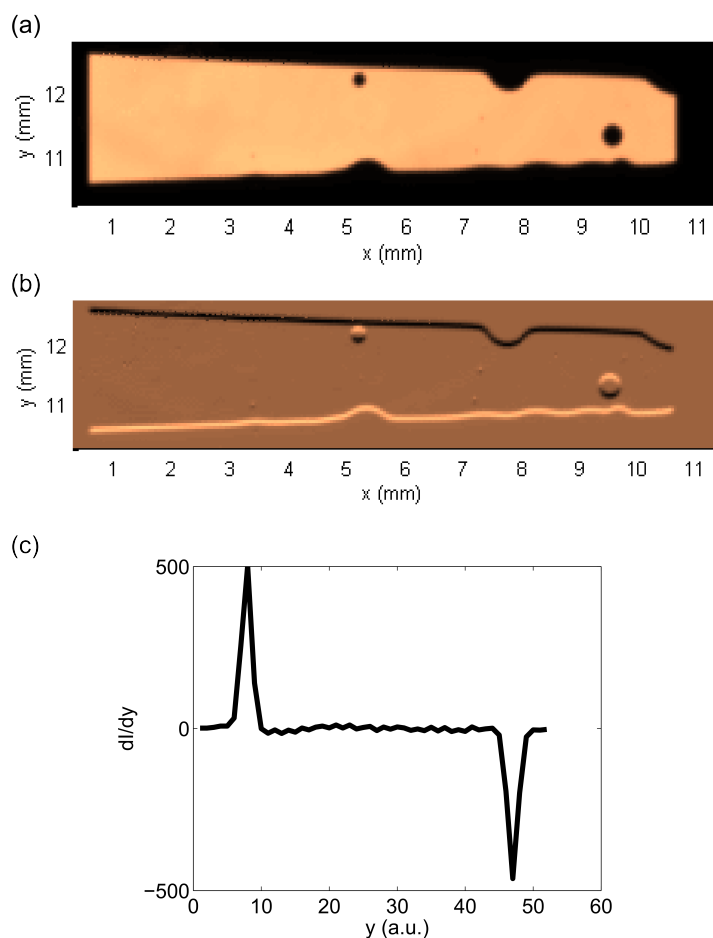


FIGURE 10.6: (a) a photocurrent map of a degrading OPV devices (b) the spatial derivative of (a) with respect to y (c) a line extracted from the spatial derivative map.

concentration, we would expect x to increase with time, t , as [298]:

$$x(t) = \operatorname{erf}^{-1} \left(1 - \frac{C^*}{C_0} \right) \sqrt{4Dt} = a\sqrt{t} \quad (10.3)$$

where D is the diffusion coefficient for the contaminant in the device, C_0 is the contaminant concentration outside the device, C^* is the contaminant concentration required to cause complete local degradation, and a is a rate pre-factor that captures all constants. For a device with a PEDOT:PSS hole-transport layer (HTL) we observe a good fit to this relation (Figure 10.7), consistent with a degradation mechanism that is caused by diffusion from the edges of the device. Based on this fit we extract a value for a of $7.6 \times 10^{-3} \text{ ms}^{-1/2}$ in this device.

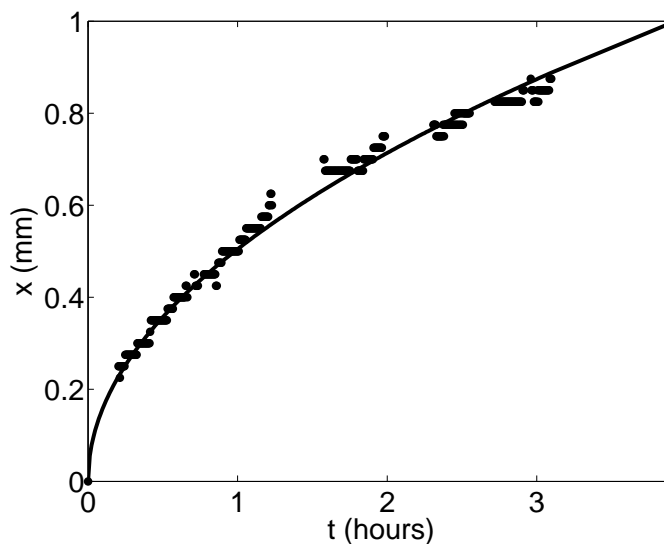


FIGURE 10.7: Degradation length, x , extracted from photocurrent maps, evolves in a \sqrt{t} relationship with time.

10.3.6 Quantifying the increase in water uptake due to PEDOT:PSS

The hygroscopic nature of PEDOT:PSS is known to accelerate water uptake and consequently shorten device lifetimes [281]. This understanding has prompted the use of different materials for the HTL that do not influence water uptake [118]. For example, devices that use MoO_3 instead of PEDOT:PSS have been shown to exhibit longer lifetimes [281]. In order to determine a lower limit for water uptake we prepared and tested a device without any HTL. The result is shown in Figure 10.8(b), where the square of the degradation length exhibits a linear evolution with time and fits with zero intercept as expected. The equivalent result for the device with a PEDOT:PSS layer is included in Figure 10.8(a) for comparison. From the slope of Figure 10.8(b) we determine a value of a for the device with no HTL of $6.3 \times 10^{-4} \text{ ms}^{-1/2}$. Since this parameter effectively describes the rate of diffusion of the contaminant into the device, the result indicates that the presence of a PEDOT:PSS layer has increased the rate of ingress by approximately one order of magnitude.

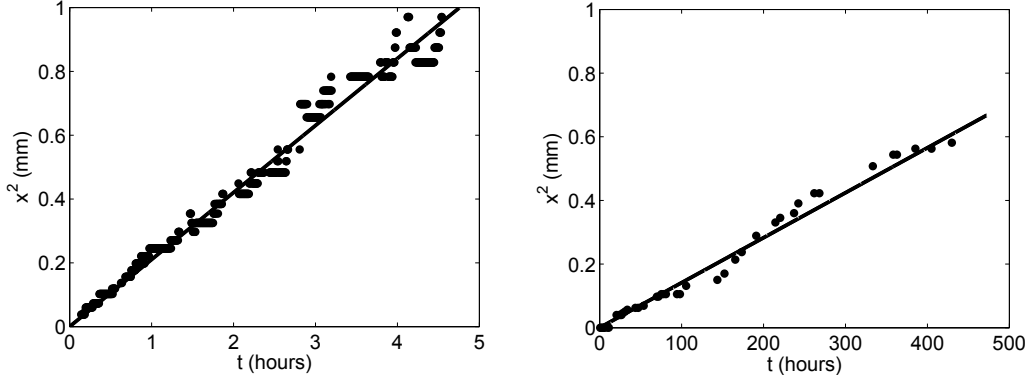


FIGURE 10.8: Evolution of the square of the degradation length with time for a device (a) using a PEDOT:PSS layer and (b) without any hole-transport layer.

10.3.7 Extracting the diffusion coefficient

Equation (10.3) suggests a known relationship between the rate of degradation and the external contaminant concentration, C_0 . Since the degradation-triggering contaminant is water, this provides an opportunity to extract further information about the degradation process by repeating the LBIC measurements under atmospheres with different, known relative humidity levels. Provided temperature and pressure are held constant, the concentration of water in the environment is linearly related to the relative humidity. Hence, for relative humidities r_1 and r_2 , we expect a variation in the rate pre-factor, a , according to:

$$\frac{a_2}{a_1} = \frac{\operatorname{erf}^{-1}(1 - f_2)}{\operatorname{erf}^{-1}(1 - f_1)} = \frac{\operatorname{erf}^{-1}\left(1 - \frac{r_1}{r_2} f_1\right)}{\operatorname{erf}^{-1}(1 - f_1)} \quad (10.4)$$

where $f_n = C^*/C_{0n}$ at the relative humidity of the n th atmosphere.

We repeated the measurement presented in Figure 10.7 under controlled conditions, keeping the relative humidity at 54 % for the first 2.2 hours and then at 66 % for the remainder of the experiment. As shown in Figure 10.9, the growth of degradation was highly sensitive to the change in humidity consistent with our expectations. Based on the slopes of the fits in the two humidity regimes, we observe a relative increase in the rate pre-factor of $a_2/a_1 = 2.58$. On the basis that C^* is independent of the external humidity, we can use a_2/a_1 along with Equation (10.3) to determine a value for the

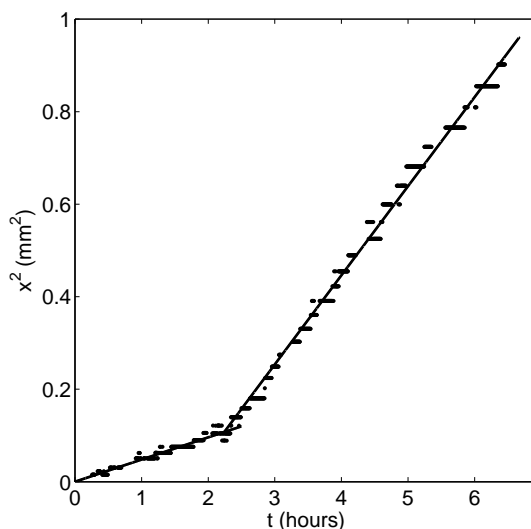


FIGURE 10.9: The square of degradation length as a function of time. At $t = 2.2$ hours, the relative humidity was increased from 54% to 66% while keeping the temperature constant. The lines indicate fits of equation (10.3) to each humidity regime.

diffusion coefficient for water in PEDOT:PSS. We calculate a value of $D = (5.0 \pm 2.7) \times 10^{-6} \text{ cm}^2\text{s}^{-1}$. This result is of the same order as published values for the diffusivity of water in other polymers [299]. For example, Long et al. [300] determined $D = 0.5 \times 10^{-6} \text{ cm}^2\text{s}^{-1}$ for water in cellulose acetate, Sultana et al. [301] determined $D = 1.65 \times 10^{-6} \text{ cm}^2\text{s}^{-1}$ at 50 °C for water in poly(hydroxybutyrate-co-hydroxyvalerate) and Müller-Plathe [302] used molecular dynamics simulations to calculate that D varies from 10^{-7} to $10^{-5} \text{ cm}^2\text{s}^{-1}$ for water in swollen poly(vinyl alcohol) membranes.

The results presented in Figure 10.9 also allow a value for C^* to be extracted using Equation (10.3). Using the 20 °C value for the saturation vapour pressure of water, 2.34 kPa [303], we obtain a water concentration $C^* = 8.4 \pm 0.6 \text{ gm}^{-3}$, or around 6 parts per million by weight in the PEDOT:PSS layer. The premise of a value for C^* however, implies that below this level no degradation occurs. This premise seems to lead to a somewhat non-physical scenario, particularly given that the equivalent concentration in air represents a relative humidity of 49 %. A quick test with a new sample stored under 33 % relative humidity showed that degradation still occurred, albeit more slowly. This test supports the assumption that any water in the device

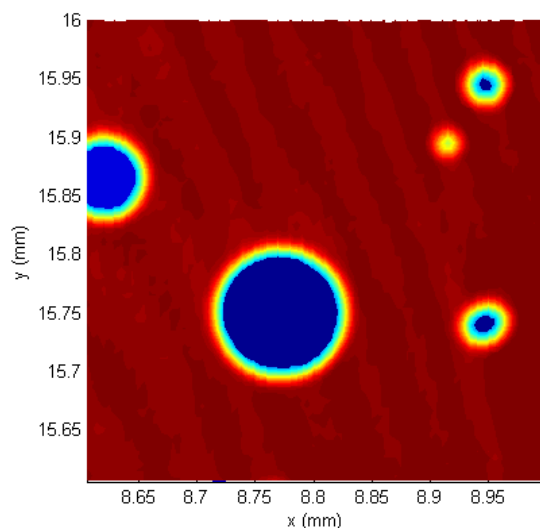


FIGURE 10.10: A photocurrent map of pinholes with different sizes. The spot radius used to obtain this map was $10\ \mu\text{m}$.

leads to degradation at some rate, and hence that the real value for C^* is very small as can be deduced from the data presented in Voroshazi et al. [281]. It follows that the value we have calculated for C^* is too high. This discrepancy can be explained if we challenge our earlier assumption that the degradation rate depends only on the rate of water diffusion in the PEDOT:PSS layer. In this we have ignored the time taken for any other part of the degradation process, including the passage of water across the P3HT:PCBM layer of the cell. If these other steps require significant time, the outcome is that our estimate of the diffusion constant in PEDOT:PSS is slightly low, and our estimate of C^* is high.

10.3.8 Quantifying ingress at pinholes

Since some authors [287–289, 304] have observed that degradation due to water ingress at pinholes is more significant than at the device edges, we have examined the LBIC photocurrent maps to measure the rate of device degradation at pinholes. Pinholes are difficult to control and are observed to have a variety of sizes (see Figure 10.2 and 10.10). Most dead zones appear to be perfectly circular (to within the measurement

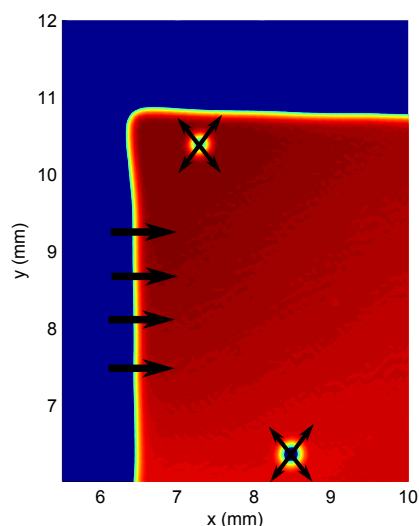


FIGURE 10.11: Photocurrent map of a device with two pinholes, each with a slightly different size, and water entering from the left edge, as indicated by the black arrows.

error), however, the top right and bottom right pinholes in Figure 10.10 are not exactly circular; instead, they resemble some of the shape of the physical pinhole. As diffusion and thus degradation proceeds the original shape of the pinhole blurs until the dead zone appears to be perfectly circular.

Two large round defects were identified (see Figure 10.11) and the growth of their diameter was determined based on twelve consecutive photocurrent maps. The pathway for ingress through a pinhole differs only from that at the device edge by the fact that the pinhole is laterally small. Hence, we assume a \sqrt{t} dependence of the degradation length and a suitable fit takes the form

$$x = a\sqrt{t} + b \quad (10.5)$$

where b is the size of the dead zone at $t = 0$. Since this value is likely to correspond to the size of the physical pinhole, a fit of this form means that the pinhole size can be determined even though pinholes are typically smaller than the resolution of the LBIC measurement.

The results are presented in Figure 10.12 and these show that the degradation length at pinholes is indeed also proportional to \sqrt{t} . Based on the evolution of the degradation

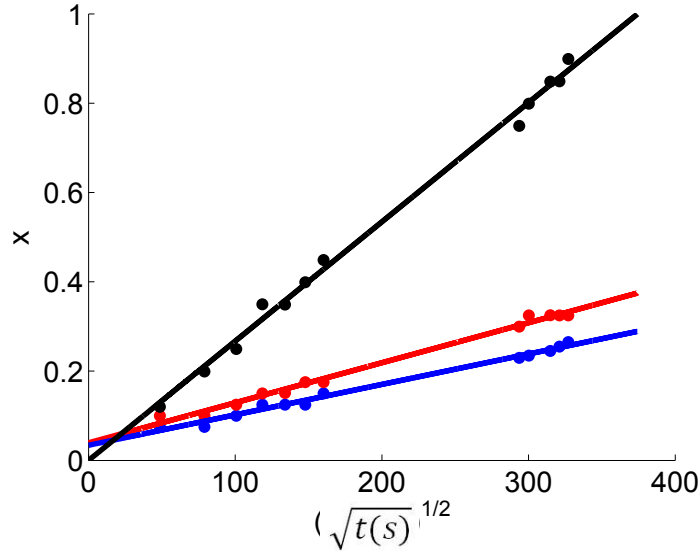


FIGURE 10.12: Degradation length against \sqrt{t} for contaminant ingress at a pinhole with $66 \mu\text{m}$ diameter (blue), $78 \mu\text{m}$ diameter (red) and at the device edge for comparison (black).

length, we determine the diameters of the smaller and larger pinholes to be $66 \mu\text{m}$ and $78 \mu\text{m}$ respectively. The corresponding values for the rate pre-factor, a , for these are $6.8 \times 10^{-3} \text{ ms}^{-1/2}$ and $9.0 \times 10^{-3} \text{ ms}^{-1/2}$, respectively. Since this parameter depends on the environmental humidity, a measurement of edge degradation was extracted from the same photocurrent maps for direct comparison. This result is also shown in Figure 10.12 and for diffusion at an edge the value for a is determined to be $2.7 \times 10^{-2} \text{ ms}^{-1/2}$.

These results indicate that degradation at the chosen pinholes occurs more slowly than at the device edge, and occurs faster for the larger hole. The latter is not unexpected, since it is reasonable to assume that diffusive conductance may be limited by the aperture of a pinhole, with diffusion at an edge being equivalent to a pinhole of infinite diameter. Based on the range of sizes for the round features in Figures 10.2 and 10.10, and our further observation, it is clear that pinholes typically occur in a wide range of sizes. Without examining more pinholes we cannot establish a detailed relationship between pinhole size and the rate pre-factor. However, since we have selected two of the largest round features we have seen in our devices, we can conclude

that degradation at pinholes is unlikely to ever exceed the degradation we observe at the device edge.

10.3.9 Ingress in devices with a silver cathode

We have demonstrated that LBIC photocurrent maps can be used to track the diffusion of water in OPV devices with aluminium cathodes, which suffer a total loss of photoactivity in the affected areas. While aluminium is a common cathode in conventional device designs, inverted device designs typically use a silver cathode. Although silver also oxidises, oxides of silver are electrically conductive and have even been used as interfacial layers to improve performance in OPV devices [305, 306]. Despite the absence of severe degradation, we have found that LBIC measurements can still be used to track the ingress of water in devices with a silver cathode. A representative linescan for a conventional device with a silver cathode is shown in Figure 10.13(a). Figure 10.13 and other linescans indicate a small increase in photocurrent (approx. 3%), which is symmetrically localised to a particular distance from each long edge of the device. This effect can be seen in Figure 10.13(a) in the form of two small bumps at $y = 30$ and $y = 31$ mm (marked A). Analysis of the complete LBIC image (not shown) indicates that these features move inward toward the centre of the cell at approximately the same rate as degradation proceeds in the aluminium cathode devices. Furthermore, the progress of these features exhibits the same \sqrt{t} dependence that we observe in the aluminium cathode devices (see Figure 10.13(b)). We propose that oxidation of the silver cathode is also a result of the ingress of water into the PEDOT:PSS layer, and that the localised increase in photocurrent is due to a favourable temporary oxidation state. The work function of sub stoichiometric oxides of silver varies with oxygen concentration [307] and our results suggest that the most favourable form of silver oxide is not the final oxidation state, but rather some partial oxidation state that occurs during the oxidation process, proceeding through the cell as water diffuses. Kim et al. [308] showed that as silver oxidises its work function increases to the point that the device transitions from a conventional (silver mainly collects electrons) to an inverted device

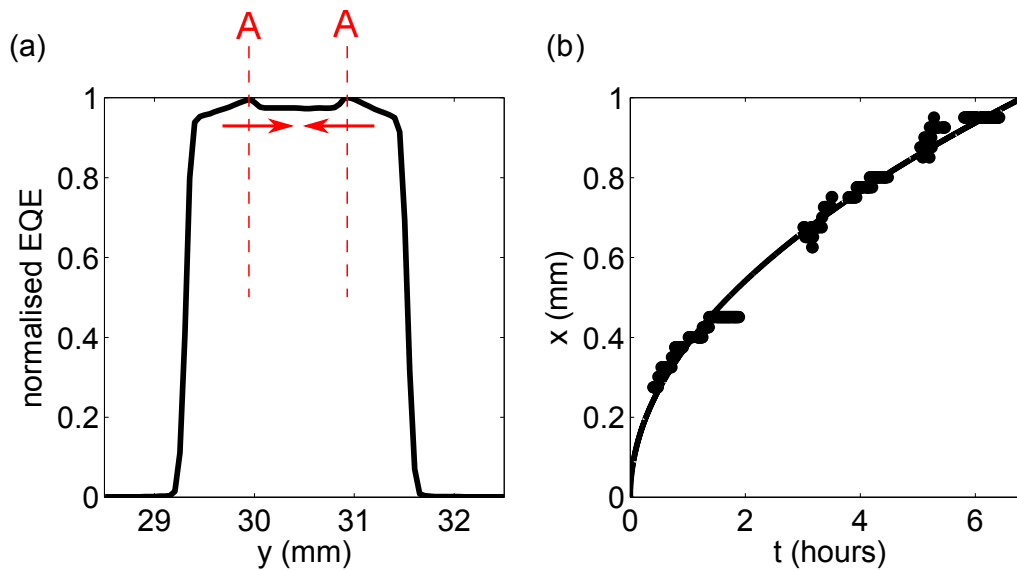


FIGURE 10.13: (a) LBIC line scan across a cell with a silver cathode, indicating two symmetrically located regions of slightly increased photocurrent. Area scans (not shown) indicate these features move inward with a \sqrt{t} time dependence as shown in (b).

(silver mainly collects holes), which supports our theory that the ripple of increased photocurrent must be related to a change in the work function of the non-transparent electrode.

10.3.10 Optimising lateral design for device durability

In order to relate the growth of local degradation to the decay in power conversion efficiency, η , fresh devices were prepared without encapsulation for I-V studies. The devices were stored in air and I-V curves were recorded regularly over 24 hours, with the standard photovoltaic parameters extracted from the data. The two parameters most notably affected were I_{SC} , and the cell series conductance, $1/R_s$ [281, 282]. Figure 10.14 shows typical examples of the variation of these two parameters over time. In Figure 10.14(a), I_{SC} for a cell is seen to decrease linearly with \sqrt{t} . For a rectangular cell with an active length that remains constant but an active width decreasing with \sqrt{t} , this linear relation is precisely what we would expect, based purely on the loss of active cell area. In other words, I_{SC} decay is a direct result of diffusion from parallel device edges dominating the overall loss of photocurrent as observed in Figure 10.3. The variation

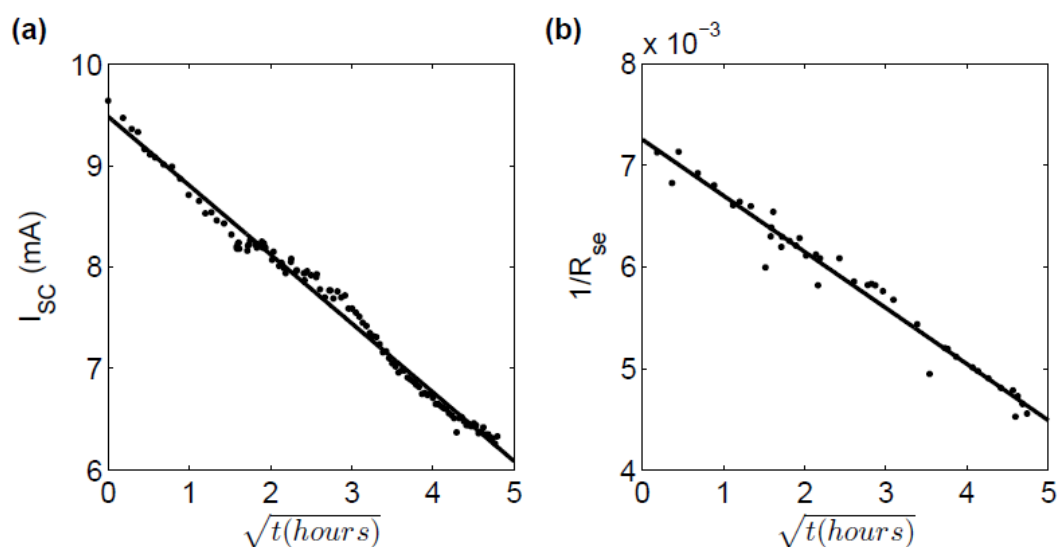


FIGURE 10.14: I-V measurements for non-encapsulated OPV cells stored in air indicate that (a) I_{SC} and (b) series conductance decay linearly with \sqrt{t} in synchrony.

in cell conductance (Figure 10.14(b)) is equally interesting. Its time dependence also shows a clearly linear decrease with \sqrt{t} , with a rate constant identical to that of the photocurrent decay. From this, we infer that the loss of conductive area occurs at the same rate as the loss of photoactive area. We conclude that the contaminant ingress responsible for degradation leads to a change in the cell that simultaneously affects both photoactivity and cell conductance, which is consistent with a decreasing area available for conduction, i.e. aluminium oxidation. Moreover, since the decrease in conductance is consistent with the decrease in photoactive area, the change in R_s of the device is entirely caused by aluminium oxidation and no additional degradation process.

It is important to remember that this ingress is a direct consequence of the lateral device design we have used: in particular, the use of a patterned cathode layer that defines the extent of the cell in a particular dimension. We could equally have designed our devices such that each cell was instead defined by the dimensions of a pattern in the ITO anode layer. This approach would have allowed a continuous cathode layer, which would have significantly delayed the ingress of environmental water at the edges of the cell. Hence, the linear decay with \sqrt{t} as seen in Figure 10.14(a) and (b) are not

universal relationships that hold for all lateral device designs. In general, I_{SC} (and also $1/R_s$) decays due to diffusion from the edges inwards as

$$I_{SC} = k_1 t - k_2 \sqrt{t} + k_3 \quad (10.6)$$

where k_1 , k_2 and k_3 are constants depending on a , the dimensions of the active area and lateral device design.

To illustrate the improvement in lifetime that could be achieved, we have calculated the expected time decay of I_{SC} , R_s and η for our 2 mm \times 10 mm OPV devices, if the cathode layer was extended beyond the cell dimension in various different combinations. While the photoactive dimensions of these devices is the same, the perimeter length that is defined by the cathode is different for each of the 8 lateral device designs. The results are presented in Figure 10.15. Here, we have taken a value for the rate prefactor, a , from our experiments reported above, and assumed that the devices are not subject to degradation by any other mechanism, including the ingress of water through pinholes. This simplification is, of course, not valid for long time scales; but it is useful for illustrating the relative effect of our primary mode of degradation. Knowing how I_{SC} and R_s change over time, efficiency values have been determined assuming the classical one diode model for photovoltaics. The shunt resistance is assumed to be constant with time, as suggested by I-V measurements, and the diode ideality factor was also held constant. For a device of our design, the most durable case is one in which the cathode size and shape permits water ingress only at one of the 2 mm edges of the device, which reduces efficiency by 15 % over the first 5.5 hours. In the worst case, the cell edges are defined entirely by the cathode pattern, thus permitting water ingress at all four edges, resulting in a drop in efficiency of 99.5 % over the same time period. While these explicit decay rates are specific to 2 mm \times 10 mm cells, the concept remains important for all research scale OPV devices of this axial design.

For the best case described here, i.e. edge-diffusion at one short edge only, the rate of degradation is slow enough that we would expect degradation at pinholes to dominate. Indeed, some researchers have reported pinhole-dominated degradation. For example, Seeland et al. [289], used electroluminescence imaging to demonstrate a

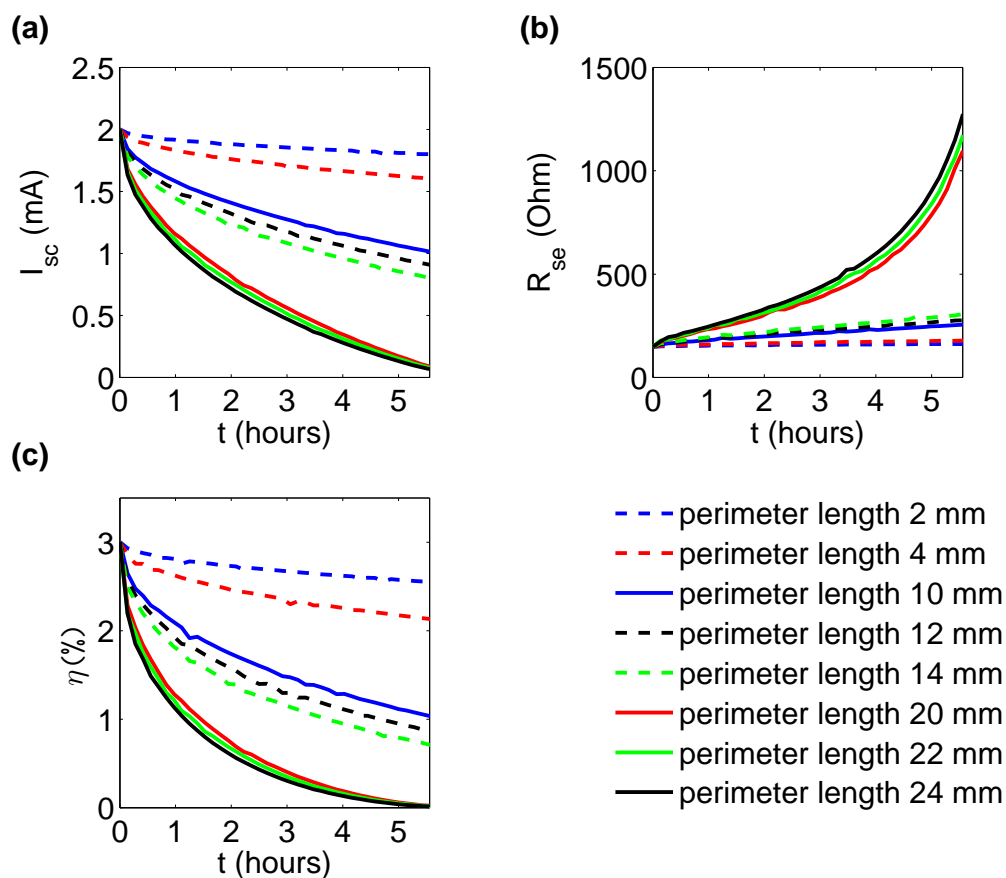


FIGURE 10.15: Predictions for the decay of (a) short-circuit current, (b) series resistance and (c) cell efficiency for a 2 mm \times 10 mm OPV cell of the type used for this study. The eight curves correspond to the eight possible anode-cathode configurations for a rectangular device without changing the cell dimensions. Specifically, dashed blue represents a cathode allowing water ingress at one short edge only; dashed red, at the two short edges; solid blue, at one long edge; dotted red, at one short edge and one long edge; dotted green, at two short edges and one long edge; solid red, at two long edges; solid green, at two long edges and one short edge; and solid black, at all edges of the device. The corresponding perimeter length of the photoactive area that is defined by the cathode is shown in the legend.

degradation pattern consistent with water ingress through pinholes, rather than from edges. In that study, devices of the same axial structure (i.e. ITO / PEDOT:PSS / P3HT:PCBM / aluminium) had a lifetime that was an order of magnitude higher than the results presented here. On the basis of our results, we argue that the choice of a particular lateral device design can strongly influence the rate and the pattern of device degradation and should be discussed whenever results of OPV cell degradation are reported, especially when devices with different lateral device designs are compared.

10.4 Conclusion

We have used a photocurrent mapping technique to study degradation features in organic solar cells with the common axial structure of ITO / PEDOT:PSS / (P3HT PCBM) / cathode, in which the primary degradation mechanism is the oxidation of the aluminium cathode due to water ingress as established by XPS depth profiling measurements and LBIC measurements under various atmospheres. Aluminium oxidation leads to complete local inhibition of charge extraction as well as an increase in the series resistance and hence fill-factor of the device. Over most of its area the cathode layer is protective against water ingress, however water enters the device via diffusion through pinholes in the layer, and also at the edge. This effect is accelerated by the presence of the hygroscopic PEDOT:PSS layer. Using a model for diffusion into the device we have established that the acceleration of the diffusion rate due to a 35 nm PEDOT:PSS layer is approximately a factor of 10.

We see evidence that degradation at pinholes occurs more slowly than at the device edge, and that a larger pinhole leads to a higher rate of local degradation near the pinhole, compared with a smaller pinhole. We find this reasonable on the basis that the diffusive ingress of water through pinholes is likely to be limited to a degree by the conductance of the pinhole aperture. Since pinholes in the cathode exhibit a distribution of sizes, their role in degradation varies, however even for the largest pinhole in our devices, the rate of water ingress is lower than occurs at the cathode edge by a factor of approximately 3.

We observe that degradation at the edges of a cell may be significantly slowed by designing the device such that the cathode layer extends beyond the edge of the active cell, i.e. by defining the edges of the cell with the ITO pattern, rather than the cathode pattern. Such a lateral device design would significantly increase the time taken for water to reach the active area of the cell, and explains why some authors report degradation at pinholes as more important.

Our diffusion calculation was used to determine the diffusivity of water in PEDOT:PSS to be $(5.0 \pm 2.7) \times 10^{-6} \text{ cm}^2\text{s}^{-1}$. The determination of this value did not

exclusively require complete local degradation of cell performance; the method also worked for devices with a silver cathode, where we instead tracked the path of a localised region showing improved cell performance. We attribute this small improvement to the formation of a temporary sub oxide of silver that moves through the device along with the front of water ingress. The applicability of the method to more than one cathode material suggests it may be useful for a range of OPV device types, both traditional and inverted, and may provide a useful tool for studying the performance of encapsulation in devices close to the commercialisation stage.

The diffusion calculation was combined with the classical one-diode model for photovoltaics to model the impact of lateral device design on the overall cell performance. We quantify the sensitivity of the device lifetime to the placement of the cathode edge. It is clear that the lateral architecture of the device affects its durability and hence any reported durability results should be placed in the context of a specific device design.

Thus, under certain conditions degradation could be slowed down sufficiently to not significantly affect relatively fast I-V measurements conducted in air. However, considering the multitude of factors that accelerate degradation, it is always better to encapsulate devices prior to device characterisation in air.

11

Conclusion and Further Work

11.1 Conclusion

A DMC model has been developed and is designed to function as a virtual organic solar cell. The DMC approach provides a platform where various established theoretical models can be combined to model all relevant processes in an organic solar cell. Each OPV process has a probability of occurring and has an associated rate, which may be estimated using established theories.

Optical modelling was conducted using a transfer-matrix approach and provided the exciton generation profile in an OPV device.

Exciton transport was modelled using FRET. In chapter 5 the modular nature of the DMC approach was highlighted by comparing a simple random walk to FRET for exciton transport modelling. Exciton transport single component systems modelled

using FRET cannot be distinguished from the exciton hopping behaviour as modelled using a simple random walk. Consequently, increased computational efficiency may be achieved when determining exciton diffusion parameters in single component systems. In a two-component OPV system, however, a simple random walk approach will result in an underestimation of geminate recombination and overestimates photocurrent by up to 2 % due to the neglect of energy relaxation and non-nearest neighbour hopping. Simulation results indicate that materials with larger exciton diffusion lengths will be less susceptible to variations in the morphology.

Marcus theory was used to predict charge transport behaviour while accounting for Gaussian energy disorder, Coulomb interaction with other charge carriers and image charge carriers, the internal electric field and energy barriers at the electrodes. Experimental validation of the DMC model was provided by simulating and measuring IQE and J_{SC} as a function of thickness for a standard P3HT:PCBM device. Excellent agreement was achieved and the model was further used to investigate the electrode/active layer interface of our devices and in particular the ability of this interface to block charge carriers. It was found that this interface is the dominant recombination process for thin active layers (< 100 nm). Further support for this conclusion was found in XPS depth profiling results, which reveal interface mixing at both electrode interfaces. A substantial gain in efficiency may be achieved by improving charge selectivity at the electrodes, in particular the anode. This work demonstrated the effectiveness of DMC models to analyse and predict OPV device performance.

Charge injection was modelled using Miller-Abrahams expressions thus allowing for the calculation of full I-V curves, the standard experimental measurement for determining solar cell efficiency. A model is most useful when it is able to simulate both well performing OPV devices and devices that exhibit poor performance in the form of anomalous I-V behaviour. Simulating s-shaped I-V curves in a meaningful manner has been proven to be a challenge when using models such as the electrical circuit equivalent model or drift-diffusion type approaches. The ability of the DMC model to predict s-shaped I-V curves was explored. While excitons cannot induce a voltage dependent

change in current (excitons are an electrically neutral species), DMC modelling predicts that energy traps certainly reduces the exciton diffusion length and consequently affects exciton dissociation. Electron traps were predicted to affect I-V behaviour. Traps in the bulk of the active layer lead to a reduction in J_{SC} , V_{OC} and PCE, but do not induce s-shaped I-V curves nor do they reduce FF significantly. Traps that are located at the electrode interface, on the other hand, do induce s-shaped behaviour. The s-shape becomes more pronounced as the trap density or depth increases. As such, the electrode-active layer interface was identified as being crucial in preventing s-shape effects. Despite the fact that interface recombination is found to cause s-shaped behaviour, measured and simulated I-V measurements under various light intensities show that injected charges do not induce s-shaped I-V curves, rather photogenerated charge carriers are necessary to observe the s-shape anomaly. Contrary to expectations, DMC simulations indicate that increasing bulk charge recombination reduces the severity of the s-shape, which suggests that OPV material systems that exhibit little charge recombination are more likely to exhibit s-shaped I-V curves. V_{OC} is observed to not always coincide with the centre of the 's' and could be changed by tuning charge recombination. Previous reports showed that a thermal annealing treatment removes s-shaped behaviour and also showed that annealing influences both vertical phase segregation and clustering of isolated aluminium islands. Since the latter two effects occur at the same time it is difficult to identify which of the two removed the inflection. DMC modelling allowed us to investigate the two effects separately. Vertical phase composition was found to affect J_{SC} , V_{OC} , FF and PCE, but did not induce s-shape I-V curves. Instead charge traps such as isolated islands of organic material or aluminium could induce s-shaped I-V behaviour. Hence, DMC modelling suggests that vertical phase composition at the electrodes is not the cause of inflected I-V curves, but rather the presence aluminium nanoclusters is the cause of this anomalous behaviour.

The ability of the DMC model to model any 3D nanostructure has been highlighted in literature. While many different axial architectures have been explored, an investigation of core-shell nanoparticle morphologies was not reported. Nanoparticle based active layer eliminate the need for organic solvents during the deposition stage and

is consequently the preferred approach from a health, safety and environmental point of view. For the first time, core-shell morphologies have been analysed using a DMC model. STXM measurements were used to estimate and construct 3D core-shell structures. The impact that the core-shell morphology has on IQE and J_{SC} was investigated and results were compared to that of a BHJ structure. Modelling results show that an optimum nanoparticle size exists. This optimum as found in the simulations approximately corresponds to the optimum nanoparticle size as determined experimentally. Not only the effect of nanoparticle size was explored, but nanostructures with different feature sizes were investigated. Nanoparticle morphologies systematically performed better as the feature size increases up to the maximum feature size that was investigated (~ 14.1 nm). Since the experimentally measured data has a similar evolution with nanoparticle size as the simulated morphologies with a small feature size, it is likely that significant improvements could be achieved by annealing for a longer period of time or at a higher temperature in order to induce a larger feature size. Indeed, Stapleton's [106] results show that unlike the BHJ morphology, P3HT:PCBM nanoparticle device performance could indeed be systematically improved by increasing the annealing time. J_{SC} as a function of nanoparticle size exhibited a second maximum for the morphologies with a larger feature size. Thus, DMC modelling highlights that devices should be re-optimised for nanoparticle size when changing annealing conditions. The shell of P3HT:PCBM nanoparticles consist of ~ 75 % P3HT and ~ 25 % PCBM. The lack of PCBM in the shell may severely limit charge extraction. Indeed, in all instances, the BHJ structure was found to perform better than the core-shell structure. However, the performance of core-shell nanoparticles approaches that of the BHJ morphology, when optimised for both feature size and nanoparticle size. Hence, the core-shell morphology need not be severely limited by a P3HT-rich shell and, in theory, optimised nanoparticle devices should yield similar efficiencies as optimised BHJ devices.

The performance of organic solar cells is not only affected by nanoscopic processes, but is also influenced by a range of macroscopic variations. These spatial variations are the result of imperfect fabrication techniques or degradation. These two undesired effects are not explicitly considered in the DMC model and can skew experimental

results, which obscures the comparison of experimental and simulated results. Hence, it is important to investigate these lateral effects. The spatially non-uniform nature of these effects requires a spatially sensitive characterisation technique, which is why a photocurrent mapping technique was developed. This apparatus was developed to allow for photocurrent mapping of devices up to 25 cm^2 with a resolution down to $\sim 3 \mu\text{m}$. The technique was applied to identify and understand a range of lateral non-uniformities. Photocurrent mapping results highlight the importance of masking OPV devices to prevent erroneous whole-cell measurements.

The photocurrent mapping apparatus was also employed to investigate the primary degradation mechanism in standard P3HT:PCBM devices. The primary degradation mechanism in our organic solar cells is the oxidation of the aluminium cathode, which is driven by water ingress at the device edge and through pinholes in the cathode. A diffusion model was applied, which allowed for the determination of the diffusion rate and also the diffusivity of water in PEDOT:PSS. It was established that the diffusion rate of water into a standard OPV device due to the incorporation of a 35 nm PEDOT:PSS layer is approximately a factor of 10 higher compared to a device without PEDOT:PSS. By monitoring the diffusion through a pinhole the physical pinhole size could be estimated. It was also shown that diffusion through pinholes is significantly slower than at an aluminium edge. The diffusion calculation was combined with the classical one-diode model to quantify the effect of lateral device design on the degradation rate. It was found that even when the nominal photoactive dimensions are the same, lateral device design can substantially influence the degradation rate and pattern. Consequently, a comparison of device lifetimes is only meaningful if the lateral device design is equivalent in terms of the diffusion rate and pattern. The photocurrent mapping technique was thus demonstrated to be very useful in assessing diffusion rates and patterns and since the same approach can be taken for devices that utilize silver instead of aluminium, the method may provide a useful tool for studying the performance of encapsulation in (mini)modules (with an inverted structure). Finally, it was concluded that encapsulation prior to device characterisation in air is necessary to prevent apparent mismatch between simulated and measured results.

11.2 Further Work

In this thesis the DMC model has been shown to accurately predict device performance and the model was also used to understand OPV device behaviour.

Many more OPV material systems (not just P3HT:PCBM) could be investigated using the DMC model. Furthermore, continuing to use the DMC model to understand OPV device behaviour is valuable in increasing the general understanding of these devices. For example, FF is often poorly understood and the DMC model could aid in identifying which parameters (charge mobility, charge blocking properties at electrode interfaces, bulk recombination, Gaussian energy disorder, morphology etc.) affect FF the most.

In addition to using the DMC model for certain purposes, the model itself should continue to be improved. Recently, it has been reported that the HOMO-HOMO offset drives the charge creation yield in a manner that is consistent with Marcus theory [181]. In the DMC model the charge recombination rate and exciton dissociation rate are fitting parameters. Instead, Marcus theory could be used to determine these straight from the HOMO and LUMO levels of the organic semiconductors. Such an approach would further expand the capabilities of the virtual organic solar cell as material systems could be investigated without having to fit against experimental data. However, more experimental data would be needed to conclusively justify the use of Marcus theory in determining charge recombination rates.

The DMC model contains several fitting parameters that may be determined from separate measurements. For example, exciton hopping parameters may be determined from photoluminescence measurements and charge hopping parameters from current-voltage characteristics and charge mobility measurements. Energy levels as well as energy barriers at interfaces can be determined from ultraviolet photoelectron spectroscopy. However, in order to truly make an organic solar cell, experimental measurements should not be needed to pin down these parameters. Instead, these parameters should follow from quantum mechanical calculations. The DMC model was developed, because the calculations involved with a purely quantum mechanical approach to model

an entire organic solar cell is too time consuming. However, future work may be focussed on extracting the fitting parameters from quantum-chemical calculations, which could then be fed into the DMC model. In this way, a truly virtual organic solar cell could be created. Such a model would be extremely powerful as materials could be screened prior to synthesis and time would not be wasted in trying to make efficient solar cells with materials that have inherent drawbacks in terms of their photovoltaic performance. Energy levels are frequently determined using density functional theory. In principle, this quantum mechanical method should also provide enough information to estimate the optical properties of materials. An estimation of charge and energy transfer properties between nearby molecules could also be obtained from quantum mechanical approaches. Perhaps the biggest challenge would be to predict the morphology of an OPV device, purely based on quantum chemical calculations. However, I do believe these challenges can eventually be met and research should continue to focus on creating a virtual organic solar cell that does not need input from experimental measurements.

Finally, the main downside of DMC modelling, the computational load, should be addressed as well. The most time consuming part is calculating Coulomb interaction between all charge carriers. Since this calculation involves addition and subtraction of many numbers, parallel computing may assist in decreasing the computational time. From an implementation point of view, an additional decrease in computational time may be achieved by switching from the programming language Matlab to Fortran.



Random walk diffusion length relations

By definition, L is given by

$$L^2 = \langle r^2 \rangle \quad (\text{A.1})$$

where r is the distance between start point and end point. For a random walk, the diffusion length scales with the number of steps taken, N . The distance after N steps is denoted as r_N . The distance travelled in one step is always either $+a$ or $-a$. So, if we consider the 1 dimensional case and relate r_N to the distance of its previous step we have

$$\langle r_N^2 \rangle = \langle (r_{N-1} \pm a)^2 \rangle = \langle r_{N-1}^2 + a^2 \pm 2ar_{N-1} \rangle = \langle r_{N-1}^2 \rangle + \langle a^2 \rangle \pm 2\langle a \rangle \langle r_{N-1} \rangle \quad (\text{A.2})$$

Since $\langle a \rangle = 0$, the last term disappears and we have

$$\langle r_N^2 \rangle = \langle r_{N-1}^2 \rangle + \langle a^2 \rangle \quad (\text{A.3})$$

Now, the same can be done for r_{N-1} , which would give

$$\langle r_N^2 \rangle = \langle r_{N-2}^2 \rangle + \langle a^2 \rangle + \langle a^2 \rangle = \langle r_{N-2}^2 \rangle + 2\langle a^2 \rangle \quad (\text{A.4})$$

We can keep doing this until we reach the very first step, which gives us the equation we are looking for:

$$\langle r_N^2 \rangle = N\langle a^2 \rangle \quad (\text{A.5})$$

The lattice constant used in the DMC model is 1 nm and thus

$$N = L^2 \quad (\text{A.6})$$

The three dimensional version is easily found as

$$\langle r^2 \rangle = \langle r_x^2 \rangle + \langle r_y^2 \rangle + \langle r_z^2 \rangle = 3N\langle a^2 \rangle \quad (\text{A.7})$$

or

$$L = \sqrt{3}L_x \quad (\text{A.8})$$

where L_x is the diffusion length in one dimension.

References

- [1] M. Zeman. *Solar energy*. In *Solar Cells (Introduction to photovoltaic solar energy, course reading)*, chap. 1, p. 1 (Delft). [1](#)
- [2] E.-D. Graßl, H.; Kokott, J.; Kulesa, M.; Luther, J.; Nuscheler, S.; Sauerborn, R.; Schellnhuber, H.-J.; Schubert, R.; Schulze. *World in Transition: Towards Sustainable Energy Systems* (Earthscan, London: Sterling, VA, 2004). [1](#), [2](#)
- [3] O. Teske, Sven; Zervos, Arthouros; Schäfer. *Energy Revolution: A sustainable world energy outlook* (2007). [1](#), [2](#)
- [4] M. D. Archer and R. Hill, eds. *Clean electricity from photovoltaics* (World Scientific Pub Co Inc, London, 2001). [1](#), [2](#)
- [5] T. Ameri, G. Dennler, C. Lungenschmied, and C. J. Brabec. *Organic tandem solar cells: A review*. *Energy Environ. Sci.* **2**(4), 347 (2009). [2](#)
- [6] A. Mishra and P. Bäuerle. *Small molecule organic semiconductors on the move: promises for future solar energy technology*. *Angew. Chem. Int. Ed.* **51**(9), 2020 (2012). [2](#)
- [7] F. C. Krebs. *Fabrication and processing of polymer solar cells: A review of printing and coating techniques*. *Sol. Energy Mater. Sol. Cells* **93**(4), 394 (2009). [2](#)

- [8] S. E. Shaheen, D. S. Ginley, G. E. Jabbour, and G. Editors. *Organic-Based Photovoltaics : Toward Low-Cost Power Generation*. MRS Bull. **30**(January), 10 (2005). [2](#)
- [9] M. A. Green, K. Emery, Y. Hishikawa, W. Warta, and E. D. Dunlop. *Solar cell efficiency tables (version 39)*. Prog. Photovoltaics Res. Appl. **20**(1), 12 (2012). [2](#), [19](#)
- [10] B. Muhsin, J. Renz, K.-H. Drüe, G. Gobsch, and H. Hoppe. *Efficient polymer solar cell modules*. Synth. Met. **159**(21-22), 2358 (2009). [2](#)
- [11] M. Niggemann, B. Zimmermann, J. Haschke, M. Glatthaar, and a. Gombert. *Organic solar cell modules for specific applications From energy autonomous systems to large area photovoltaics*. Thin Solid Films **516**(20), 7181 (2008). [2](#)
- [12] W. Salaneck, R. Friend, and J. Brédas. *Electronic structure of conjugated polymers: consequences of electronlattice coupling*. Phys. Rep. **319**(6), 231 (1999). [6](#)
- [13] C. Deibel and V. Dyakonov. *Polymerfullerene bulk heterojunction solar cells*. Rep. Prog. Phys. **73**(9), 096401 (2010). [6](#)
- [14] J. C. Bernède. *Organic Photovoltaic Cells: History, Principle and Techniques*. J. Chil. Chem. Soc. **53**(3), 1549 (2008). [6](#)
- [15] Wikipedia. *Benzene* (2009). [7](#)
- [16] H. Hoppe, S. N. Sariciftci, and N. Serdar. *Polymer Solar Cells*. In S. Marder and K.-S. Lee, eds., *Photoresponsive Polymers II: Advances in Polymer Science*, vol. 214, pp. 1–86 (Springer Berlin/Heidelberg, 2008). [7](#), [12](#), [15](#)
- [17] H. Spanggaard and F. C. Krebs. *A brief history of the development of organic and polymeric photovoltaics*. Sol. Energy Mater. Sol. Cells **83**, 125 (2004). [7](#), [14](#), [16](#)

- [18] F. Meyers, A. J. Heeger, and J. L. Bredas. *Fine tuning of the band gap in conjugated polymers via control of block copolymer sequences*. J. Chem. Phys. **97**(4), 2750 (1992). [7](#)
- [19] C. Winder and N. S. Sariciftci. *Low bandgap polymers for photon harvesting in bulk heterojunction solar cells*. J. Mater. Chem. **14**(7), 1077 (2004). [8](#), [9](#), [10](#), [11](#)
- [20] P. W. M. Blom, V. D. Mihailetschi, L. J. A. Koster, and D. E. Markov. *Device Physics of Polymer:Fullerene Bulk Heterojunction Solar Cells*. Adv. Mater. **19**(12), 1551 (2007). [8](#), [9](#), [10](#), [12](#), [13](#), [14](#)
- [21] L. Bian, E. Zhu, J. Tang, W. Tang, and F. Zhang. *Recent progress in the design of narrow bandgap conjugated polymers for high-efficiency organic solar cells*. Prog. Polym. Sci. **37**(9), 1292 (2012). [8](#)
- [22] R. Kroon, M. Lenes, J. C. Hummelen, P. W. M. Blom, and B. de Boer. *Small Bandgap Polymers for Organic Solar Cells (Polymer Material Development in the Last 5 Years)*. Polym. Rev. **48**(3), 531 (2008). [8](#)
- [23] A. Mozer and N. Sariciftci. *Conjugated polymer photovoltaic devices and materials*. C.R. Chim. **9**(5-6), 568 (2006). [8](#)
- [24] M. C. Scharber, D. Mühlbacher, M. Koppe, P. Denk, C. Waldauf, A. J. Heeger, and C. J. Brabec. *Design Rules for Donors in Bulk-Heterojunction Solar Cells Towards 10 % Energy-Conversion Efficiency*. Adv. Mater. **18**(6), 789 (2006). [9](#), [54](#)
- [25] C. J. Brabec, A. Cravino, D. Meissner, N. S. Sariciftci, T. Fromherz, M. T. Rispens, L. Sanchez, and J. C. Hummelen. *Origin of the Open Circuit Voltage of Plastic Solar Cells*. Adv. Funct. Mater. **11**(5), 374 (2001). [9](#), [54](#)
- [26] A. Gupta, A. Ali, A. Bilic, M. Gao, K. Hegedus, B. Singh, S. E. Watkins, G. J. Wilson, U. Bach, and R. A. Evans. *Absorption enhancement of oligothiophene dyes through the use of a cyanopyridone acceptor group in solution-processed organic solar cells*. Chem. Commun. **48**(13), 1889 (2012). [9](#)

- [27] O. Güllü and A. Türüt. *Photovoltaic and electronic properties of quercetin/p-InP solar cells*. Sol. Energy Mater. Sol. Cells **92**(10), 1205 (2008). [9](#)
- [28] K. R. Rajesh and C. S. Menon. *Electrical and optical properties of vacuum deposited MnPc thin films*. Eur. Phys. J. B **47**(2), 171 (2005).
- [29] F. Yakuphanoglu. *Electrical conductivity, optical and metalsemiconductor contact properties of organic semiconductor based on MEH-PPV/fullerene blend*. J. Phys. Chem. Solids **69**(4), 949 (2008). [9](#)
- [30] L. A. A. Pettersson, L. S. Roman, and O. Inganäs. *Modeling photocurrent action spectra of photovoltaic devices based on organic thin films*. J. Appl. Phys. **86**(1), 487 (1999). [9](#), [10](#), [37](#), [104](#)
- [31] B. Jin, Y. Kim, S. H. Kim, H.-H. H.-h. Lee, K. Lee, W. Ma, X. Gong, A. J. Heeger, and J. Y. Y. Kim. *New Architecture for High-Efficiency Polymer Photovoltaic Cells Using Solution-Based Titanium Oxide as an Optical Spacer*. Adv. Mater. **18**(5), 572 (2006). [9](#), [10](#)
- [32] B. A. Gregg and M. C. Hanna. *Comparing organic to inorganic photovoltaic cells: Theory, experiment, and simulation*. J. Appl. Phys. **93**(6), 3605 (2003). [10](#), [12](#), [13](#), [14](#), [16](#)
- [33] S. Günes, H. Neugebauer, and N. S. Sariciftci. *Conjugated polymer-based organic solar cells*. Chem. Rev. **107**(4), 1324 (2007). [10](#), [16](#), [22](#)
- [34] H. Borchert. *Elementary processes and limiting factors in hybrid polymer/nanoparticle solar cells*. Energy Environ. Sci. **3**(11), 1682 (2010). [10](#)
- [35] B. A. Gregg. *The photoconversion mechanism of excitonic solar cells*. MRS Bull. **30**, 20 (2005). [10](#), [12](#)
- [36] J. L. Birman and N. Q. Huong. *Wannier-Frenkel hybrid exciton in organic semiconductor quantum dot heterostructures*. J. Lumin. **125**(1-2), 196 (2007). [11](#), [12](#)

- [37] M. Knupfer and J. Fink. *Size and dispersion of excitons in organic semiconductors*. Synth. Met. **141**(1-2), 21 (2004). [11](#), [12](#), [47](#)
- [38] B. A. Gregg. *Excitonic Solar Cells*. J. Phys. Chem. B **107**(20), 4688 (2003). [14](#), [16](#)
- [39] Y. Liu, M. A. Summers, C. Edder, J. M. J. Fréchet, and M. D. McGehee. *Using Resonance Energy Transfer to Improve Exciton Harvesting in Organic-Inorganic Hybrid Photovoltaic Cells*. Adv. Mater. **17**(24), 2960 (2005).
- [40] R. N. Marks, J. J. M. Halls, D. D. C. Bradley, R. H. Friend, and A. B. Holmes. *The photovoltaic response in poly(p-phenylene vinylene) thin-film devices*. J. Phys. Condens. Matter **6**(7), 1379 (1994).
- [41] R. C. Powell and Z. G. Soos. *Singlet exciton energy transfer in organic solids*. J. Lumin. **11**(1-2), 1 (1975).
- [42] G. Li, R. Zhu, and Y. Yang. *Polymer solar cells*. Nat. Photonics **6**(3), 153 (2012).
- [43] R. R. Lunt, N. C. Giebink, A. A. Belak, J. B. Benziger, and S. R. Forrest. *Exciton diffusion lengths of organic semiconductor thin films measured by spectrally resolved photoluminescence quenching*. J. Appl. Phys. **105**(5), 053711 (2009). [56](#), [57](#), [82](#), [88](#)
- [44] M. Riede, T. Mueller, W. Tress, R. Schueppel, and K. Leo. *Small-molecule solar cells-status and perspectives*. Nanotechnology **19**(42), 424001 (2008). [143](#)
- [45] E. Faulques, V. G. Ivanov, G. Jonusauskas, H. Athalin, O. Pyshkin, J. Wéry, F. Massuyeau, and S. Lefrant. *Ultrafast photoluminescence spectroscopy of exciton-exciton annihilation in oligoaniline films with nanoscale ordering*. Phys. Rev. B **74**(7), 075202 (2006). [12](#)
- [46] P. Peumans, A. Yakimov, and S. R. Forrest. *Small molecular weight organic thin-film photodetectors and solar cells*. J. Appl. Phys. **93**(7), 3693 (2003). [12](#), [57](#), [82](#), [83](#), [86](#), [92](#), [103](#), [129](#)

- [47] J. Kalinowski, W. Stampor, P. Di Marco, and F. Garnier. *Photogeneration of charge in solid films of α -sexithiophene*. Chem. Phys. **237**(1-2), 233 (1998). [12](#), [57](#), [60](#), [92](#)
- [48] V. Gulbinas, Y. Zaushitsyn, V. Sundström, D. Hertel, H. Bässler, and A. Yartsev. *Dynamics of the Electric Field-Assisted Charge Carrier Photogeneration in Ladder-Type Poly(Para-Phenylene) at a Low Excitation Intensity*. Phys. Rev. Lett. **89**(10), 89 (2002). [12](#), [13](#)
- [49] D. Basko and E. Conwell. *Theory of hot exciton dissociation in conjugated polymers*. Synth. Met. **139**(3), 819 (2003). [13](#)
- [50] V. I. Arkhipov, E. V. Emelianova, and H. Bässler. *Hot Exciton Dissociation in a Conjugated Polymer*. Phys. Rev. Lett. **82**(6), 1321 (1999). [13](#), [15](#)
- [51] C. Im, E. V. Emelianova, H. Bässler, H. Spreitzer, and H. Becker. *Intrinsic and extrinsic charge carrier photogeneration in phenyl-substituted polyphenylenevinylene-trinitrofluorenone blend systems*. J. Chem. Phys. **117**(6), 2961 (2002). [13](#)
- [52] C. Im, W. Tian, H. Bässler, A. Fechtenkötter, M. D. Watson, K. Müllen, H. Ba, K. Mu, A. Fechtenko, and I. Introduction. *Photoconduction in organic donor acceptor systems*. J. Chem. Phys. **119**(7), 3952 (2003). [13](#)
- [53] L. Kan and K. C. Kao. *Ultraviolet absorption and photoconduction spectra of polyimide films fabricated at various curing temperatures*. J. Chem. Phys. **98**(4), 3445 (1993). [13](#)
- [54] C. J. Brabec, G. Zerza, G. Cerullo, S. D. Silvestri, S. Luzzati, J. C. Hummelen, and S. Sariciftci. *Tracing photoinduced electron transfer process in conjugated polymer / fullerene bulk heterojunctions in real time*. Chem. Phys. Lett. **340**(June), 232 (2001). [14](#), [56](#)
- [55] J. Nelson. *Diffusion-limited recombination in polymer-fullerene blends and its influence on photocurrent collection*. Phys. Rev. B **67**, 1 (2003). [14](#), [123](#)

- [56] A. F. Nogueira, I. Montanari, J. Nelson, J. R. Durrant, C. Winder, N. S. Sariciftci, and C. Brabec. *Charge Recombination in Conjugated Polymer / Fullerene Blended Films Studied by Transient Absorption Spectroscopy*. *J. Phys. Chem. B* **107**(7), 1567 (2003). [14](#)
- [57] M. Theander, A. Yartsev, D. Zigmantas, V. Sundström, W. Mammo, M. Andersson, and O. Inganäs. *Photoluminescence quenching at a polythiophene/C60 heterojunction*. *Phys. Rev. B* **61**(19), 12957 (2000). [14](#), [20](#)
- [58] V. Dyakonov and E. Frankevich. *On the role played by polaron pairs in photophysical processes in semiconducting polymers*. *Chem. Phys.* **227**(1-2), 203 (1998). [14](#)
- [59] B. A. Gregg, J. Sprague, and M. W. Peterson. *Long-Range Singlet Energy Transfer in Perylene Bis(phenethylimide) Films*. *J. Phys. Chem. B* **101**(27), 5362 (1997). [14](#)
- [60] C. W. Tang. *Two-layer organic photovoltaic cell*. *Appl. Phys. Lett.* **48**(2), 183 (1986). [14](#), [20](#)
- [61] G. Chamberlain. *Organic solar cells: A review*. *Solar Cells* **8**(1), 47 (1983). [14](#)
- [62] G. Yu and A. J. Heeger. *Charge separation and photovoltaic conversion in polymer composites with internal donor/acceptor heterojunctions*. *J. Appl. Phys.* **78**(7), 4510 (1995). [14](#)
- [63] T. M. Clarke and J. R. Durrant. *Charge photogeneration in organic solar cells*. *Chem. Rev.* **110**(11), 6736 (2010). [15](#), [17](#), [65](#)
- [64] H. Imahori, K. Tamaki, D. M. Guldi, C. Luo, M. Fujitsuka, O. Ito, Y. Sakata, and S. Fukuzumi. *Modulating charge separation and charge recombination dynamics in porphyrin-fullerene linked dyads and triads: Marcus-normal versus inverted region*. *J. Am. Chem. Soc.* **123**(11), 2607 (2001). [66](#)

- [65] M. A. Loi, S. Toffanin, M. Muccini, M. Forster, U. Scherf, and M. Scharber. *Charge Transfer Excitons in Bulk Heterojunctions of a Polyfluorene Copolymer and a Fullerene Derivative*. *Adv. Funct. Mater.* **17**(13), 2111 (2007).
- [66] A. C. Morteani, P. Sreearunothai, L. M. Herz, R. H. Friend, and C. Silva. *Exciton Regeneration at Polymeric Semiconductor Heterojunctions*. *Phys. Rev. Lett.* **92**(24), 247402 (2004). [15](#), [26](#)
- [67] H. Ohkita, S. Cook, Y. Astuti, W. Duffy, S. Tierney, W. Zhang, M. Heeney, I. McCulloch, J. Nelson, D. D. C. Bradley, and J. R. Durrant. *Charge carrier formation in polythiophene/fullerene blend films studied by transient absorption spectroscopy*. *J. Am. Chem. Soc.* **130**(10), 3030 (2008). [76](#)
- [68] J. D. Servaites, B. M. Savoie, J. B. Brink, T. J. Marks, and M. A. Ratner. *Modeling geminate pair dissociation in organic solar cells: high power conversion efficiencies achieved with moderate optical bandgaps*. *Energy Environ. Sci.* **5**(8), 8343 (2012). [75](#)
- [69] K. Tvingstedt, K. Vandewal, A. Gadisa, F. Zhang, J. Manca, and O. Inganäs. *Electroluminescence from charge transfer states in polymer solar cells*. *J. Am. Chem. Soc.* **131**(33), 11819 (2009). [15](#), [76](#)
- [70] R. A. Marsh, C. Groves, and N. C. Greenham. *A microscopic model for the behavior of nanostructured organic photovoltaic devices*. *J. Appl. Phys.* **101**(8), 083509 (2007). [15](#), [21](#), [27](#), [48](#), [63](#), [66](#), [68](#), [88](#), [96](#), [102](#), [103](#), [127](#), [137](#), [147](#), [150](#), [170](#)
- [71] G. Dennler and N. N. S. Sariciftci. *Flexible Conjugated Polymer-Based Plastic Solar Cells: From Basics to Applications*. *Proc. IEEE* **93**(8), 1429 (2005). [16](#), [17](#)
- [72] D. Gundlach, S. Nelson, and T. Jackson. *Pentacene-based organic thin-film transistors*. *IEEE Trans. Electron Devices* **44**(8), 1325 (1997). [16](#)
- [73] J. G. Laquindanum, H. E. Katz, A. J. Lovinger, and A. Dodabalapur. *Morphological Origin of High Mobility in Pentacene Thin-Film Transistors*. *Chem. Mater.* **8**(11), 2542 (1996).

- [74] N. Karl and J. Marktanner. *Electron and Hole Mobilities in High Purity Anthracene Single Crystals*. Mol. Cryst. Liq. Cryst. Sci. Technol., Sect. A **355**(1), 149 (2001). [16](#)
- [75] V. Dyakonov. *The polymerfullerene interpenetrating network: one route to a solar cell approach*. Physica E **14**(1-2), 53 (2002). [16](#)
- [76] J.-F. Chang, B. Sun, D. W. Breiby, M. M. Nielsen, T. I. Sölling, M. Giles, I. McCulloch, and H. Sirringhaus. *Enhanced Mobility of Poly(3-hexylthiophene) Transistors by Spin-Coating from High-Boiling-Point Solvents*. Chem. Mater. **16**(23), 4772 (2004).
- [77] W. Geens, S. E. Shaheen, B. Wessling, C. J. Brabec, J. Poortmans, N. S. Sariciftci, and N. Serdar Sariciftci. *Dependence of field-effect hole mobility of PPV-based polymer films on the spin-casting solvent*. Org. Electron. **3**(3-4), 105 (2002).
- [78] R. Kline, M. McGehee, E. Kadnikova, J. Liu, and J. Fréchet. *Controlling the Field-Effect Mobility of Regioregular Polythiophene by Changing the Molecular Weight*. Adv. Mater. **15**(18), 1519 (2003). [16](#)
- [79] K. Feron, X. Zhou, W. J. Belcher, and P. C. Dastoor. *Exciton transport in organic semiconductors: Forster resonance energy transfer compared with a simple random walk*. J. Appl. Phys. **111**(4), 044510 (2012). [17](#), [66](#), [81](#)
- [80] L. Onsager. *Initial Recombination of Ions*. Phys. Rev. **54**(8), 554 (1938). [17](#), [26](#)
- [81] M. Abkowitz, J. S. Facci, and J. Rehm. *Direct evaluation of contact injection efficiency into small molecule based transport layers: Influence of extrinsic factors*. J. Appl. Phys. **83**(5), 2670 (1998). [17](#)
- [82] T. Schwieger, X. Liu, H. Peisert, B. Adolphi, N. Kiriya, and M. Knupfer. *Electronic properties of interfaces between different sexithiophenes and gold*. J. Appl. Phys. **97**(12), 123712 (2005). [17](#), [69](#)

- [83] M. A. Baldo and S. R. Forrest. *Interface-limited injection in amorphous organic semiconductors*. Phys. Rev. B **64**(8), 1 (2001). [17](#)
- [84] Y. Shen, A. R. Hosseini, M. H. Wong, and G. G. Malliaras. *How to make ohmic contacts to organic semiconductors*. ChemPhysChem **5**(1), 16 (2004). [17](#), [54](#)
- [85] R. Steim, F. R. Kogler, and C. J. Brabec. *Interface materials for organic solar cells*. J. Mater. Chem. **20**(13), 2499 (2010). [17](#), [117](#), [121](#), [143](#)
- [86] C. L. Braun. *Electric field assisted dissociation of charge transfer states as a mechanism of photocarrier production*. J. Chem. Phys. **80**(9), 4157 (1984). [19](#), [26](#), [27](#)
- [87] J. J. Jasieniak, J. Seifert, J. Jo, T. Mates, and A. J. Heeger. *A Solution-Processed MoOx Anode Interlayer for Use within Organic Photovoltaic Devices*. Adv. Funct. Mater. **22**(12), 2594 (2012). [20](#)
- [88] N. S. Sariciftci, L. Smilowitz, a. J. Heeger, and F. Wudl. *Photoinduced electron transfer from a conducting polymer to buckminsterfullerene*. Science **258**(5087), 1474 (1992). [20](#)
- [89] J. J. M. Halls, K. Pichler, R. H. Friend, S. C. Moratti, and A. B. Holmes. *Exciton diffusion and dissociation in a poly(p-phenylenevinylene)/C60 heterojunction photovoltaic cell*. Appl. Phys. Lett. **68**(22), 3120 (1996). [20](#)
- [90] T. Stubinger and W. Brütting. *Exciton diffusion and optical interference in organic donoracceptor photovoltaic cells*. J. Appl. Phys. **90**(7), 3632 (2001).
- [91] A. Haugeneder, M. Neges, C. Kallinger, W. Spirkel, U. Lemmer, J. Feldmann, U. Scherf, E. Harth, A. Gügel, and K. Müllen. *Exciton diffusion and dissociation in conjugated polymer/fullerene blends and heterostructures*. Phys. Rev. B **59**(23), 15346 (1999). [20](#)
- [92] J. J. M. Halls, C. A. Walsh, N. C. Greenham, E. A. Marseglia, R. H. Friend, S. C. Moratti, and A. B. Holmes. *Efficient photodiodes from interpenetrating polymer networks*. Nature **376**(6540), 498 (1995). [20](#)

- [93] G. Yu, J. Gao, J. C. Hummelen, F. Wudl, and A. J. Heeger. *Polymer Photovoltaic Cells: Enhanced Efficiencies via a Network of Internal Donor-Acceptor Heterojunctions*. *Science* **270**(5243), 1789 (1995). [20](#)
- [94] Y. Kim, S. A. Choulis, J. Nelson, D. D. C. Bradley, S. Cook, and J. R. Durrant. *Composition and annealing effects in polythiophene/fullerene solar cells*. *J. Mater. Sci.* **40**(6), 1371 (2005). [21](#), [104](#)
- [95] S. Miller, G. Fanchini, Y.-Y. Lin, C. Li, C.-W. Chen, W.-F. Su, and M. Chhowalla. *Investigation of nanoscale morphological changes in organic photovoltaics during solvent vapor annealing*. *J. Mater. Chem.* **18**(3), 306 (2008). [21](#)
- [96] F.-C. Chen, C.-J. Ko, J.-L. Wu, and W.-C. Chen. *Morphological study of P3HT:PCBM blend films prepared through solvent annealing for solar cell applications*. *Sol. Energy Mater. Sol. Cells* **94**(12), 2426 (2010). [21](#)
- [97] J.-p. Liu, K.-L. Choy, and X.-h. Hou. *Charge transport in flexible solar cells based on conjugated polymer and ZnO nanoparticulate thin films*. *J. Mater. Chem.* **21**(6), 1966 (2011). [21](#), [104](#)
- [98] G. Itskos, A. Othonos, T. Rauch, S. F. Tedde, O. Hayden, M. V. Kovalenko, W. Heiss, and S. A. Choulis. *Optical Properties of Organic Semiconductor Blends with Near-Infrared Quantum-Dot Sensitizers for Light Harvesting Applications*. *Adv. Energy Mater.* **1**(5), 802 (2011). [21](#)
- [99] Z. He, C. Zhong, X. Huang, W.-Y. Wong, H. Wu, L. Chen, S. Su, and Y. Cao. *Simultaneous enhancement of open-circuit voltage, short-circuit current density, and fill factor in polymer solar cells*. *Adv. Mater.* **23**(40), 4636 (2011). [22](#)
- [100] K. M. Coakley, Y. Liu, C. Goh, and M. D. McGehee. *Ordered Organic/Inorganic Bulk Heterojunction Photovoltaic Cells*. *MRS Bull.* **30**(01), 37 (2011). [22](#)
- [101] P. K. Watkins, A. B. Walker, and G. L. B. Verschoor. *Dynamical Monte Carlo modelling of organic solar cells: the dependence of internal quantum efficiency*

- on morphology*. Nano Lett. **5**(9), 1814 (2005). [23](#), [27](#), [48](#), [63](#), [76](#), [81](#), [82](#), [84](#), [96](#), [103](#), [147](#)
- [102] C. R. McNeill. *Morphology of all-polymer solar cells*. Energy Environ. Sci. **5**(2), 5653 (2012). [23](#), [143](#)
- [103] K. Landfester, R. Montenegro, U. Scherf, R. Güntner, U. Asawapirom, S. Patil, D. Neher, and T. Kietzke. *Semiconducting Polymer Nanospheres in Aqueous*. Adv. Mater. **14**(9), 651 (2002). [24](#), [147](#)
- [104] K. B. Burke, A. J. Stapleton, B. Vaughan, X. Zhou, A. L. D. Kilcoyne, W. J. Belcher, and P. C. Dastoor. *Scanning transmission x-ray microscopy of polymer nanoparticles: probing morphology on sub-10 nm length scales*. Nanotechnology **22**(26), 265710 (2011). [24](#), [149](#), [154](#)
- [105] E. Hittinger, A. Kokil, and C. Weder. *Synthesis and characterization of cross-linked conjugated polymer milli-, micro-, and nanoparticles*. Angew. Chem. Int. Ed. **43**(14), 1808 (2004). [24](#), [147](#)
- [106] A. J. Stapleton. *Nanoparticle Based Organic Photovoltaic Devices*. Phd thesis, University of Newcastle (2010). [24](#), [148](#), [149](#), [154](#), [162](#), [220](#)
- [107] K. B. Burke. *Characterisation of Organic Photovoltaics by Synchrotron Soft X-ray Techniques*. Phd thesis, University of Newcastle, Callaghan, NSW, Australia (2012). [24](#), [149](#)
- [108] J. Chuan, L. Tianze, H. Luan, and Z. Xia. *Research on the Characteristics of Organic Solar Cells*. J. Phys. Conf. Ser. **276**, 012169 (2011). [26](#)
- [109] A. Cheknane, H. S. Hilal, F. Djeflal, B. Benyoucef, and J.-P. Charles. *An equivalent circuit approach to organic solar cell modelling*. Microelectron. J. **39**(10), 1173 (2008). [26](#), [119](#)
- [110] S. Yoo, B. Domercq, and B. Kippelen. *Intensity-dependent equivalent circuit parameters of organic solar cells based on pentacene and C₆₀*. J. Appl. Phys. **97**(10), 103706 (2005). [26](#)

- [111] J. Huang, J. Yu, H. Lin, and Y. Jiang. *Polaron-pair-dependent equivalent circuit parameters of organic solar cells based on CuPc and C60*. Chin. Sci. Bull. **55**(13), 1317 (2010). [26](#)
- [112] L. J. A. Koster, E. C. P. Smits, V. D. Mihailetschi, and P. W. M. Blom. *Device model for the operation of polymer/fullerene bulk heterojunction solar cells*. Phys. Rev. B **72**(8), 085205 (2005). [26](#), [119](#)
- [113] R. Hausermann, E. Knapp, M. Moos, N. A. Reinke, T. Flatz, and B. Ruhstaller. *Coupled optoelectronic simulation of organic bulk-heterojunction solar cells: Parameter extraction and sensitivity analysis*. J. Appl. Phys. **106**(10), 104507 (2009). [26](#), [27](#)
- [114] M. Tachiya. *Breakdown of the Onsager theory of geminate ion recombination*. J. Chem. Phys. **89**(11), 6929 (1988). [27](#)
- [115] M. Wojcik and M. Tachiya. *Geminate charge recombination with distance-dependent intrinsic reaction rate: Escape probability and its electric field effect*. Radiat. Phys. Chem. **74**(3-4), 132 (2005). [27](#)
- [116] L. J. A. Koster, V. D. Mihailetschi, and P. W. M. Blom. *Bimolecular recombination in polymer/fullerene bulk heterojunction solar cells*. Appl. Phys. Lett. **88**(5), 052104 (2006). [27](#), [102](#)
- [117] F. Yang and S. R. Forrest. *Photocurrent generation in nanostructured organic solar cells*. ACS Nano **2**(5), 1022 (2008). [27](#), [81](#), [82](#), [88](#), [96](#), [102](#), [103](#)
- [118] M. Jørgensen, K. Norrman, S. A. Gevorgyan, T. Tromholt, B. Andreasen, and F. C. Krebs. *Stability of polymer solar cells*. Adv. Mater. **24**(5), 580 (2012). [28](#), [192](#), [203](#)
- [119] M. Cecchi, H. Smith, and D. Braun. *Method to optimize polymer film spin coating for polymer LED displays*. Synth. Met. **121**(1-3), 1715 (2001). [31](#)

- [120] S. Panigrahi, S. Waugh, A. K. Hassan, S. K. Rout, and A. K. Ray. *Study of Spin Coated Organic Thin Film Under Spectrophotometer*. Indian J. Phys. **78**(8), 823 (2004). [31](#)
- [121] C. J. Brabec, S. E. Shaheen, C. Winder, N. S. Sariciftci, and P. Denk. *Effect of LiF/metal electrodes on the performance of plastic solar cells*. Appl. Phys. Lett. **80**(7), 1288 (2002). [32](#)
- [122] Z. Xu, L. M. Chen, G. Yang, C. H. Huang, J. Hou, Y. Wu, G. Li, C. S. Hsu, and Y. Yang. *Vertical Phase Separation in Poly (3-hexylthiophene): Fullerene Derivative Blends and its Advantage for Inverted Structure Solar Cells*. Adv. Funct. Mater. **19**(8), 1227 (2009). [34](#), [109](#), [121](#)
- [123] H. Hoppe, M. Niggemann, C. Winder, J. Kraut, R. Hiesgen, A. Hinsch, D. Meissner, and N. S. Sariciftci. *Nanoscale Morphology of Conjugated Polymer/Fullerene-Based Bulk- Heterojunction Solar Cells*. Adv. Funct. Mater. **14**(10), 1005 (2004). [37](#), [104](#)
- [124] H. Hoppe, N. S. Sariciftci, and D. Meissner. *Optical constants of conjugated polymer/fullerene based bulk-heterojunction organic solar cells*. Mol. Cryst. Liq. Cryst. Sci. **385**(1), 113 (2002). [37](#), [104](#)
- [125] M. C. Gurau, D. M. Delongchamp, B. M. Vogel, E. K. Lin, D. A. Fischer, S. Sambasivan, and L. J. Richter. *Measuring molecular order in poly(3-alkylthiophene) thin films with polarizing spectroscopies*. Langmuir **23**(2), 834 (2007). [37](#), [104](#)
- [126] D. T. Gillespie. *Exact stochastic simulation of coupled chemical reactions*. J. Phys. Chem. **81**(25), 2340 (1977). [43](#)
- [127] D. T. Gillespie. *A general method for numerically simulating the stochastic time evolution of coupled chemical reactions*. J. Comput. Phys. **22**(4), 403 (1976). [44](#)
- [128] C. Groves, R. G. E. Kimber, and A. B. Walker. *Simulation of loss mechanisms in organic solar cells: A description of the mesoscopic Monte Carlo technique*

- and an evaluation of the first reaction method.* J. Chem. Phys. **133**(14), 144110 (2010). [44](#), [63](#)
- [129] M. Rice and Y. Gartstein. *Excitons and Interband Excitations in Conducting Polymers Based on Phenylene.* Phys. Rev. Lett. **73**(18), 2504 (1994). [47](#)
- [130] P. Peumans, S. Uchida, and S. R. Forrest. *Efficient bulk heterojunction photovoltaic cells using small-molecular-weight organic thin films.* Nature **425**(6954), 158 (2003). [47](#), [49](#), [111](#)
- [131] M. T. Dang, L. Hirsch, and G. Wantz. *P3HT:PCBM, Best Seller in Polymer Photovoltaic Research.* Adv. Mater. **23**(31), 3597 (2011). [48](#), [189](#)
- [132] U. Wolff. *Collective Monte Carlo updating for spin systems.* Phys. Rev. Lett. **62**(4), 361 (1989). [49](#)
- [133] B. P. Lyons, N. Clarke, and C. Groves. *The Quantitative Effect of Surface Wetting Layers on the Performance of Organic Bulk Heterojunction Photovoltaic Devices.* J. Phys. Chem. C **115**(45), 22572 (2011). [49](#), [143](#)
- [134] Z. Gu, T. Kanto, K. Tsuchiya, and K. Ogino. *Synthesis of Poly(3-hexylthiophene)-b-poly(ethylene oxide) for Application to Photovoltaic Device.* J. Photopolym. Sci. Technol. **23**(3), 405 (2010). [50](#)
- [135] B. Ray and M. A. Alam. *Random vs regularized OPV: Limits of performance gain of organic bulk heterojunction solar cells by morphology engineering.* Sol. Energy Mater. Sol. Cells **99**, 204 (2012). [50](#)
- [136] F. C. Jamieson, E. B. Domingo, T. McCarthy-Ward, M. Heeney, N. Stingelin, and J. R. Durrant. *Fullerene crystallisation as a key driver of charge separation in polymer/fullerene bulk heterojunction solar cells.* Chem. Sci. **3**(2), 485 (2012). [50](#)
- [137] H. Bässler. *Charge Transport in Disordered Organic Photoconductors a Monte Carlo Simulation Study.* Phys. Status Solidi B **175**(1), 15 (1993). [52](#), [53](#)

- [138] R. Kersting, U. Lemmer, R. F. Mahrt, K. Leo, H. Kurz, H. Bässler, and E. O. Göbel. *Femtosecond energy relaxation in π -conjugated polymers*. Phys. Rev. Lett. **70**(24), 3820 (1993). [52](#)
- [139] M. Scheidler, U. Lemmer, R. Kersting, S. Karg, W. Riess, B. Cleve, R. F. Mahrt, H. Kurz, H. Bässler, E. O. Göbel, and P. Thomas. *Monte Carlo study of picosecond exciton relaxation and dissociation in poly(phenylenevinylene)*. Phys. Rev. B **54**(8), 5536 (1996). [53](#), [63](#), [82](#), [88](#), [96](#)
- [140] V. D. Mihailetschi, P. W. M. Blom, J. C. Hummelen, and M. T. Rispen. *Cathode dependence of the open-circuit voltage of polymer:fullerene bulk heterojunction solar cells*. J. Appl. Phys. **94**(10), 6849 (2003). [54](#)
- [141] C. Uhrich, D. Wynands, S. Olthof, M. K. Riede, K. Leo, S. Sonntag, B. Maennig, and M. Pfeiffer. *Origin of open circuit voltage in planar and bulk heterojunction organic thin-film photovoltaics depending on doped transport layers*. J. Appl. Phys. **104**(4), 043107 (2008). [54](#)
- [142] W. J. Potscavage, S. Yoo, and B. Kippelen. *Origin of the open-circuit voltage in multilayer heterojunction organic solar cells*. Appl. Phys. Lett. **93**(19), 193308 (2008). [54](#)
- [143] C. Zhang, S.-w. Tong, C.-y. Jiang, E.-t. Kang, D. S. H. Chan, and C. Zhu. *Origin of Different Dependences of Open-Circuit Voltage on the Electrodes in Layered and Bulk Heterojunction Organic Photovoltaic Cells*. IEEE Trans. Electron Devices **57**(2), 397 (2010). [54](#)
- [144] L. J. A. Koster, V. D. Mihailetschi, R. Ramaker, and P. W. M. Blom. *Light intensity dependence of open-circuit voltage of polymer:fullerene solar cells*. Appl. Phys. Lett. **86**(12), 123509 (2005). [54](#), [137](#), [139](#)
- [145] B. Ray, M. S. Lundstrom, and M. A. Alam. *Can morphology tailoring improve the open circuit voltage of organic solar cells?* Appl. Phys. Lett. **100**(1), 013307 (2012). [54](#), [75](#), [139](#)

- [146] D. J. Griffiths. *Introduction to electrodynamics* (Prentice Hall, 1999). [55](#), [56](#)
- [147] P. Yu, D. Mencaraglia, A. Darga, A. Migan, R. Rabdbeh, B. Ratier, and A. Molliton. *Investigation of electric charge transport in conjugated polymer P3HT:PCBM solar cell with temperature dependent current and capacitance measurements*. *Phys. Status Solidi C* **7**(3-4), 1000 (2010). [55](#), [103](#), [127](#), [150](#)
- [148] M. Casalegno, G. Raos, and R. Po. *Methodological assessment of kinetic Monte Carlo simulations of organic photovoltaic devices: the treatment of electrostatic interactions*. *J. Chem. Phys.* **132**(9), 094705 (2010). [55](#), [81](#), [83](#)
- [149] M. T. Lloyd, Y.-F. Lim, and G. G. Malliaras. *Two-step exciton dissociation in poly(3-hexylthiophene)/fullerene heterojunctions*. *Appl. Phys. Lett.* **92**(14), 143308 (2008). [56](#)
- [150] X. Gong, S.-H. Lim, J. C. Ostrowski, D. Moses, C. J. Bardeen, and G. C. Bazan. *Phosphorescence from iridium complexes doped into polymer blends*. *J. Appl. Phys.* **95**(3), 948 (2004). [57](#)
- [151] S. Cook, R. Katoh, and A. Furube. *Ultrafast Studies of Charge Generation in PCBM:P3HT Blend Films following Excitation of the Fullerene PCBM*. *J. Phys. Chem. C* **113**(6), 2547 (2009). [57](#)
- [152] G. Horowitz, P. Valat, F. Garnier, F. Kouki, and V. Wintgens. *Photoinduced spontaneous and stimulated emission in sexithiophene single crystals*. *Opt. Mater.* **9**(1-4), 46 (1998). [60](#)
- [153] P. E. Shaw, A. Ruseckas, and I. D. W. Samuel. *Exciton Diffusion Measurements in Poly(3-hexylthiophene)*. *Adv. Mater.* **20**(18), 3516 (2008). [57](#), [60](#), [103](#), [127](#), [129](#), [150](#), [157](#)
- [154] X. Cheng, K. Ichimura, D. Fichou, and T. Kobayashi. *Nanosecond time-resolved absorption spectra of thin films of α -conjugated thiophene oligomers*. *Chem. Phys. Lett.* **185**(3-4), 286 (1991). [57](#)

- [155] S. Cook, H. Ohkita, J. R. Durrant, Y. Kim, J. J. Benson-Smith, J. Nelson, and D. D. C. Bradley. *Singlet exciton transfer and fullerene triplet formation in polymer-fullerene blend films*. Appl. Phys. Lett. **89**(10), 101128 (2006). [58](#), [103](#), [127](#), [150](#)
- [156] Y. Shao and Y. Yang. *Efficient Organic Heterojunction Photovoltaic Cells Based on Triplet Materials*. Adv. Mater. **17**(23), 2841 (2005). [57](#), [82](#)
- [157] S. Brazovskii and N. Kirova. *Physical theory of excitons in conducting polymers*. Chem. Soc. Rev. **39**(7), 2453 (2010). [57](#)
- [158] C. Deibel. *Chapter 9 - Photocurrent Generation in Organic Solar Cells*, vol. 85 (Elsevier Inc., 2011). [57](#), [170](#)
- [159] T. N. Singh-Rachford and F. N. Castellano. *Photon upconversion based on sensitized triplet-triplet annihilation*. Coord. Chem. Rev. **254**(21-22), 2560 (2010). [58](#)
- [160] T. F. Schulze, Y. Y. Cheng, B. Fückel, R. W. MacQueen, A. Danos, N. J. L. K. Davis, M. J. Y. Tayebjee, T. Khoury, R. G. C. R. Clady, N. J. Ekins-Daukes, M. J. Crossley, B. Stannowski, K. Lips, and T. W. Schmidt. *Photochemical Upconversion Enhanced Solar Cells: Effect of a Back Reflector*. Aust. J. Chem. **65**(5), 480 (2012). [58](#)
- [161] M. B. Smith and J. Michl. *Singlet fission*. Chem. Rev. **110**(11), 6891 (2010). [58](#)
- [162] J. Lee, P. Jadhav, and M. A. Baldo. *High efficiency organic multilayer photodetectors based on singlet exciton fission*. Appl. Phys. Lett. **95**(3), 033301 (2009). [58](#)
- [163] B. Ehrler, M. W. B. Wilson, A. Rao, R. H. Friend, and N. C. Greenham. *Singlet exciton fission-sensitized infrared quantum dot solar cells*. Nano Lett. **12**(2), 1053 (2012). [59](#)

- [164] P. D. Reusswig, D. N. Congreve, N. J. Thompson, and M. A. Baldo. *Enhanced external quantum efficiency in an organic photovoltaic cell via singlet fission exciton sensitizer*. *Appl. Phys. Lett.* **101**(11), 113304 (2012). [59](#)
- [165] I. A. Howard, R. Mauer, M. Meister, and F. Laquai. *Effect of morphology on ultrafast free carrier generation in polythiophene:fullerene organic solar cells*. *J. Am. Chem. Soc.* **132**(42), 14866 (2010). [59](#)
- [166] M. F. Fuhrer, J. Connolly, M. Mazzer, I. M. Ballard, D. Johnson, K. W. J. Barnham, A. Bessiere, J. S. Roberts, R. Airey, C. Calder, G. Hill, T. Tibbits, M. Pate, and M. Geen. *Hot carriers in strain balanced quantum well solar cells*. In *33rd IEEE Photovoltaic Specialists Conference*, vol. 3, pp. 1–5 (IEEE, 2008). [59](#)
- [167] M. Saba, C. Ciuti, S. Kundermann, J. Staehli, B. Deveaud, J. Bloch, V. Thierry-Mieg, R. André, L. Si Dang, G. Bongiovanni, and A. Mura. *Towards a Room Temperature Polariton Amplifier*. *Phys. Status Solidi A* **190**(2), 315 (2002). [59](#)
- [168] F. Spano. *Fermion excited states in one-dimensional molecular aggregates with site disorder: Nonlinear optical response*. *Phys. Rev. Lett.* **67**(24), 3424 (1991). [59](#)
- [169] M. C. Heiber and A. Dhinojwala. *Dynamic Monte Carlo modeling of exciton dissociation in organic donor-acceptor solar cells*. *J. Chem. Phys.* **137**(1), 014903 (2012). [59](#)
- [170] S. Cook, A. Furube, R. Katoh, and L. Han. *Estimate of singlet diffusion lengths in PCBM films by time-resolved emission studies*. *Chem. Phys. Lett.* **478**(1-3), 33 (2009). [60](#), [83](#), [129](#), [157](#)
- [171] T. Förster. *Zwischenmolekulare Energiewanderung und Fluoreszenz*. *Ann. Phys.* **437**(1-2), 55 (1948). [60](#), [82](#)

- [172] A. B. Walker, A. Kambili, and S. J. Martin. *Electrical transport modelling in organic electroluminescent devices*. J. Phys. Condens. Matter **14**(47), 9825 (2002). [62](#), [63](#)
- [173] A. Miller and E. Abrahams. *Impurity Conduction at Low Concentrations*. Phys. Rev. **120**(3), 745 (1960). [63](#)
- [174] R. A. Marcus. *On the Theory of Oxidation Reduction Reactions Involving Electron Transfer. I*. J. Chem. Phys. **42**(1952), 966 (1956). [63](#)
- [175] N. S. Hush. *Adiabatic theory of outer sphere electron-transfer reactions in solution*. Trans. Faraday Soc. **57**, 557 (1961). [63](#)
- [176] J. Mattay, ed. *Photoinduced Electron Transfer I*, vol. 156 of *Topics in Current Chemistry* (Springer Berlin Heidelberg, Berlin, Heidelberg, 1990). [63](#), [67](#)
- [177] R. G. E. Kimber, A. B. Walker, G. E. Schröder-Turk, and D. J. Cleaver. *Bicontinuous minimal surface nanostructures for polymer blend solar cells*. PCCP **12**(4), 844 (2010). [63](#), [68](#), [147](#)
- [178] L. Meng, D. Wang, Q. Li, Y. Yi, J.-L. Brédas, and Z. Shuai. *An improved dynamic Monte Carlo model coupled with Poisson equation to simulate the performance of organic photovoltaic devices*. J. Chem. Phys. **134**(12), 124102 (2011). [63](#), [68](#), [69](#), [70](#), [76](#), [102](#)
- [179] G. Grampp. *The Marcus Inverted Region from Theory to Experiment*. Angew. Chem. Int. Ed. **32**(5), 691 (1993). [66](#)
- [180] H. Imahori, D. M. Guldi, K. Tamaki, Y. Yoshida, C. Luo, Y. Sakata, and S. Fukuzumi. *Charge separation in a novel artificial photosynthetic reaction center lives 380 ms*. J. Am. Chem. Soc. **123**(27), 6617 (2001). [66](#), [68](#)
- [181] D. C. Coffey, B. W. Larson, A. W. Hains, J. B. Whitaker, N. Kopidakis, O. V. Boltalina, S. H. Strauss, and G. Rumbles. *An Optimal Driving Force for Converting Excitons into Free Carriers in Excitonic Solar Cells*. J. Phys. Chem. C **116**(16), 8916 (2012). [66](#), [103](#), [127](#), [150](#), [222](#)

- [182] J. Bolt, N. Mataga, and G. McLendon, eds. *Electron Transfer in Inorganic, Organic and Biological Systems* (American Chemical Society, Washington, DC, 1991). 66
- [183] H. L. Tavernier and M. D. Fayer. *Distance Dependence of Electron Transfer in DNA: The Role of the Reorganization Energy and Free Energy*. J. Phys. Chem. B **104**(48), 11541 (2000). 67
- [184] B. P. Lyons, N. Clarke, and C. Groves. *The relative importance of domain size, domain purity and domain interfaces to the performance of bulk-heterojunction organic photovoltaics*. Energy Environ. Sci. pp. 7657–7663 (2012). 68, 76
- [185] U. Wolf, V. Arkhipov, and H. Bässler. *Current injection from a metal to a disordered hopping system. I. Monte Carlo simulation*. Phys. Rev. B **59**(11), 7507 (1999). 68, 69
- [186] Z. Liu, M. Kobayashi, B. C. Paul, Z. Bao, and Y. Nishi. *Fermi level depinning at metal-organic semiconductor interface for low-resistance Ohmic contacts*. In *2009 IEEE International Electron Devices Meeting (IEDM)*, pp. 1–4 (IEEE, 2009). 68, 69
- [187] J. A. Freire and G. Voss. *Master equation approach to charge injection and transport in organic insulators*. J. Chem. Phys. **122**(12), 124705 (2005). 68, 69
- [188] K. Feron, T. J. Nagle, L. J. Rozanski, B. B. Gong, and C. J. Fell. *Spatially resolved photocurrent measurements of organic solar cells: Tracking water ingress at edges and pinholes*. Sol. Energy Mater. Sol. Cells **109**, 169 (2013). 68, 191
- [189] S. Novikov and G. Malliaras. *Roughness-induced energetic disorder at the metal/organic interface*. Phys. Rev. B **73**(3), 1 (2006). 69
- [190] J. Godlewski. *Currents and photocurrents in organic materials determined by the interface phenomena*. Adv. Colloid Interface Sci. **116**(1-3), 227 (2005). 69, 117

- [191] L. J. A. Koster, V. D. Mihailetschi, H. Xie, and P. W. M. Blom. *Origin of the light intensity dependence of the short-circuit current of polymer/fullerene solar cells*. Appl. Phys. Lett. **87**(20), 203502 (2005). [72](#), [137](#), [170](#)
- [192] N. Giebink, G. Wiederrecht, M. Wasielewski, and S. Forrest. *Ideal diode equation for organic heterojunctions. I. Derivation and application*. Phys. Rev. B **82**(15), 1 (2010). [72](#), [123](#), [131](#), [135](#)
- [193] P. A. van Hal, S. C. J. Meskers, and R. A. J. Janssen. *Photoinduced energy and electron transfer in oligo(p -phenylene vinylene)-fullerene dyads*. Appl. Phys. A **79**(1), 41 (2004). [75](#)
- [194] R. A. Street and M. Schoendorf. *Interface state recombination in organic solar cells*. Phys. Rev. B **81**(20), 1 (2010). [76](#), [111](#), [117](#)
- [195] L. Meng, Y. Shang, Q. Li, Y. Li, X. Zhan, Z. Shuai, R. G. E. Kimber, and A. B. Walker. *Dynamic Monte Carlo Simulation for Highly Efficient Polymer Blend Photovoltaics*. J. Phys. Chem. B **114**(1), 36 (2010). [81](#), [82](#), [103](#), [127](#), [147](#), [150](#)
- [196] K. A. Colby, J. J. Burdett, R. F. Frisbee, L. Zhu, R. J. Dillon, and C. J. Bardeen. *Electronic energy migration on different time scales: concentration dependence of the time-resolved anisotropy and fluorescence quenching of Lumogen Red in poly(methyl methacrylate)*. J. Phys. Chem. A **114**(10), 3471 (2010). [82](#), [86](#)
- [197] S. Athanasopoulos, E. V. Emelianova, A. B. Walker, and D. Beljonne. *Exciton diffusion in energetically disordered organic materials*. Phys. Rev. B **80**(19), 195209 (2009). [82](#), [86](#), [92](#)
- [198] A. Mani, J. Schoonman, and A. Goossens. *Photoluminescence study of sexithiophene thin films*. J. Phys. Chem. B **109**(11), 4829 (2005). [82](#), [83](#), [85](#), [91](#)
- [199] Y. C. Zhou, Y. Wu, L. L. Ma, J. Zhou, X. M. Ding, and X. Y. Hou. *Exciton migration in organic thin films*. J. Appl. Phys. **100**(2), 023712 (2006). [82](#)

- [200] A. Richter, R. Ries, K. Szulzewsky, B. Pietzak, and R. Smith. *The growth mechanisms and morphology of C60 films on different substrates*. Surf. Sci. **394**(1-3), 201 (1997). [83](#)
- [201] K. Yase, N. Ara-Kato, T. Hanada, H. Takiguchi, Y. Yoshida, G. Back, K. Abe, and N. Tanigaki. *Aggregation mechanism in fullerene thin films on several substrates*. Thin Solid Films **331**(1-2), 131 (1998).
- [202] Y. Kim, L. Jiang, T. Iyoda, K. Hashimoto, and A. Fujishima. *AFM study of surface phenomena based on C60 film growth*. Appl. Surf. Sci. **130-132**, 602 (1998). [83](#)
- [203] M. Terekhin, N. Svechnikov, V. Stankevitch, A. Kolmakov, V. Stepanov, N. Bezmelnitsin, M. Kamada, K. Kan'no, and I. Akimoto. *Radiative transitions in C60 thin films under SR excitation*. J. Electron. Spectrosc. Relat. Phenom. **78**, 445 (1996). [83](#)
- [204] R. Taylor, J. P. Parsons, A. G. Avent, S. P. Rannard, T. J. Dennis, J. P. Hare, H. W. Kroto, and D. R. M. Walton. *Degradation of C60 by light*. Nature **351**(6324), 277 (1991). [83](#)
- [205] G. F. Burkhard, E. T. Hoke, S. R. Scully, and M. D. McGehee. *Incomplete exciton harvesting from fullerenes in bulk heterojunction solar cells*. Nano Lett. **9**(12), 4037 (2009). [83](#)
- [206] J. Lakowicz. *Principles of Fluorescence Spectroscopy* (Plenum Press, New York, 1983), 3 ed. [85](#), [90](#)
- [207] O. V. Mikhnenko, R. Ruiter, P. W. M. Blom, and M. A. Loi. *Direct Measurement of the Triplet Exciton Diffusion Length in Organic Semiconductors*. Phys. Rev. Lett. **108**(13), 137401 (2012). [86](#)
- [208] O. V. Mikhnenko, H. Azimi, M. Scharber, M. Morana, P. W. M. Blom, and M. A. Loi. *Exciton diffusion length in narrow bandgap polymers*. Energy Environ. Sci. **5**(5), 6960 (2012). [86](#)

- [209] C. Madigan and V. Bulović. *Modeling of Exciton Diffusion in Amorphous Organic Thin Films*. Phys. Rev. Lett. **96**(4), 046404 (2006). [88](#)
- [210] D. L. Dexter. *A Theory of Sensitized Luminescence in Solids*. J. Chem. Phys. **21**(5), 836 (1953). [88](#)
- [211] A. Köhler and H. Bässler. *What controls triplet exciton transfer in organic semiconductors?* J. Mater. Chem. **21**(12), 4003 (2011). [88](#)
- [212] C. Groves, J. C. Blakesley, and N. C. Greenham. *Effect of charge trapping on geminate recombination and polymer solar cell performance*. Nano Lett. **10**(3) Groves, C., Blakesley, J. C., & Greenham, N. C. (2010). Effect of charge trapping on geminate recombination and polymer solar cell performance. Nano Lett., 10(3), 10639. doi:10.1021/nl100080r), 1063 (2010). [93](#), [94](#), [95](#), [96](#)
- [213] C. Groves, R. A. Marsh, and N. C. Greenham. *Monte Carlo modeling of geminate recombination in polymer-polymer photovoltaic devices*. J. Chem. Phys. **129**(11), 114903 (2008). [96](#)
- [214] X. Yang and J. Loos. *Toward High-Performance Polymer Solar Cells: The Importance of Morphology Control*. Macromolecules **40**(5), 1353 (2007). [97](#)
- [215] K. Feron, C. J. Fell, L. J. Rozanski, B. B. Gong, N. Nicolaidis, W. J. Belcher, X. Zhou, E. Sesa, B. V. King, and P. C. Dastoor. *Towards the development of a virtual organic solar cell: An experimental and dynamic Monte Carlo study of the role of charge blocking layers and active layer thickness*. Appl. Phys. Lett. **101**(19), 193306 (2012). [101](#)
- [216] J. H. Choi, K.-I. Son, T. Kim, K. Kim, K. Ohkubo, and S. Fukuzumi. *Thienyl-substituted methanofullerene derivatives for organic photovoltaic cells*. J. Mater. Chem. **20**(3), 475 (2010). [102](#)
- [217] T. Liu and A. Troisi. *Absolute Rate of Charge Separation and Recombination in a Molecular Model of the P3HT/PCBM Interface*. J. Phys. Chem. C **115**(5), 2406 (2011). [102](#)

- [218] X. Ai, M. C. Beard, K. P. Knutsen, S. E. Shaheen, G. Rumbles, and R. J. Ellingson. *Photoinduced charge carrier generation in a poly(3-hexylthiophene) and methanofullerene bulk heterojunction investigated by time-resolved terahertz spectroscopy*. *J. Phys. Chem. B* **110**(50), 25462 (2006). [103](#)
- [219] Y. S. Eo, H. W. Rhee, B. D. Chin, and J.-W. Yu. *Influence of metal cathode for organic photovoltaic device performance*. *Synth. Met.* **159**(17-18), 1910 (2009). [103](#), [127](#), [150](#)
- [220] S. Falke, P. Eravuchira, A. Materny, and C. Lienau. *Raman spectroscopic identification of fullerene inclusions in polymer/fullerene blends*. *J. Raman Spectrosc.* **42**(10), 1897 (2011). [104](#)
- [221] N. A. Nismy, K. D. G. I. Jayawardena, A. A. D. T. Adikaari, and S. R. P. Silva. *Photoluminescence Quenching in Carbon Nanotube-Polymer/Fullerene Films: Carbon Nanotubes as Exciton Dissociation Centres in Organic Photovoltaics*. *Adv. Mater.* **23**, 3796 (2011). [104](#)
- [222] C. J. Fell, T. J. Nagle, L. J. Rozanski, and K. Feron. *Understanding the Performance of Organic Photovoltaic Mini-modules*. In *48th Annual Australian Solar Energy Society*, December (Canberra, Australia, 2010). [107](#)
- [223] S.-Y. Ma, Y.-M. Shen, P.-C. Yang, C.-S. Chen, and C.-F. Lin. *Morphological modification induced by external electric field during solution process of organic solar cells*. *Org. Electron.* **13**(2), 297 (2012). [109](#)
- [224] W. Möller and M. Posselt. *TRIDYN-FZR User Manual*. Tech. rep., Institute of Ion Beam Physics and Materials Research, Forschungszentrum Rossendorf (2001). [109](#), [115](#), [116](#)
- [225] W. Möller and W. Eckstein. *Tridyn A TRIM simulation code including dynamic composition changes*. *Phys. Res. B* **2**(1-3), 814 (1984). [109](#)
- [226] W. Eckstein and J. P. Biersack. *Computer simulation of two-component target sputtering*. *Appl. Phys. A* **37**(2), 95 (1985). [109](#)

- [227] M. Campoy-Quiles, T. Ferenczi, T. Agostinelli, P. G. Etchegoin, Y. Kim, T. D. Anthopoulos, P. N. Stavrinou, D. D. C. Bradley, and J. Nelson. *Morphology evolution via self-organization and lateral and vertical diffusion in polymer: fullerene solar cell blends*. *Nat. Mater.* **7**(2), 158 (2008). [111](#)
- [228] A. J. Parnell, A. D. F. Dunbar, A. J. Pearson, P. A. Staniec, A. J. C. Dennison, H. Hamamatsu, M. W. A. Skoda, D. G. Lidzey, and R. A. L. Jones. *Depletion of PCBM at the Cathode Interface in P3HT/PCBM Thin Films as Quantified via Neutron Reflectivity Measurements*. *Adv. Mater.* **22**(22), 2444 (2010). [111](#), [121](#)
- [229] H. J. Kim, H. H. Lee, and J.-J. Kim. *Real Time Investigation of the Interface between a P3HT:PCBM Layer and an Al Electrode during Thermal Annealing*. *Macromol. Rapid Commun.* **30**(14), 1269 (2009). [114](#), [115](#)
- [230] D. Briggs and M. Seah, eds. *Practical Surface Analysis: Ion and neutral spectroscopy (Volume 2)* (John Wiley and Sons, Chichester, 1996). [114](#), [115](#)
- [231] H. Wang, E. D. Gomez, J. Kim, Z. Guan, C. Jaye, D. A. Fischer, A. Kahn, and Y.-l. Loo. *Device Characteristics of Bulk-Heterojunction Polymer Solar Cells are Independent of Interfacial Segregation of Active Layers*. *Chem. Mater.* **23**(8), 2020 (2011). [115](#)
- [232] D. S. Germack, C. K. Chan, R. J. Kline, D. A. Fischer, D. J. Gundlach, M. F. Toney, L. J. Richter, and D. M. DeLongchamp. *Interfacial Segregation in Polymer/Fullerene Blend Films for Photovoltaic Devices*. *Macromolecules* **43**(8), 3828 (2010). [116](#)
- [233] H. Yan, P. Lee, N. R. Armstrong, A. Graham, G. A. Evmenenko, P. Dutta, and T. J. Marks. *High-performance hole-transport layers for polymer light-emitting diodes. Implementation of organosiloxane cross-linking chemistry in polymeric electroluminescent devices*. *J. Am. Chem. Soc.* **127**(9), 3172 (2005). [116](#)

- [234] M. Glatthaar, N. Mingirulli, B. Zimmermann, T. Ziegler, R. Kern, M. Niggemann, A. Hinsch, and A. Gombert. *Impedance spectroscopy on organic bulk-heterojunction solar cells*. Phys. Status Solidi A **202**(11), R125 (2005). [116](#)
- [235] J. Wagner, M. Gruber, A. Wilke, Y. Tanaka, K. Topczak, A. Steindamm, U. Hornmann, A. Opitz, Y. Nakayama, H. Ishii, J. Pflaum, N. Koch, and W. Brütting. *Identification of different origins for s-shaped current voltage characteristics in planar heterojunction organic solar cells*. J. Appl. Phys. **111**(5), 054509 (2012). [119](#), [121](#), [122](#), [123](#), [132](#)
- [236] B. Ecker, H.-j. Egelhaaf, R. Steim, J. Parisi, and E. von Hauff. *Understanding S-Shaped Current-Voltage Characteristics in Organic Solar Cells Containing a TiO_x Interlayer with Impedance Spectroscopy and Equivalent Circuit Analysis*. J. Phys. Chem. C **116**, 16333 (2012). [119](#), [120](#)
- [237] A. Wagenpfahl, D. Rauh, M. Binder, C. Deibel, and V. Dyakonov. *S-shaped current-voltage characteristics of organic solar devices*. Phys. Rev. B **82**(11), 115306 (2010). [120](#), [121](#), [122](#)
- [238] B. Tremolet de Villers, C. J. Tassone, S. H. Tolbert, and B. J. Schwartz. *Improving the Reproducibility of P3HT:PCBM Solar Cells by Controlling the PCBM/Cathode Interface*. The Journal of Physical Chemistry C **113**(44), 18978 (2009). [120](#), [121](#), [132](#)
- [239] B. Romero, G. del Pozo, and B. Arredondo. *Exact analytical solution of a two diode circuit model for organic solar cells showing S-shape using Lambert W-functions*. Sol. Energy **86**(10), 3026 (2012). [120](#)
- [240] F. A. de Castro, J. Heier, F. Nüesch, and R. Hany. *Origin of the Kink in Current-Density Versus Voltage Curves and Efficiency Enhancement of Polymer-C60 Heterojunction Solar Cells*. IEEE J. Sel. Top. Quantum Electron. **16**(6), 1690 (2010). [120](#), [123](#), [132](#), [141](#)

- [241] A. Kumar, S. Sista, and Y. Yang. *Dipole induced anomalous S-shape I-V curves in polymer solar cells*. J. Appl. Phys. **105**(9), 094512 (2009). [120](#), [123](#)
- [242] G. del Pozo, B. Romero, and B. Arredondo. *Evolution with annealing of solar cell parameters modeling the S-shape of the current-voltage characteristic*. Sol. Energy Mater. Sol. Cells **104**, 81 (2012). [121](#), [132](#), [138](#)
- [243] B. Xue, B. Vaughan, C.-h. Poh, K. B. Burke, L. Thomsen, A. Stapleton, X. Zhou, G. W. Bryant, W. Belcher, and P. C. Dastoor. *Vertical Stratification and Interfacial Structure in P3HT:PCBM Organic Solar Cells*. J. Phys. Chem. C **114**(37), 15797 (2010). [121](#)
- [244] G. Parthasarathy, C. Adachi, P. E. Burrows, and S. R. Forrest. *High-efficiency transparent organic light-emitting devices*. Appl. Phys. Lett. **76**(15), 2128 (2000). [121](#)
- [245] W. Tress, K. Leo, and M. Riede. *Effect of concentration gradients in ZnPc:C60 bulk heterojunction organic solar cells*. Sol. Energy Mater. Sol. Cells **95**(11), 2981 (2011). [122](#)
- [246] J. Schafferhans, A. Baumann, A. Wagenpfahl, C. Deibel, and V. Dyakonov. *Oxygen doping of P3HT:PCBM blends: Influence on trap states, charge carrier mobility and solar cell performance*. Org. Electron. **11**(10), 1693 (2010). [123](#), [124](#), [131](#), [135](#)
- [247] H. Gommans, B. Verreert, B. P. Rand, R. Muller, J. Poortmans, P. Heremans, and J. Genoe. *On the Role of Bathocuproine in Organic Photovoltaic Cells*. Adv. Funct. Mater. **18**(22), 3686 (2008). [123](#)
- [248] M. M. Mandoc, F. B. Kooistra, J. C. Hummelen, B. de Boer, and P. W. M. Blom. *Effect of traps on the performance of bulk heterojunction organic solar cells*. Appl. Phys. Lett. **91**(26), 263505 (2007). [123](#)
- [249] A. Baumann, J. Lorrmann, C. Deibel, and V. Dyakonov. *Bipolar charge transport*

- in poly(3-hexyl thiophene)/methanofullerene blends: A ratio dependent study.* Appl. Phys. Lett. **93**(25), 252104 (2008). [arXiv:0810.5460v3](#). 123
- [250] G.-J. A. H. Wetzelaer, M. Kuik, and P. W. M. Blom. *Identifying the Nature of Charge Recombination in Organic Solar Cells from Charge-Transfer State Electroluminescence.* Adv. Energy Mater. pp. n/a–n/a (2012). 124
- [251] Z. Chiguvare and V. Dyakonov. *Trap-limited hole mobility in semiconducting poly(3-hexylthiophene).* Phys. Rev. B **70**(23), 235207 (2004). 124
- [252] R. C. I. MacKenzie, T. Kirchartz, G. F. a. Dibb, and J. Nelson. *Modeling Nongeminate Recombination in P3HT:PCBM Solar Cells.* J. Phys. Chem. C **115**(19), 9806 (2011). 124
- [253] W. Tress, K. Leo, and M. Riede. *Influence of Hole-Transport Layers and Donor Materials on Open-Circuit Voltage and Shape of I-V Curves of Organic Solar Cells.* Adv. Funct. Mater. **21**(11), 2140 (2011). 132
- [254] J. Xue, B. P. Rand, S. Uchida, and S. R. Forrest. *Mixed donor-acceptor molecular heterojunctions for photovoltaic applications. II. Device performance.* J. Appl. Phys. **98**(12), 124903 (2005). 143
- [255] J. Drechsel, B. Männig, F. Kozlowski, D. Gebeyehu, A. Werner, M. Koch, K. Leo, and M. Pfeiffer. *High efficiency organic solar cells based on single or multiple PIN structures.* Thin Solid Films **451-452**, 515 (2004). 143
- [256] J. Chappell, D. G. Lidzey, P. C. Jukes, A. M. Higgins, R. L. Thompson, S. O'Connor, I. Grizzi, R. Fletcher, J. O'Brien, M. Geoghegan, and R. A. L. Jones. *Correlating structure with fluorescence emission in phase-separated conjugated-polymer blends.* Nature materials **2**(9), 616 (2003). 143
- [257] A. C. Arias, N. Corcoran, M. Banach, R. H. Friend, J. D. MacKenzie, and W. T. S. Huck. *Vertically segregated polymer-blend photovoltaic thin-film structures through surface-mediated solution processing.* Appl. Phys. Lett. **80**(10), 1695 (2002). 143

- [258] R.-Q. Png, P.-J. Chia, J.-C. Tang, B. Liu, S. Sivaramakrishnan, M. Zhou, S.-H. Khong, H. S. O. Chan, J. H. Burroughes, L.-L. Chua, R. H. Friend, and P. K. H. Ho. *High-performance polymer semiconducting heterostructure devices by nitrene-mediated photocrosslinking of alkyl side chains*. *Nat. Mater.* **9**(2), 152 (2010). [143](#)
- [259] H. J. Snaith and R. H. Friend. *Photovoltaic devices fabricated from an aqueous dispersion of polyfluorene nanoparticles using an electroplating method*. *Synth. Met.* **147**(1-3), 105 (2004). [147](#)
- [260] S. Ulum, N. Holmes, D. Darwis, K. Burke, A. David Kilcoyne, X. Zhou, W. Belcher, and P. Dastoor. *Determining the structural motif of P3HT:PCBM nanoparticulate organic photovoltaic devices*. *Sol. Energy Mater. Sol. Cells* **110**, 43 (2013). [148](#), [154](#)
- [261] A. L. D. Kilcoyne, T. Tylliszczak, W. F. Steele, S. Fakra, P. Hitchcock, K. Franck, E. Anderson, B. Harteneck, E. G. Rightor, G. E. Mitchell, A. P. Hitchcock, L. Yang, T. Warwick, and H. Ade. *Interferometer-controlled scanning transmission X-ray microscopes at the Advanced Light Source*. *J. Synchrotron Radiat.* **10**(2), 125 (2003). [149](#)
- [262] B. J. Leever, M. F. Durstock, M. D. Irwin, A. W. Hains, T. J. Marks, L. S. C. Pingree, and M. C. Hersam. *Spatially resolved photocurrent mapping of operating organic photovoltaic devices using atomic force photovoltaic microscopy*. *Appl. Phys. Lett.* **92**(1), 013302 (2008). [165](#)
- [263] D. C. Coffey, O. G. Reid, D. B. Rodovsky, G. P. Bartholomew, and D. S. Ginger. *Mapping local photocurrents in polymer/fullerene solar cells with photoconductive atomic force microscopy*. *Nano Lett.* **7**(3), 738 (2007). [165](#)
- [264] C. R. McNeill, H. Frohne, J. L. Holdsworth, J. E. Furst, B. V. King, and P. C. Dastoor. *Direct Photocurrent Mapping of Organic Solar Cells Using a Near-Field Scanning Optical Microscope*. *Nano Lett.* **4**(2), 219 (2004). [165](#)

- [265] O. Breitenstein and M. Langenkamp. *Lock-in Thermography - Basics and Use for Functional Diagnostics of Electronic Components* (Springer, Berlin, 2003). [166](#)
- [266] R. Rösch, D. M. Tanenbaum, M. Jørgensen, M. Seeland, M. Bärenklau, M. Hermenau, E. Voroshazi, M. T. Lloyd, Y. Galagan, B. Zimmermann, U. Würfel, M. Hösel, H. F. Dam, S. A. Gevorgyan, S. Kudret, W. Maes, L. Lutsen, D. Vanderzande, R. Andriessen, G. Teran-Escobar, M. Lira-Cantu, A. Rivaton, G. Y. Uzunolu, D. Germack, B. Andreasen, M. V. Madsen, K. Norrman, H. Hoppe, and F. C. Krebs. *Investigation of the degradation mechanisms of a variety of organic photovoltaic devices by combination of imaging techniques the ISOS-3 inter-laboratory collaboration*. *Energy Environ. Sci.* **5**(4), 6521 (2012). [166](#), [192](#), [193](#), [198](#)
- [267] M. Acciarri, S. Binetti, A. Racz, S. Pizzini, and G. Agostinelli. *Fast LBIC inline characterization for process quality control in the photovoltaic industry*. *Sol. Energy Mater. Sol. Cells* **72**(1-4), 417 (2002). [166](#)
- [268] C. R. Corwine, A. O. Pudov, M. Gloeckler, S. H. Demtsu, and J. R. Sites. *Copper inclusion and migration from the back contact in CdTe solar cells*. *Sol. Energy Mater. Sol. Cells* **82**, 481 (2004). [166](#)
- [269] G. E. Jellison, J. D. Budai, C. J. C. Bennett, J. Z. Tischler, C. E. Duty, V. Yelundur, and A. Rohatgi. *High-resolution x-ray and light beam induced current (LBIC) measurements of multicrystalline silicon solar cells*. In *2010 35th IEEE Photovoltaic Specialists Conference*, pp. 001715–001720 (IEEE, 2010). [166](#)
- [270] T. Jeranko, H. Tributsch, N. S. Sariciftci, and J. C. Hummelen. *Patterns of efficiency and degradation of composite polymer solar cells*. *Sol. Energy Mater. Sol. Cells* **83**, 247 (2004). [166](#), [193](#), [198](#)
- [271] F. C. Krebs, R. Søndergaard, and M. Jørgensen. *Printed metal back electrodes for R2R fabricated polymer solar cells studied using the LBIC technique*. *Sol. Energy Mater. Sol. Cells* **95**(5), 1348 (2011). [166](#)

- [272] Y. Galagan, B. Zimmermann, E. W. Coenen, M. Jørgensen, D. M. Tanenbaum, F. C. Krebs, H. Gortler, S. Sabik, L. H. Slooff, S. C. Veenstra, J. M. Kroon, and R. Andriessen. *Current Collecting Grids for ITO-Free Solar Cells*. *Adv. Energy Mater.* **2**(1), 103 (2012). [166](#)
- [273] T. R. Andersen, T. T. Larsen-Olsen, B. Andreasen, A. P. L. Böttiger, J. E. Carlé, M. Helgesen, E. Bundgaard, K. Norrman, J. W. Andreasen, M. Jørgensen, and F. C. Krebs. *Aqueous processing of low-band-gap polymer solar cells using roll-to-roll methods*. *ACS Nano* **5**(5), 4188 (2011). [166](#)
- [274] R. A. Serway. *Principles of Physics* (Saunders College Publications, London, 1998), 2nd ed. [173](#)
- [275] F. Wen, W. Li, Z. Liu, and H. Wei. *Effect of electrode modification on organic photovoltaic devices*. *Mater. Chem. Phys.* **95**(1), 94 (2006). [174](#)
- [276] I. Kim, H. M. Haverinen, J. Li, and G. E. Jabbour. *Enhancement of device performance of organic solar cells by an interfacial perylene derivative layer*. *ACS Appl. Mater. Interfaces* **2**(5), 1390 (2010). [174](#)
- [277] N. C. Nicolaidis, B. S. Routley, J. L. Holdsworth, W. J. Belcher, X. Zhou, and P. C. Dastoor. *Fullerene Contribution to Photocurrent Generation in Organic Photovoltaic Cells*. *J. Phys. Chem. C* **115**(15), 7801 (2011). [188](#)
- [278] T. J. Nagle, K. Feron, L. J. Rozanski, and C. J. Fell. *Lessons from Photocurrent Mapping of Organic Solar Cells*. In *47th Annual Conference of ANZSES*, October (Townsville, Australia, 2009). [191](#)
- [279] M. O. Reese, A. J. Morfa, M. S. White, N. Kopidakis, S. E. Shaheen, G. Rumbles, and D. S. Ginley. *Pathways for the degradation of organic photovoltaic P3HT:PCBM based devices*. *Sol. Energy Mater. Sol. Cells* **92**(7), 746 (2008). [192](#)
- [280] K. Norrman, N. Larsen, and F. Krebs. *Lifetimes of organic photovoltaics: Combining chemical and physical characterisation techniques to study degradation mechanisms*. *Sol. Energy Mater. Sol. Cells* **90**(17), 2793 (2006). [192](#)

- [281] E. Voroshazi, B. Verreet, A. Buri, R. Müller, D. Di Nuzzo, and P. Heremans. *Influence of cathode oxidation via the hole extraction layer in polymer:fullerene solar cells*. *Org. Electron.* **12**(5), 736 (2011). [192](#), [193](#), [198](#), [199](#), [200](#), [203](#), [206](#), [210](#)
- [282] K. Kawano, R. Pacios, D. Poplavskyy, J. Nelson, D. D. Bradley, and J. R. Durrant. *Degradation of organic solar cells due to air exposure*. *Sol. Energy Mater. Sol. Cells* **90**(20), 3520 (2006). [192](#), [197](#), [199](#), [210](#)
- [283] M. Hermenau, M. Riede, K. Leo, S. A. Gevorgyan, F. C. Krebs, and K. Norrman. *Water and oxygen induced degradation of small molecule organic solar cells*. *Sol. Energy Mater. Sol. Cells* **95**(5), 1268 (2011). [192](#), [193](#), [198](#), [200](#)
- [284] M. P. de Jong, L. J. van Ijzendoorn, and M. J. A. de Voigt. *Stability of the interface between indium-tin-oxide and poly(3,4-ethylenedioxythiophene)/poly(styrenesulfonate) in polymer light-emitting diodes*. *Appl. Phys. Lett.* **77**(14), 2255 (2000). [192](#)
- [285] F. So and D. Kondakov. *Degradation mechanisms in small-molecule and polymer organic light-emitting diodes*. *Adv. Mater.* **22**(34), 3762 (2010). [192](#)
- [286] M. M. de Kok, M. Buechel, S. I. E. Vulto, P. van de Weijer, E. A. Meulenkaamp, S. H. P. M. de Winter, A. J. G. Mank, H. J. M. Vorstenbosch, C. H. L. Weijtens, and V. van Elsbergen. *Modification of PEDOT:PSS as hole injection layer in polymer LEDs*. *Phys. Status Solidi A* **201**(6), 1342 (2004). [192](#)
- [287] K. Norrman, S. A. Gevorgyan, and F. C. Krebs. *Water-induced degradation of polymer solar cells studied by H₂(18)O labeling*. *ACS Appl. Mater. Interfaces* **1**(1), 102 (2009). [192](#), [198](#), [200](#), [206](#)
- [288] F. C. Krebs and K. Norrman. *Analysis of the failure mechanism for a stable organic photovoltaic during 10 000 h of testing*. *Prog. Photovoltaics Res. Appl.* **15**(8), 697 (2007). [196](#)

- [289] M. Seeland, R. Rosch, and H. Hoppe. *Luminescence imaging of polymer solar cells: Visualization of progressing degradation*. J. Appl. Phys. **109**(6), 064513 (2011). [192](#), [198](#), [206](#), [212](#)
- [290] M. Hermenau, S. Schubert, H. Klumbies, J. Fahlteich, L. Müller-Meskamp, K. Leo, and M. Riede. *The effect of barrier performance on the lifetime of small-molecule organic solar cells*. Sol. Energy Mater. Sol. Cells **97**, 102 (2012). [193](#), [198](#)
- [291] G. Li, C.-W. Chu, V. Shrotriya, J. Huang, and Y. Yang. *Efficient inverted polymer solar cells*. Appl. Phys. Lett. **88**(25), 253503 (2006). [193](#)
- [292] J. Kroon, M. Wienk, W. Verhees, and J. Hummelen. *Accurate efficiency determination and stability studies of conjugated polymer/fullerene solar cells*. Thin Solid Films **403-404**, 223 (2002). [193](#)
- [293] F. C. Krebs, J. Fyenbo, D. M. Tanenbaum, S. A. Gevorgyan, R. Andriessen, B. van Remoortere, Y. Galagan, and M. Jørgensen. *The OE-A OPV demonstrator anno domini 2011*. Energy Environ. Sci. **4**(10), 4116 (2011). [193](#)
- [294] D. M. Tanenbaum, H. F. Dam, R. Rösch, M. Jørgensen, H. Hoppe, and F. C. Krebs. *Edge sealing for low cost stability enhancement of roll-to-roll processed flexible polymer solar cell modules*. Sol. Energy Mater. Sol. Cells **97**, 157 (2012). [193](#)
- [295] A. Burgers, J. Eikelboom, A. Schonecker, and W. Sinke. *Improved treatment of the strongly varying slope in fitting solar cell I-V curves*. In *Conference Record of the Twenty Fifth IEEE Photovoltaic Specialists Conference*, pp. 569–572 (Ieee, 1996). [195](#)
- [296] M. T. Lloyd, C. H. Peters, A. Garcia, I. V. Kauvar, J. J. Berry, M. O. Reese, M. D. McGehee, D. S. Ginley, and D. C. Olson. *Influence of the hole-transport layer on the initial behavior and lifetime of inverted organic photovoltaics*. Sol. Energy Mater. Sol. Cells **95**(5), 1382 (2011). [199](#)

- [297] S. Ghorashi, A. Behjat, and R. Ajeian. *The effect of a buffer layer on the performance and optimal encapsulation time of ITO/CuPc/C60/buffer/Cu bilayer cells*. Sol. Energy Mater. Sol. Cells **96**, 50 (2012). [200](#)
- [298] S. Harris. *Microscopic theory for the diffusive evolution of an isoconcentration surface*. Phys. Rev. A **42**(6), 3504 (1990). [202](#)
- [299] A. L. Iordanskii and G. E. Zaikov. *The General Aspects of Diffusion of Water in Polymers*. Int. J. Polym. Mater. **24**(1-4), 193 (1994). [205](#)
- [300] F. A. Long and L. J. Thompson. *Diffusion of water vapor in polymers*. J. Polymer Sci. **15**(80), 413 (1955). [205](#)
- [301] N. Sultana and M. Wang. *Water Uptake and Diffusion in PHBV Tissue Engineering Scaffolds and Non-porous Thin Films*. In *Proceedings of the 2011 International Conference on Biomedical Engineering and Technology*, vol. 11, pp. 24–28 (2011). [205](#)
- [302] F. Müller-Plathe. *Diffusion of water in swollen poly(vinyl alcohol) membranes studied by molecular dynamics simulation*. J. Membr. Sci. **141**(2), 147 (1998). [205](#)
- [303] W. Wagner and A. Pruss. *International Equations for the Saturation Properties of Ordinary Water Substance. Revised According to the International Temperature Scale of 1990*. J. Phys. Chem. Ref. Data **22**(3), 783 (1993). [205](#)
- [304] M. Jørgensen, K. Norrman, and F. C. Krebs. *Stability/degradation of polymer solar cells*. Sol. Energy Mater. Sol. Cells **92**(7), 686 (2008). [206](#)
- [305] C.-F. Lin, S.-W. Liu, W.-F. Hsu, M. Zhang, T.-L. Chiu, Y. Wu, and J.-H. Lee. *Modification of silver anode and cathode for a top-illuminated organic photovoltaic device*. J. Phys. D: Appl. Phys. **43**(39), 395101 (2010). [209](#)
- [306] W.-J. Yoon and P. R. Berger. *4.8% efficient poly(3-hexylthiophene)-fullerene derivative (1:0.8) bulk heterojunction photovoltaic devices with plasma treated*

- AgO*[sub *x*]/indium tin oxide anode modification. *Appl. Phys. Lett.* **92**(1), 013306 (2008). [209](#)
- [307] U. Kumar Barik, S. Srinivasan, C. Nagendra, and a. Subrahmanyam. *Electrical and optical properties of reactive DC magnetron sputtered silver oxide thin films: role of oxygen*. *Thin Solid Films* **429**(1-2), 129 (2003). [209](#)
- [308] J. B. Kim, C. S. Kim, Y. S. Kim, and Y.-L. Loo. *Oxidation of silver electrodes induces transition from conventional to inverted photovoltaic characteristics in polymer solar cells*. *Appl. Phys. Lett.* **95**(18), 183301 (2009). [209](#)